8-20-2013 12:00 AM

Investigations of the Crystallization Processes of Molecular Sieves

Lu Zhang
The University of Western Ontario

Supervisor
Dr. Yining Huang
The University of Western Ontario

Graduate Program in Chemistry
A thesis submitted in partial fulfillment of the requirements for the degree in Doctor of Philosophy

Recommended Citation

Zhang, Lu, "Investigations of the Crystallization Processes of Molecular Sieves" (2013). *Electronic Thesis and Dissertation Repository*. 1457.
https://ir.lib.uwo.ca/etd/1457

Investigations of the Crystallization Processes of Molecular Sieves

(Thesis format: Integrated Article)

by

Lu Zhang

Graduate Program in Chemistry

A thesis submitted in partial fulfillment
of the requirements for the degree of
Doctor of Philosophy

The School of Graduate and Postdoctoral Studies
The University of Western Ontario
London, Ontario, Canada

ABSTRACT

Molecular sieves have been used extensively in industrial fields. A better understanding of their crystallization processes is very useful for controlling the structural properties in order to meet the industrial needs. This thesis focuses on examining the crystallization of several catalytically important molecular sieves by dry gel conversion (DGC) method which includes steam-assisted conversion (SAC) and vapor-phase transport (VPT), or hydrothermal synthesis (HTS) method or a combination of both.

For SAPO-34 templated by diethylamine, it crystallizes similarly under SAC and VPT conditions. It forms from the transformation of a semi-crystalline layered phase. When morpholine was used as the template, the crystallization pathways vary under different conditions. For DGC with HF, SAPO-34 in both triclinic and trigonal phases crystallizes from a highly crystalline prephase held by covalent bonds. For DGC without HF, SAPO-34 in pure trigonal form crystallizes from an amorphous phase held by weak nonbonding interactions. For VPT without HF, SAPO-34 forms from the transformation of an amorphous material and a dense phase. Moreover, all SAPO-34 samples show good catalytic properties.

For SAPO-37, its crystallization under HTS and DGC conditions follows somewhat similar pathway. It involves the formation of a precursor initially composed of only large cavities or both large cavities and quasi-sodalite cages. The size of a large cavity equals two directly connected supercages. Sodalite cages are formed at a later stage when increasing the crystallization time. They connect with the large cavities then forming SAPO-37 framework.

For zeolite LSX, it crystallizes from an amorphous aluminosilicate phase under HTS conditions. For ETS-10, a similar amorphous phase containing structure-building units of ETS-10 is formed under HTS and DGC conditions. Upon heating, the amorphous phase transforms to ETS-10 via a series of structural reorganization. Partially hydrated sodium cations are a crucial factor for the crystallization of ETS-10. For ETS-4, our work shows that small ETS-4 crystallites are formed quickly under HTS conditions. The crystallites are composed of layers, the distance between which is the same as the *d*-spacing of the *(001)* plane of ETS-4. Further heating results the formation of large ETS-4 crystals.

KEYWORDS: molecular sieves, aluminosilicates, silicoaluminophosphate, titanosilicates, dry gel conversion, hydrothermal synthesis, crystallization, assembly, cations.

CO-AUTHORSHIP

This thesis contains materials from previously published manuscripts. Dr. Yining Huang is the corresponding author on all published manuscripts and was responsible for the supervision of Lu Zhang during the course of her Ph.D. study. For copyright releases see the Appendix.

The manuscript presented in Chapter 3 (except the catalytic characterization) was published and co-authored by Lu Zhang, Jennifer Bates, Donghan Chen, Heng-Yong Nie, and Yining Huang. The manuscript presented in Chapter 6 was published and co-authored by Lu Zhang, Donghan Chen, Heng-Yong Nie, and Yining Huang. J. Bates is thanked for synthesizing part of the dry gel samples and the corresponding XRD characterization in Chapter 3. D. Chen is thanked for the AFM characterization in both chapters. L. Zhang performed all the other experimental work, and wrote the drafts of the two manuscripts. H. Y. Nie and Y. Huang edited the final manuscripts.

Dr. Xueliang Sun is thanked for generously allowing us to use his SEM instrument and Ms. Ruying Li for her kind helps with the SEM and EDS measurements presented in Chapters 3-6.

Dr. Yang Song is thanked for the Raman measurement presented in Chapters 7 and 8.

Dr. Peng Tian and Dr. Zhongmin Liu (Dalian Institute of Chemical Physics, China) are thanked for checking the catalytic performances of all SAPO-34 samples presented in Chapters 3-5.

Peng He is thanked for simulating ^{23}Na and ^{39}K NMR spectra presented in Chapters 7 and 8.

ACKNOWLEDGEMENTS

In the first 28 years of my life, completing the Ph.D. degree is probably the most challenging acitivity. It has been a great privilege to spend around five years in the Department of Chemistry at the Univeristy of Western Ontario. I have lots of great memories here.

First and foremost, undoubtedly, I must give gratitude to my advisor, Dr. Yining Huang, for giving me the opportunity to work under his supervision for the last five years. He provided patience, encouragement, and advice, which is necessary for me to proceed through the Ph.D. program and complete the thesis. I want to thank Dr. Huang for his from-time-to-time encouragement. He has been a strong supervisor to me throughout my school years at UWO, but he has always given me sufficient freedom to carry out independent work.

I would like to give sincerest thanks to my examiners: Dr. Paul Ragogna, Dr. John Corrigan, Dr. Jin Zhang, and Dr. Jianzhi Hu; and Dr. Andrew Watson for serving on the advisory committee. I also want to give special thanks to other academic staff in the department. To be specific, I thank Dr. Mathew Willans for his technical help on the NMR spectrometer. Without his guidance, I cannot run many NMR experiments smoothly. I also thank Dr. Xueliang Sun and Ms. Ruying Li for the SEM/ EDX instrument and Dr. Yang Song and Song's group for the Raman instrument in their labs. I thank Dr. Victor Terskikh at the *National Ultrahigh-field NMR Facility for Solids* for ^{39}K NMR characterization. Thanks to Dr. Heng-Yong Nie for the AFM help and Dr. Peng Tian and Dr. Zhongmin Liu for the catalytic tests in my thesis. Thanks to Dr. Nick Payne, Dr. Yang Song, Dr. Lyudmila Goncharova (Physics), and Dr. François Lagugné-Labarthet for the interesting courses that I took during my graduate career. I thank Ms. Kim Law (Earth Science) and Ms. Grace Yau

(Earth Science) for the powder XRD characterization, and Dr. Charles Wu (Earth Science) for the XRF characterization. I would also like to thank Ms. Darlene McDonald, who is always here whenever I have questions about the paperwork and other trivial things. I thank Ms. Anna Vandendries-Barr, Ms. Clara Fernandes, Ms. Lesley Tchorek, Ms. Marylou Hart, Ms. Monica Chirigel, Ms. Sandy McCaw, Ms. Sandy Zakaria Holtslag, Ms. Sherrie McPhee, Ms. Susan England, Mr. Barakat Misk, Mr. John Vanstone, and Mr. Robert Harbottle for their help and support throughout my graduate studies. The five-year financial support from the Chemistry Department is also gratefully acknowledged.

I would like to extend my thanks to my previous and present labmates: Dr. Andre Sutrisno, Dr. Banghao Chen, Dr. Li Liu, Dr. Wei (David) Wang, Dr. Zhimin Yan, Adam Macintosh, Donghan Chen, Janice Lee, Jennifer Bates, Jun Xu, Margaret Hanson, Maxwell Goldman, Peng He, Rachel Fu, Tetyana Levchenko, Yue Hu, and Zheng (Sonia) Lin. I thank Maxwell Goldman for proofreading the introduction chapter. During the past five years, I have learned patience, enthusiasm, and cooperation from them. These characteristics will accompany me for the whole lifetime.

Finally, I wish to thank my family (my parents and my younger brother) and my relatives in China. Their love and support have provided me inspiration and driving force during the tough times. I thank my husband, Hao Cong, whose love, strong support, and continuous encouragement allows me to finish the long journey.

TABLE OF CONTENTS

LIST OF TABLES

LIST OF FIGURES

LIST OF SCHEMES

LIST OF ABBREVIATIONS

3QMAS	triple-quantum magic-angle spinning
3R	three-membered ring
4R	four-membered ring
5R	five-membered ring
6R	six-membered ring
7R	seven-membered ring
8R	eight-membered ring
12R	twelve-membered ring
ABW	Li-A (Barrer and White)
AEL	aluminophosphate-eleven
AFM	atomic force microscopy
$AlPO_4$	aluminophosphate
AS	aluminosilicate
CHA	chabazite
CP	cross polarization
D6R	double six-membered ring
DEA	diethylamine
DGC	dry gel conversion
EDX	energy dispersive X-ray

ETAS	Engelhard titanoaluminosilicate
ETGS	Engelhard titanogallosilicate
FAU	faujasite
HF	hydrofluoric acid
HTS	hydrothermal synthesis
IR	infrared spectroscopy
IZA	international zeolite association
LSX	low silicon zeolite X
LTA	Linde type A
MAS	magic-angle spinning
MOR	morpholine
MQMAS	multiple-quantum magic-angle spinning
MTO	methanol to olefin
REDOR	rotational-echo double resonance
SAC	steam-assisted conversion
SAPO	silicoaluminophosphate
SBU	structural-building unit
SDA	structure-directing agent
SEM	scanning electron microscopy
SM	substitution mechanism

SS NMR	solid-state nuclear magnetic resonance
TEOS	tetraethyl orthosilicate
TMA	tetramethylammonium
TPA	tetrapropylammonium
TTMSS	tetrakis(trimethylsilyl)-silane
VPT	vapor-phase transport
XRD	X-ray diffraction
XRF	X-ray fluorescence
ZnPO-FAU	zincophosphate-faujasite
ZSM	zeolite Socony Mobil

LIST OF SYMBOLS

$\mathbf{B_1}$	strength of the radiofrequency field during a pulse
C_Q	nuclear quadrupolar coupling constant
F1, F2	indirect and direct dimensions in 3QMAS experiment
I , S	spin quantum number
γ	gyromagnetic ratio
δ_{iso}	isotropic chemical shift
θ	angle between two axes
λ	wavelength
v	spinning speed

Chapter 1 General Introduction

1.1 Introduction to microporous materials

Microporous materials, which are often referred to as molecular sieves, are porous solids containing channels and cavities with pore diameters in the range of 0.3-2.0 nm. The most well-known family of such materials is zeolites, which are microporous aluminosilicates. Zeolites are characterized by three-dimensional structures constructed of $[SiO_4]^{4-}$ and $[AlO_4]^{5-}$ tetrahedra linked to each other by sharing all oxygen atoms. They have negatively charged oxide frameworks with one framework Al^{3+} creating a charge, which is balanced by an exchangeable cation held electrostatically outside frameworks of zeolites.[1] Zeolites possess remarkable chemical and physical properties such as acidity and selective adsorption, which are closely related to their structures.

Since the early discovery of natural zeolites in the 1800s,[2] a lot of effort has been focused on their microporous properties and usefulness in industrial applications as ion-exchangers, adsorbents, and catalysts.[3] Later, due to the fact that natural zeolites cannot meet the expanding demands in industry, exploring synthetic zeolites became a necessity.[3] Such attempts weren't successful until Professor R. Barrer discovered the proper conditions to hydrothermally synthesize chabazite and mordenite in the 1940s.[4,5] During the 1980s another milestone in zeolite synthesis was the discovery of titanosilicates and aluminophosphates.[6,7] Shortly after this, a new class of zeolites, such as silicoaluminophosphates, were synthesized.[7,8]

1.1.1 Silicoaluminophosphates

1.1.2.1 Overview

Besides zeolites, another important type of molecular sieves are aluminophosphate ($AlPO_4$)-based materials ($AlPO_4$-*n*), which were discovered by Wilson *et al.* in 1982.[6] The structures of some $AlPO_4$-*n* are similar to those of zeolites, but many have novel topology. Their primary building units are formed by Al-O-P linkages as opposed to Si-O-Si or Si-O-Al bridges found in zeolites.[9] Due to the neutral frameworks of $AlPO_4$-*n*, the absence of Brønsted acidity has greatly limited their application as acidic catalysts. Nevertheless, substitution of P and Al atoms by Si can generate negatively charged frameworks, and thus increase the possibility of using the resulting materials, silicoaluminophosphates (SAPOs), as catalysts. The common linkages in SAPOs are Si-O-Al, Si-O-Si, and P-O-Al, while Si-O-P linkages have been proven to be energetically unfavorable.[9-11]

1.1.2.1 Nomenclature

To facilitate communication among researchers who work in the field of porous materials, a system of terms, the definitions of which are generally accepted, is thus proposed.[12] The nomenclature of zeolites follows six rules, which are described in detail in the literature.[13] Basically, they can be described in terms of a host structure and a pore structure.[12] Those having a three-dimensional host structure that is composed of corner-sharing tetrahedra and the same host topology consist of a zeolite framework type. To differentiate the structure types, the International Zeolite Association has assigned a three-letter code to each confirmed framework topology.[12] The nomenclature of SAPOs (Figure 1.1) follows the same roles as those for that of zeolites.

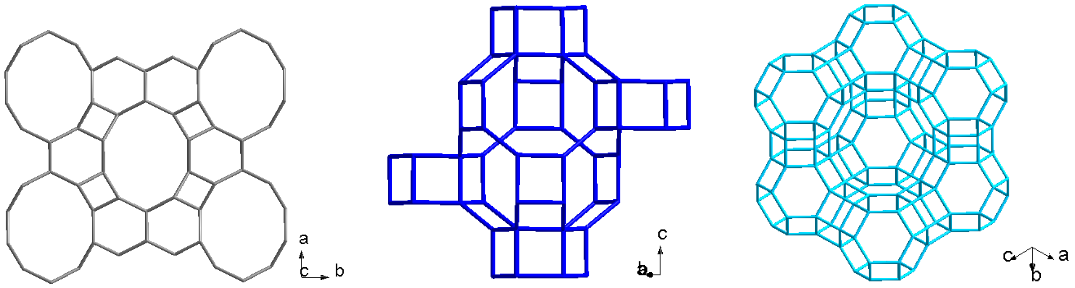

SAPO-11 (AEL) SAPO-34 (CHA) SAPO-37 (FAU)

Figure 1.1 Several examples of SAPO molecular sieves with different nomenclatures.

1.1.2.1 Silicon incorporation

As mentioned earlier, SAPOs can be viewed as the incorporation of Si atoms into the frameworks of $AlPO_4$-*n*. Three different types of mechanisms for incorporating Si into $AlPO_4$-based molecular sieves have been proposed: (1) Si is incorporated into an Al site (SM I). (2) Si is incorporated into a P site (SM II). This type gives rise to a Brønsted acid site and a dispersed Si species in SAPO domains. (3) Two Si substitute for neighboring Al and P (SM III).[9,14-17] A combination of SM II and SM III forms silicon islands with $Si(OAl)_n(OSi)_{4-n}$ (n = 0, 1, 2, 3, or 4) environments. This leads to a stronger acidity in SAPOs and various Si environments in aluminosilicate (AS) domains (Figure 1.2).

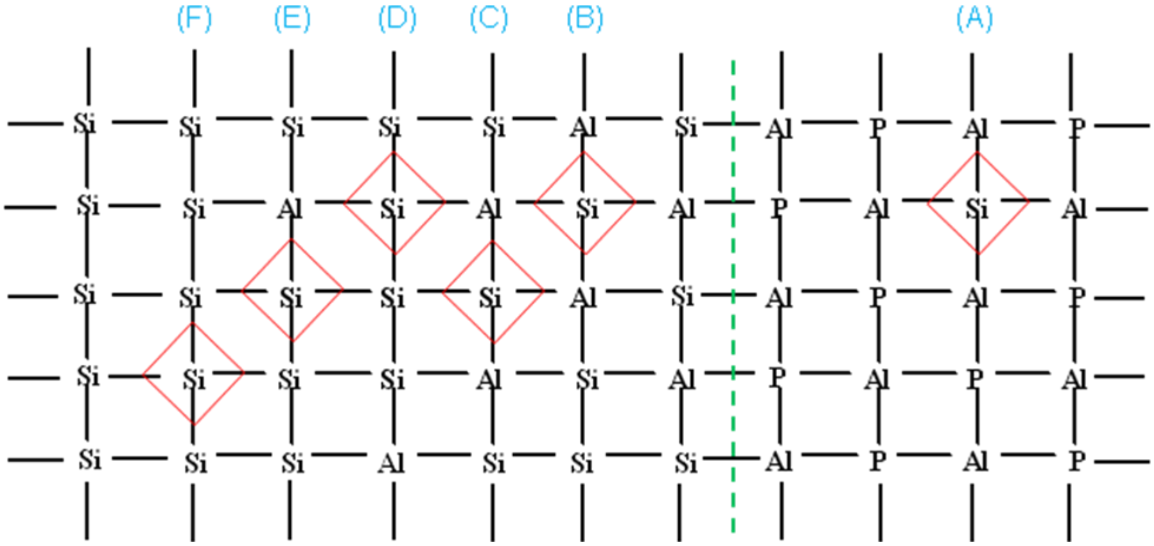

Figure 1.2 A schematic diagram of Si, Al, and P environments in SAPO molecular sieves (O atoms are not represented for clarity). (A) Isolated Si in SAPO domains; (B)-(F) various Si species in AS domains.[18]

1.1.2 Titanosilicates

1.1.2.1 Overview

Catalytic oxidation processes play a critical role in the industrial production of fine chemicals.[19] For many selected oxidation reactions, zeolite-based metal oxide systems are valid catalysts. Particularly, titanium-containing zeolites have been very attractive catalysts for this area in the last several decades.[20,21] More recently, it is recognized that these types of zeolites can be applied to liquid-phase epoxidation of alkenes.[22]

The discovery of Ti-substituted silicate molecular sieve TS-1 in the 1980s[8,23] has created more research opportunities in the area of titanosilicates.[24-28] Similar to zeolites and SAPOs, most titanosilicates are composed of tetrahedrally coordinated framework atoms. The need for different coordination environments of the catalytically active Ti centers[19] led to the development of a novel type material of titanosilicates, which consists of interlinked octahedra and tetrahedra. This new class of titanosilicates has high cation exchange capacity, which brings in many application possibilities, especially in base catalysis.[1] Two particularly important titanosilicates are ETS-10 and ETS-4, which were reported by Engelhard Corporation in the late 1980s and early 1990s, respectively.[29,30] Due to the presence of stoichiometric quantities of the transition metal in the structures of these novel microporous materials, they have great potentials in optoelectronic and nonlinear optical applications.[31]

1.1.2.2 Isomorphous substitution

The incorporation of heteroatoms in the frameworks of titanosilicates is a good approach to tune their properties. In the past few years, Anderson and co-workers have attempted to incorporate aluminum and gallium into tetrahedral silicon sites in ETS-10 for creating zeolite-type acidity.[32-34] These materials are named as ETAS-10 and ETGS-10, respectively. A phenomenon that is often observed is Al or Ga tetrahedra which are not incorporated in adjacent to Ti in the resulting microporous materials. However, a slight deviation from this avoidance rule is found at relatively high Al or Ga framework concentrations.[35]

1.2 Synthesis of microporous materials

Most of microporous materials including zeolites, titanosilicates, $AlPO_4$s, and SAPOs are conventionally synthesized via hydrothermal synthetic reactions.[36] Several other techniques have also been developed as alternative approaches for the synthesis of these materials. They include nonaqueous medium synthesis, dry gel conversion synthesis, and microwave synthesis.

1.2.1 Hydrothermal synthesis method (HTS)

HTS refers to heterogeneous reactions in aqueous media within a specially sealed container or high-pressure autoclave at high temperature and autogeneous pressure.[37] By conducting synthesis under HTS conditions using various synthetic conditions, numerous microporous materials with different structures can be formed. It is also an effective approach to explore the synthesis of new materials.

Zeolites and titanosilicates are normally synthesized in a high alkaline environment using organic molecules or alkali-metal cations. For example, using alkali-metal hydroxides, a silicon source, an aluminum source, and water to form the gel, with a pH greater than 12 zeolite X can be crystallized.[38] Differently, $AlPO_4$-*n* and SAPOs are synthesized under acidic or mildly basic conditions. pH lower than 3 can cause the formation of dense phases; and higher than 10 would result in a reduced yield due to solubilization or a lower crystallization rate.[39] $AlPO_4$-*n* and SAPOs are generally synthesized in the presence of organic compounds such as quaternary ammonium cations and amines.[40] However, there are cases where $AlPO_4$-*n* and SAPOs are made using alkali-metal cations, a case would be the synthesis of a SAPO with the SOD framework.[38] A typical $AlPO_4$ or SAPO synthesis mixture, for example, is prepared from an aluminum source, a phosphorous source, a silicon source (only for SAPO), water, and an organic compound.

1.2.1.2 Water

Water is the only solvent for most hydrothermal syntheses; the amount of water in different gel molar compositions varies. Due to a large amount of water applied to HTS synthesis, an open question that remains is the effect of water on the crystallization process of microporous materials. It is reported that the presence of reagent quantities of water is necessary for the successful synthesis of microporous materials, which helps the hydrolysis and condensation reactions and greatly enhances the crystallization kinetics.[41] An extreme is that microporous materials can be produced by "dry gel" method with a minimum amount of water (see dry gel conversion method).[42]

1.2.1.2 Structure-directing agents (SDAs)

Tetramethylammonium cations were introduced as the first organic quaternary ammonium base in zeolite synthesis by Barrer and Denny in the early 1960s.[43] After extensive studies on the synthetic chemistry, it was found that high silica or pure silica zeolites and $AlPO_4$-based molecular sieves can be obtained in the presence of alkylammonium cations or amines.[44]

Presently, the relationship between organic molecules and the structures of molecular sieves, is still not completely understood.[45] Some researchers have tried to differentiate the structure-directing role from the templating role played by organic molecules in the synthesis. Under most circumstances, these two terms are used interchangeably. The roles played by organic molecules include: (1) space-filling effect, which means that by occupying the cages and channels, the organic molecules could increase the thermodynamic stability of the organic-framework composite over that of the framework alone;[38] (2) structure-directing effect, which implies that a specific structure is synthesized by using one organic compound; (3) true templating effect, which refers to that the geometric and electron configurations of the organic molecule match those of the framework of the molecular sieve very well.[38,46] For example, at least 22 different organic molecules can be used to direct the formation of aluminosilicate ZSM-5.[38] Clearly, these organic compounds play a spacing-filling role rather than a structure-directing effect. One example that organic molecules are structure-directing agents is the synthesis of zeolite SSZ-24 using the N,N,N-trimethyl-1-adamantammonium cation.[47] For the true templating effect, in all the literature there may be only one example of the very close match between the zeolite framework and the organic molecule.[48] It is the synthesis of ZSM-18 using the triquaternary amine $C_{18}H_{36}N_3^{3+}$.[49,50] As indicated in Figure 1.3, both the ZSM-18 cage (C_{3h} symmetry) that hosts the organic molecule and the molecule itself (D_{3h} point symmetry) have the same 3-fold rotational symmetry.[38] Further, the organic molecule has no free rotation in the cage. This stronger host-guest interactions distinguish the true templating effect from the structure-directing effect.[38]

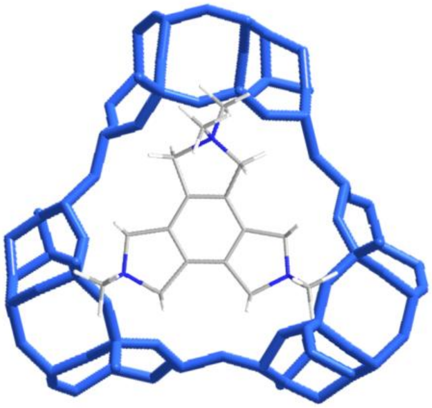

Figure 1.3 A schematic illustration of the triquaternary amine $C_{18}H_{36}N_3^{3+}$ located in the ZSM-18 cage.[51]

1.2.1.3 Alkali or alkaline earth cations

As mentioned earlier, the synthesis of zeolites and titanosilicates requires strong basic environments. The introduction of OH^- ions to the hydrothermal synthesis system will inevitably create cations.[3] It has been found that alkali or alkaline earth cations in the reactant mixtures determine or influence the kind of zeolite that forms from the synthesis system.[52] Table 1.1 indicates the influence of the cation environments on the formation of certain zeolites.

Table 1.1 Syntheses of certain zeolites in relation to cation environments.[52]

Zeolites	Cations in reaction mixture	Preferred cations
Faujasite types	Na, (Na, NMe_4), (Na, Li), *etc.*	Na
Zeolite A types	Na, (Na, NMe_4), (Na, K), *etc.*	Na
Mazzite type (Zeolite Ω)	(Na, NMe_4)	(Na, NMe_4)
Mordenites	Na, Ca, Sr	Na, alkaline earth ions
Analcimes and isotypes	Na, K, Rb, *etc.*	Various
Chabazite types	K, Sr, (K, Na), *etc.*	K
Zeolite L	(K, Na), K, Ba, *etc.*	K, Ba
Ferrierite type	Sr	Sr

Zeolite Ba-J	Ba	Ba
Zeolite ZK-5 types	Ba, (Na, Ba), (K, Ba), *etc.*	Ba
Zeolite Li-ABW	Li, (Li, K), (Li, Na), *etc.*	Li
Zeolite Li-H	Li	Li
Zeolite ZSM-2 type	(Li, Cs, NMe_4)	Li

These positively charged cations also play a vital role during the formation of titanosilicates. For example, crystallization kinetics of ETS-4 is influenced by the concentration of Na^+ ions in the gel. If a large percentage of Na^+ ions are replaced by Li^+, K^+, or Ca^{2+}, the crystallization time will be increased compared to that in the pure Na-containing system.[53]

Alkali cations are regarded to play a limited structure-directing role in the formation of zeolites and titanosilicates.[38] When introduced into a hydrothermal aqueous system, these charged alkali cations will interact with water molecules and become hydrated. This results in an increase in saturation up to possible supersaturation of the solution. In the basic medium, the negatively charged siliceous, aluminosilicate, or titanosilicate precursor species, interact with the hydrated alkali cations and gradually replace the water molecules around the cations to form nucleation centers. The so-formed nuclei will precipitate out because of the (super) saturation of the solution (salting-out effect). The efficiency of such effect depends on the charge density and ionic radius of the cations. The precipitating strength of the alkali cations decreases in the following order: Li > Na > K > Rb > Cs.[54] The alkali cations with different sizes are expected to compete for the negatively charged precursors, and thus favor or inhibit the formation of specific nuclei of a microporous framework.[54,55] Such effect is termed as the structure-directing role of the alkali cations.[52] Alkaline earth cations have a higher charge-to-diameter ratio and are likely to be good candidates for structure-direction in the formation of aluminum-rich zeolites. However, due to their relatively low solubilities in aqueous media, the use of them has not been studied in depth.[38]

1.2.1.4 Reactant

Reactants used in the synthesis of different types of molecular sieves vary, depending on their structures and reactant compositions (gel molar compositions). For zeolites, SAPOs, and titanosilicates, reactants include a silicon source, an aluminum source, a phosphorous source, a titanium source, a SDA, water, and sometimes a mineralizer. Frequently used main source reactants are listed in Table 1.2.

Table 1.2 Common reactants used in the synthesis of zeolites, SAPOs, and titanosilicates.

Sources	Examples
Silicon	Water glass: sodium silicate; silica gel: Ludox® HS-40; colloidal solution: SiO_2 40 wt.% and 30 wt.%; fumed silica: Aerosil® 200 and 300; ethyl orthosilicate; methyl orthosilicate
Aluminum	Sodium aluminate $NaAlO_2$; pseudoboehmite® AlOOH, Al_2O_3 ~70 wt.% and H_2O 30 wt.%; aluminum hydroxide; aluminum isopropoxide; aluminum nitrate; metallic aluminum

Phosphorous	85 wt.% orthophosphoric acid; organic phosphates; aluminophosphates
Titanium	Titanium sulphate; titanium trichloride; titanium fluoride; titanium dioxide; titanium chloride

1.2.1.5 Mineralizers

The use of high hydroxide concentration in the hydrothermal synthesis of zeolites can facilitate the mineralization of silicon and aluminum sources in the reactant gel.[56,57] Besides the hydroxide ion (OH^-), the fluoride ion (F^-) can also be used as a mineralizer for the synthesis of zeolites and other microporous materials. Flanigen *et al.* first introduced the F^- into the synthesis of zeolites and a highly siliceous material called “silicalite” was produced.[58] Later, Guth *et al.* systematically developed this field.[59] The roles identified for the F^- ion in molecular sieve synthesis include the following: (1) as a mineralizer and complexing agent, which helps solubilize framework-forming elements such as Si and Al.[60] Molecular sieves synthesized by using the OH^- route have a significant degree of connectivity defects due to the necessity to counterbalance the positive charge of organic molecules located within the cavities.[61] However, in the presence of F^-, large crystals with high crystallinity and few framework defects can be synthesized; (2) as a SDA. In some cases F^- ions that are present in as-synthesized molecular sieves interact strongly with their frameworks.[62] F^- anions stabilize small rings and cages. For triclinic $AlPO_4$-34 prepared in the fluorine medium, two F^- ions enter into a four-membered ring and bridge two Al atoms.[63] This greatly enhances the thermal stability of this microporous material.[64]

1.2.2 Nonaqueous medium synthesis

An alternative method to hydrothermal synthesis utilizes nonaqueous solvents instead of water. Such solvents usually refer to organic medium such as alcohols and alcohol/water mixture where water is only a minor component.[65] Due to alcohols having a higher viscosity than water, which is used in hydrothermal synthesis, crystallization rate is lower and large perfect single crystals can be synthesized very often.[40,66]

In the synthesis of zeolites, solvents play a role to guarantee efficient transport of reactants but not interact too much with individual reactant.[67] Due to the ionic nature of the inorganic precursors of zeolites, favorable organic solvents need to be relatively polar.[67] Ionic liquids (ILs) are such a class of organic solvents that have high polarity. They are commonly defined as salts that are fluid at temperatures below 100 °C and are mainly composed of ionic species.[68,69] The most interesting property of ILs, which differentiate them from other organic solvents in synthesizing zeolites, is their vanishingly low vapor pressure.[70] Because of this, ionothermal synthesis takes place at ambient pressure and there is no need for sealed reaction vessels. Safety issues that are associated with hydrothermal synthesis can thus be eliminated, and furthermore, the ILs can be recycled for further use.[68]

1.2.3 Dry gel conversion (DGC)

In 1990, Xu *et al.* first reported the transformation of dry gel to crystalline ZSM-5 by indirectly contacting the dry gel with water vapor and volatile amines. This approach was called dry gel conversion (DGC).[71] Since then, this method has been extensively studied and a large proportion of molecular sieves and even membranes have been prepared by using this method.[72] In general, the DGC method can be categorized into steam-assisted conversion (SAC) and vapor-phase transport (VPT). In the SAC method, the pre-dried gel powder is separated from a small amount of water in an autoclave. While in the VPT method, the dry gel does not contain a SDA; a small amount of SDA aqueous solution is put at the bottom of an autoclave.[41] A comparison between conventional HTS and DGC methods is shown in Figure 1.4.

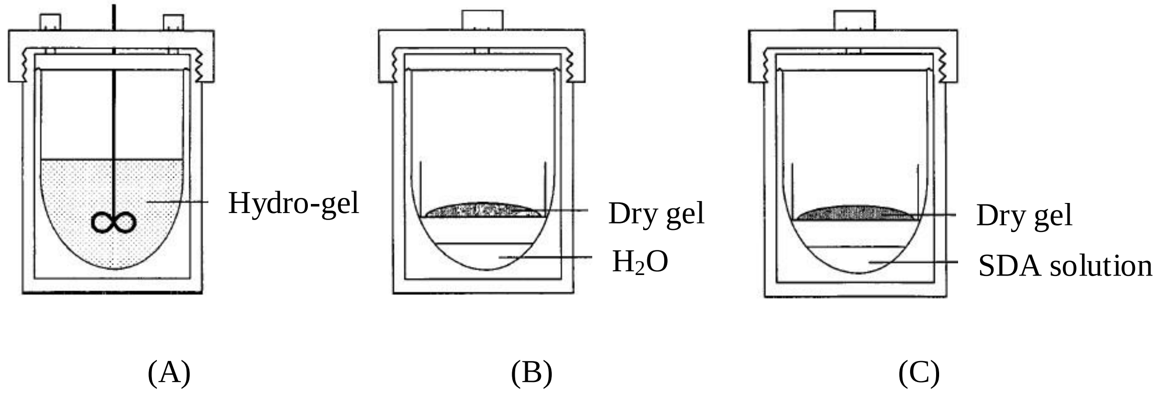

Figure 1.4 An illustration of the synthesis methods of molecular sieves: (A) HTS method; (B) SAC method; (C) VPT method.[41]

There are some benefits for the synthesis of molecular sieves by DGC compared to HTS. They include that (1) almost all initial dry gel can be converted into crystalline products with high yield; (2) minimum water disposal and energy consumption can be achieved; (3) costs are lowered by reducing the amount of SDAs used. More importantly, the DGC method is a good approach for the investigation of formation mechanisms of molecular sieves, which will be discussed in more detail later.

1.2.4 Microwave synthesis

The pioneering work on microwave synthesis of zeolites can be traced back to a US patent published in 1988, in which Mobil researchers produced zeolite NaA and ZSM-5 by using this method.[73] Since then, the number of publications by utilization of microwaves for the synthesis of microporous materials has increased year by year. The advantages of this method have been addressed in several reviews.[74,75] Very often, the synthesis time is greatly reduced under microwave irradiation, which may be due to that broken H-bonds between water molecules cause a fast gel dissolution and formation of T-O-T bonding (T signifies Al and P).[76]

1.3 Crystallization mechanisms

1.3.1 Formation mechanisms of zeolites

The zeolite formation process involves the transformation of an amorphous aluminosilicate gel into a crystalline zeolite product. The historical aspects of this topic have been summarized by Cundy *et al*.[77] At present, there are two main mechanisms proposed for the formation of zeolites.[38,78] One is called solution-mediated transport mechanism, involving the redissolution of the aluminosilicate gel and the reconstruction of silicate and aluminate ions in the solution to form the zeolite structure. The other mechanism is the solid hydrogel transformation mechanism, in which the structure of a zeolite is obtained from the rearrangement of the solid aluminosilicate gel formed from the condensation of silicate and aluminate. In the formation process of a particular zeolite structure, the true mechanism may lie somewhere between these two extremes. Further, various molecular sieves can crystallize by different mechanisms, and even a specific molecular sieve can be formed via different processes, all depending on the synthetic conditions (Figures 1.5 and 1.6).

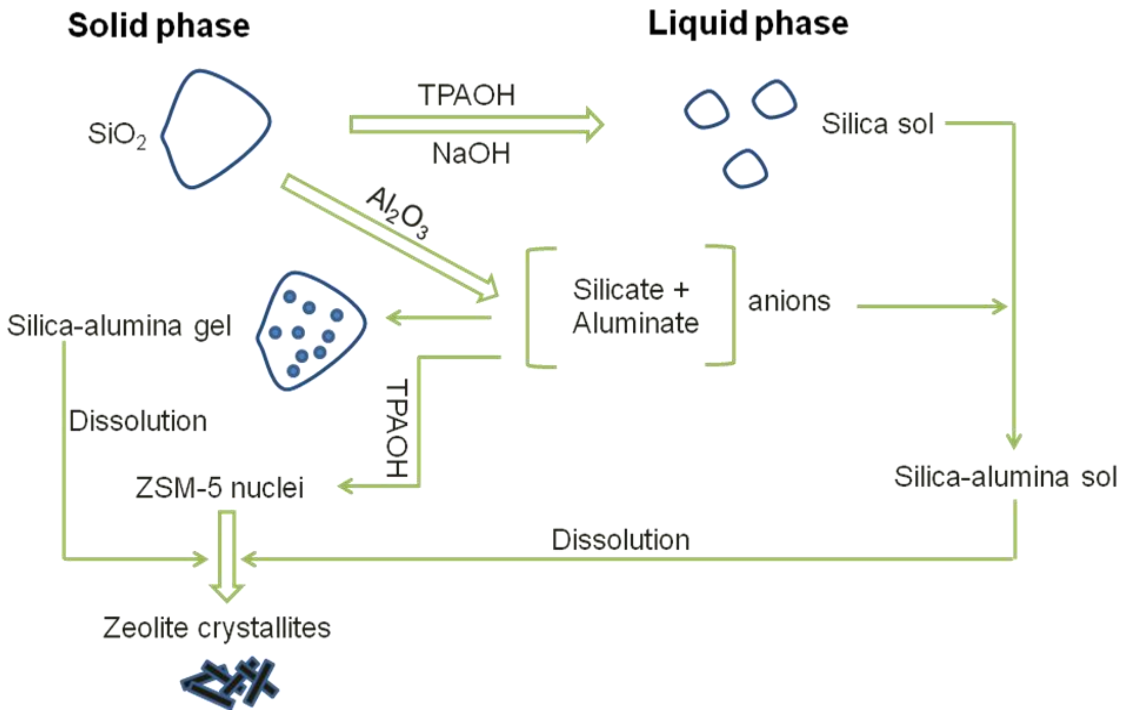

Figure 1.5 An illustration of solution-mediated transport mechanism during synthesis of ZSM-5 by using sodium aluminate and tetrapropylammonium hydroxide as the aluminum source and SDA, respectively.[79]

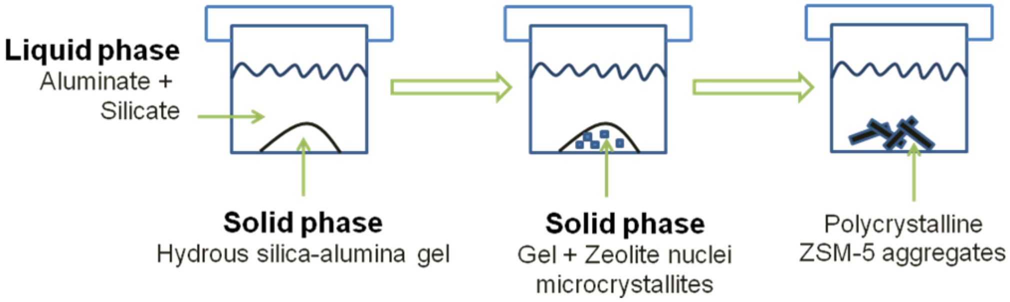

Figure 1.6 An illustration of solid hydrogel tranformation mechanism during synthesis of ZSM-5 by using aluminum sulphate and tetrapropylammonium bromide as the aluminum source and SDA, respectively.[79]

1.3.2 Formation mechanisms of $AlPO_4$-*n*

It is generally regarded that there are two stages in the formation of $AlPO_4$-*n*.[78] The first stage is the reaction of Al containing starting material and phosphorous source to form an amorphous AlPO layer. The second stage is the transformation from the layer to final crystalline product. This process is however, less clear. Some authors argued that the crystalline $AlPO_4$-*n* product forms via a direct solid-state transformation mechanism.[80] Others stated that the AlPO layer dissolves in solution completely first and the product then grows from small solution phase building units via condensation. Although some evidence has been found for the presence of AlPO entities in solution, there is a lack of evidence that such entities are the direct precursors of the crystalline $AlPO_4$ product.[78]

1.3.3 Formation mechanisms of SAPOs

In comparison with zeolites, the crystallization mechanisms of SAPOs have not been studied in depth. There is no general pathway by which SAPO molecular sieves are crystallized. The two extreme mechanisms for the formation of zeolites have been suggested to coexist in the crystallization of SAPOs under HTS conditions.[81,82]

Most SAPOs have their corresponding $AlPO_4$-*n* counterparts such as SAPO-5/$AlPO_4$-5, SAPO-11/$AlPO_4$-11, SAPO-18/$AlPO_4$-18, and SAPO-34/$AlPO_4$-34. Because of the similar structures of SAPOs and those of the corresponding $AlPO_4$s, the formation processes of SAPOs may also contain two stages. Firstly, an amorphous or crystalline precursor is formed. Secondly, the precursor is transformed to final crystalline product. Taking advantage of the DGC method, Huang *et al.* captured a crystalline or semi-crystalline intermediate phase mainly of AlPO nature. Putting a mixture of water and tetraethyl orthosilicate (TEOS, acting as the Si source) at the bottom of an autoclave, they successfully synthesized SAPO-5, SAPO-11, and SAPO-34 under DGC conditions.[83] Due to fast crystallization under HTS conditions, such a layered precursor, however, is seldom seen and also very difficult to be extracted during hydrothermal synthesis. Another issue that remains unclear is how Si is incorporated into the frameworks of $AlPO_4$-based molecular sieves. Si atoms are likely to directly participate in the crystallization with Al and P atoms at an early stage of the formation process, resulting in various Si species in the frameworks.[81,82,84] They are also probably incorporated into an AlPO intermediate at a later stage.[85] All these possibilities highly depend on synthesis conditions.

1.3.4 Formation mechanisms of titanosilicates

Among few publications that deal with the investigations of the crystallization of titanosilicates, most of them have focused on TS-1, TS-2, and ETS-10.[86-91] Different from zeolites, $AlPO_4$s, and SAPOs, the solid hydrogel tranformation is considered to be predominant in the formation process of these structures.[87,89] An X-ray amorphous solid containing a low Ti content forms first at an early stage of the crystallization process. Nucleation then takes place within the primary units of the solid to form a gel which gives the first signs of X-ray crystallinity. Through restructuring the gel, a small amount of Ti species in the liquid phase participate in the crystallization, and crystalline products with a higher Ti content are thus formed.[87,89]

1.4 General approaches to study formation mechanisms

1.4.1 *Ex situ* method

Microporous materials are generally synthesized from the transformation of a hydrogel under HTS conditions. Therefore, their formation mechanisms are normally investigated by analyzing the structures of intermediate phases obtained during hydrothermal synthesis using a combination of characterization techniques including powder X-ray diffraction (XRD), scanning electron microscopy (SEM), infrared spectroscopy (IR), Raman, and solid-state nuclear magnetic resonance spectroscopy (SS NMR). The *ex situ* method is an approach that studies crystallization indirectly by quenching the reactions at different heating times. Intermediates are obtained by stopping the reactions followed by isolation of solids from liquids. The separated solid phase is then characterized. Hydrothermal synthesis is a complicated process where multiple chemical reactions and thermodynamic equilibria involving both solid and liquid phases coexist.[38] There are difficulties in identifying the true intermediates because many of them have fragile structures, which are very easy to be altered by washing.[92]

The DGC method has emerged as an alternative to the HTS method for the synthesis of molecular sieves.[41] As mentioned earlier in Section 1.2.3, DGC is subdivided into two kinds: SAC and VPT. For VPT method, a SDA solution, separated from dry gel, is put at the bottom of an autoclave and the role of SDA during the synthesis of molecular sieves can thus be investigated. Under SAC conditions, only water is separated from dry gel and is put at the bottom of the autoclave. In spite of the lack of apparent liquid phase in DGC, the dry gel is not completely dry, as it contains a significant amount of water.[93] The fundamental crystallization mechanisms in DGC should resemble those in HTS where reactions have a more accessible liquid phase.[77] Further, the dry gel samples can be directly obtained and characterized without the need of isolation from the liquid phase. Therefore, intermediate structures will not be altered under DGC conditions. Because of this, several DGC studies have been reported on the crystallization process of $AlPO_4$s and zeolites.[83,94-97] However, few have focused on the formation of SAPO and titanosilicate molecular sieves.[98]

More recently, Xu and co-workers have developed a new strategy for investigating the hydrothermal formation processes of $AlPO_4$s on the basis of mathematical matrix and graph theories.[99,100] Instead of separating intermediate solid phases from liquid phases by centrifugation, the intermediate samples are freeze-dried so that all small species formed during crystallization are collected. A series of small fragments including dimers, trimers, tetramers, and pentamers, which contain Al and P atoms with different compositions, are extracted from the $AlPO_4$ framework. By comparing the local Al and P environments in these fragments obtained by calculation and those of the freeze-dried solid intermediates by SS NMR, possible fragments that may exist in the formation process of $AlPO_4$s can be identified. This *ex situ* approach has exploited a new way to understand the crystallization of microporous materials at a molecular level.

1.4.1 *In situ* method

An *in situ* method has been developed in order to directly monitor the crystallization process of microporous materials.[101-113] It is a real time study of the formation process without the necessity of stopping the reactions and therefore, an ideal way to unravel the crystallization mechanism. Several *in situ* techniques including *in situ* scattering, *in situ* spectroscopy, *in situ* mass spectroscopy, and *in situ* transmission electron microscopy have demonstrated great potential in monitoring hydrothermal reactions.[114] However, some of these experiments can only be carried out at special research centers. Experimental boundary conditions are indeed a problem. Further, costs compared to the value of the results should also be considered very carefully.[114]

1.5 Motivation and outline of this thesis

The layout of this thesis is the following:

(1) A description of the general preparation of DGC and HTS gel samples and characterization methods employed in this thesis is presented in **Chapter 2**.

(2) Different from the formation of zeolites which has been extensively studied, little is known about the crystallization of SAPO molecular sieves. Consequently, the formation mechanisms of these microporous materials are not understood well yet. The Si incorporation process is also unclear. SAPO-34 has demonstrated to be one of the

most important molecular sieves for the conversion of methanol to olefins. SAPO-37 has been reported to be a good catalyst for isomerization and alkylation of alkenes. **Chapters 3-5** of this thesis detail the study of the crystallization processes of SAPO-34 templated by diethylamine and morpholine under DGC conditions. **Chapter 6** talks about examining the formation of SAPO-37 under both DGC and HTS conditions.

(3) **Chapter 7** features the crystallization study of the aluminosilicate LSX. Zeolite LSX, which has high extraframework cation content, is one of the best sorbents in industrial use for the separation of nitrogen from other gases in air. The formation of zeolite LSX has been examined previously by using both *ex situ* and *in situ* methods. However, none of them has reported the evolution of the local chemical environments of Na^+ and K^+ ions during crystallization. The local environments of the two types of cations in the hydrothermal synthesis of LSX were investigated.

(4) In comparison with SAPOs and aluminosilicates, the crystallization of titanosilicates has been much less studied. Among them, ETS-10 and ETS-4 are the most important ones. There is no report about how cations participate in the formation of these two titanosilicate structures. **Chapters 8**, therefore, talks about the formation processes of ETS-10 and ETS-4.

(5) **Chapter 9** is the summary of this thesis and suggestions for future work.

1.6 References

(1) Rocha, J.; Anderson, M. W. *Eur. J. Inorg. Chem.* **2000**, *2000*, 801-818.
(2) Gottardi, G.; Galli, E. *Natural Zeolites*; Springer-Verlag: Berlin, **1985**.
(3) Xu, R; Pang, W.; Yu, J.; Huo, Q.; Chen, J. *Chemistry of Zeolites and Related Porous Materials: Synthesis and Structure*; Wiley-Interscience: New York, **2007**.
(4) Barrer, R. *J. Chem. Soc.* **1948**, 2158-2163.
(5) Barrer, R. *J. Chem. Soc.* **1948**, 127-132.
(6) Wilson, S. T.; Lok, B. M.; Messina, C. A.; Cannan, T. R.; Flanigen, E. M. *J. Am. Chem. Soc.* **1982**, *104*, 1146-1147.
(7) Lok, B. M.; Messina, C. A.; Patton, R. L.; Gajek, R. T.; Cannan, T. R.; Flanigen, E. M. *J. Am. Chem. Soc.* **1984**, *106*, 6092-6093.
(8) Taramasso, M.; Perego, G.; Notari, B. US Patent 4,410,501, 1983.
(9) Sastre, G.; Lewis, D. W.; Richard, C.; Catlow, A. *J. Phys. Chem. B* **1997**, *101*, 5249-5262.
(10) Sastre, G.; Lewis, D. W.; Catlow, C. R. A. *J. Phys. Chem.* **1996**, *100*, 6722-30.
(11) Sastre, G.; Lewis, D. W.; Catlow, C. R. A. *J. Mol. Catal. A* **1997**, *119*, 349-356.
(12) McCusker, L.; Liebau, F.; Engelhardt, G. *Microporous Mesoporous Mater.* **2003**, *58*, 3-13.
(13) Alberti, A.; Armbruster, T.; Artioli, G.; Colella, C.; Galli, E.; Grice, J. D.; Liebau, F.; Minato, H.; Nickel, E. H.; Passaglia, E. *Can. Mineral.* **1997**, *35*, 1571-1606.
(14) Prakash, A. M.; Unnikrishnan, S. *J. Chem. Soc. Faraday Trans.* **1994**, *90*, 2291-2296.
(15) Dumitriu, E.; Azzouz, A.; Vasile Hulea a, D. L.; Kessler, H. *Microporous Mater.* **1997**, *10*, 1-12.
(16) Sanchez del Campo, A. E.; Gayubo, A. G.; Aguayo, A. T.; Tarrio, A.; Bilbao, J. *Ind. Eng. Chem. Res.* **1998**, *37*, 2336-2340.
(17) Izadbakhsh, A.; Farhadi, F.; Khorasheh, F.; Sahebdelfar, S.; Asadi, M.; Feng, Y. Z. *Appl. Catal., A* **2009**, *364*, 48-56.
(18) Barthomeuf, D. *Zeolites* **1994**, *14*, 394-401.
(19) Murugavel, R.; Roesky, H. W. *Angew. Chem. Int. Ed.* **1997**, *36*, 477-479.
(20) Wu, P.; Tatsumi, T.; Komatsu, T.; Yashima, T. *J. Catal.* **2001**, *202*, 245-255.
(21) Shetti, V. N.; Manikandan, P.; Srinivas, D.; Ratnasamy, P. *J. Catal.* **2003**, *216*, 461-
(22) Wu, P.; Tatsumi, T. *Catal. Surv. Asia* **2004**, *8*, 137-148.
(23) Kraushaar, B.; Hooff, J. H. C. *Catal. Lett.* **1988**, *1*, 81-84.
(24) Galve, A.; Sieffert, D.; Vispe, E.; Tellez, C.; Coronas, J.; Staudt, C. *J. Membr. Sci.* **2011**, *370*, 131-140.
(25) Xiao, F.-S.; Qiu, S. L.; Pang, W. Q.; Xu, R. R. *Adv. Mater.* **1999**, *11*, 1091-1099.
(26) Ferdov, S.; Kostov-Kytin, V.; Petrov, O. *Chem. Commun.* **2002**, 1786-1787.
(27) Ferdov, S.; Kolitsch, U.; Lengauer, C.; Tillmanns, E.; Lin, Z.; Sa Ferreira, R. Acta Crystallogr. **2007**, *E63*, i186-i186.
(28) Sudhakar Reddy, J.; Kumar, R. *J. Catal.* **1991**, *130*, 440-446.
(29) Kuznicki, S. M.; Easton, P. US Patent 4,853,202, 1989.
(30) Kuznicki, S. M.; Easton, P. US Patent 4,938,939, 1990.
(31) Lamberti, C. *Microporous Mesoporous Mater.* **1999**, *30*, 155-163.

(32) Rocha, J.; Lin, Z.; Ferreira, A.; Anderson, M. W. *J. Chem. Soc., Chem. Commun.* **1995**, 867-868.
(33) Anderson, M. W.; Philippou, A.; Lin, Z.; Ferreira, A.; Rocha, J. *Angew. Chem. Int. Ed.* **1995**, *34*, 1003-5.
(34) Lin, Z.; Rocha, J.; Ferreira, A.; Anderson, M. W. *Colloid Surf. A* **2001**, *179*, 133-138.
(35) Anderson, M. W.; Rocha, J. In *Handbook of Porous Solids.* Schüth, F.; Sing, K.S.W.; Weitkamp, J., Eds.; John Wiley & Sons, Ltd., **2008**.
(36) Cundy, C. S.; Cox, P. A. *Microporous Mesoporous Mater.* **2005**, *82*, 1–78.
(37) Feng, S.; Xu, R. *Acc. Chem. Res.* **2001**, *34*, 239-247.
(38) Davis, M. E.; Lobo, R. F. *Chem. Mater.* **1992**, *4*, 756-768.
(39) Pastore, H.; Coluccia, S.; Marchese, L. *Annu. Rev. Mater. Res.* **2005**, *35*, 351-395.
(40) Morris, R. E.; Weigel, S. J. *Chem. Soc. Rev.* **1997**, *26*, 309-317.
(41) Ma, H.; Tian, Z.; Xu, R.; Wang, B.; Wei, Y.; Wang, L.; Xu, Y.; Zhang, W.; Lin, L. *J. Am. Chem. Soc.* **2008**, *130*, 8120-8121.
(42) Matsukata, M.; Ogura, M.; Osaki, T.; Hari Prasad Rao, P. R.; Nomura, M.; Kikuchi, E. *Top. Catal.* **1999**, *9*, 77-92.
(43) Barrer, R.; Denny, P. *J. Chem. Soc.* **1961**, 971-982.
(44) Lok, B.; Cannan, T.; Messina, C. *Zeolites* **1983**, *3*, 282-291.
(45) Yu, J.; Xu, R. *Acc. Chem. Res.* **2003**, *36*, 481-490.
(46) Yu, J.; Xu, R. *Chem. Soc. Rev.* **2006**, *35*, 593-604.
(47) van Nordstrand, R. A.; Santilli, D. S.; Zones, S. I. *ACS Symp. Ser.* **1988**, *368*, 236-245.
(48) Lewis, D.; Freeman, C.; Catlow, C. *J. Phys. Chem.* **1995**, *99*, 11194-11202.
(49) Ciric, J. US Patent 3,950,496, 1976.
(50) Lawton, S. L.; Rohrbaugh, W. J. *Science* **1990**, *247*, 1319.
(51) Čejka, J.; Van Bekkum, H.; Corma, A.; Schüth, F. *Introduction to Zeolite Science and Practice*; Elsevier: New York, **2007**.
(52) Barrer, R. M. *Zeolites* **1981**, *1*, 130-140.
(53) Mintova, S.; Valtchev, V.; Angelova, S.; Konstantinov, L. *Zeolites* **1997**, *18*, 269-273.
(54) Gabelica, Z.; Blom, N.; Derouane, E. G. *Appl. Catal.* **1983**, *5*, 227-248.
(55) Aiello, R.; Crea, F.; Nastro, A.; Subotić, B.; Testa, F. *Zeolites* **1991**, *11*, 767-775.
(56) Cejka, J.; Corma, A.; Zones, S. *Zeolites and Catalysis: Synthesis, Reactions and Applications*; Wiley-VCH: Weinheim, **2010**.
(57) Rabenau, A. *Angew. Chem. Int. Ed.* **2003**, *24*, 1026-1040.
(58) Flanigen, E. M.; Patton, R. L. US Patent 4,073,865, 1978.
(59) Guth, J.; Kessler, H.; Higel, J.; Lamblin, J.; Patarin, J.; Seive, A.; Chezeau, J.; Wey, R. *ACS Symp. Ser.* **1989**, *398*, 176-195.
(60) Egeblad, K.; Kustova, M.; Klitgaard, S. K.; Zhu, K.; Christensen, C. H. *Microporous Mesoporous Mater.* **2007**, *101*, 214-223.
(61) Pulido, A.; Corma, A.; Sastre, G. *J. Phys. Chem. B* **2006**, *110*, 23951-23961.
(62) Shayib, R. M.; George, N. C.; Seshadri, R.; Burton, A. W.; Zones, S. I.; Chmelka, B. F. *J. Am. Chem. Soc.* **2011**, *133*, 18728-18741.
(63) Marchese, L.; Frache, A.; Gianotti, E.; Martra, G.; Causa, M.; Coluccia, S. *Microporous Mesoporous Mater.* **1999**, *30*, 145-153.

(64) Li, N.; Wu, J.; Zhao, H.; Luo, Q.; He, C.; Guan, N.; Xiang, S. *Cryst. Eng. Comm.* **2012**, *14*, 8671-8676.
(65) Van Erp, W. A.; Kouwenhoven, H. W.; Nanne, J. M. *Zeolites* **1987**, *7*, 286-288.
(66) Kuperman, A.; Nadimi, S.; Oliver, S.; Ozin, G. A.; Garces, J. M.; Olken, M. M. *Nature* **1993**, *365*, 239-242.
(67) Parnham, E. R.; Morris, R. E. *Acc. Chem. Res.* **2007**, *40*, 1005-1013.
(68) Cooper, E. R.; Andrews, C. D.; Wheatley, P. S.; Webb, P. B.; Wormald, P.; Morris, R. E. *Nature* **2004**, *430*, 1012-1016.
(69) Morris, R. E. *Chem. Commun.* **2009**, *0*, 2990-2998.
(70) Morris, R. E. *Angew. Chem. Int. Ed.* **2007**, *47*, 442-444.
(71) Xu, W.; Dong, J.; Li, J.; Li, J.; Wu, F. *J. Chem. Soc., Chem. Commun.* **1990**, 755-756.
(72) Alfaro, S.; Arruebo, M.; Coronas, J.; Menéndez, M.; Santamaŕia, J. *Microporous Mesoporous Mater.* **2001**, *50*, 195-200.
(73) Chu, P.; Dwyer, F. G.; Vartuli, J. C. US Patent 4,778,666, 1988.
(74) Cundy, C. S. *Collect. Czech. Chem. Commun.* **1998**, *63*, 1699-1723.
(75) Li, Y.; Yang, W. *J. Membr. Sci.* **2008**, *316*, 3-17.
(76) Girnus, I.; Jancke, K.; Vetter, R.; Richter-Mendau, J.; Caro, J. *Zeolites* **1995**, *15*, 33-39.
(77) Cundy, C. S.; Cox, P. A. *Microporous Mesoporous Mater.* **2005**, *82*, 1-78.
(78) Francis, R. J.; O'Hare, D. *J. Chem. Soc. Dalton Trans.* **1998**, *0*, 3133-3148.
(79) Derouane, E. G.; Determmerie, S.; Gabelica, Z.; Blom, N. *Appl. Catal.* **1981**, *1*, 201-224.
(80) Fan, F.; Feng, Z.; Sun, K.; Guo, M.; Guo, Q.; Song, Y.; Li, W.; Li, C. *Angew. Chem. Int. Ed.* **2009**, *48*, 8743-8747.
(81) Tan, J.; Liu, Z.; Bao, X.; Liu, X.; Han, X.; He, C.; Zhai, R. *Microporous Mesoporous Mater.* **2002**, *53*, 97–108.
(82) Liu, G.; Tian, P.; Zhang, Y.; Li, J.; Xu, L.; Meng, S.; Liu, Z. *Microporous Mesoporous Mater.* **2008**, *114*, 416-423.
(83) Chen, B.; Huang, Y. *Microporous Mesoporous Mater.* **2009**, *123*, 71-77.
(84) Xu, L.; Du, A.; Wei, Y.; Wang, Y.; Yu, Z.; He, Y.; Zhang, X.; Liu, Z. *Microporous Mesoporous Mater.* **2008**, *115*, 332-337.
(85) Zhang, L.; Bates, J.; Chen, D.; Nie, H. Y.; Huang, Y. *J. Phys. Chem. C* **2011**, *115*, 22309-22319.
(86) Zhao, Q.; Bao, X.; Han, X.; Liu, X.; Tan, D.; Lin, L.; Guo, X.; Li, G.; Wang, X. *Mater. Chem. Phys.* **2000**, *66*, 41-50.
(87) Fan, W.; Duan, R. G.; Yokoi, T.; Wu, P.; Kubota, Y.; Tatsumi, T. *J. Am. Chem. Soc.* **2008**, *130*, 10150-10164.
(88) Guo, M.; Feng, Z.; Li, G.; Hofmann, J. P.; Pidko, E. A.; Magusin, P. C. M. M.; Guo, Q.; Weckhuysen, B. M.; Hensen, E. J. M.; Fan, F.; Li, C. *Chem. Eur. J.* **2012**, *18*, 12078-12084.
(89) Serrano, D.; Uguina, M.; Sanz, R.; Castillo, E.; Rodŕiguez, A.; Sanchez, P. *Microporous Mesoporous Mater.* **2004**, *69*, 197-208.
(90) Serrano, D.; Uguina, M.; Ovejero, G.; Van Grieken, R.; Camacho, M. *Microporous Mater.* **1996**, *7*, 309-321.
(91) Lv, L.; Su, F.; Zhao, X. *Microporous Mesoporous Mater.* **2004**, *76*, 113-122.

(92) Kim, M. H.; Li, H. X.; Davis, M. E. *Microporous Mater.* **1993**, *1*, 191-200.
(93) Matsukata, M.; Ogura, M.; Osaki, T.; Raja, P.; Rao, H. P.; Nomura, M.; Kikuchi, E. *Top. Catal.* **1999**, *9*, 77-92.
(94) Chen, B.; Kirby, C. W.; Huang, Y. *J. Phys. Chem. C* **2009**, *113*, 15868-15876.
(95) Chen, B.; Huang, Y. *Microporous Mesoporous Mater.* **2011**, *143*, 14-21.
(96) Chen, B.; Huang, Y. *J. Phys. Chem. C* **2007**, *111*, 15236-15243.
(97) Hari Prasad Rao, P. R.; Leon y Leon, C. A.; Ueyama, K.; Matsukata, M. *Microporous Mesoporous Mater.* **1998**, *21*, 305-313.
(98) Song, C. M.; Feng, Y.; Ma, L. L. *Microporous Mesoporous Mater.* **2012**, *147*, 205-211.
(99) Cheng, T.; Xu, J.; Li, X.; Li, Y.; Zhang, B.; Yan, W.; Yu, J.; Sun, H.; Deng, F.; Xu, R. *Microporous Mesoporous Mater.* **2011**, *152*, 190-207.
(100) Yan, W.; Song, X.; Xu, R. *Microporous Mesoporous Mater.* **2009**, *123*, 50-62.
(101) Vistad, Ø. B.; Akporiaye, D. E.; Taulelle, F.; Lillerud, K. P. *Chem. Mater.* **2003**, *15*, 1639-1649.
(102) Fan, F.; Feng, Z.; Li, G.; Sun, K.; Ying, P.; Li, C. *Chem. Eur. J.* **2008**, *14*, 5125-5129.
(103) Walton, R. I.; Millange, F.; O'Hare, D.; Davies, A. T.; Sankar, G.; Catlow, C. R. A. *J. Phys. Chem. B* **2001**, *105*, 83-90.
(104) Norby, P. *Curr. Opin. Colloid Int.* **2006**, *11*, 118-125.
(105) Schaack, B. B.; Schrader, W.; Corma, A.; Schüth, F. *Chem. Mater.* **2009**, *21*, 4448-4453.
(106) Schaack, B. B.; Schrader, W.; Schüth, F. *J. Phys. Chem. B* **2009**, *113*, 11240-11246.
(107) Simonsen, M. E.; Søgaard, E. G. *Int. J. Mass Spectrom.* **2009**, *285*, 78-85.
(108) Norby, P. *J. Am. Chem. Soc.* **1997**, *119*, 5215-5221.
(109) Zhang, B.; Xu, J.; Fan, F.; Guo, Q.; Tong, X.; Yan, W.; Yu, J.; Deng, F.; Li, C.; Xu, R. *Microporous Mesoporous Mater.* **2012**, *147*, 212-221.
(110) Lim, I. H.; Schrader, W.; Schüth, F. *Microporous Mesoporous Mater.* **2013**, *166*, 20-36.
(111) Depla, A.; Verheyen, E.; Veyfeyken, A.; Gobechiya, E.; Hartmann, T.; Schaefer, R.; Martens, J. A.; Kirschhock, C. E. A. *Phys. Chem. Chem. Phys.* **2011**, *13*, 13730-13737.
(112) O'Brien, M. G.; Beale, A. M.; Catlow, C. R. A.; Weckhuysen, B. M. *J. Am. Chem. Soc.* **2006**, *128*, 11744-11745.
(113) Beale, A. M.; O'Brien, M. G.; Kasunič, M.; Golobič, A.; Sanchez-Sanchez, M.; Lobo, A. J. W.; Lewis, D. W.; Wragg, D. S.; Nikitenko, S.; Bras, W.; Weckhuysen, B. M. *J. Phys. Chem. C* **2011**, *115*, 6331-6340.
(114) Pienack, N.; Bensch, W. *Angew. Chem. Int. Ed.* **2011**, *50*, 2014-2034.

Chapter 2 Experimental Section

2.1 Sample preparation

2.1.1 Dry gel sample preparation

The reaction vessel for the DGC method is illustrated in Figure 2.1. For SAC, pre-dried dry powder that contains a SDA is put in a Teflon cup and a small amount of distilled water (0.3-1.5 ml of water for 1 g of dry gel) is put at the bottom of an autoclave. For VPT, a small amount of aqueous solution containing a SDA is put at the bottom of an autoclave, and the SDA molecule is brought into contact with the dry gel through vapor slowly upon heating treatment.

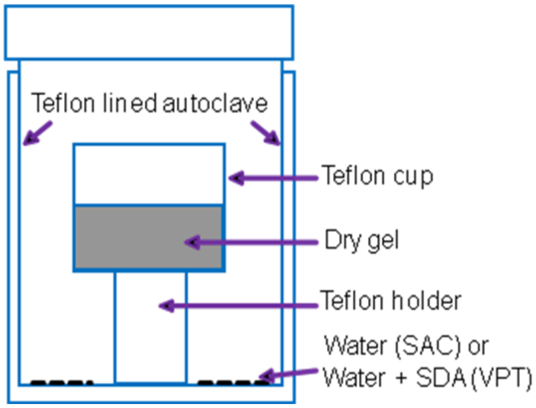

Figure 2.1 Schematic diagram of the reaction vessel for DGC method.

A typical procedure for the preparation of initial SAC dry gel is the following:[1] according to the gel molar composition of a specific molecular sieve, different sources are mixed together to form a homogeneous solution. The solution is dried at 353 K with constant stirring to allow evaporation of water until white solid is formed. The initial dry gel is then distributed into a series of small Teflon cups with Teflon holders, each of which is placed into a Teflon-lined autoclave with a small amount of distilled water placed at the bottom of the autoclave. By doing this, the dry gel in the cup does not contact directly with external water. Crystallization then proceeds at specific temperature in an oven. After different heating times, the autoclaves are taken out of the oven and the reactions are quenched in cold water. For comparison, each solid sample is divided into two parts. One part is dried in air and the other part is first washed with distilled water in a beaker and then dried in the same beaker in air without isolation from the liquid phase. This ensures that solid particles are not washed away. All dried samples are kept in the sealed vials for further analysis. For the VPT method, the initial dry gel is prepared similarly to the SAC method, but without SDA. Instead, a small amount of aqueous SDA solution (0.3-1.5 ml of the solution for 1 g of dry gel) is placed at the bottom of each autoclave.

2.1.1 HTS gel sample preparation

The preparation of the HTS gel samples is as follows: according to a specific gel molar composition, various elemental sources and distilled water are mixed under stirring, and a mixture with high homogeneity is thus produced. The mixture is then divided into several proportions, which are put into a series of Teflon bottles in autoclaves (Figure 2.2). Crystallization is carried out at a certain temperature in an oven. The autoclaves are taken out of the oven individually after being heated for different crystallization time. The solid phase is separated from liquid phase by centrifugation. The solid samples are then stored in sealed vials for later analysis. For the solid sample that is obtained by separating the initial mixture without heating from water, it is referred to as the initial HTS gel without heating.

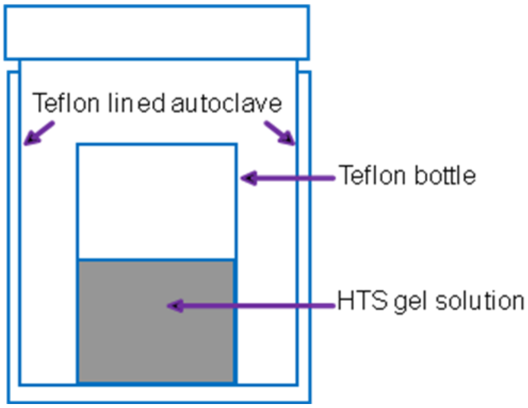

Figure 2.2 Schematic diagram of the reaction vessel for HTS method.

2.2 Characterization techniques

Since one analysis technique can only provide information about one particular aspect of molecular sieves, a combination of different analytical methods becomes necessary. Here, several techniques applied in this thesis are discussed briefly, including powder X-ray diffraction (powder XRD), scanning electron microscopy (SEM), energy dispersive X-ray (EDX), and solid-state nuclear magnetic resonance (SS NMR).

2.2.1 Powder XRD

For the determination of the long-range ordering and the phase purity of molecular sieves, XRD is the most frequently used technique. Because of the poly-crystalline nature of most materials, structure determination is often limited to powder samples. For samples that are available as large crystals or in a crystal morphology in favor of a preferred orientation, it has to be assured that all crystallites are randomly oriented when analyzed, which can be achieved by carefully sample grinding.[2]

In poly-crystalline samples, each reflection observed at a given angle 2θ in a powder XRD pattern, which is measured at wavelength λ, is related to lattice planes (Figure 2.3) with a distance d and an orientation indicated by the Millers indices hkl as described by the Bragg's law:[3]

$$n\lambda = 2d_{(hkl)} \sin\theta \qquad \textbf{(Equation 2-1)}$$

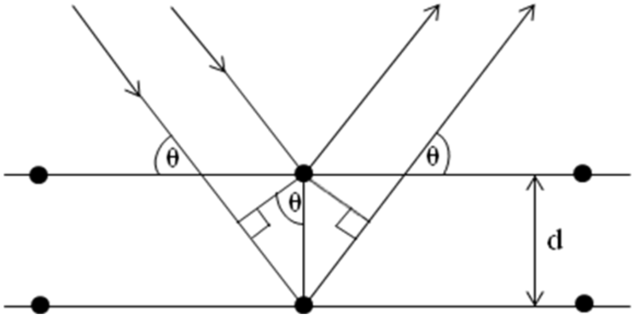

Figure 2.3 Deriving Bragg's law using the reflection geometry and applying trigonometry.[3]

Each molecular sieve exhibits a unique powder XRD pattern, which is characteristic of its structure. The XRD patterns of molecular sieves with known structures are compiled in the "Collection of Simulated XRD Patterns for Zeolites"[4] as well as in the online database (http://www.iza-online.org) of the International Zeolite Association (IZA). Therefore, the structure of a molecular sieve sample can be identified by comparing its experimental powder pattern with a reference pattern. XRD data can also be used to obtain information about crystal structure, crystal size, and crystallinity of a sample.[2]

In this thesis, all XRD patterns are recorded within the range 5° < 2θ < 65° on a Rigaku Rotating Anode diffractometer using Co Kα radiation (λ = 1.7902 Å) with a 10° / min step width and 6 min count time.

2.2.2 SEM and EDX

A scanning electron microscope (SEM) is a type of electron microscope that uses a beam of highly energetic electrons to scan over a sample and produce images of the sample on a very fine scale. The theoretical fundamentals of SEM can be found in the literature.[5] When a finely focused electron beam scans over the surface of a molecular sieve, secondary electrons that are ejected from the surface are used to form an image. X-rays are also emitted under bombardment, which are used to determine the composition of the region imaged. In this thesis, a LEO 1540XB Field Emission SEM equipped with an EDX spectrometer for elemental analysis is used to examine the morphology of selected gel samples and determine the composition of the imaged area.

2.2.3 Solid-state NMR spectroscopy

2.2.3.1 Overview

NMR spectroscopy relies on the fact that transitions can be induced between magnetic spin energy levels of certain atomic nuclei in a magnetic field.[2] The transition frequency measured in the NMR spectrum of an atomic nucleus is very sensitive to a particular chemical or structural environment, from which information about local structure and dynamics can be obtained. NMR is not only widely used to study the structures of molecules in solution, but also can be applied to solid samples.

The initial lack of utilization of solid-state NMR (SS NMR) compared to solution NMR is due to its inherent lack of resolution. The main difference between solution and solid state NMR is the directional dependence of the various spin interactions. In liquids, the different orientations are averaged by fast and essentially isotropic motions of the molecules. NMR spectra of liquid samples often exhibit sharp lines characterized by distinct chemical shifts or line positions and intensities. However, in solids, the orientation-dependent nuclear spin interactions are not averaged and often broad and relatively featureless signals are observed. High-resolution SS NMR becomes achievable as its popularity and invention of new techniques increase. By using these techniques, many of the line-broadening interactions can be reduced or removed so that narrow signals are obtained. Since high-resolution SS NMR gives information on the local order of the structure and can be applied to crystalline, microcrystalline, and amorphous samples, it is a valuable complementary technique to powder XRD which probes the long-range ordering of crystalline samples.[6]

2.2.3.2 Magic-angle spinning (MAS)

The interactions of nuclear spins in an applied magnetic field can be divided into five major types, and the relative magnitudes of them are shown in Table 2.1.

Table 2.1 Typical magnitudes of main nuclear spin interactions.[7]

Interactions	Description of interaction	Magnitude
Zeeman	Interaction with static magnetic field	10^7-10^9 Hz
Chemical shielding	Shielding due to electronic environment	10^2-10^5 Hz
Dipolar coupling	Through space spin-spin interaction	10^3-10^4 Hz
Scalar or indirect spin-spin coupling	Spin-spin interaction mediated via the bonding electrons through the contact interaction	1-10^3 Hz
Quadrupolar	Interaction with the electric field gradient for spins $\boldsymbol{I} > 1/2$	10^3-10^7 Hz

The NMR spectra of solids suffer from broadening due to all of these interactions. It has been found that considerable line narrowing can be achieved if the sample is rapidly rotated at an angle of 54.74° to the axis along the applied magnetic field (the so-called magic angle). Broadening in spin $\boldsymbol{I} = ½$ mainly arises from interactions between the magnetic dipoles of adjacent nuclei. In quadrupolar nuclei where the spin $\boldsymbol{I} > ½$, the non-zero nuclear electric quadrupole moment results from the fact that the charge distribution is non-spherically symmetric. Interaction of this quadrupole moment with the electric field gradient at the nucleus causes peak broadening, peak displacement from the isotropic chemical shift, and peak shape distortion.[8]

Some of the interactions in Table 2.1 contain terms in ($3\cos^2\theta-1$). At the magic angle, this term becomes zero. MAS thus removes the dipole-dipole and chemical shift anisotropy interactions, as well as the first-order quadrupolar interactions.[7,9,10] As the most widely used technique, MAS approach is employed in this thesis to explore the local information of atoms involved in the crystallization of molecular sieves.

2.2.3.3 Cross-polarization (CP)

Even with MAS technique that can produce line-narrowing spectra, NMR experiments on solids with dilute spin-½ nuclei are still relatively unattractive for two principal reasons. One is the lack of sensitivity due to their low net polarization and the other is the relatively long spin-lattice relaxation time that is often encountered. In solids where both abundant ***I*** and dilute nuclei ***S*** coexist, polarization transfer techniques can usually be used to overcome these two problems. CP is the most common technique, which is created to affect such a transfer. Figure 2.4 illustrates the pulse sequence used in the CP experiment, where the amplitudes of the two contact pulses have to be carefully set to achieve the Hartmann-Hahn matching condition:[11]

$$\gamma_I \mathbf{B}_{1I} = \gamma_S \mathbf{B}_{1S} \qquad \textbf{(Equation 2-2)}$$

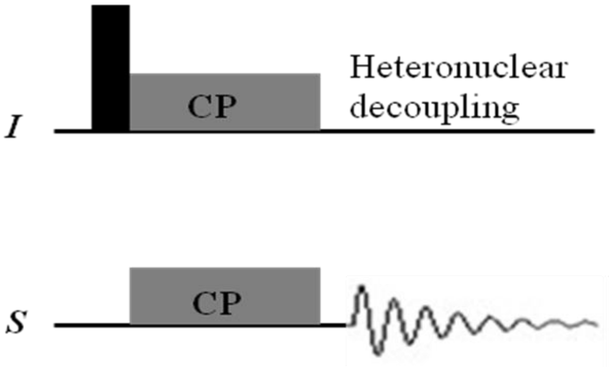

Figure 2.4 Pulse sequence for cross-polarization of dilute nucleus ***S*** by abundant nucleus ***I*** with detection of the ***S*** magnetization.

For quadrupolar nuclei, the spin locking of the central transition in an MAS experiment is a complex process due to the time dependence of the first-order quadrupolar interaction.[12] Direct CP experiments therefore have limited efficiency.[13] Vega has presented a modified Hartmann-Hahn matching condition involving quadrupolar nuclei under MAS conditions (with a spinning speed of ν_r):[14]

$$\gamma_I B_{1I} = (S + 1/2)\, \gamma_S B_{1S} \pm \nu_r \qquad \textbf{(Equation 2-3)}$$

In the experiments, CP can be used to increase signal intensity.

2.2.3.4 Rotational-echo double resonance (REDOR)

The REDOR experiment is a rotor synchronized double-resonance MAS technique designed to probe the heteronuclear dipolar interactions. This technique involves two experiments with the first one being normal spin-echo experiment on observing spin as a control experiment and in the second one, a number of 180° pulses are applied to the dephasing nucleus during the spin-echo. The echo intensity of a REDOR experiment decreases due to non-zero average of dipolar coupling compared to the normal echo without the 180° dephasing pulses. The REDOR difference spectrum

($\Delta \boldsymbol{S}$) is obtained by subtracting the REDOR spectrum ($\boldsymbol{S}$) from the control spectrum ($\boldsymbol{S_0}$). The extent of $\Delta \boldsymbol{S}$ is monitored as a function of the number of rotor period $\boldsymbol{n}$. A plot of $\Delta \boldsymbol{S}$ versus $\boldsymbol{n}$ can be quantitatively analyzed to determine the $\boldsymbol{I}$-$\boldsymbol{S}$ dipolar-coupling constant or internuclear distance.[15,16] In this thesis, REDOR experiments are carried out to probe the dipolar interactions for spin pairs such as ^{27}Al-^{31}P and ^{19}F-^{29}Si.

2.2.3.5 Multiple-quantum MAS (MQMAS)

MAS alone is not effective to average anisotropic interactions for quadrupolar nuclei, which leads to significant broadening of signals in rigid spin systems. Although most of the quadrupolar broadening can be prevented by limiting excitations to the central -1/2 ⟷ +1/2 transition, the second-order interaction can still broaden the resulting resonances and result in poor resolution of chemically inequivalent sites. A two-dimensional MAS technique has been developed for half-integer quadrupolar nuclei.[17,18] Because this method could completely average out second-order quadrupolar broadening, much higher spectral resolution is achieved. In this thesis, ^{27}Al and ^{23}Na 3QMAS experiments are performed to separate the overlapping peaks in the corresponding MAS spectra.

2.3 References

(1) Bandyopadhyay, R.; Bandyopadhyay, M.; Kubota, Y.; Sugi, Y. *J. Porous. Mater.* **2002**, *9*, 83-95.
(2) Van Bekkum, H.; Flanigen, E. M.; Jacobs, P. A.; Janse, J. C., Eds., *Introduction to Zeolite Science and Practice*; Elsevier Science Limited, Amsterdam, **2001**.
(3) Bragg, W.; Bragg, W. *Proc. R. Soc. London, Ser. A* **1913**, *88*, 428-438.
(4) Treacy, M. M. J.; Higgins, J. B. in "*Collection of Simulated XRD Powder Patterns for Zeolites" 5th Revised Edition*; Elsevier Science, **2007**.
(5) Goldstein, J.; Newbury, D. E.; Joy, D. C.; Lyman, C. E.; Echlin, P.; Lifshin, E.; Sawyer, L.; Michael, J. R. *Scanning Electron Microscopy and X-ray Microanalysis*; Springer, New York, **2003**.
(6) Duer, M. J. *Solid-State NMR Spectroscopy: Principles and Applications*, Oxford, Malden, MA, Blackwell, Science, **2002**.
(7) MacKenzie, K. J. D.; Smith, M. E. *Multinuclear Solid-State Nuclear Magnetic Resonance of Inorganic Materials*; Pergamon: Amsterdam, **2002**.
(8) Daněk, V. *Physico-Chemical Analysis of Molten Electrolytes*; Elsevier: Amsterdam, **2006**.
(9) Andrew, E. R. *Encyclopedia of Magnetic Resonance*; Wiley InterScience, New York, **2007**.
(10) Fyfe, C. A.; Thomas, J. M.; Klinowski, J.; Gobbi, G. C. *Angew. Chem. Int. Ed.* **1983**, *22*, 259-275.
(11) Hartmann, S.; Hahn, E. *Phys. Rev.* **1962**, *128,* 2042.
(12) Vega, A. J. *J. Magn. Reson.* **1992**, *96*, 50-68.
(13) Fyfe, C. A.; Wong-Moon, K. C.; Huang, Y.; Grondey, H.; Mueller, K. T. *J. Phys. Chem.* **1995**, *99*, 8707-16.
(14) Vega, A. J. *Solid State Nucl. Magn. Reson.* **1992**, *1*, 17-32.
(15) Gullion, T.; Schaefer, J. *J. Magn. Reson.* **1989**, *81*, 196-200.
(16) Gullion, T. *Concepts Magn. Reson.* **1998**, *10*, 277-289.
(17) Frydman, L.; Harwood, J. S. *J. Am. Chem. Soc.* **1995**, *117*, 5367-5368.
(18) Medek, A.; Harwood, J. S.; Frydman, L. *J. Am. Chem. Soc.* **1995**, *117*, 12779-12787.

Chapter 3 Investigations of Formation of Molecular Sieve SAPO-34 Using Diethylamine as a SDA

3.1 Introduction

Zeolites have been extensively used in industry as ion-exchangers, sorbents, and, in particular, catalysts. Another important type of microporous materials is aluminophosphate ($AlPO_4$)-based molecular sieves.[1] Unlike zeolites whose frameworks are negatively charged, $AlPO_4$-based molecular sieves have neutral frameworks and therefore cannot be directly used as acidic catalysts. However, introducing Si into the $AlPO_4$ frameworks yields negatively charged frameworks. Therefore, the resulting silicoaluminophosphates (SAPOs) can be used as catalysts for several reactions catalyzed by acids.

Among SAPO-based catalysts, SAPO-34 is of particular importance. It has CHA topology (Figure 3.1).[2] The framework contains chabazite (CHA) cages which can be accessed via an eight-membered ring (8R) window with a pore diameter ~0.38 nm. SAPO-34 has shown potentials for several applications including gas separation and water adsorption.[3,4] Perhaps, the most important use of this material is to catalyze the methanol-to-light olefin (MTO) reactions.[5-10] SAPO-34-based catalysts have been used commercially to convert methanol to ethylene and propylene. The catalytic performance is determined by the Si content and distribution within the framework, and these factors

---

* A version of this chapter (without catalytic tests) has been published: Zhang, L.; Bates, J.; Chen, D.; Nie, H. Y.; Huang, Y. *J. Phys. Chem. C*, **2011**, *115*, 22309-22319.

are often influenced by the synthetic conditions and the structure directing agent (SDA) used. The formation of SAPO-34 under hydrothermal synthesis (HTS) conditions has been studied with various SDAs.[11-19] Since the early work by Liu and co-workers,[15,18] diethylamine (DEA) has increasingly become a choice of SDA due to its ability of producing SAPO-34 with high thermal stability, high Si content, and high crystallinity as well as its relatively low cost. Despite that the crystallization of SAPO-34 with DEA as SDA has been examined, its formation on a molecular level is still not completely understood.

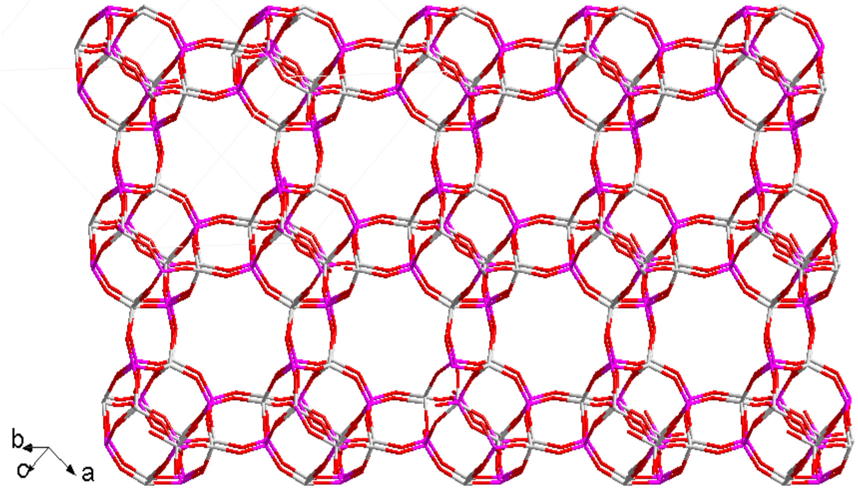

Figure 3.1 Framework of SAPO-34.

One of the alternative methods for SAPO synthesis is dry gel conversion (DGC).[20-30] This method involves treating predried gel powder at elevated temperatures and autogenous pressures to form crystalline molecular sieves. The DGC synthesis can be carried out in two ways: (i) steam-assisted conversion (SAC) where the initial dry gel containing SDA is separated from a small amount of water in an autoclave and (ii) vapor-phase transport (VPT), which is similar to SAC except that a small amount of SDA solution/liquid is put at the bottom of an autoclave (Figure 3.2). The differences and similarities in crystallization under DGC and HTS conditions have been discussed by several authors.[31,32] The pre-dried gel powder usually contains 20–40% water by weight. The water occluded inside the "dry" gel and the water initially placed at the bottom of an autoclave have been found to play a critical role in crystallization.[31,32] It is recognized that the mechanisms underlying the crystallization under the DGC and HTS conditions may be fundamentally similar. The lack of apparent liquid phase, however, does limit mass transport and therefore may result in lower crystal growth rates. Consequently, the intermediates may be obtained under the favorable circumstances.

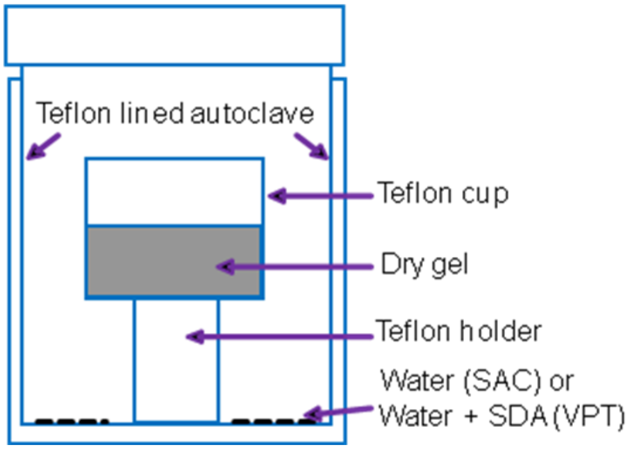

Figure 3.2 Diagram of the reaction vessel used for DGC method.

In the present work, SAPO-34 crystallization under both SAC and VPT conditions has been investigated by using diethylamine as a SDA. Attention was also placed in Si incorporation. Evolution of long-range ordering in the dry gel was followed by powder X-ray diffraction (PXRD); the changes in gel morphology were monitored by scanning electron microscopy (SEM); the development of short-range ordering of framework elements was probed by ^{31}P, ^{27}Al, and ^{29}Si magic-angle spinning (MAS) NMR; and the behavior of the SDA was examined by ^{13}C NMR. Different Al species in the gel were differentiated by ^{27}Al triple quantum MAS (3QMAS) NMR. The P–O–Al connectivity was established by ^{31}P{^{27}Al} and ^{27}Al{^{31}P} rotational-echo double-resonance (REDOR) experiments. Si incorporation was investigated by ^{1}H $\rightarrow$ ^{29}Si cross polarization (CP) NMR. Further, the nucleation and growth were examined by atomic force microscopy (AFM). From the data obtained from these techniques, some new insights into SAPO-34 formation process were obtained. To test the catalytic performances of SAPO-34 products obtained by two methods, MTO reaction experiments were also carried out.

3.2 Experimental section

3.2.1 Sample preparation

The reagents used were pseudoboehmite (Catapal-B, Vista, ca. 65% Al_2O_3), H_3PO_4 (EM Science, 85%), diethylamine (Alfa Aesar), colloidal silica (Ludox LS-30, Aldrich) and the remainder was distilled water. The initial dry gel molar compositions (Al_2O_3:P_2O_5:SiO_2:DEA:H_2O) for SAC and VPT were 1.0:0.8:0.4:2.0:50 and 1.0:0.8:0.4:0:50, respectively. A typical procedure[22] for the preparation of SAC dry gel is the following: 15.7 g of Catapal B was mixed with 76.1 g of distilled water, and the mixture was stirred at room temperature for 10 minutes followed by adding 18.4 g of H_3PO_4 slowly with continuous stirring. The solution containing 8 g of colloidal silica and 14.6 g of DEA, which was also stirred for 10 minutes at room temperature, was then added to the above mixture under vigorous stirring for homogeneity. The final mixture was stirred for 1 h and then dried at 353 K with constant stirring to allow evaporation of water until white solids formed. The solid sample was then ground into a fine powder and sealed in glass vials. A series of intermediates was synthesized by placing 1.0 g of the initial SAC dry gel powder into small Teflon cups. Each cup was placed in a 23-mL Teflon-lined autoclave with 0.4 g distilled water at the bottom and heated in an oven at 473 K for different times. The reactions were quenched in cold water. For comparison, each solid sample was divided into two parts. One part was dried in air, and the other part was first washed with distilled water in a beaker and then dried in the same beaker in air without isolation from the liquid phase. This ensured that solid particles were not washed away. All dried samples were kept in sealed vials for further analysis. For the VPT method, the initial dry gel was prepared similarly to SAC method, but without DEA. Instead, 1.2 g of 25% aqueous DEA solution was place at the bottom of each autoclave.

3.2.2 Characterization

PXRD patterns were recorded on a Rigaku diffractometer using Co Kα radiation (λ=1.7902 Å). Morphological investigations and energy dispersive X-ray (EDX) analyses were performed on a LEO 1540XB Field Emission Scanning Electron Microscope.

All the NMR experiments were carried out on a Varian/Chemagnetics Infinityplus 400 WB spectrometer equipped with three rf channels operating at the field strength of 9.4 T. The Larmor frequencies of ^{1}H, ^{13}C, ^{31}P, ^{27}Al, and ^{29}Si were 399.5, 100.4, 161.7, 104.1, and 79.4 MHz, respectively. The chemical shifts of ^{13}C, ^{31}P, ^{27}Al, and ^{29}Si were referenced to adamantane, $NH_4H_2PO_4$, 1M $Al(NO_3)_3$, and tetrakis(trimethylsilyl)-silane (TTMSS). Depending on the requirements of individual experiment, three MAS probes were used (a Varian/Chemagnetics 7.5 mm, a 4.0 mm H/X/Y triple-tuned T3 MAS, and a 5.0 mm H/F/X/Y triple-tuned MAS probe). The ^{13}C

CP MAS spectra were recorded by using the 5.0 mm probe with the Hartmann-Hahn conditions set on adamantane, and the ^{1}H 90° pulse length was 4 μs. A contact time of 2 ms was used, and the pulse delay was 9 s. The proton-decoupling field was about 60 kHz. For ^{31}P MAS experiments, a 45° pulse was typically used, and the recycle delay was 60s. The ^{27}Al spectra were acquired using a 30° pulse with a pulse delay of 1 s. For the ^{29}Si MAS experiments, a 45° pulse was used with a pulse delay of 60 s. For ^{29}Si CP MAS experiments, the ^{1}H 90° pulse length was 5 μs, and the Hartmann-Hahn condition was determined on TTMSS. ^{31}P{^{27}Al} and ^{27}Al{^{31}P} REDOR experiments were performed with the 5.0 mm probe with a spinning speed of 8 kHz using the standard REDOR pulse sequence.[33] The details for REDOR experiments were described in the previous work.[34] ^{27}Al 3QMAS experiments were performed using the 4.0 mm probe, and the spinning rate was 10 kHz. The spectra were obtained by utilization of a three-pulse z-filter sequence.[35] The rf strengths of the first two hard pulses and third soft pulse were optimized individually, and the optimized pulse lengths were 5.7, 2.0, and 15.0 μs for the three consecutive pulses.

AFM used in surface structure study was a Park Systems XE-100. A cantilever with nominal spring constant of 40 N/m, resonant frequency of 300 kHz, and tip radius of 10 nm (NSC15, Mikro Masch) was operated under the dynamic force mode. In this mode, the cantilever is vibrated at around the resonant frequency, and its amplitude reduces when the tip is in proximity with the sample surface caused by the tip–sample interaction. Reduced amplitude is set as the feedback parameter (set point) so that the AFM system scans the surface contour of the sample with minimized error signals (the difference between the set point and the amplitude measured) by adjusting the distance between the tip and the sample surface. Mapping of this distance constructs topographic image for the surface morphology. Mapping the error signal results in an image removing the height contribution and stressing only the shape of surface features. When the height range is large, surface features with small height differences are obscured. In this case, it is advantageous to use the error signal image to show the shapes of surface features, while using the topographic image to estimate the height distribution. The scan rate for obtaining images in an area of 45×45 μm^2 is 0.5 Hz and for images in an area of 10 × 10 μm^2 is 1 Hz. The experiment was conducted in air with a relative humidity of ~40%.

3.2.3 Catalytic tests

MTO reactions were performed at the Dalian Institute of Chemical Physics, China. They were carried out with a fixed-bed reactor at atmospheric pressure. 0.3 g of catalyst (40-60 mesh) was loaded into the reactor. The sample was preheated in nitrogen flow at 773 K for 1 h and then the temperature of the reactor was decreased to 723 – 730 K. The methanol and nitrogen mixture was then pumped into the reactor. The weight hourly space velocity (WHSV) was 2.9 h^{-1}. The products were analyzed on-line by a Varian GC3800 gas chromatograph equipped with a FID detector and a PoraplotQ-HT capillary column.

3.3 Results and discussion

3.3.1 Formation of SAPO-34 under SAC conditions

Powder X-ray diffraction was used to monitor the evolution of long-range ordering in SAC gel, and the selected patterns are shown in Figure 3.3A. The pattern of the unwashed initial SAC dry gel has sharp reflections with a very strong low angle peak, which means that the major component of the initial dry gel is a layered material with long-range ordering. Upon heating, the peaks due to the layered phase gradually become weaker and broader. It appears that the crystalline layered phase became a semicrystalline material. Heating the dry gel for 2 days resulted in the emergence of several sharp peaks whose positions correspond to (101), (211) and (300) reflections of SAPO-34. However, the pattern also contains the peaks due to $AlPO_4$-11, implying that $AlPO_4$-11 is likely an intermdiate. Seeing $AlPO_4$-11 is not surprising since DEA is known to template $AlPO_4$-11.[36] Further heating the gel leads to continuing increase in the intensity of the peaks due to SAPO-34 and disappearance of the reflections belonging to $AlPO_4$-11. The pattern of the 5-day sample only contains the peaks solely due to trigonal SAPO-34, and no peak from $AlPO_4$-11 is seen in the pattern.

Previous work[37-40] has shown that the structure of the intermediates formed during the crystallization of SAPO- and AlPO-based molecular sieves under DGC conditions is held by weak, noncovalent bonding interactions. To investigate the nature of the bonding in the SAC gel samples, we washed the intermediates with water. Upon washing, all the reflections due to the layered phases and the broad reflections due to the semicrystalline layered phase disappeared in the corresponding XRD patterns (Figure 3.3B). Only broad amorphous halos remained in the washed samples heated for less than 2 days. These findings suggest that the structure of the crystalline and semicrystalline layered phases is also held by the weak hydrogen bonding and van der Waals forces.

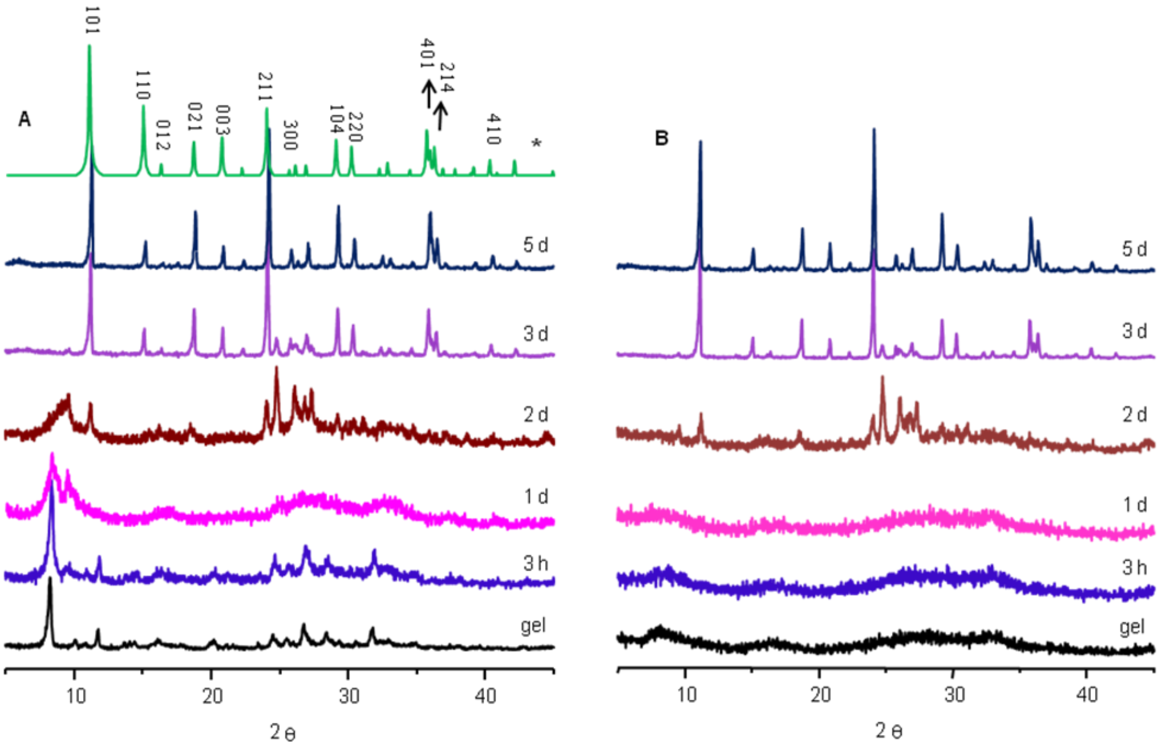

Figure 3.3 Powder XRD patterns of (A) unwashed and (B) washed SAC dry gel samples. * is simulated trigonal SAPO-34 XRD data.[19]

Several representative samples were chosen for SEM analysis to examine the morphological evolution of SAC gel samples as a function of crystallization time (Figure 3.4). The image of the initial SAC dry gel exhibits layered morphology. Disordered aggregates were observed after 1 day of heating. The image of 2 d sample shows the formation of SAPO-34 crystals resulting from the transformation of the semicrystalline phase (see Figure 3.4C). The highly crystalline SAPO-34 product is formed after 5 days. The trend agrees with the XRD result very well.

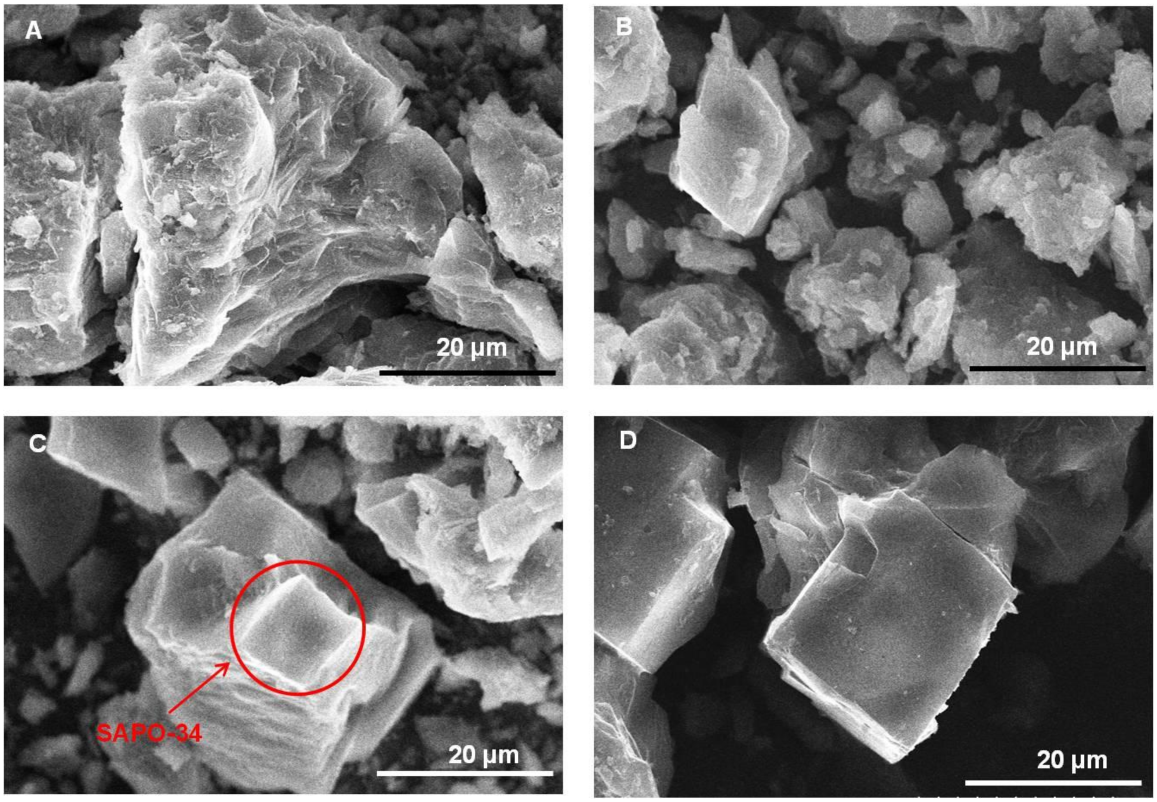

Figure 3.4 SEM images of unwashed (A) initial dry gel, (B) 1 d, (C) 2 d and (D) 5 d SAC gel samples.

To characterize the local environments of P and Al atoms in the intermediate phases, ^{31}P and ^{27}Al solid-state MAS NMR spectra were obtained. Figure 3.5A shows the ^{31}P spectra of unwashed SAC gel samples. The ^{31}P spectrum of the initial dry gel has three sharp peaks at -19, -20, and -23 ppm, indicating that the crystalline layered phase has, at least, three different P sites. There are also several broader and weaker peaks between 0 and 10 ppm, and they are likely due to a small amount of amorphous material. Upon heating, the three crystallographically nonequivalent peaks gradually become a single peak at around -20 ppm due to the transformation to the semicrystalline intermediate. This peak is broader than those of initial gel, but still relatively narrow, implying that the semicrystalline phase still maintains the ordered local environment around P despite losing long-range ordering. The chemical shift indicates that the P in the layered phase is not fully condensed.[41-43] After 2 days of the SAC treatment, a new peak starts emerging at around -30 ppm, indicating the formation of fully condensed P with $P(OAl)_4$ environment. The spectrum of the final product (5 d sample) only has a single peak at -30 ppm, which is consistent with that trigonal SAPO-34 only has a single T (tetrahedral) site. There are two very weak and broad peaks in the spectrum, suggesting the existence of a small amount of amorphous impurity.

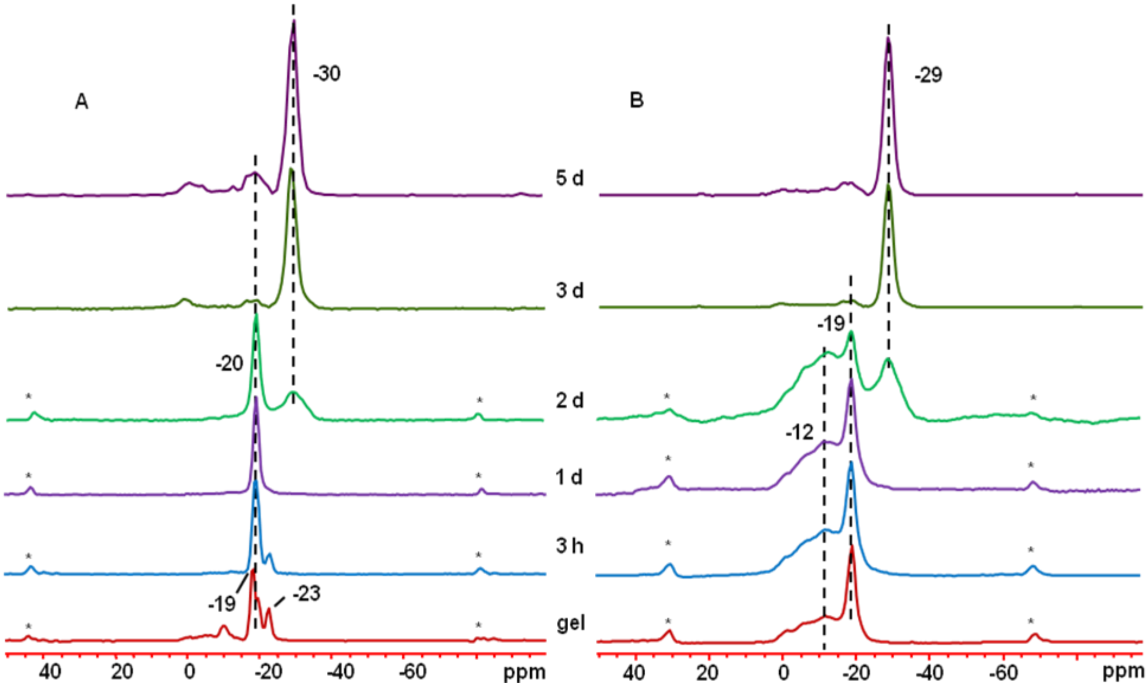

Figure 3.5 ^{31}P MAS spectra of (A) unwashed and (B) washed SAC dry gel samples. Asterisks indicate spinning sidebands.

Although it is believed that the initial dry gel is AlPO in nature, the possibility that it might be a layered diethylammonium phosphate cannot be ruled out without additional experiment. To clarify this situation, the $^{31}P\{^{27}Al\}$ REDOR experiment on 3 h sample was carried out. This sample has a PXRD pattern identical to that of the initial gel. REDOR is a technique designed to detect weak heteronuclear dipolar interaction involving two unlike spins. In the present case, the $^{31}P\{^{27}Al\}$ REDOR is used to detect P–O–Al connectivity because only the P dipolar coupled to Al will be seen in the $^{31}P\{^{27}Al\}$ REDOR difference spectrum. Figure 3.6 shows that the P peaks between -19 and -23 ppm appear in the REDOR difference spectra (ΔS), unambiguously confirming that the layered phase is an AlPO material and not an amine phosphate.

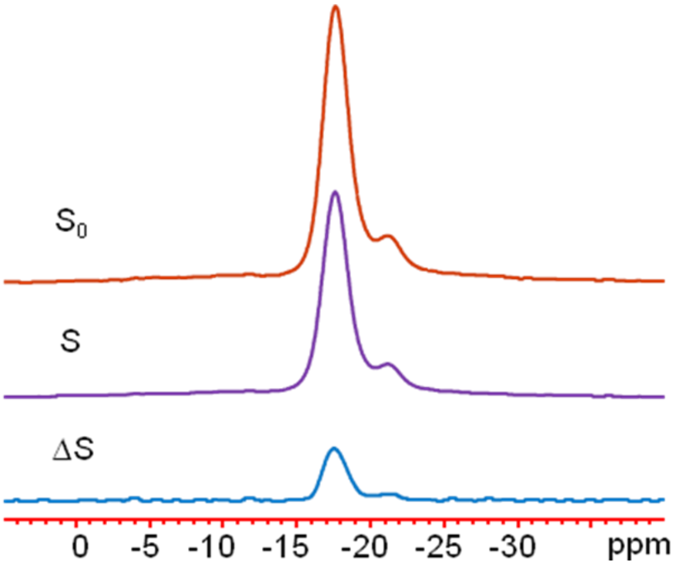

Figure 3.6 $^{31}P\{^{27}Al\}$ REDOR spectrum of unwashed 3 h SAC sample with a dephasing time of 1.25 ms.

The ^{27}Al MAS spectrum of the initial dry gel shows two strong peaks at 40 and 6 ppm (Figure 3.7A). The peak at 40 ppm indicates the existence of tetrahedral Al in the layered phase. The one at 6 ppm is likely due to either unreacted aluminum oxide or 5-coordinated Al with $Al(OP)_4(OH_2)$ environment in AlPO species.[13] The spectra did not change significantly with increasing heating time except that the peaks gradually become broader. The spectrum of the 5 d sample (the final product) is consistent with those reported in the literature.[2]

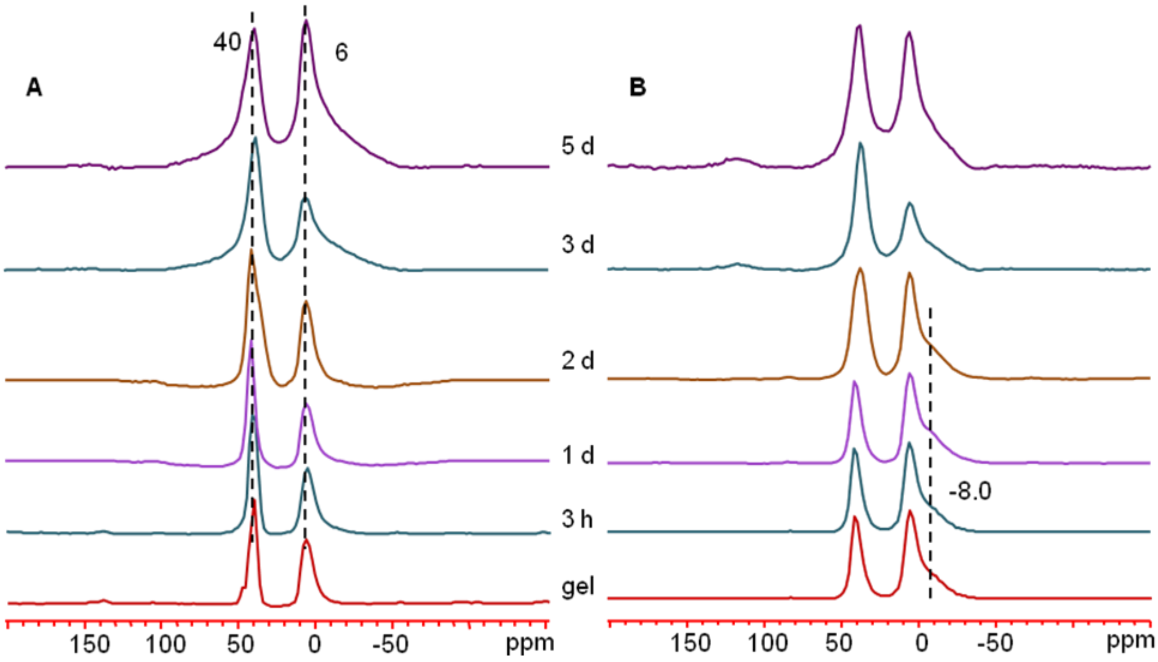

Figure 3.7 ^{27}Al MAS spectra of (A) unwashed and (B) washed SAC dry gel samples.

To identify the nature of the peak at 6 ppm the ^{27}Al{^{31}P} REDOR experiments on selected samples heated for 3 h, 2 d and 5 d were also performed (Figure 3.8). For all the samples, the REDOR difference spectra (ΔS in Figure 3.8) clearly show only the tetrahedral Al peak. The peak at 6 ppm seen in the MAS spectra did not appear in the REDOR difference spectra. These results clearly indicate that this peak is due to unreacted alumina with no P atom in the second coordination sphere. The ^{27}Al 3QMAS spectrum of SAPO-34 (5 d sample) is illustrated in Figure 3.9A, which clearly exhibits three signals. The broad peak at around 40 ppm seen in the MAS spectra is actually composed of two components with isotropic chemical shift values of about 45 (strong) and 55 ppm (weak). On the basis of the previous work,[44-46] the peak at 45 ppm was assigned to the tetrahedral Al with Al(OP)$_4$ environment and the 55 pm peak to the tetrahedral Al atoms in aluminosilicate domains with Si as the nearest neighbour. The peak at 6 ppm in the MAS spectrum appears in the F1 dimension with an isotropic chemical shift of 15 ppm, and as mentioned earlier it originates from the unreacted alumina.

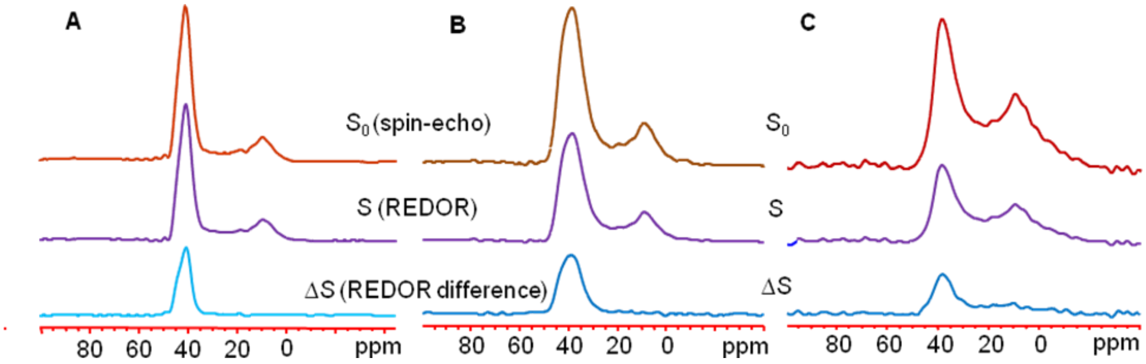

Figure 3.8 ^{27}Al{^{31}P} REDOR spectra of the 3 h (A), 2 d (B) and 5 d (C) samples with a dephasing time of 1.25 ms.

Washing the sample with water results in a significant change in the ^{31}P MAS spectra (Figure 3.5B). The gel samples heated for less than 2 days are X-ray amorphous upon washing. Their corresponding ^{31}P spectra now contain a very broad envelop resulting from many overlapping peaks with a maximum at around -12 ppm and a relatively sharp peak at near -20 ppm seen in the unwashed samples. It appears that part of the layered materials transforms to a completely amorphous material with no short-range ordering, but a significant portion of the layered material was able to retain the ordered local P environment, although long-rang ordering is lost.

The ^{13}C CP MAS spectra of selected SAC gel samples were obtained to follow the behavior of the SDA molecules inside the gel samples (Figure 3.9B). The ^{13}C chemical shifts of the methylene and methyl carbons in free DEA molecule are 44.2 and 15.4 ppm, and in a protonated DEA molecule (DEA-H$^+$) the chemical shifts of these two resonances are shifted to 43.6 and 12.2 ppm.[19,47,48] In the ^{13}C CP MAS spectrum of the initial dry gel without heating, the methyl group appears as a relatively sharp peak at 12 ppm with a shoulder at around 11 ppm, and the methylene region has three peaks at 43, 42 and 40 ppm. The chemical shift values indicate that the DEA molecules are in a protonated form, and the multiple signals suggest that the protonated DEA-H^+ have different environments. The sharpness of the peaks suggests that the SDA located between the layers has high mobility, resulting in a weaker proton–carbon dipolar interaction. In the final SAPO-34 product, the ^{13}C peaks become much broader, and the methyl region has at least four peaks. Such a spectrum implies that the DEA-H^+ ions in the CHA cages may be disordered: the number of DEA molecules may vary from one to two, and the orientation of the DEA-H^+ may differ from cage to cage, both of which depend on the Si distribution. The broad peaks also indicate that the SDA is less mobile once it is trapped inside the CHA cage.

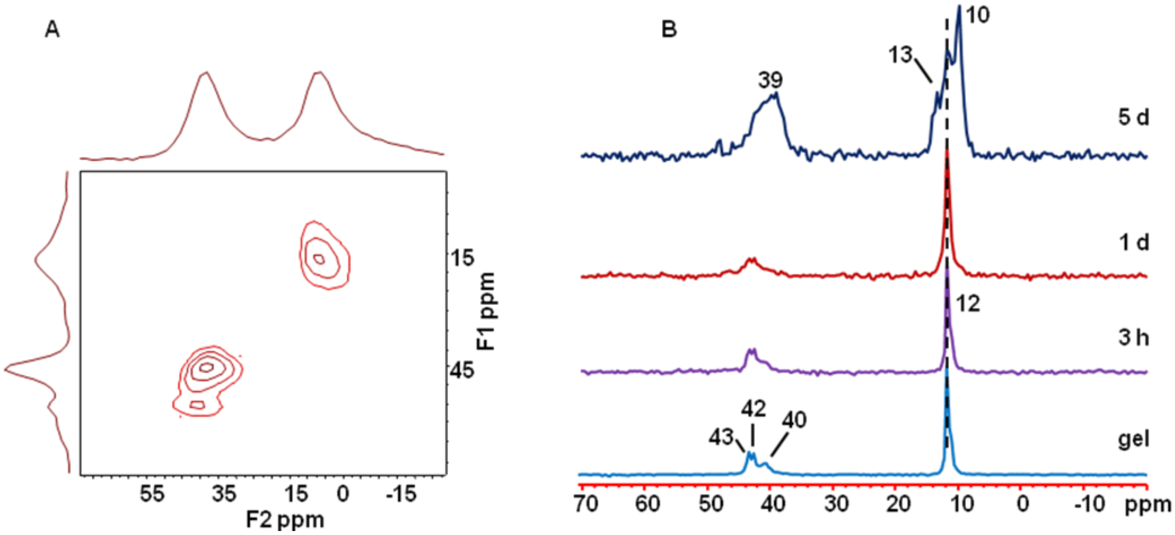

Figure 3.9 ^{27}Al 3QMAS spectrum of SAC 5d sample (A) and ^{13}C CP MAS spectra of selected unwashed SAC gel samples.

To investigate the Si incorporation, ^{29}Si MAS and ^{1}H → ^{29}Si CP spectra were obtained (Figure 3.10). The ^{29}Si MAS spectra of the gel samples heated for less than 2 days show that the initial gel only has a single peak at around -112 ppm, which can be assigned to unreacted amorphous silica with $Si(OSi)_4$ environments.[2,30,49,50] This observation indicates that the vast majority of the silica in the gel has not started reacting, implying that the crystalline and semicrystalline layered phases are mainly AlPO in nature. This result is not surprising since the lack of bulk water will inevitably slow down the dissolution of silica. After 2 days of heating, a new peak begins to appear at -90 ppm characteristic of $Si(OAl)_4$ environment often observed in SAPOs. This is consistent with the corresponding XRD pattern, SEM image and ^{31}P MAS spectrum of the 2 d sample showing the appearance of SAPO-34 crystals. The spectrum of the final product of SAPO-34 only has a sharp peak at -90, which is due to the isolated $Si(OAl)_4$ species in SAPO-34 as was reported previously in HTS.[14-16,18,50]

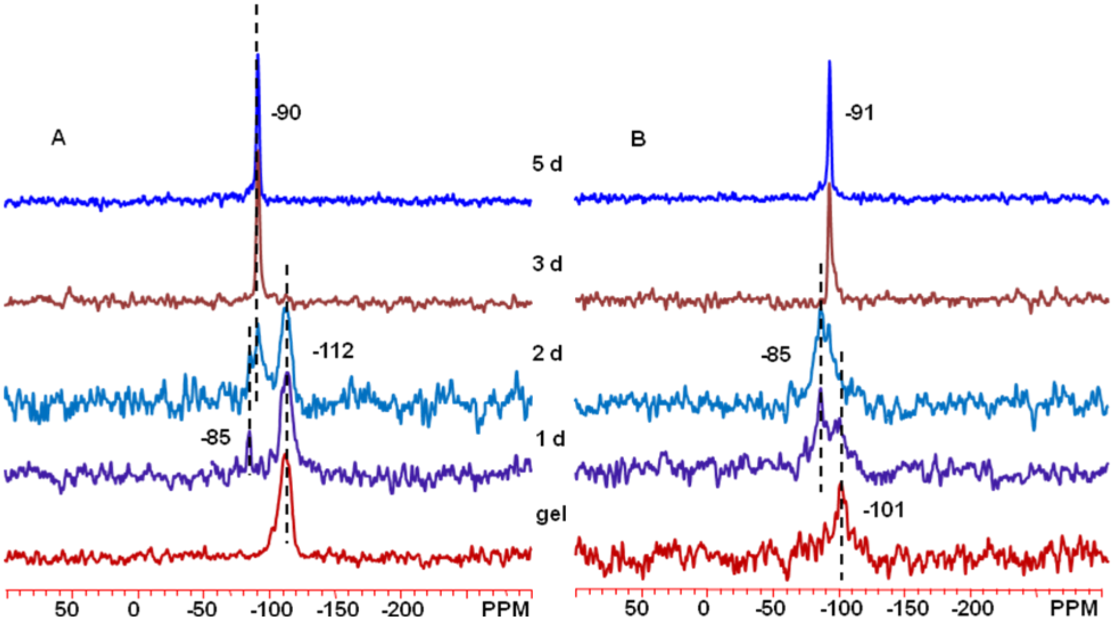

Figure 3.10 ^{29}Si MAS (A) and ^{1}H → ^{29}Si CP spectra of selected unwashed SAC gel samples with a contact time of 0.5 ms (B).

$^1H \rightarrow ^{29}Si$ CP NMR experiments were also carried out. Because CP is a technique that utilizes the ^1H – ^{29}Si dipolar interaction, it can be used for spectral editing. Specifically, CP selectively enhances the intensity of the ^{29}Si nuclides with protons in their close proximity. The CP spectrum of the initial dry gel (Figure 3.10B) exhibits a relatively weak signal at -101 ppm, which is not clearly visible in the corresponding MAS spectrum. This signal represents a small amount of Si atoms on the surface of silica particles with a chemical environment of $(SiO)_3SiOH$. As mentioned earlier, the strong peak seen in the MAS at -112 ppm is due to the Si in the bulk silica with $Si(OSi)_4$ environments. Because this species has no silanol groups directly attached, its signal does not show up in the CP spectra obtained with a very short contact time (0.5 ms). The CP spectra of 1- and 2-day samples show a new peak appearing at around -85 ppm (Figure 3.10B). The chemical shift of this peak corresponds to $(AlO)_3SiOH$ or $(SiO)(AlO)Si(OH)_2$ in amorphous aluminosilicates.[51] The protons on the silinol groups are the reason that these Si species are seen in the CP spectra. Thus, CP data imply that the SAC treatment leads to the formation of a small amount of amorphous aluminosilicate particles due to the reaction of silica with alumina. This aluminosilicate species further reacts with layered AlPO phase, resulting in Si incorporation upon transforming to SAPO-34. It seems that under the DGC conditions (i.e., the lack of bulk water), forming aluminosilicates is one way to “dissolute” or activate silica for further reaction. This peak disappeared in the final SAPO-34 (3- and 5-day samples), implying they were consumed at the end of crystallization.

In general, there are three Si substitution mechanisms (SM) in $AlPO_4$-based frameworks: (1) Si incorporation into an Al site (SM I), (2) Si incorporation into a P site

(SM II), and (3) 2Si for Al + P (SM III).[52] The P/Al ratio in $AlPO_4$-based molecular sieves is strictly 1:1. The change in the P/Al ratio upon Si substitution reflects the mechanisms through which Si is incorporated. EDX analysis was performed to obtain semi-quantitative information on elemental composition. The results reported in Table 3.1 were averaged from the data obtained from at least three different SAPO-34 crystals. The average Si content in SAPO-34 (5 d sample) is about 12 mol.%, which is very close to the proposed upper threshold value (11%) of SM II mechanism in SAPO-34.[53,54] Further, the (Si + P)/Al is equal to 1. Therefore, the EDX data indicate that one Si only substitutes for one P atom (SM II). This argument is supported by the ^{29}Si NMR spectra of SAPO-34, which show only a single peak at about -90 ppm due to the $Si(OAl)_4$ environment.

Table 3.1 Elemental compositions (molar basis) of SAPO-34 from EDX analysis.

Method	Sample	Si	Al	P	P/Al	(Si + P)/Al
SAC	5 d	0.12	0.50	0.38	0.76	1.00
VPT	7 d	0.16	0.47	0.37	0.79	1.13

From the information obtained from both XRD and NMR data, a scheme which quantitatively describes the formation of SAPO-34 under the SAC conditions (Figure 3.11) is proposed. Upon drying the wet gel resulting from mixing Al and P and Si sources as well as DEA, a crystalline layered phase formed immediately. Previous AFM studies showed that the step height of terraces on (001) faces SAPO-34[55] and related STA-7[56] correspond to the tilted double-six-ring (D6R) on the surface, suggesting that the D6R is energetically stable to terminate the structure of SAPO-34 and other frameworks composed of D6Rs on the crystal surface. Thus, we suggest that the layer of the crystalline phase bears a resemblance to the (001) face of SAPO-34 in that it contains titled D6Rs, and they are held together by the weak nonbonding forces. However, the D6R units may not possess the same orientation with respect to the lattice plan as they do on the (001) face of SAPO-34. Upon heating, under the influence of water vapor, the layered phase partially loses its crystallinity and becomes semicrystalline. It is likely accompanied by the slight rearrangement the tilted D6Rs via bond breaking and re-forming to orientate themselves to the same orientation along the three crystallographic axes. The layered phases are mainly AlPO in nature with little Si. Meanwhile, silica appears to reacts with alumina under SAC conditions, yielding small aluminosilicate particles presumably dispersed between the AlPO layers. The last step is that the layers are cooperatively cross-linked together forming the CHA cages around protonated DEA cations, yielding the SAPO-34 framework. It is at this stage that the Si atoms are incorporated into the framework as isolated $Si(OAl)_4$ species. The key component for the proposed scheme is that the layers of the intermediates contain D6Rs. Besides the AFM studies of SAPO-34[55] and STA-7[56] mentioned earlier, additional evidence that the D6R is the immediate precursor to the zeolite with FAU topology can be found in the literature.[57,58]

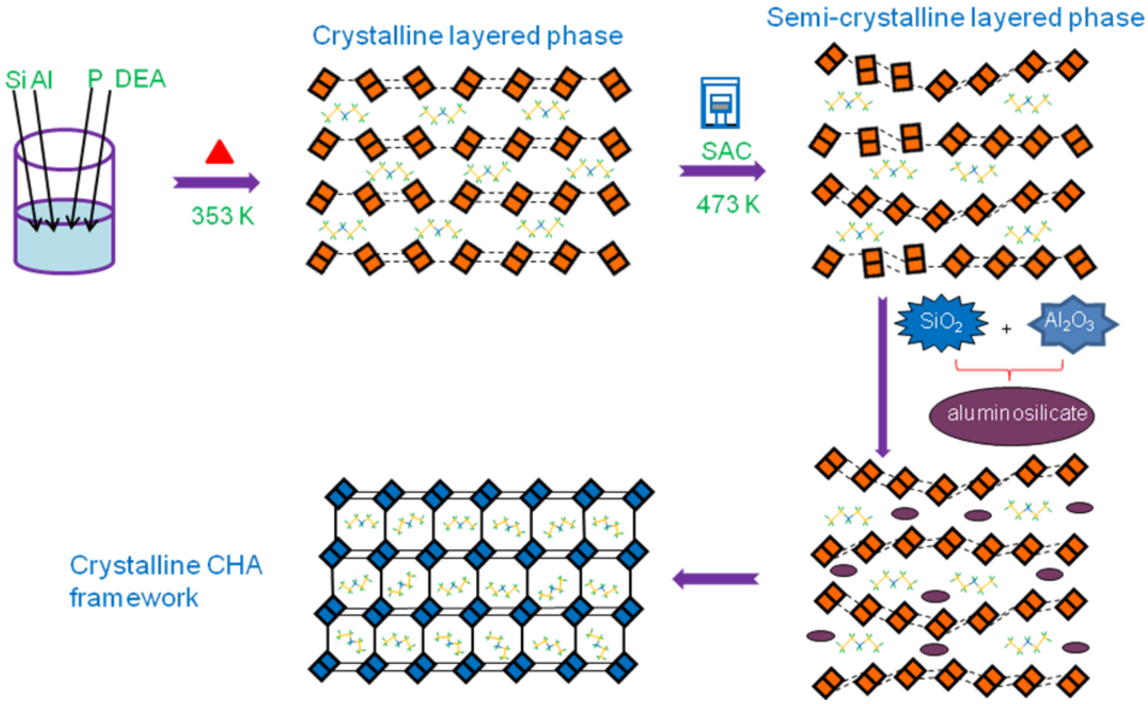

Figure 3.11 Illustration of formation of SAPO-34 under SAC conditions.

3.3.2 Formation of SAPO-34 under VPT conditions

The VPT method differs from SAC in that the initial dry gel does not contain SDA. The structure of initial VPT dry gel without heating is remarkably different from that of the SAC initial dry gel. Its powder XRD pattern indicates that the VPT dry gel is mainly amorphous, but does not necessarily have a layered structure (Figure 3.12). The ^{31}P MAS spectrum (Figure 3.13) implies that the P local environments are also different. The corresponding ^{27}Al MAS spectrum (Figure 3.14) shows that both tetrahedral (38 ppm) and octahedral Al (-14 ppm) exist. The ^{31}P{^{27}Al} and ^{27}Al{^{31}P} REDOR data (Figure 3.15A-B) suggest that the amorphous sample contains mainly an amorphous

AlPO phase and some unreacted pseudoboehmite. The SEM image (Figure 3.16) shows amorphous aggregates. Such difference is due to the lack of DEA in the gel.

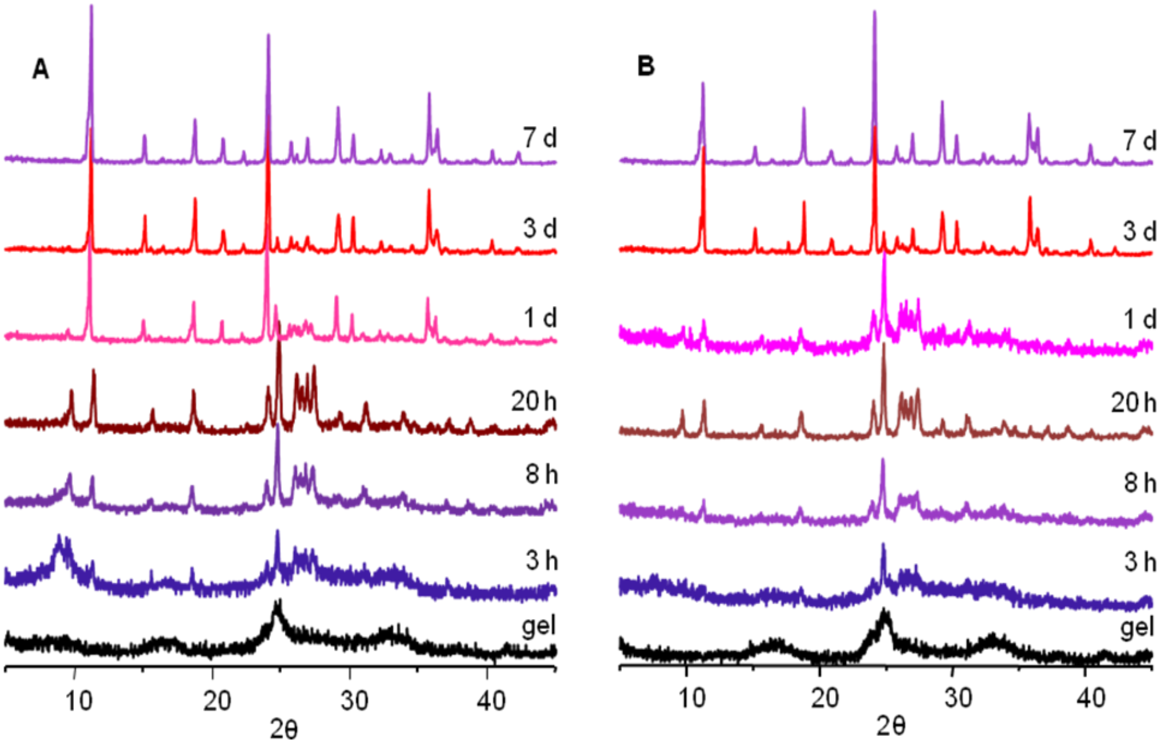

Figure 3.12 Powder XRD patterns of (A) unwashed and (B) washed VPT dry gel samples.

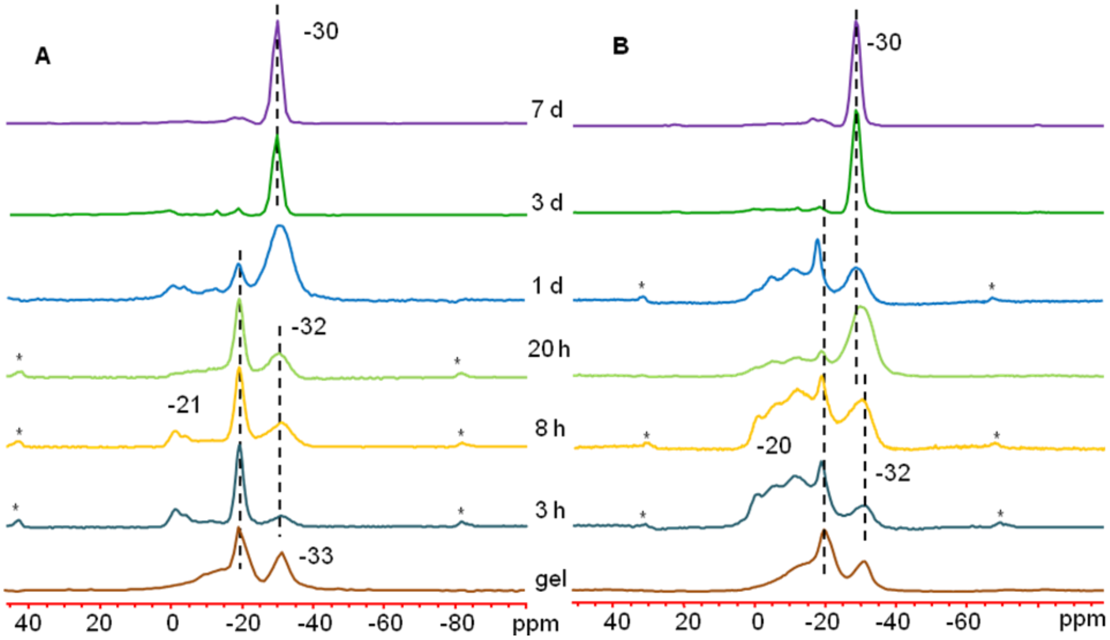

Figure 3.13 ^{31}P MAS spectra of (A) unwashed and (B) washed VPT dry gel samples. Asterisks indicate spinning sidebands.

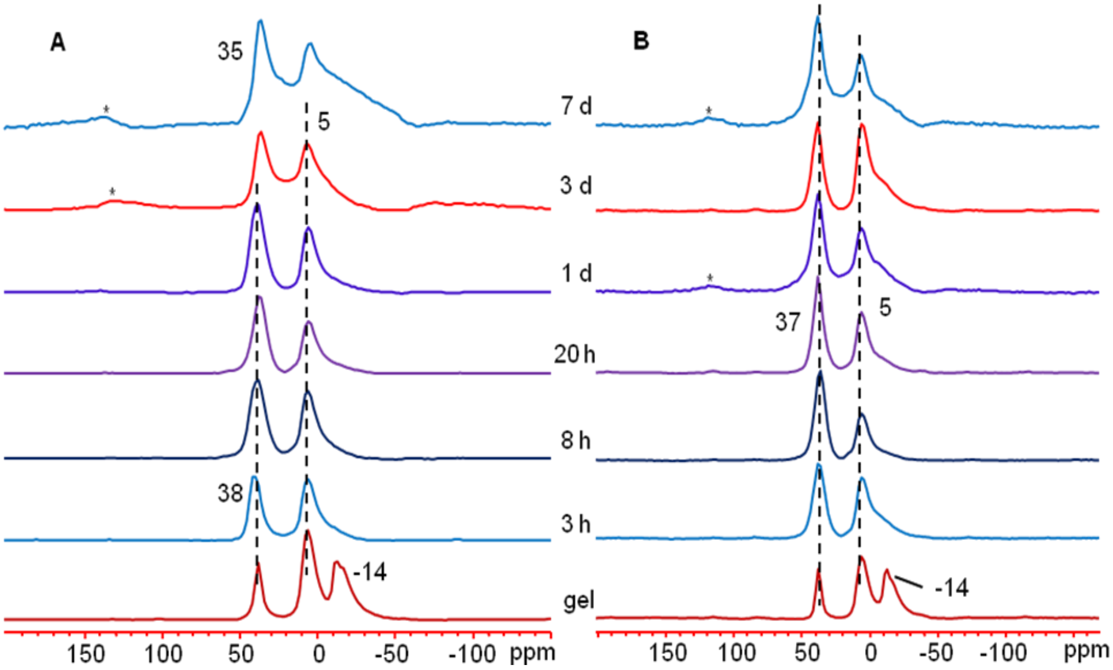

Figure 3.14 ^{27}Al MAS spectra of (A) unwashed and (B) washed VPT dry gel samples. Asterisks indicate spinning sidebands.

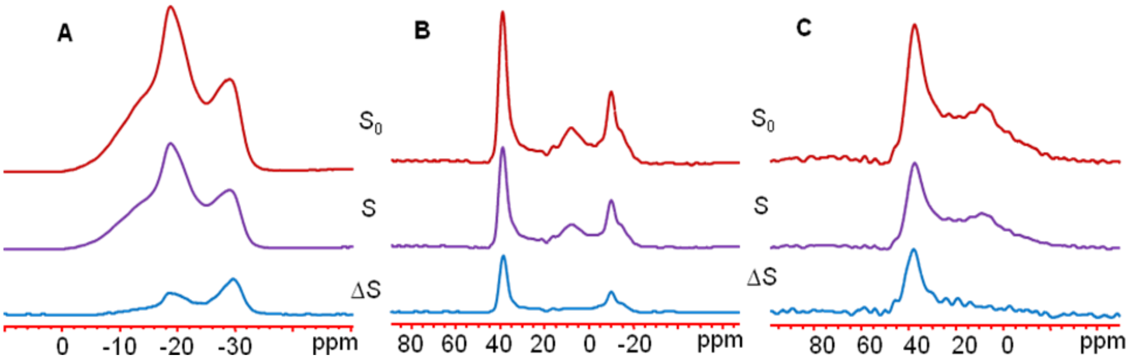

Figure 3.15 (A) ^{31}P{^{27}Al} REDOR and (B) ^{27}Al{^{31}P} REDOR spectra of the unwashed initial VPT dry gel and (C) ^{27}Al{^{31}P} REDOR spectra of unwashed 7 d with a dephasing time of 1.25 ms.

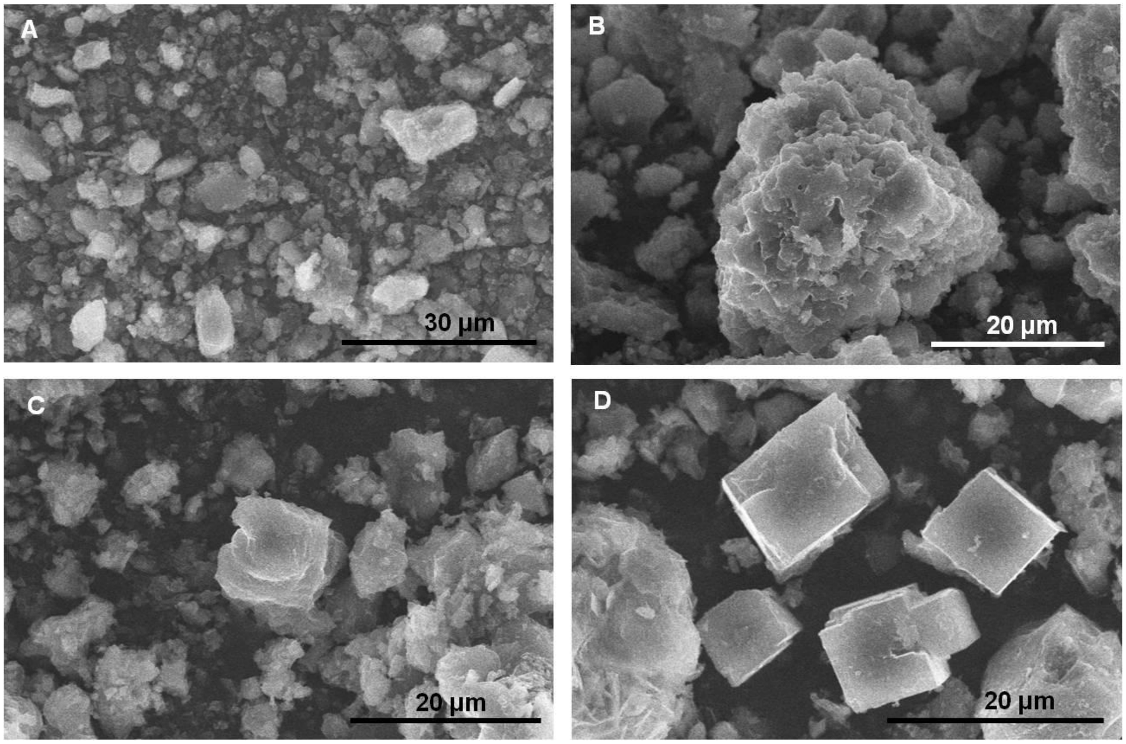

Figure 3.16 SEM images of unwashed (A) initial dry gel, (B) 3 h, (C) 8 h and (D) 7 d VPT gel samples.

Interestingly, once the DEA molecules are brought in contact with the gel, a semi-crystalline layered phase forms immediately as evidenced by a very broad low angle peak in the powder XRD pattern of 3 h sample. Because the powder XRD pattern and the ^{31}P and ^{27}Al MAS spectra of this sample are almost identical to that of semi-crystalline phase formed during SAC process (Figures 3.13 and 3.14), it is reasonable to believe that both semicrystalline phases have similar layered structures with the same local P and Al environments. The results indicate that one of the roles of DEA is to promote the formation of the layered AlPO phase. For this semicrystalline phase formed under VPT conditions, the changes in the PXRD, ^{31}P, ^{27}Al and ^{13}C NMR spectra as a function of time follow the same tends as seen during the SAC process (Figures 3.12-3.14 and 3.17B). Formation of a small amount of $AlPO_4$-11 as a competing phase is also observed in the early stage of the crystallization. The PXRD pattern and NMR spectra of washed samples confirm that the semicrystalline phase is also held by weak nonbonding interactions (Figures 3.12 and 3.13). The final product (7 d sample) is fairly pure without $AlPO_4$-11. The corresponding SEM image (Figure 3.16D) shows well-crystallized SAPO-34 with trigonal morphology. The ^{27}Al 3QMAS spectrum (Figure 3.17A) of 7 d sample is also the same as that of the SAPO-34 obtained from SAC method, and ^{27}Al{^{31}P} REDOR difference spectrum (Figure 3.15C) shows that SAPO-34 only has tetrahedral Al.

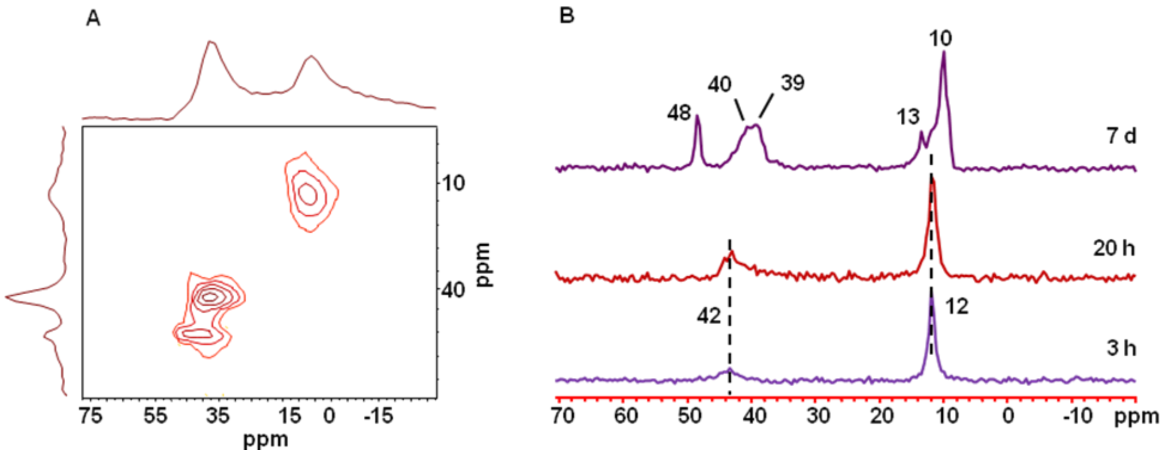

Figure 3.17 ^{27}Al 3QMAS spectrum of VPT 7d sample (A) and ^{13}C CP MAS spectra of selected unwashed VPT gel samples (B).

Similar to SAC, ^{29}Si MAS and ^{1}H → ^{29}Si CP NMR spectra (Figure 3.18) reveal that the Si incorporation occurs through the mechanism very similar to that observed during the SAC process; that is, the silica is activated via formation of aluminosilicate species. The spectrum of final SAPO-34 has a sharp peak at -91 ppm representing $Si(OAl)_4$ species. There is also a small peak at -95 ppm. This peak is associated with a small amount of $Si(OAl)_3(OSi)$ species. The EDX results are given in Table 3.1. The (Si+P)/Al ratio (1.13) and the Si content (16%) indicate that, in addition to isolated $Si(OAl)_4$ species, a very small amount of Si island also exist, which is consistent with the small Si peak at -95 ppm.

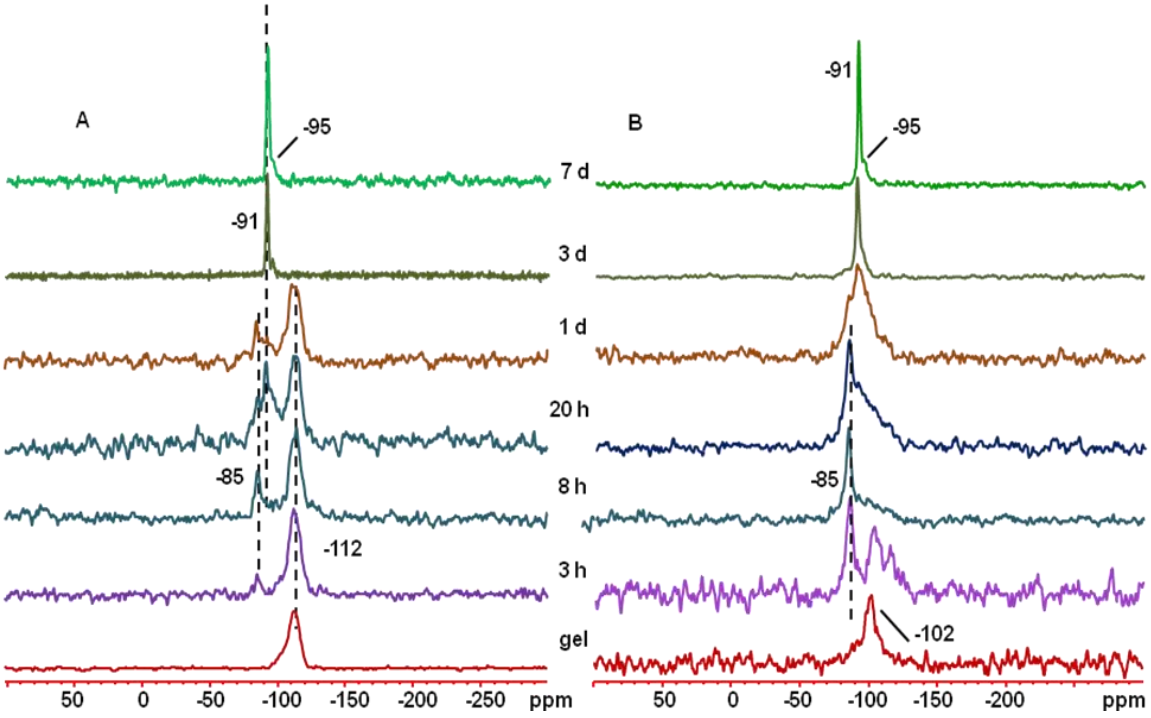

Figure 3.18 ^{29}Si MAS (A) and ^{1}H → ^{29}Si CP spectra of selected unwashed SAC gel samples with a contact time of 0.5 ms (B).

To gain further information regarding the nucleation and growth, the surface morphology of SAPO-34 was examined by AFM. In recent years, AFM has emerged as a powerful technique to study the crystallization of microporous materials due to its nanometer scale resolution of surface feature.[59-62] Recently, growth mechanisms of SAPO-34 under hydrothermal synthesis conditions with morpholine as SDA were examined[55], and the results provide a benchmark for interpretation of our data.

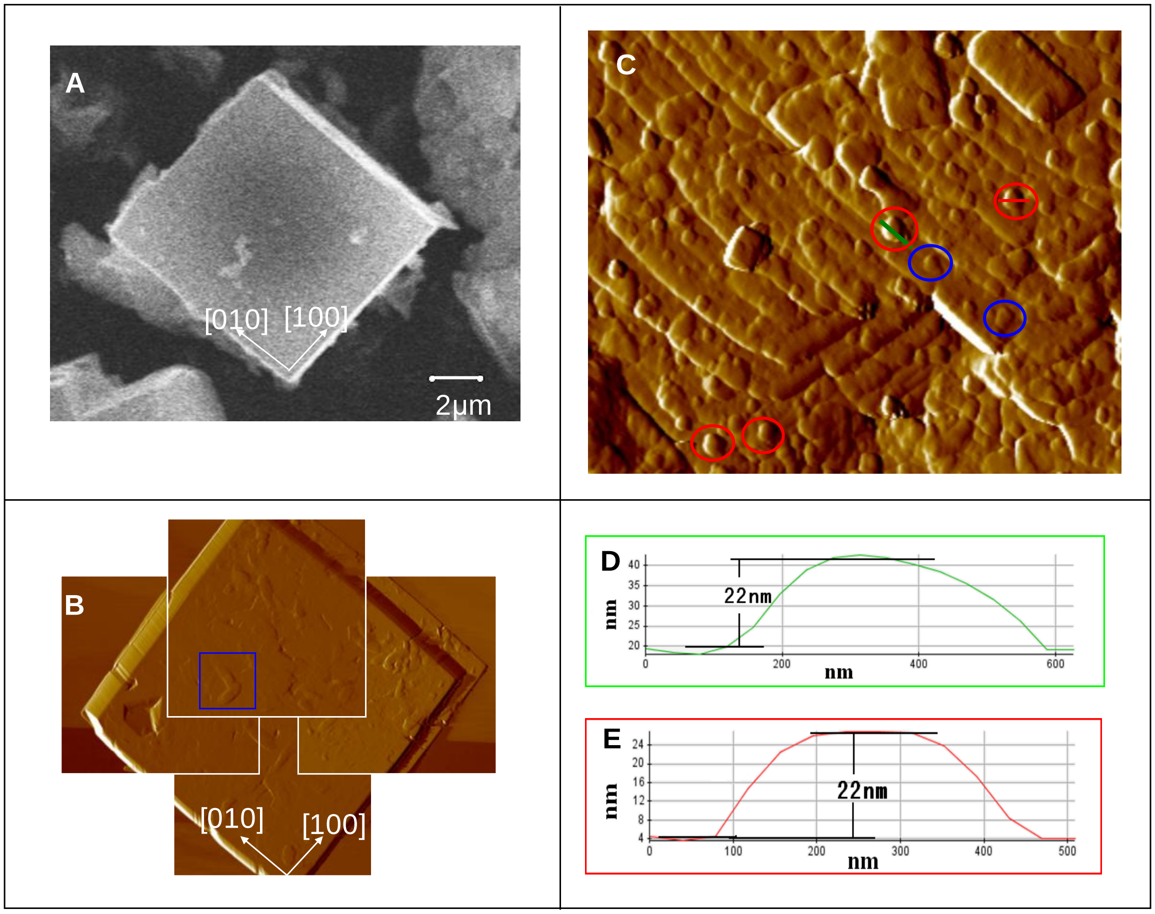

Figure 3.19 SEM and AFM images of the (001) face of SAPO-34 crystals (VPT 7 d sample): (A) SEM image of a crystal; (B) top-view AFM images (error signals are shown here for clarity) of another large crystal, each image taken in size of 45 ×45 μm^2; (C) enlarged view a square area in (B), 10 ×10 μm^2; and (D,E) cross-section height profile from the topographic image (not shown) along different lines as shown in (C), showing the height of two nuclei.

Figure 3.19A shows the SEM image of SAPO-34 prepared by VPT approach. On the basis of the crystal morphology and the recent AFM work on SAPO-34 prepared by HTS,[55] the crystal surface can be assigned to the (001) face of rhombohedral unit cell. For the SAPO-34 samples prepared by DGC methods, the crystal surfaces are often covered by a significant amount of surface debris even after extensive washing.

Therefore, finding crystals with good surface conditions suitable for AFM analysis is very challenging and time consuming. Nonetheless, few crystals with relatively good surface conditions were found. The AFM images of one of such crystals are shown in Figure 3.19B (because the topographic image has a large height range, which obscures the visualization of the crystals having small height differences, the error signal image is shown for clarity). As the maximum scanning area of the AFM instrument used (45×45 μm^2) is smaller than the crystal face, four AFM images of (001) face containing four corners from the same crystal were recorded separately, and piecing them together provides the outline of the 2D surface (Figure 3.19B). "Pseudo-rectangular" terraces parallel to [100] and [010] directions can be found at several locations on the same crystal surface (two such terraces are shown inside the blue box inside Figure 3.19B). The spiral growth was previously observed on the (001) surface of the SAPO-34 crystals synthesized with morpholine under HTS conditions,[55] but no such spiral was found for the SAPO-34 crystals prepared by the VPT method. The magnified image (Figure 3.19C) shows the rough surface and multiple nucleation points on the surface, suggesting that the crystal growth mechanism is "birth and spread".[62] Under the VPT conditions employed in this study, the nucleation rate appears to be fast as is evident from many nuclei on the crystal surface. These nuclei quickly spread and coalesce to form terraces.

Analysis of cross-section profiles for four individual freshly formed nuclei sitting on relatively flat terraces (the ones inside red circles in Figure 3.19C) shows that the average height of the nuclei is 22 nm (Figures 3.19D-E show the cross-sectional depth profile of two such nuclei). There are several nuclei (see the ones inside blue circles in

Figure 3.19C) whose heights are about 10 nm. However, these nuclei have already partially merged with the terraces underneath.

The average nuclei height is 22 nm, which is much larger than that (0.9 nm) found for the crystals synthesized by HTS method.[55] The SAPO-34 structure is built upon the D6Rs joint together via single 4-memebered rings. As mentioned earlier, the height of the terrace (0.9 nm) reported corresponds to the repeat distance (0.94 nm) between the layers of the tilted D6Rs along the [100] direction. In the present work, the average height of nuclei formed under VPT conditions is 22 nm, corresponding to about 23 layers of D6Rs.

The AFM results provide some details that can be included in SAPO-34 formation mechanism under DGC conditions proposed earlier. Unlike hydrothermal synthesis where nutrients can come from a liquid phase, all of the reactive species in DGC are contained in the solid phases. The small amount of bulk water is separated from the dry gel, which eliminates the direct contact between the reactive species in solution and solid gel. The small amount of water in vapor is not enough to dissolve the solids. Therefore, the formation of SAPO-34 is unlikely through gel dissolution, and therefore the single D6R layer growth was not observed because the bulk liquid containing the immediate precursor such as D6R unit is lacking. Therefore, SAPO-34 is likely formed through the conversion of the layered precursor, which already has the sheet of tilted D6Rs in the layer. As mentioned earlier, the forces holding the sheets together are weak non-bonding interactions, which facilitate bond breaking and reforming in the absence of bulk liquid and therefore assist in the transformation from the layered phase to SAPO-34. Such transformation might occur in a small domain involving several sheets of D6Rs in the precursor at once via cooperative reorganization of local structure of P and Al as well as Si species in the vicinity. The number of the sheets in the precursor involved in each domain may be estimated from PXRD and AFM data. From the PXRD pattern of 3 h sample, the interlayer spacing can be estimated at 1.3 nm. Thus, observed nuclei with a height of 22 nm, corresponding to 23 layers of D6Rs in SAPO-34, may result from the simultaneous transformation of 23 sheets of precursor (with a total height of 30 nm). Such a nucleation process is illustrated in Figure 3.20. Seeing many nuclei in Figure 3.19C indicates that the transformation happens in many locations within the precursor.

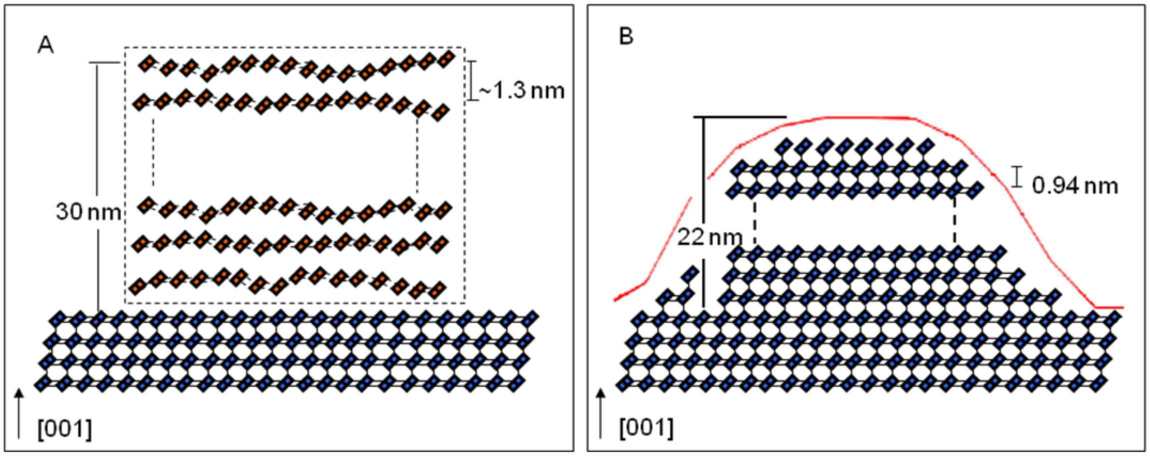

Figure 3.20 Illustration of nucleus formation on (001) face. (A) 23 sheets of precursor with a total height of about 30 nm; (B) a SAPO-34 nucleus containing 23 layers of D6Rs with a height of 22 nm.

3.4 Summary

The formation of SAPO-34 was examined under DGC conditions. The evolution of the solid gel phase as a function of heating time was followed by PXRD and solid-state NMR. Crystallization pathways appear to be the same under the SAC and VPT conditions for SAPO-34. SAPO-34 crystallizes from a semicrystalline precursor. This precursor has a layered structure held together by weak nonbonding interactions. Although the observation that the formation process under SAC and VPT are the same is not totally surprising, the VPT experiment does indicate that DEA promotes the formation of the layered intermediate. The AFM data suggest that nucleation occurs through simultaneous conversion of the domains within the precursor to SAPO-34. The crystal growth follows the "birth and spread" mechanism. The Si NMR results indicate that the silica first reacts with alumina to form a more reactive aluminosilicate species before Si being incorporated into the framework. A combination of the data obtained from different techniques provides a better picture of the formation of SAPO-34.

3.5 Catalytic tests

As introduced earlier, SAPO-34 is famous for its catalytic application in MTO reactions. The catalytic performance of the two SAPO-34 products was also tested. Figure 3.21 presents the methanol conversion with time on the two samples. Both of them show a complete conversion of methanol within 150 min of reaction time. The SAC sample deactivated after 190 min of time on stream (TOS) while on the VPT sample the conversion decreased below 100 wt% after 157 min of TOS. Under the test conditions, the SAC sample seems to have longer lifetime than the VPT sample. Further, it is shown in Table 3.2 that the SAC sample has higher selectivity to light olefins (C_2H_4 + C_3H_6, 82.6 wt%) than the VPT sample (81.9 wt%). As they have similar crystal size, which is in the range of 12–16 μm (Figures 3.4D and 3.16D), the different catalytic activities may be due to the different silicon content.

The main steps for MTO reactions can be summarized as follows:[63]

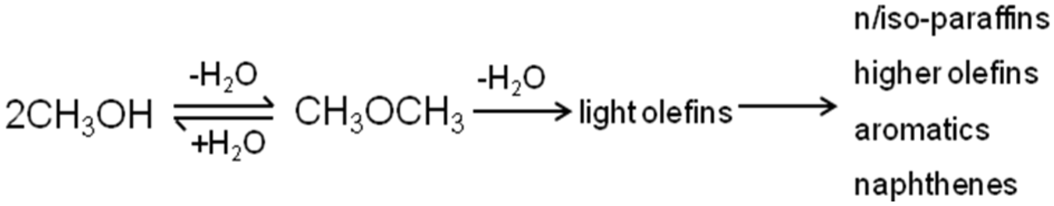

Scheme 3.1 Main steps for MTO reactions.

In the scheme, two methanol molecules are first dehydrated to form dimethyl ether (DME). The equilibrium mixture containing methanol, DME, and water, is then converted to light olefins. The final step is the conversion of light olefins to form paraffins, aromatics, naphthenes, and higher olefins by hydrgeon transfer, alkylation, and polycondensation.[63] The nature and content of last step is governed by many factors such as acid strength and acid site density.[64] Comparted to the SAC sample, there is a higher Si content in the VPT one, which could result in an increased acidity. The stronger acidity promoted the formation of coke and hydride transfer reaction of light olefins to form saturated hydrocarbons (e. g., higher selectivity to propane, Table 3.2).[15]

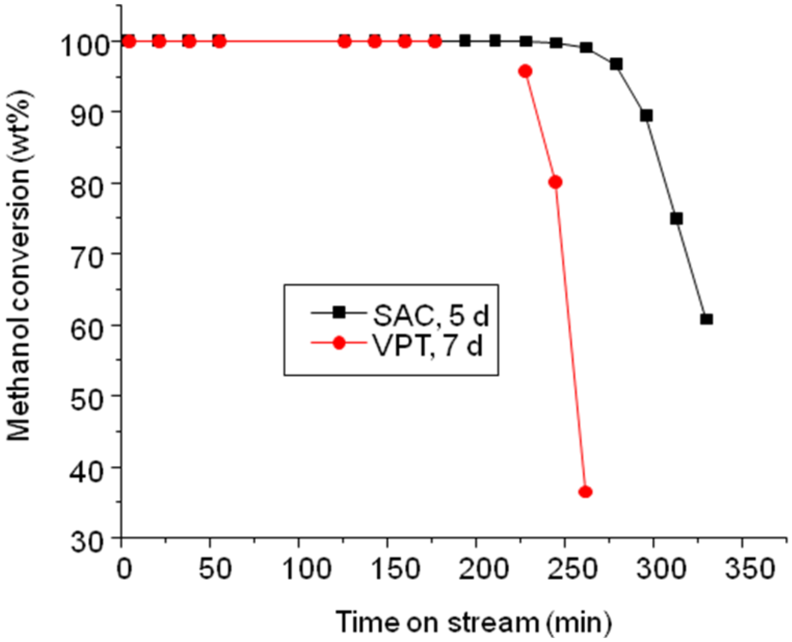

Figure 3.21 Methanol conversion vs. time-on-stream for different SAPO-34 products.

Table 3.2 MTO reaction results for different SAPO-34 samples.

Samples	Si content	Crystal size (μm)	Selectivity (wt%)[a]								
			CH_4	C_2H_4	C_2H_6	C_3H_6	C_3H_8	C_4	C_5	C_6	$C_2^= + C_3^=$
SAC	0.12	12-16	1.3	46.7	0.5	35.9	1.6	9.3	3.6	1.0	82.6
VPT	0.16	12-16	1.3	45.4	0.8	36.6	2.7	10.1	2.5	0.6	81.9

[a] The highest selectivity of ($C_2H_4 + C_3H_6$) under 100% methanol conversion.

3.6 References

(1) Yu, J.; Xu, R. *Chem. Soc. Rev.* **2006**, *35*, 593-604.
(2) Prakash, A. M.; Unnikrishnan, S. *J. Chem. Soc. Faraday Trans.* **1994**, *90*, 2291-2296.
(3) Li, S.; Falconer, J. L.; Noble, R. D. *J. Membr. Sci.* **2004**, *241*, 121-135.

(4 Wragg, D. S.; Johnsen, R. E.; Norby, P.; Fjellvag, H. *Microporous Mesoporous Mater.* **2010**, *134*, 210-215.
(5) Song, W.; Nicholas, J. B.; Haw, J. F. *J. Phys. Chem. B* **2001**, *105*, 4317-4323.
(6) Song, W.; Fu, H.; Haw, J. F. *J. Am. Chem. Soc.* **2001**, *105*, 4749-4754.
(7) Wu, X.; Abraha, M. G.; Anthony, R. G. *Appl. Catal. A* **2004**, *260*, 63-69.
(8) Hereijgers, B. P. C.; Bleken, F.; Nilsen, M. H.; Svelle, S.; Lillerud, K.-P.; Bjorgen, M.; Weckhuysen, B. M.; Olsbye, U. *J. Catal.* **2009**, *264*, 77-87.
(9) Vora, B.; Chen, J. Q.; Bozzano, A.; Glover, B.; Barger, P. *Catal. Today* **2009**, *141*, 77-83.
(10) Liu, Z.; Liang, J. *Curr. Opin. Solid State Mater. Sci.* **1999**, *4*, 80-84.
(11) Vistad, Ø. B.; Hansen, E. W.; Akporiaye, D. E.; Lillerud, K. P. *J. Phys. Chem. A* **1999**, *103*, 2540-2552.
(12) Vistad, Ø. B.; Akporiaye, D. E.; Lillerud, K. P. *J. Phys. Chem. B* **2001**, *105*, 12437-12447.
(13) Yan, Z.; Chen, B.; Huang, Y. *Solid State Nucl. Magn. Reson.* **2009**, *35*, 49-60.
(14) Xu, L.; Du, A.; Wei, Y.; Wang, Y.; Yu, Z.; He, Y.; Zhang, X.; Liu, Z. *Microporous Mesoporous Mater.* **2008**, *115*, 332-337.
(15) Liu, G.; Tian, P.; Zhang, Y.; Li, J.; Xu, L.; Meng, S.; Liu, Z. *Microporous Mesoporous Mater.* **2008**, *114*, 416-423.
(16) Tan, J. L., J.; Bao, X.; Liu, X.; Han, X.; He, C.; Zhai, R. *Microporous Mesoporous Mater.* **2002**, *53*, 97-108.
(17) Vistad, Ø. B.; Akporiaye, D. E.; Taulelle, F.; Lillerud, K. P. *Chem. Mater.* **2003**, *15*, 1639-1649.
(18) Liu, G.; Tian, P.; Li, J.; Zhang, D.; Zhou, F.; Liu, Z. *Microporous Mesoporous Mater.* **2008**, *111*, 143-149.
(19) Ito, M.; Shimoyama, Y.; Saito, Y.; Tsurita, Y.; Otake, M. *Acta Crystallogr., Sect. C: Cryst. Struct. Commun.* **1985**, *C41*, 1698-1700.
(20) Kim, M. H.; Li, H. X.; Davis, M. E. *Microporous Mater.* **1993**, *1*, 191-200.

(21) Xu, W.; Dong, J.; Li, J.; Li, J.; Wu, F. *J. Chem. Soc., Chem. Commun.* **1990**, *10*,755-756.
(22) Bandyopadhyay, R.; Bandyopadhyay, M.; Kubota, Y.; Sugi, Y. *J. Porous. Mater.* **2002**, *9*, 83-95.
(23) Zhang, L.; Yao, J.; Zeng, C.; Xu, N. CN Patent 1,314,587C, 2007.
(24) Hirota, Y.; Murata, K.; Tanaka, S.; Nishiyama, N.; Egashira, Y.; Ueyama, K. *Mater. Chem. Phys.* **2010**, *123*, 507-509.
(25) Zhang, L.; Yao, J.; Zeng, C.; Xu, N. *Chem. Commun.* **2003**, *17*, 2232-2233
(26) Yao, J.; Wang, H.; Ringer, S. P.; Chan, K. Y.; Zhang, L.; Xu, N. *Microporous Mesoporous Mater.* **2005**, *85*, 267-272.
(27) Khan, N. A.; Park, J. H.; Jhung, S. H. *Mater. Res. Bull.* **2010**, *45*, 377-381.
(28) Yang, H.; Liu, Z.; Gao, H.; Xie, Z. *J. Mater. Chem.* **2010**, *20*, 3227-3231.
(29) Bandyopadhyay, M.; Bandyopadhyay, R.; Tawada, S.; Kubota, Y.; Sugi, Y. *Appl. Catal., A* **2002**, *225*, 51-62.
(30) Chen, B.; Huang, Y. *Microporous Mesoporous Mater.* **2009**, *123*, 71-77.
(31) Matsukata, M.; Ogura, M.; Osaki, T.; Hari Prasad Rao, P. R.; Nomura, M.; Kikuchi, E. *Top. Catal.* **1999**, *9*, 77-92.
(32) Cundy, C. S.; Cox, P. A. *Chem. Rev.* **2003**, *103*, 663-702.

(33) Gullion, T.; Schaefer, J. *J. Magn. Reson.* **1989**, *81*, 196-200.
(34) Huang, Y.; Richer, R.; Kirby, C. W. *J. Phys. Chem. B* **2003**, *107*, 1326-1337.
(35) Amoureux, J. *J. Magn. Reson., Ser. A* **1996**, *123*, 116-118.
(36) Tapp, N.; Milestone, N.; Bibby, D. *Zeolites* **1988**, *8*, 183-188.
(37) Chen, B.; Huang, Y. *J. Am. Chem. Soc.* **2006**, *128*, 6437-6446.
(38) Chen, B.; Huang, Y. *J. Phys. Chem. C* **2007**, *111*, 15236-15243.
(39) Chen, B.; Kirby, C. W.; Huang, Y. *J. Phys. Chem. C* **2009**, *113*, 15868-15876.
(40) Chen, B.; Huang, Y. *Microporous Mesoporous Mater.* **2011,** *143*, 14-21.
(41) Huang, Y.; Yan, Z. *J. Am. Chem. Soc.* **2005**, *127*, 2731-2740.
(42) Zhou, D.; Xu, J.; Yu, J.; Chen, L.; Deng, F.; Xu, R. *J. Phys. Chem. B* **2006**, *110*, 2131-2137.
(43) Huang, Y.; Demko, B. A.; Kirby, C. W. *Chem. Mater.* **2003**, *15*, 2437-2444.
(44) Akporiaye, D. E.; Dahl, I. M.; Mostad, H. B.; Wendelbo, R. *J. Phys. Chem.* **1996**, *100*, 4148-4153.
(45) Prakash, A. M.; Unnikrishnan, S.; Rao, K. V. *Appl. Catal., A* **1994**, *110*, 1-10.
(46) Yan, Z.; Zhuang, J.; Xu, L.; Han, X.; Liu, Z.; Bao, X. *Chin. Chem. Lett.*, **2003**, *14*, 87-90.
(47) Sarneski, J. E.; Surprenant, H. L.; Molen, F. K.; Reilley, C. N. *Anal. Chem.* **1975**, *47*, 2116-2124.
(48) Challoner, R.; Harris, R. K.; Packer, K. J.; Taylor, M. J. *Zeolites* **1990**, *10*, 539-545.
(49) Ye, L.; Cao, F.; Ying, W.; Fang, D.; Sun, Q. *J. Porous Mater.* **2011**, *18*, 225-232.
(50) Ashtekar, S.; Chilukuri, S. V. V.; Chakrabarty, D. K. *J. Phys. Chem.* **1994**, *98*, 4878-4883.
(51) Doremieux-Morin, C.; Martin, C.; Bregeault, J. M.; Fraissard, J. *Appl. Catal.* **1991**, *77*, 149-161.
(52) Sastre, G.; Lewis, D. W.; Richard, C.; Catlow, A. *J. Phys. Chem. B* **1997**, *101*, 5249-5262.
(53) Vomscheid, R.; Briend, M.; Peltre, M. J.; Man, P. P.; Barthomeuf, D. *J. Phys. Chem.* **1994**, *98*, 9614-9618.
(54) Barthomeuf, D. *J. Phys. Chem.* **1993**, *97*, 10092-10096.
(55) Holme, B.; Cubillas, P.; Cavka, J. H.; Slater, B.; Anderson, M. W.; Akporiaye, D. *Cryst. Growth Des.* **2010**, *10*, 2824-2828.
(56) Cubillas, P.; Castro, M.; Jelfs, K. E.; Lobo, A. J. W.; Slater, B.; Lewis, D. W.; Wright, P. A.; Stevens, S. M.; Anderson, M. W. *Cryst. Growth Des.* **2009**, *9*, 4041-4050.
(57) Melchior, M. T.; Vaughan, D. E. W; Pictroski, C. F. *J. Phys. Chem.* **1995**, *99*, 6128-6144.
(58) Wakihara, T.; Sugiyama, A.; Okubo, T. *Microporous Mesoporous Mater.* **2004**, *70*, 7-13.
(59) Ono, S. S.; Matsuoka, O.; Yamamoto, S. *Microporous Mesoporous Mater.* **2001**, *48*, 103-110.
(60) Anderson, M. W. *Curr. Opin. Solid State Mater. Sci.* **2001**, *5*, 407-415.
(61) Paredes, J. I.; Martinez-Alonso, A.; Tascon, J. M. D. *Microporous Mesoporous Mater.* **2003**, *65*, 93-126.
(62) Cubillas, P.; Anderson, M. W. In *Zeolites and Catalysis: Synthesis, Reactions and Applications*, 1st ed.; Čejka, J.; Corma, A.; Zones, S., Eds.; Wiley-VCH: Weinheim, Germany, 2010; Vol. 1, pp 1-55.

(63) Stöcker, M. *Microporous Mesoporous Mater*. **1999**, *29*, 3-48.
(64) Haw, J. F.; Song, W. G.; Marcus, D. M.; Nicholas, J. B. *Acc. Chem. Res.* **2003**, *36*, 317-326.

Chapter 4 Examining the Formation of Molecular Sieve SAPO-34 by Vapor Phase Transport Method

4.1 Introduction

Since the discovery of aluminophosphate ($AlPO_4$)-based materials by Union Carbide in 1982,[1] much work has gone into this type of molecular sieves. The structures of many $AlPO_4$-n are similar to those of zeolites, but their primary building units are formed by Al-O-P linkages rather than by Si-O-Si or Si-O-Al bridges in zeolites.[2-4] The neutral framework of $AlPO_4$s limits their application as catalysts. The incorporation of silicon atoms into their framework introduces the negative charges, and consequently the resulting materials, silicoaluminophosphates (SAPOs) can be used as acid catalysts.[3] Among SAPOs, SAPO-34 is recognized as one of the most important molecular sieves because of its intermediate acidity and small pore size (around 0.38 nm).[5] It has a CHA topology analogous to natural zeolite chabazite. The framework is composed of CHA cages with an eight-membered ring (8R) window (Figure 4.1).[6] Among its various applications including ion-exchange, heat storage, gas adsorption and separation as well as catalysis,[7-17] SAPO-34 is best known for its high selectivity of ethene and propene from the conversion of methanol (MTO reactions).[18-20] The catalytic properties of SAPO-34 are closely related to its framework compositions, which are influenced by the synthesis conditions such as the choice of structure-directing agent (SDA). SAPO-34 is usually prepared using hydrothermal synthesis method (HTS). A variety of SDAs has been used for the HTS synthesis.[21-28] Among them, morpholine is a good choice for preparing SAPO-34 with high thermal and hydrothermal stability, high crystallinity, and high Si content at relatively low cost. To optimize the catalytic properties of SAPO-34, understanding its formation mechanism as well as the role of SDA during crystallization is very critical for controlling the Si incorporation and distribution as well as crystal size and morphology. There are several studies using morpholine as a SDA to examine the formation of SAPO-34 under HTS conditions.[28-31] However, SAPO-34 crystallization with morpholine as SDA is still not fully understood at an atomic level.

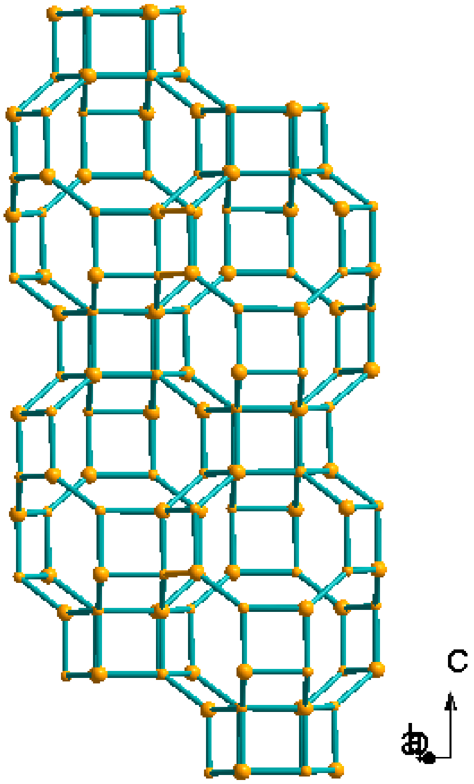

Figure 4.1 Framework of SAPO-34. Oxygen atoms are not shown for clarity.

An alternative synthetic method to HTS is vapor-phase transport (VPT) which was first reported by Xu *et al.*[32] VPT is an approach where a SDA solution placed at the bottom of an autoclave is separated from dry gel powder (for the reaction vessel used for this method, see Figure 4.2). Under heating treatment, the SDA molecules transported via vapor phase will be in contact with the dry gel and help convert the amorphous dry gel powder into crystalline sieves. The VPT method has been used to synthesize various zeolites and $AlPO_4$s.[33-38] SAPO-34 has been previously synthesized by VPT method.[35,39,40] Using diethylamine as the SDA, the Huang group proposed that SAPO-34 crystallizes from a semi-crystalline layered precursor with weak nonbonding interactions held within it.[40]

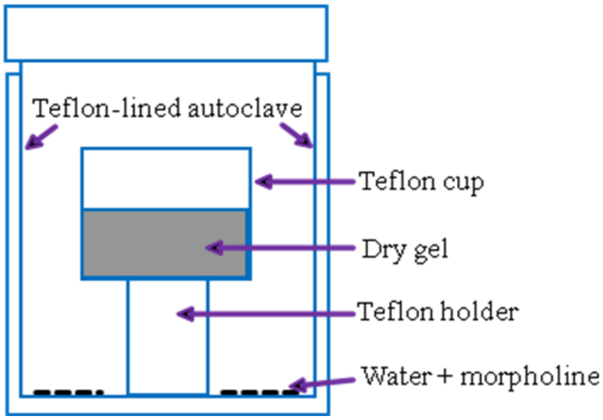

Figure 4.2 Reaction vessel used for VPT method.

Since the initial “dry” gel powder contains 20–40% water by weight, it is now generally recognized that the fundamental mechanisms underlying the crystallization in hydrothermal synthesis and VPT should be similar.[41,42] The reaction is, however, slower under the VPT conditions compared to the HTS due to the lack of bulk liquid, which allows the intermediates to be captured. Thus, examination of the evolution of the dry gel phase may provide additional information on understanding the crystallization in conventional hydrothermal process. Further, as mentioned earlier, the SDA molecules are slowly brought in contact with the dry gel powder, it can be employed to probe the role of SDAs during synthesis.

In this chapter, the formation of SAPO-34 was examined under the VPT conditions using morpholine as a SDA with attention being paid to Si incorporation. For the reaction intermediates captured during crystallization, the long-range ordering and the local environments of P, Al, and Si were probed by powder X-ray diffraction (PXRD) and various solid-state NMR techniques including ^{31}P, ^{27}Al, and ^{29}Si magic-angle spinning (MAS), and ^{27}Al triple-quantum MAS (3QMAS) NMR. The combination of these techniques provides insights into the formation of SAPO-34. Furthermore, the catalytic performance of the as-made product in MTO reactions was also tested.

4.2 Experimental

4.2.1 Sample preparation

The synthesis of SAPO-34 was performed according to the general VPT technique described elsewhere.[35,39] The reagents used were pseudo-boehmite (Catapal-B, ca. 65 wt% Al_2O_3, Vista), H_3PO_4 (85%, EM Science), morpholine (Aldrich), colloidal silica (Ludox LS-30, Aldrich), and distilled water. The initial gel molar composition (Al_2O_3:P_2O_5:SiO_2:H_2O) was 1.0:1.0:1.0:60.

A typical procedure for the preparation of initial VPT dry gel was the following: 31.4 g of Catapal B, 46.1 g of H_3PO_4, and 85.0 g of distilled water were combined and subjected to vigorous stirring for 15 min before adding another 42.5 g of distilled water. Separately, 40 g of colloidal silica and 42.5 g of distilled water was mixed. This solution was added slowly to the above alumina and phosphoric acid mixture under stirring for homogeneity. After being stirring at room temperature for 30 min, the uniform solution was dried at 353 K with constant stirring to allow evaporation of water until solids formed. The solid sample was then ground into fine powder and sealed in glass vials. A series of intermediates were synthesized by placing 1.0 g of initial VPT dry gel powder into small Teflon cups. Each cup was placed in a 23-mL Teflon-lined autoclave with 1.2 g of 25% aqueous morpholine solution at the bottom and heated in an oven at 473 K. The reactions were quenched in cold water. For comparison, each solid sample was divided into two parts. One part was dried in air and the other part was first washed with distilled water in a beaker and then dried in the same beaker in air without isolation from the liquid phase. This ensured that no solid particles were washed away. All dried samples were kept in sealed vials for further analysis.

To compare the catalytic performance, a SAPO-34 sample was also prepared hydrothermally according to the method reported in literature.[30,31]

4.2.2 Characterization

PXRD patterns were recorded on a Rigaku diffractometer using Co Kα radiation (λ=1.7902 Å). For SEM image, representative samples were first coated with 3 nm osmium metal using a Filgen OPC-80T instrument, and their morphology and elemental analysis were then examined using a FIB/SEM 1540XB microscope equipped with an energy-dispersive X-ray spectrometer for elemental analysis.

All the NMR experiments were carried out on a Varian/Chemagnetics Infinityplus 400 WB spectrometer equipped with three rf channels operating at the field strength of 9.4 T. The Larmor frequencies of ^{1}H, ^{31}P, ^{27}Al, and ^{29}Si were 399.5, 161.7, 104.1, and 79.4 MHz, respectively. The magic angle was set using the ^{79}Br resonance of KBr. The chemical shifts of ^{31}P, ^{27}Al, and ^{29}Si were referenced to 85% H_3PO_4 (0 ppm), 1M $Al(NO_3)_3$ aqueous solution (0 ppm), and external tetrakis(trimethylsilyl)-silane (-SiMe$_3$, -9.9 ppm), respectively. Depending on the requirements of the individual experiment, three NMR probes (a Varian/Chemagnetics 7.5-, and a 4.0-mm H/X/Y triple-tuned T3 MAS probe, and a 5.0-mm H/F/X/Y triple-tuned MAS probe) were used. For ^{31}P MAS experiments, a 45° pulse was typically used and the recycle delay was 60 s. The proton-decoupling field was about 60 kHz. The ^{27}Al spectra were acquired using a small pulse angle with a pulse delay of 1 s. For the ^{29}Si MAS experiments, a 45° pulse was used with a pulse delay of 60 s. For ^{1}H to ^{29}Si cross-polarization (CP) experiments, the ^{1}H 90° pulse length was 5 μs and the Hartmann-Hahn condition was determined using TTMSS. ^{27}Al 3QMAS experiments were performed using the 4.0-mm probe and the spinning speed was 10 kHz. The spectra were obtained by utilization of a three-pulse z-filter sequence.[43] The rf strengths of the first two hard pulses and third soft pulse were optimized individually, and the optimized pulse lengths were 5.7, 2.0, and 15.0 μs for the three consecutive pulses.

4.2.3 Catalytic tests

MTO reactions were performed at the Dalian Institute of Chemical Physics, China. They were carried out with a fixed-bed reactor at atmospheric pressure. 0.3 g of catalyst (40-60 mesh) was loaded into the reactor. The sample was preheated in nitrogen flow at 773 K for 1 h and then the temperature of the reactor was decreased to 723 – 730 K. The methanol and nitrogen mixture was then pumped into the reactor. The weight hourly space velocity (WHSV) was 2.9 h^{-1}. The products were analyzed on-line by a Varian GC3800 gas chromatograph equipped with a FID detector and a PoraplotQ-HT capillary column.

4.3 Results and discussion

To follow the evolution of the long-range ordering of the intermediate gel samples, the PXRD patterns of gel samples were recorded as a function of crystallization time (Figure 4.3). The powder pattern of the initial VPT dry gel presents a sharp and strong peak at about 24.4°, corresponding to a dense phase with a high degree of long-range ordering. A *d* spacing of 4.24Å can be calculated from this diffraction peak. This value is close to that of the *d* spacing of the *(100)* plane of $AlPO_4$ analogue of quartz, berlinite (4.28 Å).[44,45] This suggests that the dense phase is likely to be berlinite. This is not surprising since the synthesis of SAPO molecular sieves need weakly acidic or neutral conditions.[46] The lower pH value for the initial VPT dry gel, which originates from the absence of morpholine, leads to the formation of the dense phase. Further, the presence of several broad reflections suggests the co-existence of a small amount of amorphous phase.

Treating the dry gel for 0.7 h led to the appearance of several broad reflections on the lower-angle side of the main peak at 24.4°, indicating that berlinite begins to transform back to amorphous materials once morpholine was brought into contact with the dry gel. After 2 h heating, there appear several relatively sharp peaks at around 23.7°, 25.0°, and 26.3° in the powder pattern (labeled with asterisks). The corresponding *d* spacings agree with those of the dense $AlPO_4$ form of tridymite.[47,48] Heating the dry gel for 5 h resulted in the emergence of several sharp peaks, whose positions correspond to the *(101)*, *(021)*, *(211)*, *(104)*, *(401)*, and *(214)* reflections of trigonal SAPO-34. This indicates that when the dry gel is in contact with morpholine for relatively longer time, it was gradually transformed to SAPO-34. This also implies that one of the roles played by morpholine is to adjust the pH values of the dry gel, thus bypassing the formation of dense phases and promoting the transformation to SAPO-34.[42] Further heating the VPT dry gel led to sharpening the peaks due to SAPO-34. The powder pattern of 5 d sample only contains the peaks solely from SAPO-34.[6]

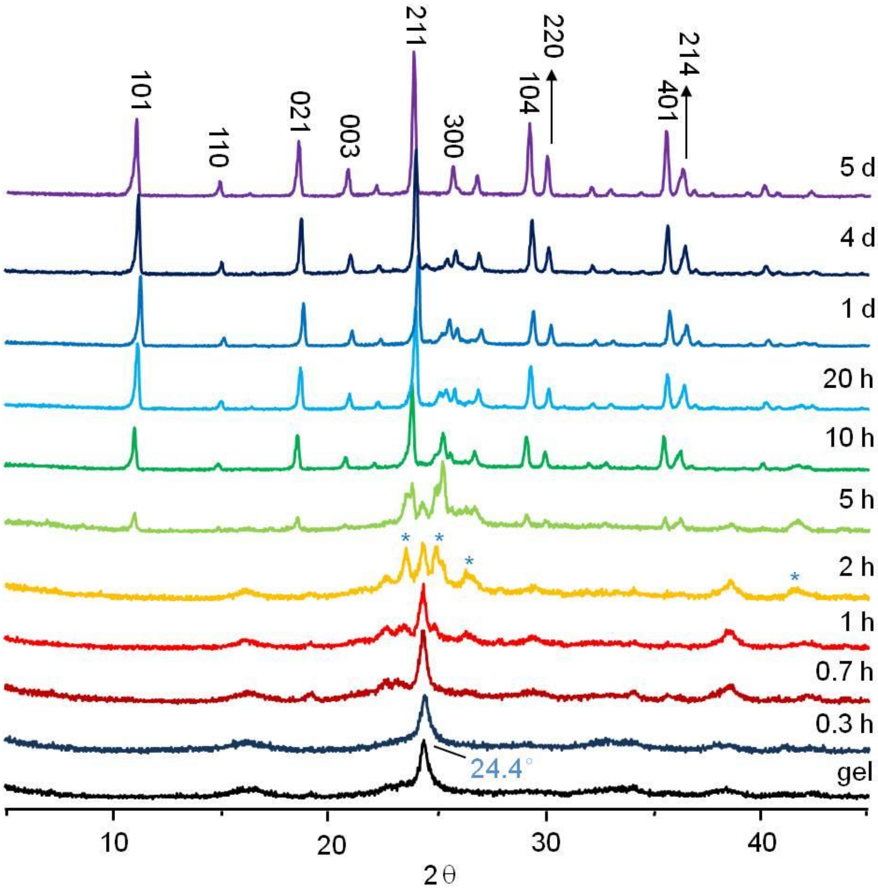

Figure 4.3 Powder XRD patterns of unwashed VPT dry gel samples. * indicates tridymite phase.

To understand the role of the SDA under the VPT condition, two gel samples obtained after VPT treatment for 2 and 5 h were put back in a Teflon cup and reheated at 473 K in the presence of a small amount of pure water at the bottom of the autoclave. Interestingly after 5 days of heating, the 5 h solids almost completely transformed into SAPO-34 (Figure 4.4). The 2 h sample, however, was only converted into pure tridymite. It appears that for gel samples heated for 2 h or less, there were not enough morpholine molecules occluded in the solids to direct the reorganization of the gel to form SAPO-34. Therefore, without supply of additional morpholine molecules, resumed heating can only produce the tridymite phase. The 5 h sample, on the other hand, contains sufficient SDA molecules. Consequently, no extra morpholine molecules are required to form the CHA structure. The fact that the tridymite phase seen in the XRD pattern of the 5 h sample disappeared after reheating implies that there appears to be an equilibrium between the tridymite phase and amorphous materials and the presence of morpholine shifts the equilibrium towards the amorphous phase, leading to the eventual formation of SAPO-34.

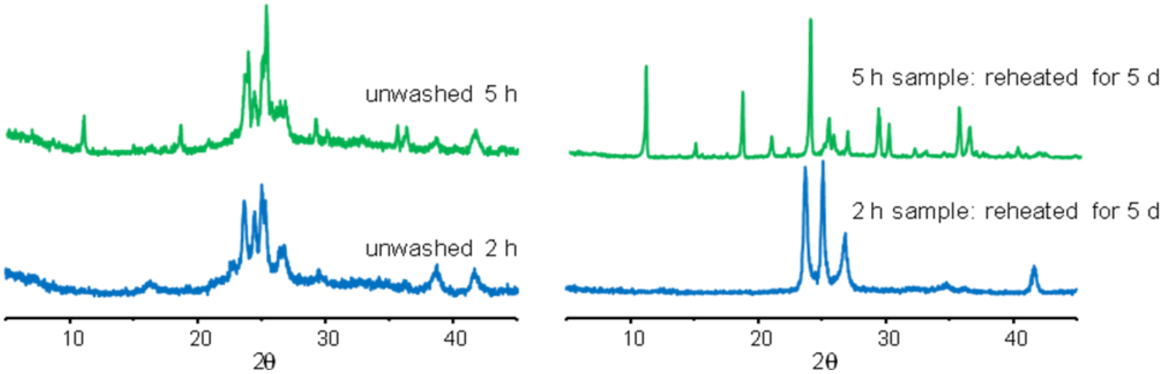

Figure 4.4 Powder XRD pattern of selected unwashed VPT dry gel samples reheated with a small amount of water.

Previous work has shown that the structures of intermediate phase formed during crystallization of several AlPO- and SAPO-based molecular sieves under VPT conditions are held together by weak non-covalent bonding interactions.[37,40,49] To investigate the nature of the bonding in VPT dry gel samples, selected intermediates were washed with water. Upon washing, the reflections due to the dense phases are still present in the corresponding XRD patterns (Figure 4.5). The powder patterns of the unwashed and washed VPT dry gel samples look identical (Figure 4.3). These findings imply that the structures of the dense phases are held by strong covalent bonds

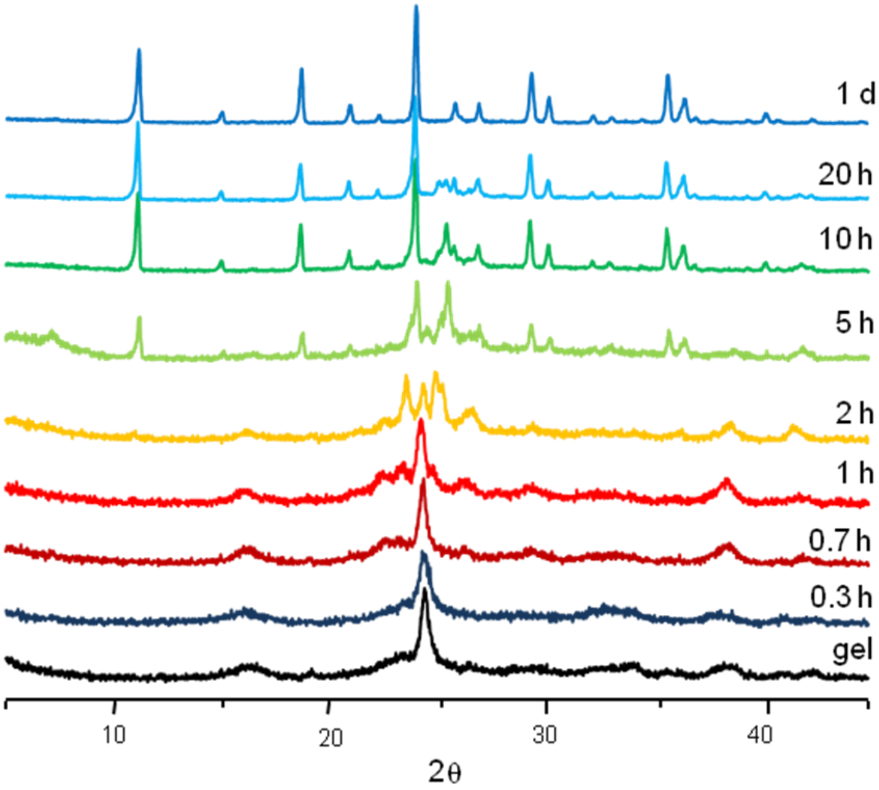

Figure 4.5 Powder XRD patterns of selected washed VPT dry gel samples.

To examine the morphological evolution as a function of crystallization time, several representative gel samples were chosen for SEM analysis (Figure 4.6). The image of the initial VPT dry gel shows the materials with amorphous nature. The image of the 5 h sample clearly indicates the beginning of the formation of SAPO-34 crystals (Figure 3B, labeled with an arrow). The picture of 1 d sample shows more SAPO-34 crystals emerged from the gel (Figure 4.6C). After 5 d of heating, highly crystalline SAPO-34 product was formed. The trend agrees with the XRD result very well.

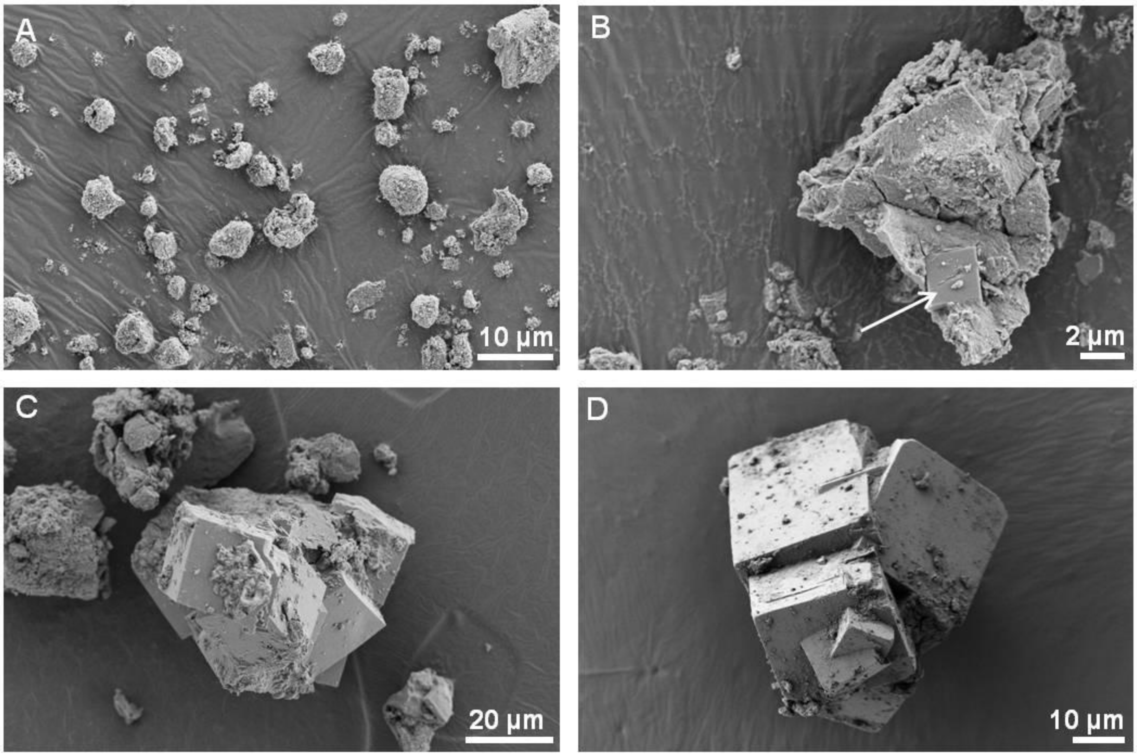

Figure 4.6 SEM images of selected unwashed VPT dry gel samples: (A) initial dry gel, (B) 5 h, (C) 1 d, and (D) 5 d.

^{31}P and ^{27}Al MAS NMR spectra were obtained to characterize the local environments of P and Al in the intermediate gel samples. Figure 4.7A shows the ^{31}P spectra of unwashed VPT dry gel samples. The ^{31}P spectrum of the initial dry gel exhibits a sharp peak at -20 ppm, a weak resonance at -30 ppm, as well as several small ones in the region from -8 to -12 ppm. The peak at -20 ppm has been observed in the dry gel phases of many $AlPO_4$ and SAPO based molecular sieves and was assigned as not fully condensed $OP(OAl)_3$ environment with a high degree of local ordering.[50-54] The reported ^{31}P MAS spectrum of berlinite contains a single P peak at -26 ppm.[55,56] However, such a peak is not observed in the present case. Instead, a peak at -30 ppm due to fully condensed $P(OAl)_4$ species is seen in the ^{31}P spectra and it is suggested that this peak is due to the dense phase represented by the reflection at 24.4° in the corresponding XRD patterns. Considering the fact that the *d*-spacing of this reflection is very similar to that of *(100)* plane of berlinite, the dense phase may have a structure similar to berlinite. Thus, hereafter this dense phase is referred to as berlinite-like phase. The ^{31}P MAS NMR spectra confirm the results of XRD that the dry gel is indeed a mixture of amorphous materials and a dense berlinite-like phase and their relative intensities further indicate that the amount of dense phase is small. After 5 h of the VPT treatment, a new peak at -28 ppm started emerging, indicating the formation of the $P(OAl)_4$ environment in SAPO-34.[57] The spectrum also shows that the previous relatively broad peak at -30 pm sharpened significantly coinciding with the formation of tridymite, whose ^{31}P MAS spectrum also exhibits a single peak at -30 ppm.[48] It is also noticed that there are significant amount of amorphous peaks with chemical shifts greater than -20 ppm, which confirms that at a longer heating time, the equilibrium between tridymite and amorphous materials shifts in favor of the amorphous phase. The spectrum of the final product (5 d sample) has a single sharp peak at -28 ppm and is consistent to that of pure trigonal SAPO-34 reported in literature.[58]

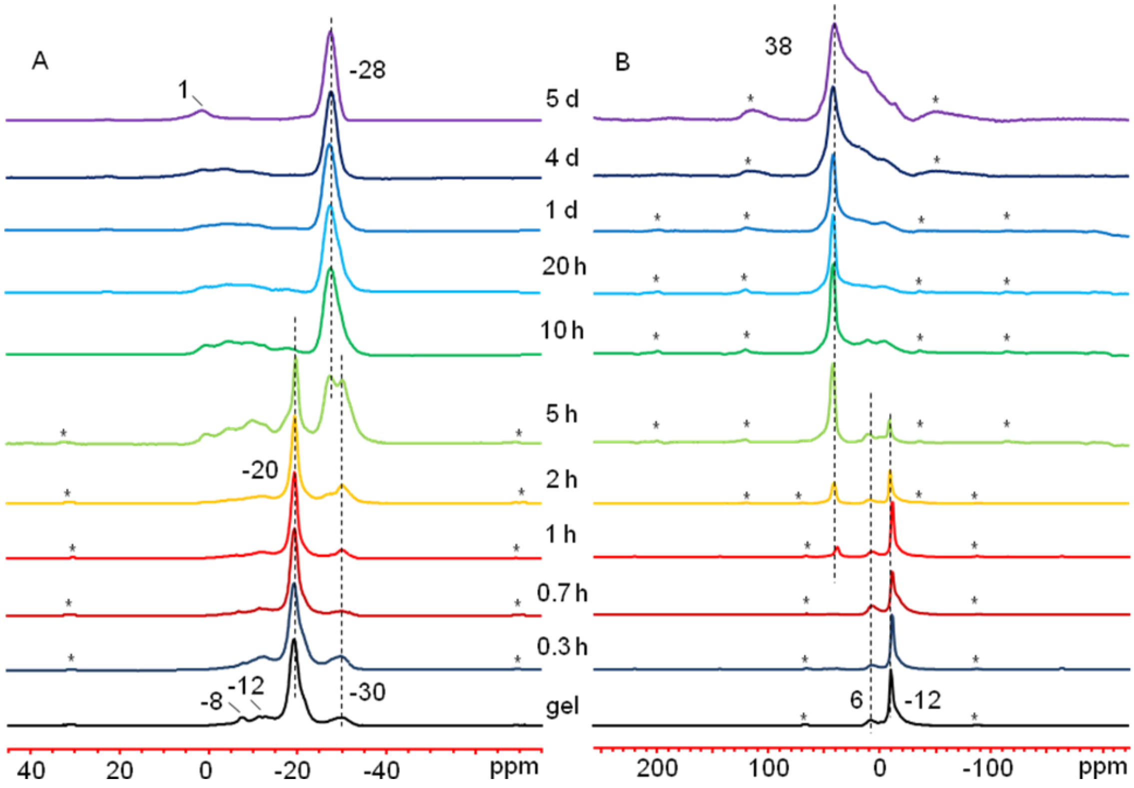

Figure 4.7 ^{31}P MAS (A) and ^{27}Al MAS (B) spectra of unwashed VPT dry gel sample. Asterisks indicate spinning sidebands.

The ^{27}Al MAS spectra convey similar information. The spectrum of the initial VPT dry gel contains a strong peak at -12 ppm and a much weaker one at 6 ppm (Figure 4.7B). The peak at -12 ppm indicates the existence of octahedral Al in the amorphous phase.[59] The one at 6 ppm is due to unreacted alumina.[31,60] There is no peak due to tetrahedral Al in the spectrum of the initial dry gel, indicating that the presence of SDA is critical to the formation of the tetrahedral Al in the gel. The lack of tetrahedral Al also confirms that the dense phase in the initial dry gel is not berlinite as it has an Al peak at 45 ppm.[55,56]

Heating the dry gel for 1 h results in the appearance of a new peak at around 38 ppm, which can be ascribed to tetrahedral Al. Upon increasing the heating time, the intensity of the signal due to the tetrahedral Al grew at the expense of that resulting from the octahedral Al, suggesting that reorganization of the gel structure has occurred under the influence of the SDA. The changes are consistent with those seen in the corresponding powder XRD patterns. The spectrum of the 5 d sample agrees with those of SAPO-34 reported in literature [6]. The ^{27}Al 3QMAS experiments were carried out to identify Al species in the final 5d products. The spectrum of the SAPO-34 product (the 5 d sample) is illustrated in Figure 4.8, which clearly exhibits four signals. The broad peak at around 38 ppm in the MAS spectra is actually composed of two components with isotropic chemical shift values of about 48 and 58 ppm. Based on previous work,[51,61] the peak at 48 ppm can be assigned to the tetrahedral Al with $Al(OP)_4$ environment and the one at 58 ppm to the tetrahedral Al in aluminosilicate domains with Si as the nearest neighbor.[59,62] The peak at 6 ppm in the MAS spectrum appears in the F1 dimension with an isotropic chemical shift value of around 12 ppm. As discussed earlier, it is due to unreacted alumina. There is also a peak with an isotropic chemical shift of -12 ppm. It originates from the octahedral Al with secondary coordination sphere containing extraframework H_2O and/or the morpholine molecules in the CHA cages.[58,59]

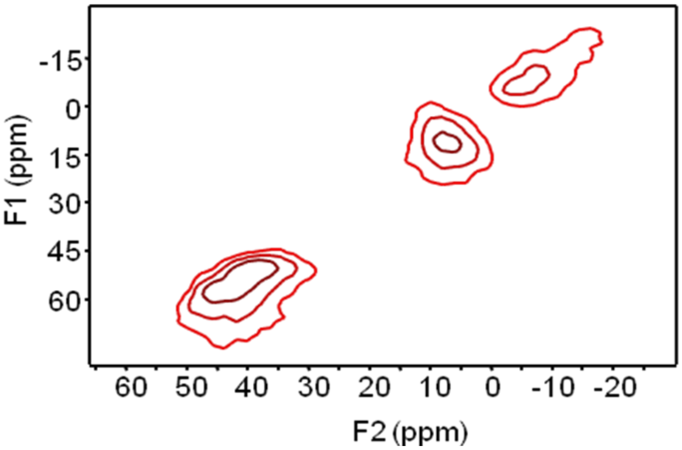

Figure 4.8 ^{27}Al 3QMAS spectrum of 5 d sample.

To follow the Si incorporation, ^{29}Si MAS spectra were obtained (Figure 4.9A). CP is a technique that utilizes the ^{1}H – ^{29}Si dipolar interaction. It can be used to selectively enhance the intensity of ^{29}Si nuclides with protons nearby. $^{1}H \rightarrow {}^{29}Si$ CP experiments were also carried out on VPT dry gel samples (Figure 4.9B). The ^{29}Si MAS spectra of the VPT dry gel samples heated for less than 2 h exhibit a broad peak at around -111 ppm. It is assigned to unreacted amorphous silica with $Si(OSi)_4$ environments.[6,63] This observation implies that the majority of silica in these gel samples has not started reacting. In the corresponding CP spectra, besides the peak at -111 ppm, there exhibits another stronger signal at -101 ppm, which is not visible in the MAS spectra. This signal mainly results from $(SiO)_3SiOH$ species on the surface of silica particles. After 5 h of heating, the CP spectrum shows the appearance of two new broad peaks at -85 and -90 ppm. They represent $(AlO)_3SiOH$ or $(SiO)(AlO)Si(OH)_2$ and $(SiO)_2Si(OH)_2$ or $Si(OAl)_4$ species, respectively.[64] It appears that the Si is incorporated into SAPO-34 via the formation of a small amount of aluminosilicate particles. This agrees with the corresponding XRD pattern, SEM image, and ^{31}P MAS spectrum of the 5 h sample which shows the appearance of SAPO-34 phase. The MAS spectrum of SAPO-34 final product contains a sharp peak at -90 ppm, which is due to isolated $Si(OAl)_4$ species in SAPO-34.[26,63,65-67] There is also a weak one at -95 ppm and a broad one at -111 ppm. They are due to a small amount of $Si(OAl)_3(OSi)_1$ and $Si(OSi)_4$ species in the framework.[62]

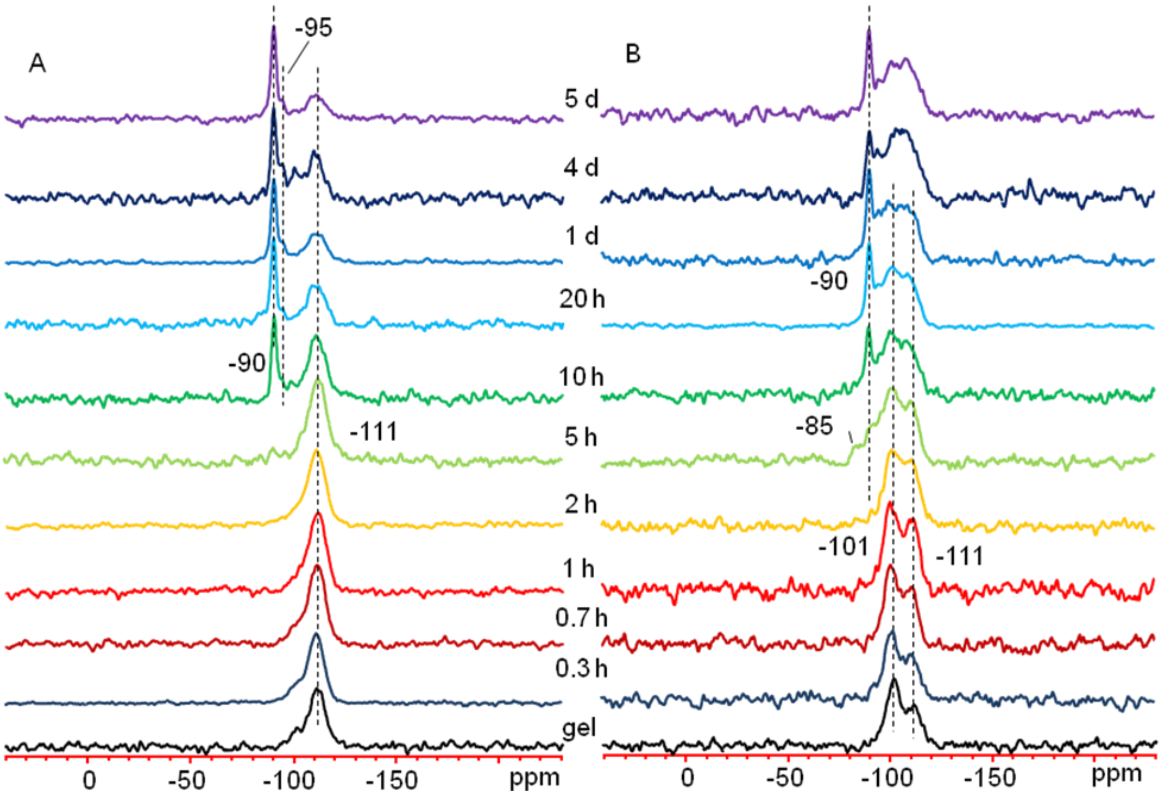

Figure 4.9 ^{29}Si MAS (A) and ^{1}H → ^{29}Si CP (B) spectra of unwashed VPT dry gel samples with a contact time of 0.5 ms.

Flanigen *et al.* have proposed three Si substitution mechanisms.[68] The first is Si incorporation into an Al site (SM I). The second is Si incorporation into a P site (SM II). This gives rise to an isolated $Si(OAl)_4$ species, therefore a Brønsted acid site. The third one involves two Si atoms replace an Al-P pair (SM III). Si islands with various Si species in $Si(OAl)_n(OSi)_{4-n}$ (n=0, 1, 2, 3, or 4) environments are produced when a combination of SM II and III occurs. In $AlPO_4$-based molecular sieves the P/Al ratio is strictly 1:1. Upon Si incorporation into $AlPO_4$s, the P/Al ratio will be changed and the actual value reflects the Si incorporation mechanisms. To obtain semi-quantitative information on elemental compositions, EDX analysis was performed on the 5 d sample. The results were the averaged data obtained from three different SAPO-34 crystals. The

Si content in as-formed SAPO-34 is about 19 mol.%, which is much higher than the proposed upper threshold value (11%) of SM II mechanism in SAPO-34.[69,70] Further, the (Si + P)/Al ratio (1.27) is greater than 1. The EDX data thus indicate that Si is incorporated via both SM II and III. SM II is the major mechanism. These results are consistent with the ^{29}Si NMR spectrum of SAPO-34 (Figure 7A), which exhibits a sharp and strong signal at -90 ppm due to dispersed $Si(OAl)_4$ environments and two weaker ones at -95 and -111 ppm originating from Si species in Si islands.

Vistad *et al.*[30] and Yan *et al.*[31] previously studied the crystallization of SAPO-34 prepared by the HTS method with morpholine as the SDA. They reported that SAPO-34 was formed from the transformation of a layered prephase or an amorphous phase after several hours of heating. Apparently, under VPT conditions, SAPO-34 crystallizes in a different process and takes a much longer crystallization time. Due to the absence of morpholine molecules and the resultant lower pH value, the initial VPT dry gel has a structure not ready to transform to the CHA structure. Once the SDA molecules were brought into contact with the dry gel via vapor, the gel quickly transformed to $AlPO_4$-tridymite phase, which eventually evolved into SAPO-34. When the SDA molecules were first brought to the surface of the dry gel, their distribution over the entire solid gel may not be homogeneous. Due to the lack of apparent liquid phase, they diffused though the solid sample slowly.

The catalytic activities of SAPO-34 in MTO reactions have been studied extensively. Most of them have focused on SAPO-34 samples obtained under various HTS conditions. To check the catalytic properties of the VPT product (5 d sample), catalytic tests on MTO reactions were carried out. A conventional SAPO-34 sample synthesized by the HTS method was also tested under the same reaction conditions for comparison. The PXRD pattern of the HTS sample shown in Figure 4.10A indicates that it is pure trigonal SAPO-34 with high crystallinity. Figure 4.11 gives the methanol conversion versus time on stream on the two samples. The results show that the VPT sample was more active. It maintained a 100% conversion within 157 min while the HTS sample deactivated after 143 min. Figure 4.12 illustrates the selectivities towards different hydrocarbons. When the reaction time was below 100 min, the production of light olefins (C_2H_4 and C_3H_6) was apparently more favored on the HTS sample (Figure 4.12A), while the selectivity to propane was higher on the VPT sample (Figure 4.12B). After 100 min on stream, the two samples show comparable product selectivities.

The ^{29}Si NMR spectrum of the HTS sample (Figure 4.10B) shows a strong signal at -90 ppm and two weak shoulders at -85 and -94 ppm. The EDX result shows that the atomic silicon content is 17%, which is lower than that of the VPT sample. This suggests that less silicon islands were formed in the HTS sample by SM II and III. It is reported that at the borders of the islands exist stronger acid centers than the isolated Brønsted acid sites.[71] The relatively lower light olefin selectivity and higher propane selectivity over the VPT sample before 100 min on stream can be attributed to its stronger acidity, which promoted hydrogen transfer reaction of the olefins to form alkanes.[72] Its longer lifetime may be related to its average smaller crystal size (40 μm, Figure 4.6D) than the HTS sample (around 60 μm, Figure 4.13). A similar size effect of SAPO-34 on its lifetime in MTO reactions was reported recently by Liu and Yu *et al*.[20]

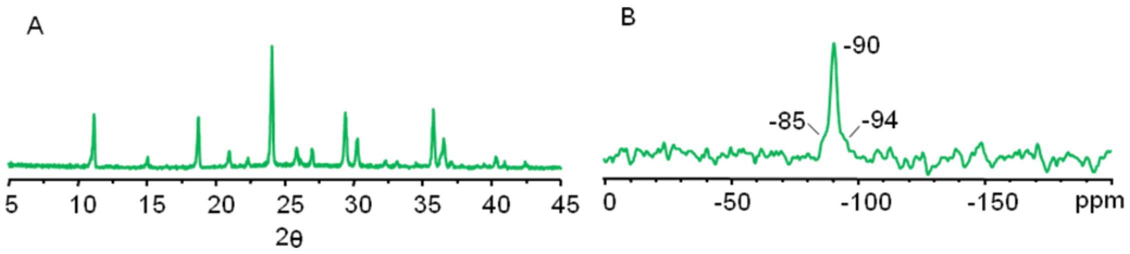

Figure 4.10 Powder XRD pattern (A) and ^{29}Si MAS spectrum (B) of SAPO-34 synthesized by HTS method. The reaction temperature and time was 473 K and 2 d, respectively.

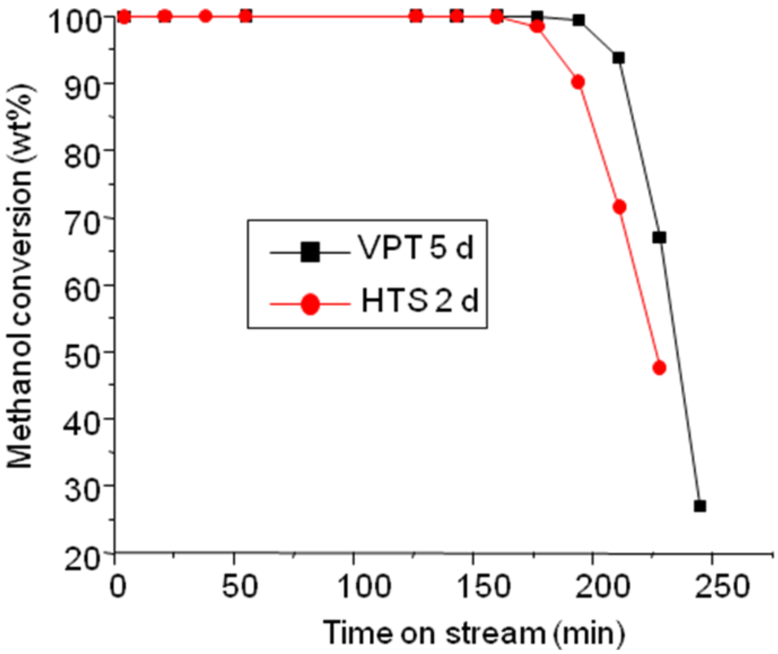

Figure 4.11 Methanol conversion vs. time-on-stream for different SAPO-34 products.

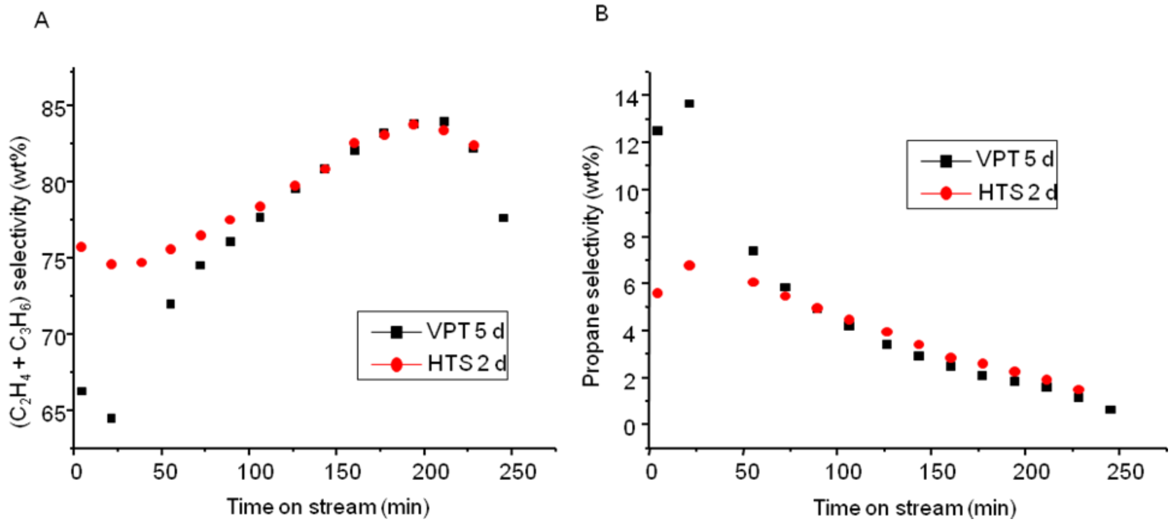

Figure 4.12 Selectivities towards light olefins (C_2H_4 and C_3H_6, A) and propane (B) vs. time-on-stream for different SAPO-34 products.

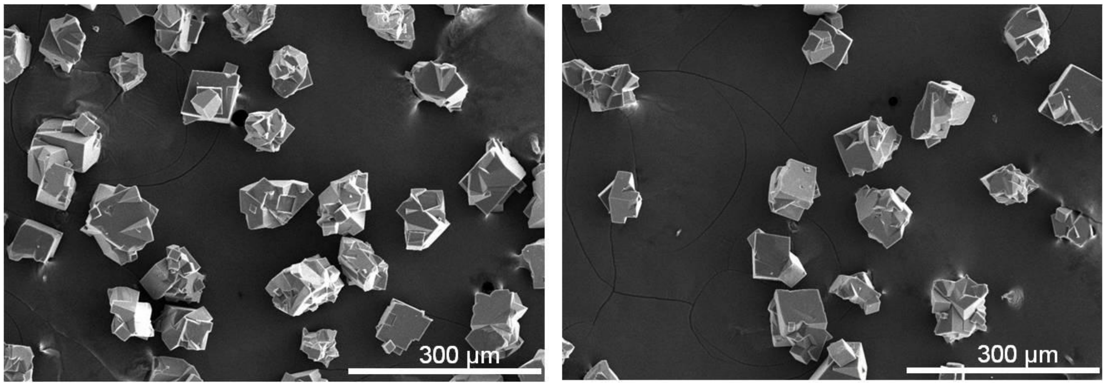

Figure 4.13 SEM pictures of SAPO-34 synthesized by HTS method.

4.4 Summary

Formation of SAPO-34 was examined by VPT method. An assortment of techniques including PXRD, SEM/EDX, and solid-state NMR were utilized to characterize the intermediate gel samples. Under VPT conditions, the initial dry gel contains a small amount of dense phase and amorphous materials which are not readily to transform to the CHA structure due to the lack of SDA in the gel phase. There appears to be an equilibrium between the dense phase and amorphous materials. Once the morpholine molecules were gradually brought onto the surface of the solid dry gel, the equilibrium shifts to the amorphous phase which subsequently reorganizes its own structure towards CHA structure. The Si incorporation involves the formation of a small amount of aluminosilicates first and then incorporating isolated Si species and Si islands into SAPO-34 framework. In MTO reactions, the VPT-synthesized SAPO-34 shows longer catalytic lifetime than the conventional HTS-synthesized SAPO-34. Before 100 min on stream, the VPT sample shows relatively lower selectivity to light olefins and higher selectivity to propane than the HTS sample. These differences are ascribed to the smaller crystal size and the presence of stronger acidity in the VPT sample.

4.5 References

(1) Wilson, S. T.; Lok, B. M.; Messina, C. A.; Cannan, T. R.; Flanigen, E. M. *J. Am. Chem. Soc.* **1982**, *104*, 1146-1147.
(2) Yan, W.; Yu, J.; Xu, R.; Zhu, G.; Xiao, F.; Han, Y.; Sugiyama, K.; Terasaki, O. *Chem. Mater.* **2000**, *12*, 2517-2519.
(3) Sastre, G.; Lewis, D. W.; Richard, C.; Catlow, A. *J. Phys. Chem. B* **1997**, *101*, 5249-5262.
(4) Yu, J.; Xu, R. *Acc. Chem. Res.* **2003**, *36*, 481-490.
(5) Hirota, Y.; Watanabe, K.; Uchida, Y.; Egashira, Y.; Yoshida, K.; Sasaki, Y.; Nishiyama, N. *J. Membr. Sci.* **2012**, *415-416*, 176-180.
(6) Prakash, A. M.; Unnikrishnan, S. *J. Chem. Soc. Faraday Trans.* **1994**, *90*, 2291-2296.
(7) Zamadics, M.; Chen, X.; Kevan, L. *J. Phys. Chem.* **1992**, *96*, 5488-5491.
8) Li, S.; Falconer, J. L.; Noble, R. D. *J. Membr. Sci.* **2004**, *241*, 121-135.
(9) Li, S.; Falconer, J. L.; Noble, R. D. *Adv. Mater.* **2006**, *18*, 2601-2603.
(10) Hong, M.; Li, S.; Funke, H. F.; Falconer, J. L.; Noble, R. D. *Microporous Mesoporous Mater.* **2007**, *106*, 140-146.
(11) Li, S.; Falconer, J. L.; Noble, R. D. *Microporous Mesoporous Mater.* **2008**, *110*, 310 -317.
(12) Carreon, M. A.; Li, S.; Falconer, J. L.; Noble, R. D. *J. Am. Chem. Soc.* **2008**, *130*,

5412-5413.
(13) Li, S.; Carreon, M. A.; Zhang, Y.; Funke, H. H.; Noble, R. D.; Falconer, J. L. *J. Membr. Sci.* **2010**, *352*, 7-13.
(14) Li, G.; Yang, J.; Wang, J.; Xiao, W.; Zhou, L.; Zhang, Y.; Lu, J.; Yin, D. *J. Membr. Sci.* **2011**, *374*, 83-92.
(15) Dahl, I. M.; Kolboe, S. *Catal. Lett.* **1993**, *20*, 329-336.
(16) Vora, B.; Chen, J. Q.; Bozzano, A.; Glover, B.; Barger, P. *Catal. Today* **2009**, *141*, 77-83.
(17) Jänchen, J.; Ackermann, D.; Weiler, E.; Stach, H.; Brösicke, W. *Thermochim. acta* **2005**, *434*, 37-41.
(18) Chen, D.; Moljord, K.; Fuglerud, T.; Holmen, A. *Microporous Mesoporous Mater.* **1999**, *29*, 191-203.
(19) Hereijgers, B. P. C.; Bleken, F.; Nilsen, M. H.; Svelle, S.; Lillerud, K.-P.; Bjorgen, M.; Weckhuysen, B. M.; Olsbye, U. *J. Catal.* **2009**, *264*, 77-87.
(20) Yang, G.; Wei, Y.; Xu, S.; Chen, J.; Li, J.; Liu, Z.; Yu, J.; Xu, R. *J. Phys. Chem. C* **2013**, *117*, 8214-8222.
(21) Schnabel, K.-H.; Fricke, R.; Girnus, l.; Jahn, E.; Loffler, E.; Parlitz, B.; Peuker, C. *J. Chem. Soc. Faraday Trans.* **1991**, *87*, 3569-3574.
(22) Ashtekar, S.; Chilukuri, S. V. V.; Chakrabarty, D. K. *Proc. Indian Acad. Sci.* **1994**, *106*, 621-628.
(23) Hendrik van Heyden, S. M., and Thomas Bein *Chem. Mater.* **2008**, *20*, 2956-2963.
(24) Mertens, M. M.; Engels, B. US Patent 6,685,905, 2004.
(25) Zhou, H.; Wang, Y.; Wei, F.; Wang, D.; Wang, Z. *Appl. Catal., A* **2008**, 112-118.
(26) Liu, G.; Tian, P.; Zhang, Y.; Li, J.; Xu, L.; Meng, S.; Liu, Z. *Microporous Mesoporous Mater.* **2008**, *114*, 416-423.
(27) Dumitriu, E.; Azzouz, A.; Vasile Hulea a, D. L.; Kessler, H. *Microporous Mater.* **1997**, 1-12.
(28) Vistad, Ø. B.; Akporiaye, D. E.; Lillerud, K. P. *J. Phys. Chem. B* **2001**, *105*, 12437-12447.
(29) Vistad, Ø. B.; Hansen, E. W.; Akporiaye, D. E.; Lillerud, K. P. *J. Phys. Chem. A* **1999**, 2540-2552.
(30) Vistad, Ø. B.; Akporiaye, D. E.; Taulelle, F.; Lillerud, K. P. *Chem. Mater.* **2003**, 1639-1649.
(31) Yan, Z.; Chen, B.; Huang, Y. *Solid State Nucl. Magn. Reson.* **2009**, *35*, 49-60.
(32) Xu, W.; Dong, J.; Li, J.; Li, J.; Wu, F. *J. Chem. Soc., Chem. Commun.* **1990**, 755-756.
(33) Kim, M. H.; Li, H. X.; Davis, M. E. *Microporous Mater.* **1993**, *1*, 191-200.
(34) Wang, Y.; Tang, Y.; Dong, A.; Wang, X.; Ren, N.; Gao, Z. *J. Mater. Chem.* **2002**, *12*, 1812-1818.
(35) Zhang, L.; Yao, J.; Zeng, C.; Xu, N. *Chem. Commun.* **2003**, 2232-2233.
(36) Yao, J.; Zeng, C.; Zhang, L.; Xu, N. *Mater. Chem. Phys.* **2008**, *112*, 637-640.
(37) Chen, B.; Kirby, C. W.; Huang, Y. *J. Phys. Chem. C* **2009**, *113*, 15868-15876.
(38) Matsukata, M.; Nishiyama, N.; Ueyama, K. *Microporous Mater.* **1996**, *7*, 109-117.
(39) Yao, J.; Wang, H.; Ringer, S. P.; Chan, K.-Y.; Zhang, L.; Xu, N. *Microporous Mesoporous Mater.* **2005**, 267-272.
(40) Zhang, L.; Bates, J.; Chen, D.; Nie, H. Y.; Huang, Y. *J. Phys. Chem. C* **2011**, *115*,

22309-22319.
(41) Matsukata, M.; Ogura, M.; Osaki, T.; Raja, P.; Rao, H. P.; Nomura, M.; Kikuchi, E. *Top. Catal.* **1999**, *9*, 77-92.
(42) Tong, X.; Xu, J.; Wang, C.; Lu, H.; Huang, P.; Yan, W.; Yu, J.; Deng, F.; Xu, R. *Microporous Mesoporous Mater.* **2012**, *155*, 153-166.
(43) Amoureux, J.; Fernandez, C.; Steuernagel, S. *J. Magn. Reson., Ser. A* **1996**, *123*, 116-118.
(44) Haines, J.; Léger, J.; Gorelli, F.; Hanfland, M. *Phys. Rev. Lett.* **2001**, *87*, 155503.
(45) Onac, B. P.; White, W. B. *Am. Mineral.* **2004**, *88*, 1395-1397.
(46) Liu, G.; Tian, P.; Liu, Z. *Chin. J. Catal.* **2012**, *33*, 174-182.
(47) Xiao, Y.; Kirkpatrick, R. J.; Kim, Y. J. *Phys. Chem. Miner.* **1995**, *22*, 30-40.
(48) Xiao, Y.; James Kirkpatrick, R. *J. Mater. Res.* **1995**, *10*, 2586-2591.
(49) Chen, B.; Huang, Y. *J. Phys. Chem. C* **2007**, *111*, 15236-15243.
(50) Chen, B.; Huang, Y. *Microporous Mesorporous Mater.* **2011**, *143*, 14-21.
(51) Huang, Y.; Demko, B. A.; Kirby, C. W. *Chem. Mater.* **2003**, *15*, 2437-2444.
(52) Huang, Y.; Kirby, C. W.; Richer, R. *Stud. Surf. Sci. Catal.* **2004**, *154B*, 1471-1477.
(53) Huang, Y.; Yan, Z.; Richer, R. *Chem. Mater.* **2005**, *17*, 6545-6554.
(54) Chen, B.; Huang, Y. *J. Am. Chem. Soc.* **2006**, *128*, 6437-6446.
(55) Blackwell, C.; Patton, R. *J. Phys. Chem.* **1988**, *92*, 3965-3970.
(56) Blackwell, C.; Patton, R. *J. Phys. Chem.* **1984**, *88*, 6135-6139.
(57) Qiu, S.; Pang, W.; Kessler, H.; Guth, J. L. *Zeolites* **1989**, *9*, 440-444.
(58) Zibrowius, B.; Loeffler, E.; Hunger, M. *Zeolites* **1992**, *12*, 167-74.
(59) Yan, Z.; Zhuang, J.; Lei, X.; Han, X.; Liu, X.; Bao, X. *Chin. Chem. Lett.* **2003**, *14*, 87-90.
(60) Zhang, B.; Xu, J.; Fan, F.; Guo, Q.; Tong, X.; Yan, W.; Yu, J.; Deng, F.; Li, C.; Xu, R. *Microporous Mesoporous Mater.* **2012**, *147*, 212-221.
(61) Zhou, D.; Xu, J.; Yu, J.; Chen, L.; Deng, F.; Xu, R. *J. Phys. Chem. B* **2006**, *110*, 2131-2137.
(62) Prakash, A. M.; Unnikrishnan, S.; Rao, K. V. *Appl. Catal., A* **1994**, *110*, 1-10.
(63) Ashtekar, S.; Chilukuri, S. V. V.; Chakrabarty, D. K. *J. Phys. Chem.* **1994**, *98*, 4878-4883.
(64) Doremieux-Morin, C.; Martin, C.; Bregeault, J. M.; Fraissard, J. *Appl. Catal.* **1991**, *77*, 149-61.
(65) Tan, J. L., J.; Bao, X.; Liu, X.; Han, X.; He, C.; Zhai, R. *Microporous Mesoporous Mater.* **2002**, *53*, 97–108.
(66) Liu, G.; Tian, P.; Li, J.; Zhang, D.; Zhou, F.; Liu, Z. *Microporous Mesoporous Mater.* **2008**, *111*, 143-149.
(67) Xu, L.; Du, A.; Wei, Y.; Wang, Y.; Yu, Z.; He, Y.; Zhang, X.; Liu, Z. *Microporous Mesoporous Mater.* **2008**, *115*, 332-337.
(68) Flanigen, E. M.; Patton, R. L.; Wilson, S. T. *Stud. Surf. Sci. Catal.* **1988**, *37*, 13-27.
(69) Vomscheid, R.; Briend, M.; Peltre, M. J.; Man, P. P.; Barthomeuf, D. *J. Phys. Chem.* **1994**, *98*, 9614-18.
(70) Barthomeuf, D. *J. Phys. Chem.* **1993**, *97*, 10092-6.
(71) Sastre, G.; Lewis, D. W. *J. Chem. Soc. Faraday Tran.* **1998**, *94*, 3049-3058.
(72) Wei, Y.; Zhang, D.; He, Y.; Xu, L.; Yang, Y.; Su, B.; Liu, Z. *Catal. Lett.* **2007**, *114*, 30-35.

Chapter 5 Formation of SAPO-34 with up to Six Framework Si Species: Hydrofluoric Acid Present vs. Absent in the Synthesis Gel

5.1 Introduction

Among various SAPO-based molecular sieves, SAPO-34 is one of the most important ones. It has two different, but structurally related phases: trigonal (space group R-3) and triclinic (space group P-1).[1] Both phases have CHA topology analogous to that of the natural zeolite chabazite. The framework contains double six-membered rings (D6Rs) joined together by four-membered rings (4Rs) enclosing CHA cages.[2] The triclinic phase can be considered as a distorted analogue of the trigonal phase due to that one fluorine bridges two Al atoms in the former structure (Figure 5.1).[3] Because of its small-pore size, SAPO-34 is considered as the most promising effective catalyst in the conversion of methanol to olefins (MTO) and also a good candidate for gas separation.[4-12]

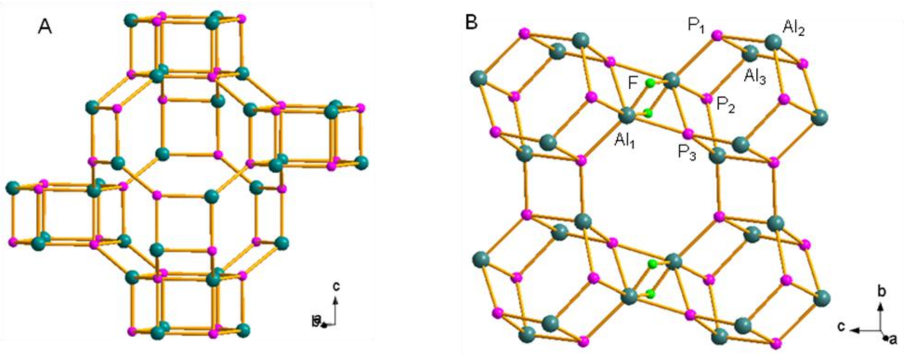

Figure 5.1 Structures of trigonal phase (A) and triclinic phase (B).

SAPO-34 has been synthesized in several ways. Microwave heating method has been used to synthesize SAPO-34 crystals with different morphologies and SAPO-34 membranes.[13,14] Hydrothermal synthesis method (HTS) is, however, the main method to synthesize the molecular sieve. Various structure-directing agents (SDAs) such as di-n-propylamine,[15] butylamine,[16] tetraethylammonium hydroxide,[17] isopropylamine,[18,19] triethylamine,[20,21] diethylamine,[22,23] piperidine,[24] and morpholine[25-29] have been used to obtain this molecular sieve. Morpholine has been demonstrated to be a good choice of SDA for the synthesis of SAPO-34 with high Si content and high crystallinity. With the presence of hydrofluoric acid (HF) and morpholine in the synthesis gel, triclinic SAPO-34 with high thermal stability can be made.[30]

As the catalytic properties of SAPO-34 are closely related to its acidity, Si content, and Si dispersion in the framework, a detailed study on its crystallization is very helpful for controlling the framework composition and optimizing the synthesis conditions for catalytic applications.[31] Formation of SAPO-34 templated by morpholine using an HTS method was previously studied by Vistad *et al.*[25,26,28] and the Huang group.[29]

Vistad *et al.* reported a shorter crystallization time of SAPO-34 in the fluoride medium compared to the synthesis without HF, and a crystalline layered material, called “prephase”, was the key intermediate to triclinic SAPO-34, which contains three T (T = Al or P) sites.[29,32,33] They pointed out that the initial gel dissolves and produces 4R type-I units first. The layered $AlPO_4F$ prephase is then formed out of these units by simple alternating stacking. However, ^{29}Si NMR studies were not applied in their work. Based on EDX measurements they proposed that Si incorporation proceeds by substitution of aluminum or phosphorous in the 4R type-I units.

Using the same HTS in the fluoride medium conditions (HTS with HF) as those by Vistad *et al.*, the Huang group investigated the local environments of ^{31}P, ^{27}Al, ^{19}F, and ^{29}Si atoms in several important intermediates of SAPO-34 by solid-state NMR. Based on the similar chemical shift value and line shape of P and Al atoms in the prephase to those of P_3 and Al_1 sites in triclinic SAPO-34 (Figure 5.1B), they proposed that some of P and Al atoms in the prephase evolve into P_3 and Al_1 sites of triclinic SAPO-34 directly without redissolution and reorganization. The Si incorporation mechanism was, however, not discussed in their work either.

Under HTS conditions, crystallization involves species dispersed into both liquid and solid phases. Post-synthesis treatments such as washing and centrifugation are required to separate solid gel samples from the liquid phase. The structures of the solid intermediates may be altered significantly if weak bond interactions are present.[34] An alternative method to HTS is the so-called dry gel conversion (DGC).[35] DGC involves conversion of pre-dried gel powder to a crystalline molecular sieve at elevated temperature and autogeneous pressure. Unlike HTS, DGC is suitable for isolating solid intermediates and examining crystallization due to its simpler reaction system where all the reactive species are confined in the solid phase.[36] The crystallization rate is lower in DGC because of the lack of the apparent liquid phase, which slows down the mass transport. The DGC method has been demonstrated to be an effective approach to study the formation of several types of molecular sieves including zeolite beta, $AlPO_4$-5, $AlPO_4$-11, $AlPO_4$-18, and SAPO-34 templated by diethylamine.[34,37-42]

Recently, Chen *et al.* obtained SAPO-34 from the transformation of the prephase under DGC conditions.[43] The as-synthesized SAPO-34, which is a mixture of triclinic and trigonal phases, contains a variety of signals in the ^{29}Si NMR spectrum. However, the assignment of these peaks to Si species in either the triclinic or trigonal phase was not made. In the present work, formation of SAPO-34 templated by morpholine was studied under DGC conditions. Two types of dry gels were used with one containing hydrofluoric acid (HF) and the other not. Si incorporation and Si distribution in as-made SAPO-34 was also investigated. Characterization techniques, which include powder XRD, SEM/EDX, and solid-state NMR, were applied to study solid intermediate phases. A comparison of crystallization of SAPO-34 under DGC with and without HF conditions was made with attention being paid to the structures of the intermediates and Si distribution in the final crystalline product, and the results provide new insights into the formation of SAPO-34. Meanwhile, the catalytic properties of the products made with and without HF were tested in MTO reactions.

5.2 Experimental

5.2.1 Sample preparation

The synthesis of SAPO-34 was performed according to the general dry gel conversion technique described elsewhere.[34,44] The reagents used were pseudo-boehmite (Catapal B, ca. 65 wt% Al_2O_3, Vista), H_3PO_4 (85%, EM Science), morpholine (Aldrich), HF (48 wt%, Caledon), colloidal silica (Ludox LS-30, Aldrich), and distilled water. The initial gel molar composition (Al_2O_3:P_2O_5:SiO_2:morpholine:HF:H_2O) was 1.0:1.0:1.0:2.1:x:60 (x = 0 or 1.0).

A typical procedure for the preparation of DGC dry gel was the following: based on the specific gel molar composition, a proper amount of Catapal B was mixed with distilled water, and the mixture was stirred at room temperature for certain minutes followed by adding H_3PO_4 aqueous solution slowly with continuous stirring. The solution containing certain proportions of colloidal silica, morpholine, and distilled water, which was also stirred for a couple of minutes at room temperature, was then added to the above mixture under vigorous stirring for homogeneity. For DGC with HF ($x = 1.0$), HF was finally added. The mixture was dried at 353 K with constant stirring to allow evaporation of water until solids formed. The solid sample was then ground into a fine powder and sealed in glass vials. A series of intermediates were synthesized by placing 1.0 g of DGC initial dry gel powder into small Teflon cups. Each cup was placed in a 23-mL Teflon-lined autoclave with 0.3 g (for DGC without HF) and 0.7 g (for DGC with HF) distilled water at the bottom and heated in an oven at 473 K. The reactions were quenched in cold water. For comparison, each solid sample was divided into two parts. One part was dried in air and the other part was first washed with distilled water in a beaker and then dried in the same beaker in air without isolation from the liquid phase. This ensured that no solid particles were washed away. All dried samples were kept in sealed vials for further analysis.

5.2.2 Characterization

Powder XRD patterns were recorded on a Rigaku diffractometer using Co Kα radiation (λ = 1.7902 Å). Representative samples were first coated with 3 nm osmium metal using a Filgen OPC-80T instrument, and their elemental analysis was then examined using a FIB/SEM 1540XB microscope equipped with an energy-dispersive X-ray spectrometer for elemental analysis. The bulk compositions of the same samples were obtained by X-ray fluorescence (XRF) using a Philips PW1450 spectrometer.

All the NMR experiments were carried out on a Varian/Chemagnetics Infinityplus 400 WB spectrometer equipped with three rf channels operating at the field strength of 9.4 T. The Larmor frequencies of ^{1}H, ^{31}P, ^{27}Al, and ^{29}Si were 399.5, 161.7, 104.1, and 79.4 MHz, respectively. The magic angle was set using the ^{79}Br resonance of KBr. The chemical shifts of ^{31}P, ^{27}Al, and ^{29}Si were referenced to 85% H_3PO_4, 1M $Al(NO_3)_3$ aqueous solution, and tetrakis(trimethylsilyl)-silane (TTMSS, $SiMe_3$, −9.9 ppm with respect to liquid tetramethylsilane), respectively. Depending on the requirements of the individual experiment, three NMR probes (a Varian/Chemagnetics 7.5-, and a 4.0-mm H/X/Y triple-tuned T3 MAS probe, and a 5.0-mm H/F/X/Y triple-tuned MAS probe) were used. For ^{31}P MAS experiments, a 45° pulse was typically used and the recycle delay was 60 s. The proton-decoupling field was about 60 kHz. The ^{27}Al spectra were acquired using a very small pulse angle with a pulse delay of 1 s. For the ^{29}Si MAS experiments, a 45° pulse was used with a pulse delay of 60 s. For ^{1}H to ^{29}Si cross-polarization (CP) experiments, the ^{1}H 90° pulse length was 5 μs and the Hartmann-Hahn condition was determined using TTMSS. ^{27}Al{^{31}P} REDOR experiments were carried out using the 5.0-mm probe with a spinning speed of 8 kHz and ^{29}Si{^{19}F} REDOR experiment was carried out using the 7.5-mm probe with a spinning speed of 5 kHz. The details for REDOR experiments were described in previous works.[45-47] ^{27}Al 3QMAS experiments were performed using the 4.0-mm probe and the spinning speed was 10 kHz. The spectra were obtained by utilization of a three-pulse z-filter sequence.[48] The rf strengths of the first two hard pulses and third soft pulse were optimized individually, and the optimized pulse lengths were 5.7, 2.0, and 15.0 μs for the three consecutive pulses.

5.2.3 Catalytic tests

MTO reactions were performed at the Dalian Institute of Chemical Physics, China. They were carried out with a fixed-bed reactor at atmospheric pressure. 0.3 g of catalyst (40-60 mesh) was loaded into the reactor. The sample was preheated in nitrogen flow at 773 K for 1 h and then the temperature of the reactor was decreased to 723 – 730 K. The methanol and nitrogen mixture was then pumped into the reactor. The weight hourly space velocity (WHSV) was 2.9 h^{-1}. The products were analyzed on-line by a Varian GC3800 gas chromatograph equipped with a FID detector and a PoraplotQ-HT capillary column.

5.3 Results and discussion

5.3.1 Crystallization under DGC with HF conditions

To monitor the evolution of the long-range ordering in the intermediate gel samples, powder XRD patterns were obtained (Figure 5.2A). It is noticeable that the powder pattern of the initial dry gel is the same as that of the prephase synthesized by Vistad *et al.* using HTS with HF method. From a different perspective it is consolidated that formation of the prephase is crucial for the crystallization of SAPO-34 in the fluoride medium with morpholine as a SDA.

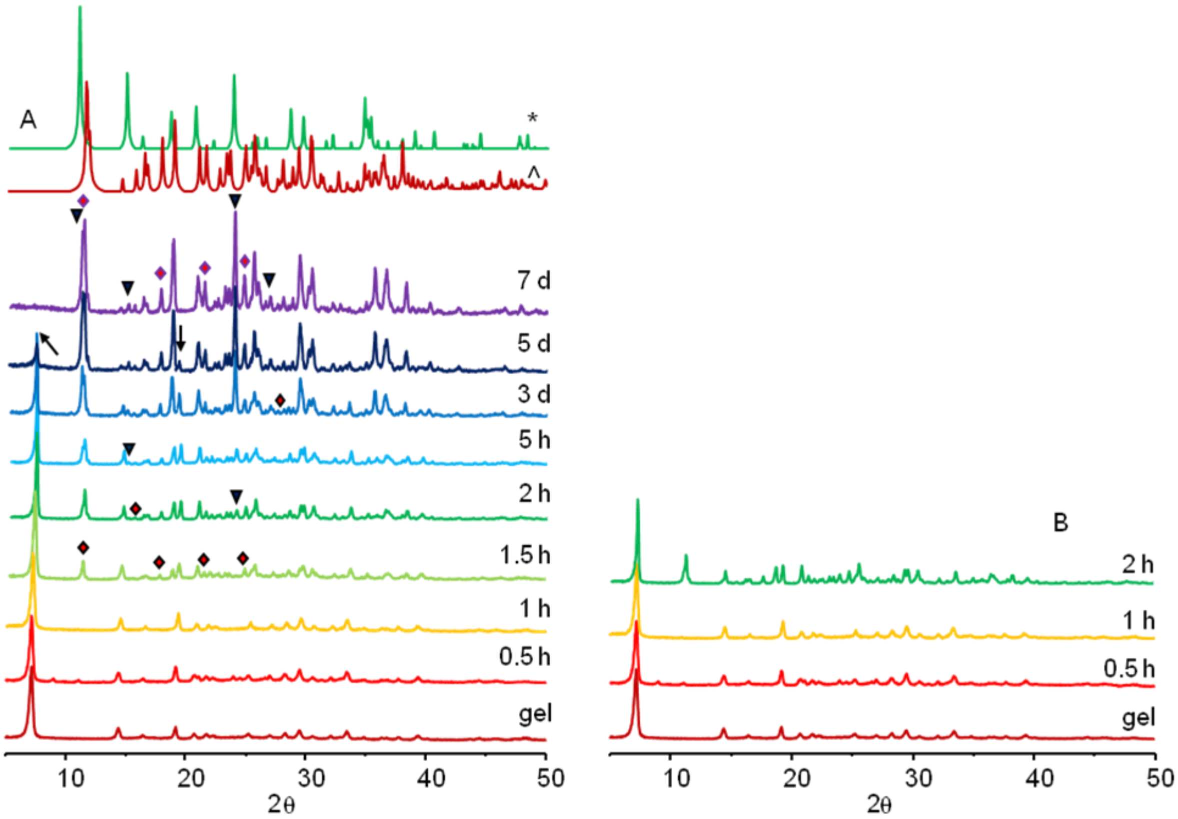

Figure 5.2 Powder XRD patterns of (A) unwashed and (B) selected washed DGC with HF dry gel samples. ◆ and ▼ denote triclinic phase and trigonal phase, respectively. * and ^ are simulated XRD data of trigonal and triclinic SAPO-34, respectively.[27]

The crystallization process of SAPO-34 under DGC with HF conditions is similar to that under HTS with HF conditions reported by the Huang group.[29] Heating the gel for 1.5 h first showed several sharp peaks labeled as ◆ (Figure 5.2A), which are due to the triclinic phase. Further heating resulted in the sharpening these reflections and more peaks belonging to the triclinic phase appeared in the powder XRD patterns of 2 h and 5 h samples. A reflection peak due to trigonal phase first showed up in the reflection pattern of 2 h sample. Upon heating the gel for 5 d, peaks due to the prephase (marked with arrows) became much weaker and completely disappeared in the powder pattern of

7 d sample. The final product (7 d sample) is purely crystalline SAPO-34 containing both triclinic and trigonal phases.

Different from HTS with HF where SAPO-34 is obtained after 4 h of heating, it takes 7 days of heating to get pure SAPO-34 by DGC with HF. Upon washing the selected gel samples with water, the reflection patterns remain unchanged (Figure 5.2B). This implies that the prephase structure is held together by covalent bonds. This is different from previous reports on crystallization of $AlPO_4$s studied using the DGC method,[34,40,41] in which the intermediates are usually held together by weak noncovalent bonding forces. The powder XRD results indicate that the SAPO-34 sample with mixed triclinic and trigonal phases is formed from the transformation of the prephase. The Huang group previously pointed out that the prephase contains similar 4Rs to triclinic SAPO-34 (Figure 5.3). They proposed that the majority of the P and Al atoms in the prephase are transformed to the P_1, P_2 and Al_1, Al_2 sites in the triclinic phase and also the P and Al sites in the trigonal phase; the remaining P and Al atoms remain unaffected and evolve into the P_3 and Al_1 sites in the triclinic phase directly.[29] The transformation of the prephase to SAPO-34 is thus likely to involve the breakage of -T-O-T linkages in the 4Rs (T = P or Al, Figure 5.3B). Due to access to limited water vapor, these bonds may be very difficult to be broken and then reorganized. This may have caused the much longer crystallization time under DGC with HF conditions.

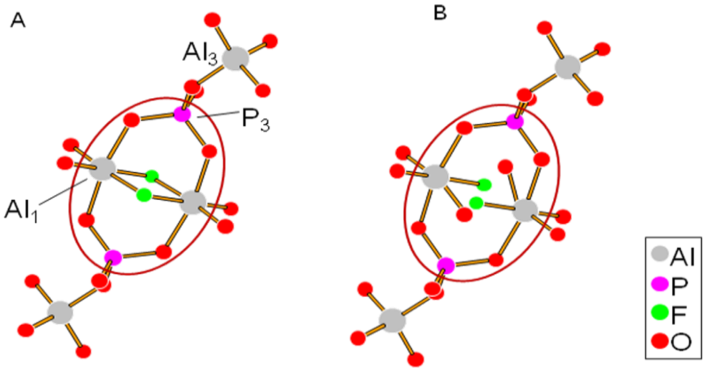

Figure 5.3 4Rs (encircled) in triclinic phase (A) and prephase (B).[29]

To get an insight into the development of the local environments of P and Al atoms within the intermediate phases as a function of crystallization time, ^{31}P and ^{27}Al MAS spectra were obtained (Figure 5.4). The ^{31}P and ^{27}Al MAS spectra of the dry gel samples heated for less than 1.5 h exhibit similar pictures to those of the prephase hydrothermally synthesized.[29] The single sharp peak at around -9 ppm in the ^{31}P spectra indicates the high local ordering around P, suggesting that the P atom is not fully condensed. In the corresponding ^{27}Al MAS spectra, the peak at 46 ppm can be assigned to tetrahedral Al and the signal at 6 ppm to unreacted Al. The broad envelop at -20 ppm contains two peaks with isotropic chemical shift values of -6 and -12 ppm as reported.[29] They are due to two nonequivalent octahedral Al sites. Heating the dry gel for 1.5 h resulted in two new broad ^{31}P peaks centered at -24 and -30 ppm, which represent the P_2 and P_1 sites of the triclinic phase, respectively (Figure 5.1B).[29] This complies with the corresponding powder pattern which shows the appearance of the triclinic phase (Figure 5.2A). Increasing the crystallization time to over 2 h, there appeared a signal at -8 ppm in the ^{31}P MAS spectra, which is due to the P_3 site in the triclinic phase.[29] The signal at -6 ppm became stronger in the ^{27}Al MAS spectra and is assigned to the Al_1 site (Figure

5.1B).[29] In the ^{31}P and ^{27}Al MAS spectra of gel samples heated for over 5 h, there are signals due to trigonal phase, which has a ^{31}P peak at -28 ppm and a ^{27}Al peak at 56 and/or 40 ppm. The ^{27}Al 3QMAS spectrum of the 7 d sample (Figure 5.5A) indicates that there are five Al sites. The peak with an isotropic chemical shift of -5 ppm can be assigned to the octahedral Al_1 site in the triclinic phase. The peaks at 47, 50, and 56 ppm are due to the tetrahedral Al sites in either the triclinic or trigonal phase. There is also little unreacted Al with an isotropic chemical shift of 5 ppm that is XRD invisible. Overall, under DGC with HF conditions, the changes in the powder XRD patterns and NMR spectra as a function of crystallization time follow the same trend.

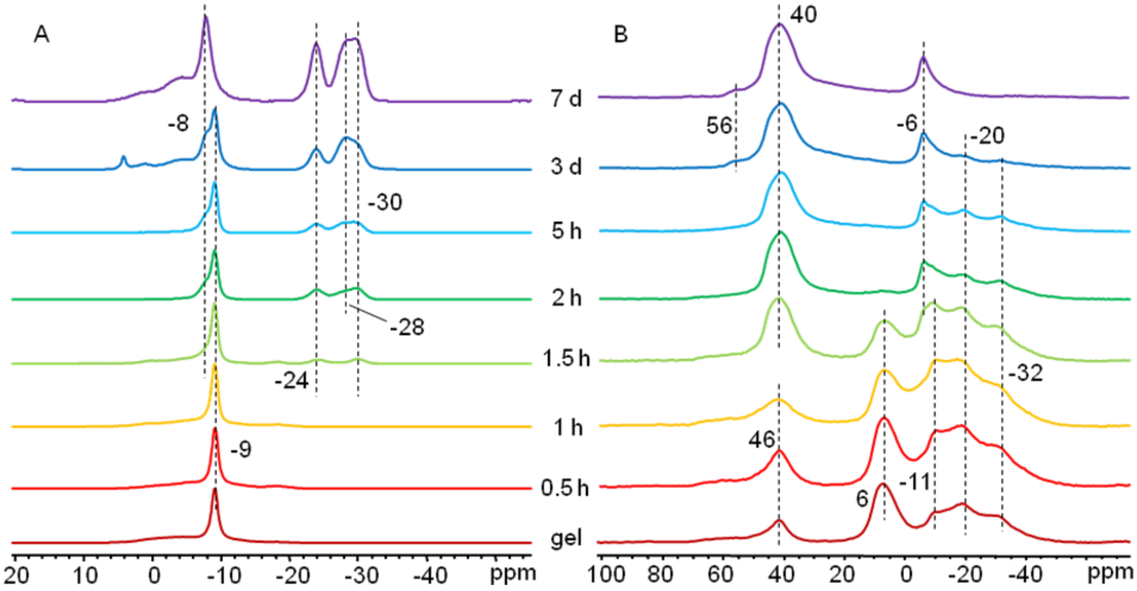

Figure 5.4 ^{31}P (A) and ^{27}Al (B) MAS spectra of unwashed DGC with HF dry gel samples. Asterisks indicate spinning sidebands.

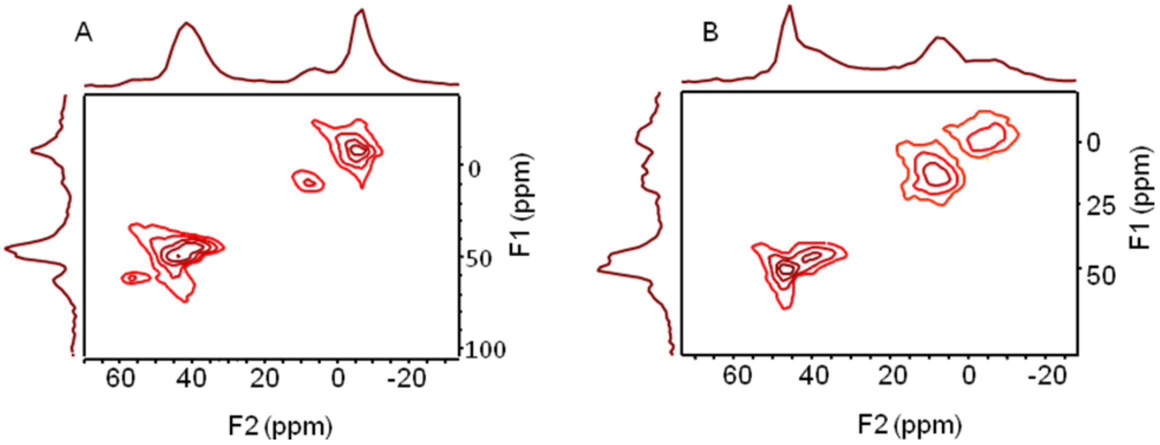

Figure 5.5 ^{27}Al 3Q MAS spectra of (A) DGC with HF 7 d sample and (B) DGC without HF 1 d sample.

To investigate the Si incorporation, ^{29}Si NMR experiments were carried out. ^{1}H → ^{29}Si CP techniques were used for selecting the Si species with protons nearby. The ^{29}Si MAS spectra of the DGC with HF dry gel samples heated for less than 1 h contain a strong broad peak at -111 ppm (Figure 5.6A). It can be assigned to unreacted amorphous silica with a $Si(OSi)_4$ environment.[49] Also shown in the MAS spectra is a much weaker signal at -101 ppm. The intensity of it increased a lot in the corresponding CP spectra (Figure 5.6B). This signal is due to a small amount of Si atoms on the surface of silica particles with a $(SiO)_3SiOH$ environment.[50] This observation suggests that the majority of the silica in these samples has not started reacting and thus the prephase is mainly AlPO in nature. This is consistent with the EDX data by Vistad *et al.* and the ^{29}Si MAS spectrum of the hydrothermally synthesized prephase reported by the Huang group.

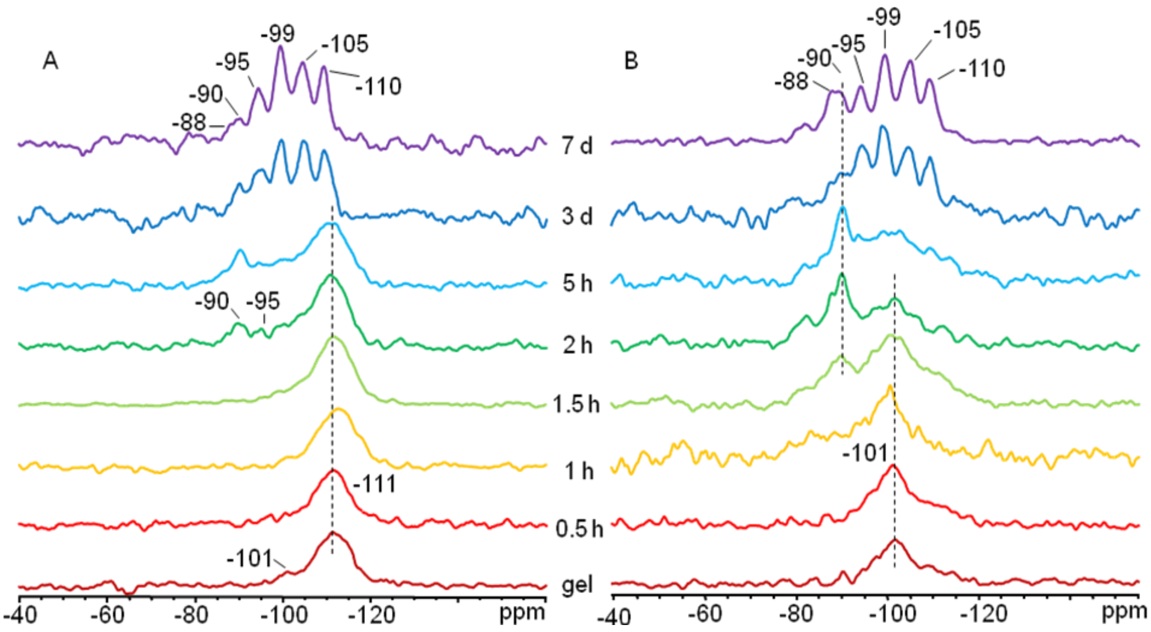

Figure 5.6 ^{29}Si MAS (A) and ^{1}H → ^{29}Si CP (B) spectra of selected unwashed DGC with HF dry gel samples with a contact time 0.5 ms.

Increasing the reaction time to 1.5 h gave rise to a new peak at -90 ppm in the CP spectrum, which may result from $Si(OAl)_4$ or $Si(OSi)_2(OH)_2$ species, considering the much higher intensity in the CP than in the MAS spectrum.[51] This implies that upon heating, silica reacted with alumina resulting in the formation of an amorphous aluminosilicate. This also demonstrates that Si started to be incorporated into the framework via the formation of aluminosilicate species. Upon heating the gel for 2 h, in the ^{29}Si MAS spectrum there appeared two resonance lines at around -90 and -95 ppm. This observation agrees with the powder XRD pattern and ^{31}P MAS spectrum (Figures 5.2A and 5.4A), which show characteristic signals of the trigonal phase and triclinic phase. The ^{29}Si MAS spectra of gel samples heated for 3 d or longer are similar to that reported by Chen *et al*.[43] There are six ^{29}Si NMR signals at -88, -90, -95, -99, -105, and -110 ppm. The peaks at -88 and -90 ppm can be assigned to $Si(OAl)_4(OP)_9$ or

$Si(OAl)_4(OSi)_9$ environments. The latter four signals are due to $Si(OAl)_3(OSi)_1$, $Si(OAl)_2(OSi)_2$, $Si(OAl)_1(OSi)_3$, and $Si(OSi)_4$ species, respectively.[52]

In general, there are three types of Si incorporation mechanisms. The first is the substitution of an Al by a Si (SM I). The second is the replacement of a P by a Si and hydrogen with the proton being attached to the oxygen on a Si-O-Al bridge (SM II). This produces a Brønsted acid site and isolated $Si(OAl)_4$ species. The third is the double substitution of neighboring Al and P by two Si atoms (SM III).[24,49,53-55] Si islands with $Si(OAl)_n(OSi)_{4-n}$ (n=0, 1, 2, 3, or 4) species are formed when a combination of SM II and III occurs. It is reported that Si incorporation by SM III begins at a threshold of Si content depending on the topology of the structure and synthesis conditions.[55,56] For the synthesis of SAPO-34 with morpholine as the SDA, Si atoms start to be incorporated into the framework via SM III when Si content is over 11 mol.%.

EDX analysis was performed to obtain semi-quantitative information on elemental compositions. It is known that the P/Al ratio is 1:1 in the structures of $AlPO_4$-n molecular sieves. Any change in the P/Al ratio reflects the incorporation of Si atoms into the framework. The (Si + P)/Al ratio is equal to 1 if Si atoms enter into the framework via SM II only. The ratio is over than 1 when the combination of SM II and III occurs. The compositions of the final product (7 d sample) are the averaged results obtained from at least three independent measurements for each phase. The Si content in the triclinic phase and trigonal phase is about 14 and 32 mol.%, respectively. Both values are higher than 11 mol.%. Further, the (Si + P)/Al ratio is 1.5 in the trigonal phase and 1.2 in the triclinic phase, both of which are greater than 1. The EDX data are consistent with the corresponding ^{29}Si NMR spectrum, implying that Si is incorporated into SAPO-34 structures via a combination of SM II and III. The higher Si content and (Si + P)/Al ratio in the trigonal phase than in the triclinic phase also suggest that the former phase contains more Si than the latter one. Moreover, the 32 mol.% of silicon content in trigonal phase was also observed previously in SAPO-34 with morpholine as the SDA, which contains a strong peak at -90 ppm and several other weaker ones between -94 and -110 ppm.[55,56] This suggests a distinctly different Si distribution in 7 d sample.

The presence of six ^{29}Si signals in 7 d sample makes it difficult to assign them to either trigonal or triclinic phase. To solve the problem, firstly the ^{29}Si{^{19}F} REDOR experiments were performed on the product, which provide information about Si-F distance using heteronuclear dipolar interaction.[29] A typical set of ^{29}Si observed REDOR spectra are shown in Figure 5.7. Due to the relatively low natural abundance of the ^{29}Si nucleus and the low silicon content in the sample, the heteronuclear dipolar coupling between Si and F is very small. A REDOR difference spectrum (ΔS) with good signal to noise ratio is very difficult to obtain. Nevertheless, a small REDOR effect for the signal at -95 ppm can be observed from the figure. The spectrum shows a 17% reduction in the peak intensity for the REDOR spectrum (S), compared to the normal ^{29}Si spin-echo (S_0). This observation suggests that Si species resulting in this signal may exist in the triclinic phase.

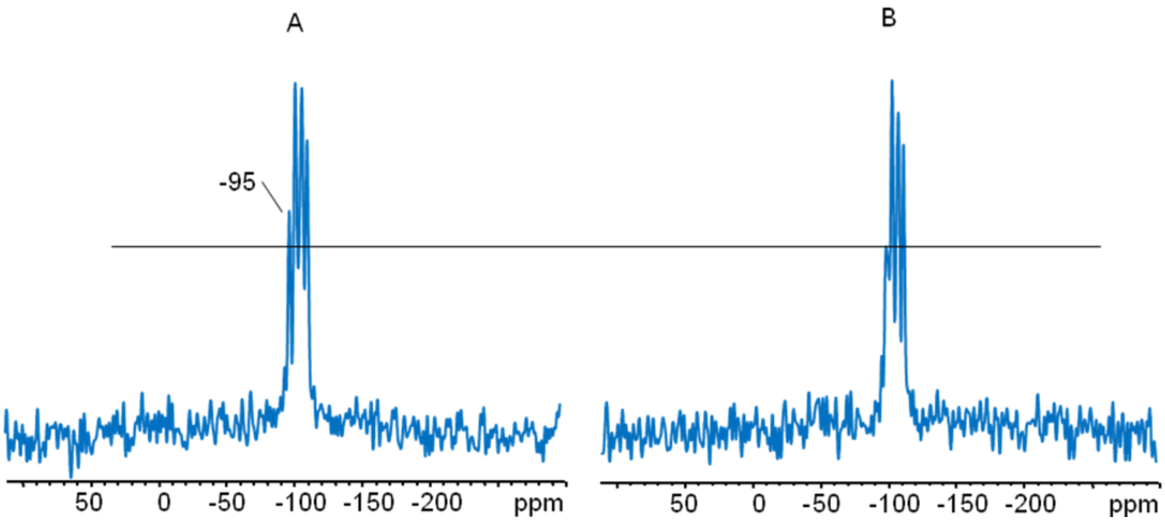

Figure 5.7 $^{29}Si\{^{19}F\}$ REDOR of unwashed 7 d sample with a dephasing time of 1.2 ms. (A) ^{29}Si spin-echo, S_0; (B) $^{29}Si\{^{19}F\}$ REDOR spectrum, S.

Now the question is: are the rest of the signals due to Si species in the trigonal phase? Other types of Si species can also give rise to these peaks: (1) Si in aluminosilicate or pure silica chabazite phase (zeolite chabazite), which exists outside the framework of SAPO-34. Zeolite chabazite gives the same powder XRD pattern as trigonal SAPO-34; (2) Si in amorphous aluminosilicate phase, which is encapsulated in the CHA cages. Zeolite chabazite is usually obtained using *N*, *N*, *N*-trimethyladamantammonium hydroxide as a SDA.[57,58] Its formation has not been observed during the synthesis of SAPO-34 so far. The synthesis gel recipe ($1.0Al_2O_3$:$1.0P_2O_5$:$1.0SiO_2$:2.1morpholine) is the same as that used by the Prakash group.[49] They reported that two morpholinium molecules occupied per CHA cage in SAPO-34 framework and that there is no extra space for amorphous species to be present in the completely filled pore.[49] The SDA molecules in 7 d sample therefore fully occupy the CHA cages. Thus, Si species in trigonal SAPO-34 may give rise to the observed ^{29}Si signals except the one at -95 ppm.

The EDX data reveal that the triclinic phase contains higher Al and P contents than the trigonal phase. Aluminophosphate phase (AlPO) is known to be soluble in an alkaline environment[59] and the amorphous species is more soluble than crystalline molecular sieve framework.[60-62] To corroborate the assignment above, 7 d sample was treated with an alkaline solution. To selectively dissolve only triclinic phase and amorphous species which may be present, and meanwhile, keep trigonal phase, an optimum alkaline treatment condition is required. Highly crystalline zeolite Y (Si/Al = 3.3-3.8) was used for trial experiments. After several trials, it is found that the crystallinity and ^{27}Al and ^{29}Si nuclei local environments (not shown) remained unchanged when the sample was soaked and stirred in 0.5 M NaOH aqueous solution for 0.5 h at room temperature. The same condition was then applied to 7 d sample. After the treatment, the solids were obtained by centrifugation upon washing using lots of distilled water.

A comparison of powder patterns and ^{31}P MAS spectra of the NaOH-treated and as-synthesized samples (Figures 5.8A and 5.9A) indicate that the NaOH-treated sample is pure trigonal SAPO-34 phase with relatively high crystallinity. The triclinic phase was completely dissolved. In the ^{27}Al spectrum (Figure 5.9B), in addition to the peak at 39 ppm due to the trignal SAPO framework Al site, there is a stronger one at 54 ppm. This chemical shift value is close to the range of 55-58 ppm for ^{27}Al signals in aluminosilicates.[63] In SAPO-34, Si is reported to be distributed in two types of domains, SAPO and aluminosilicate (AS).[64,65] In SAPO domains, only SM II occurs and gives rise to a ^{29}Si signal in a $Si(OAl)_4(OP)_9$ environment at around -90 ppm. On the other hand, in AS domains, $Si(OAl)_4(OSi)_9$ and Si islands are formed by SM II and III. The formation of AS domains was previously observed in SAPO-44, which also has the CHA framework.[64,65] This implies that under DGC with HF conditions, AS next to SAPO domains were formed. Based on this, the signal at 54 ppm is attributed to the Al site in AS phase in the trigonal SAPO-34. An illustration of SAPO and AS domains is shown in Scheme 5.1.[66] The ^{29}Si MAS NMR spectrum of the NaOH-treated sample (Figure 5.9C) shows four signals at -95, -99, -105, and -110 ppm. The appearance of these four signals implies that they arise from Si species in the trigonal framework. Moreover, the peak at -95 ppm decreased a lot in the intensity. In agreement with the ^{29}Si{^{19}F} REDOR results (Figure 5.7), this peak mainly results from Si in the triclinic framework. Some of the signal at -99 ppm may also arise from the triclinic phase, as suggested by its decreased intensity. It seems therefore that both the triclinic and trigonal phases contain the same Si species giving rise to the signals at -95 and -99 ppm. Meanwhile, the peaks at -88 and -90 ppm disappeared. However, due to the small amount in the product, their assignment cannot be unambiguously made. They may exist in either the triclinic or trigonal phase.

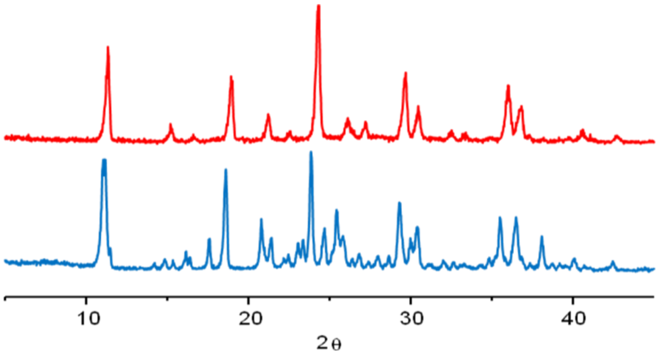

Figure 5.8 Powder XRD patterns of NaOH-treated (top) and as-synthesized (bottom) DGC with HF 7 d sample.

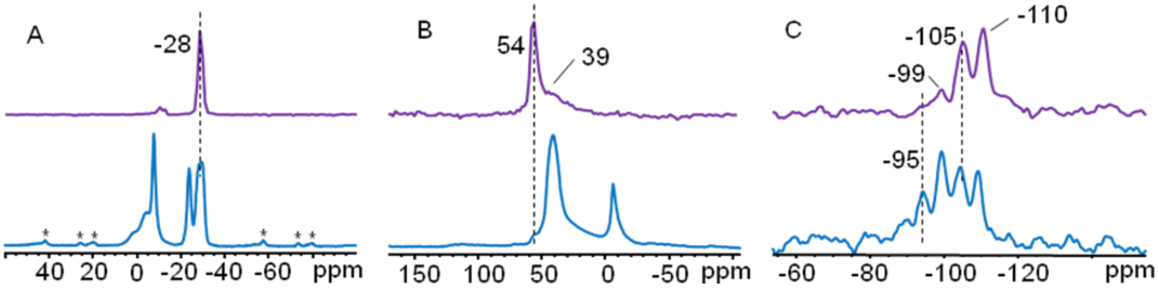

Figure 5.9 ^{31}P MAS (A), ^{27}Al MAS (B), and ^{29}Si MAS (C) NMR spectra of NaOH-treated (top) and as-synthesized (bottom) 7 d sample. * indicates spinning sidebands.

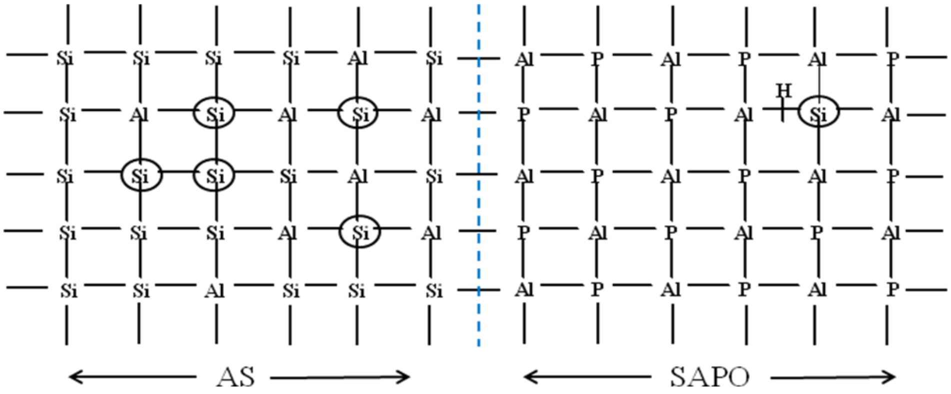

Scheme 5.1 Schematic diagram of Si, Al and P environments in AS and SAPO domains of SAPO-34 molecular sieve. The encircled elements have different ^{29}Si NMR chemical shifts.

Based on these results, the six different ^{29}Si signals in the SAPO-34 product (Figure 5.6A) is assigned as follows: -95 and -99 ppm to $Si(OAl)_3(OSi)_1$ and $Si(OAl)_2(OSi)_2$ species in AS domains of both triclinic and trigonal phases; -105 and -110 ppm to $Si(OAl)_1(OSi)_3$, and $Si(OSi)_4$ species in AS domains of trigonal phase. The signals at –88 and 90 ppm may result from $Si(OAl)_4$ species in AS or SAPO domains of either triclinic or trigonal phase. This conclusion agrees with the EDX results of each phase, suggesting the Si incorporation via SM II and III into triclinic and trigonal SAPO-34 frameworks.

In summary, under DGC with HF conditions, the initial dry gel is a layered highly crystalline phase namely “prephase”. It is mainly AlPO in nature. Upon heating, it was first reorganized to form triclinic phase and then to form trigonal phase. The final product is a mixture of both phases. Si was incorporated by forming aluminosilicate species. The as-made SAPO-34 contains up to six framework Si species and most of them are located in trigonal phase.

5.3.2 Crystallization under DGC without HF conditions

To compare the formation of SAPO-34 with the presence or absence of HF in the synthesis gel, a DGC without HF method was also applied. The powder pattern of the initial gel (Figure 5.10A) shows one weak peak at about 8.38° (labeled with an arrow) and several broad halos. The broad reflections indicate the existence of a large amount of amorphous phase in the dry gel, and the relatively sharp peak is due to a very small amount of layered phase with certain degree of long-range ordering. Upon treating the dry gel for 0.5 h, the intensity of the peak at 8.38° increased significantly at the expense of the broad amorphous halos. The reflection pattern of this sample is typical of a crystalline layered phase. This demonstrates reorganization of the initial gel. Upon heating for 1 h, the powder pattern exhibits a small, new, weak peak at 9.14°, signifying that another phase was beginning to form. After 1.5 h of heating treatment, the powder patterns indicate that the sample is a semi-crystalline layered phase with a characteristic low-angle peak at 9.14°. The reflections belonging to the crystalline layered phase completely disappeared, suggesting that the crystalline phase was reorganized and transformed to the semi-crystalline phase. Upon heating the gel for 4 h, several broad reflections with similar 2θ values as trigonal SAPO-34 grew from the semi-crystalline phase (labeled with ♦). This indicates that the semi-crystalline phase contains similarities with SAPO-34. Highly crystalline SAPO-34 was obtained after heating the dry gel for 1 d or longer, and all peaks of final products can be assigned to the *hkl* reflections of the trigonal phase (Figure 5.10A).[67]

Compared to 7 days of heating in DGC with HF for the synthesis of SAPO-34, it only takes 1 day in DGC without HF. To investigate the nature of bonding interactions in DGC gel samples without HF, the intermediates were therefore treated with distilled water. Upon washing, all of the diffraction peaks due to the crystalline layered phase and the broad signal due to the semi-crystalline phase disappeared in the corresponding powder XRD patterns (Figure 5.10B). Only broad reflections remained in the washed gel samples heated for less than 4 h. The results indicate that the crystalline and semi-crystalline phases are held by weak noncovalent bonding interactions such as weak hydrogen bonding and van der Waals forces. Such interactions are much weaker than the covalent bonds in the prephase and therefore facilitate the transformation and reorganization of the layered intermediates to SAPO-34.

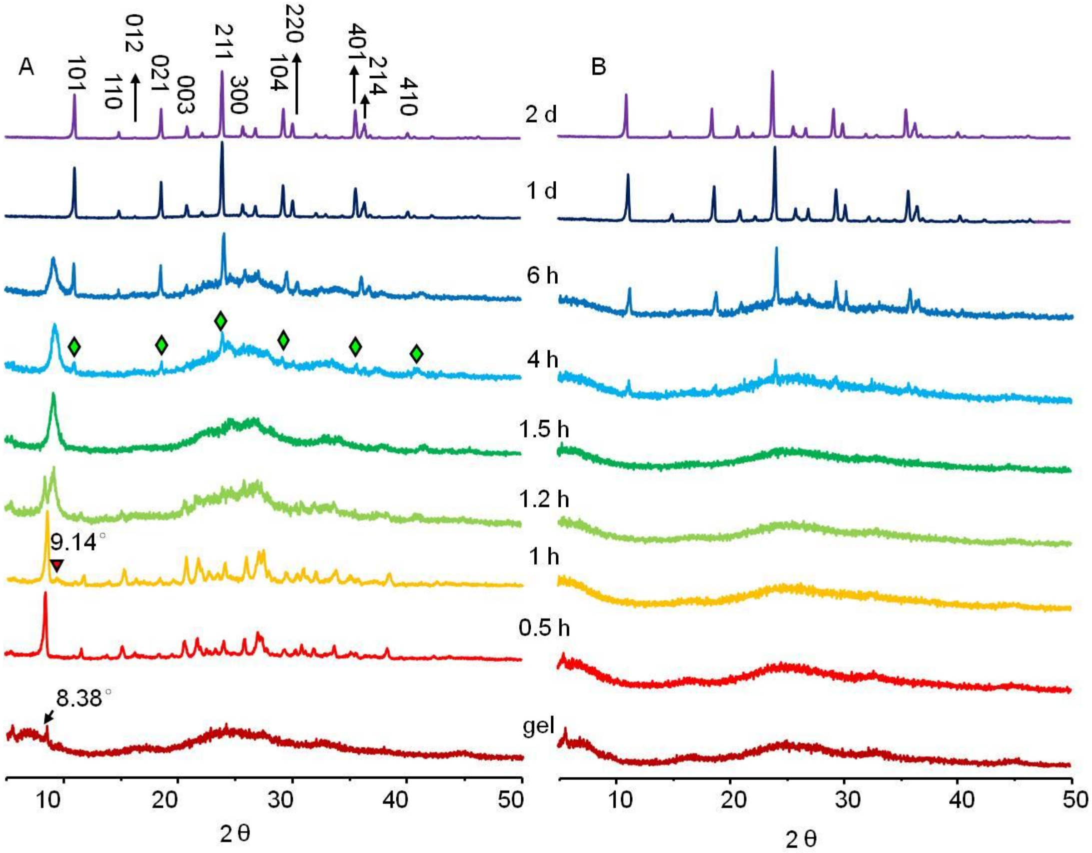

Figure 5.10 Powder XRD patterns of (A) unwashed and (B) washed DGC without HF dry gel samples.

The ^{31}P spectrum of the unwashed initial gel (Figure 5.11A) exhibits several broad overlapped peaks at around -6, -10, -13, -18, and -26 ppm, indicating that the amorphous initial gel has at least five different P sites. Upon heating, the intensities of the peaks between -5 and -13 ppm became much weaker, suggesting reorganization within the sample. The much stronger intensity of the signal at -18 ppm and the appearance of two sharp peaks at -20 and -22 ppm are consistent with the powder XRD pattern. They correspond to the formation of the crystalline layered phase, as the intensity of these three peaks decreased a lot upon washing (Figure 5.11B). The chemical shifts of these three peaks indicate that the P sites in the layered phase are not fully condensed.[68]

Heating the gel for 1.2 h, the three peaks became a single symmetric one at -18 ppm due to the transformation to the semi-crystalline phase. After 4 h of heating, the appearance of a new signal at -28 ppm, suggesting the formation of fully condensed P with a $P(OAl)_4$ environment, exactly matches the powder pattern which shows the appearance of several *hkl* reflections of SAPO-34. The spectrum of the final product (1 d sample) exhibits a single, sharp, signal at -28 ppm, which agrees with that trigonal SAPO-34 only contains one fully-condensed P site. A very broad bump observed in the spectrum may result from a small amount of impurity that is powder XRD invisible.

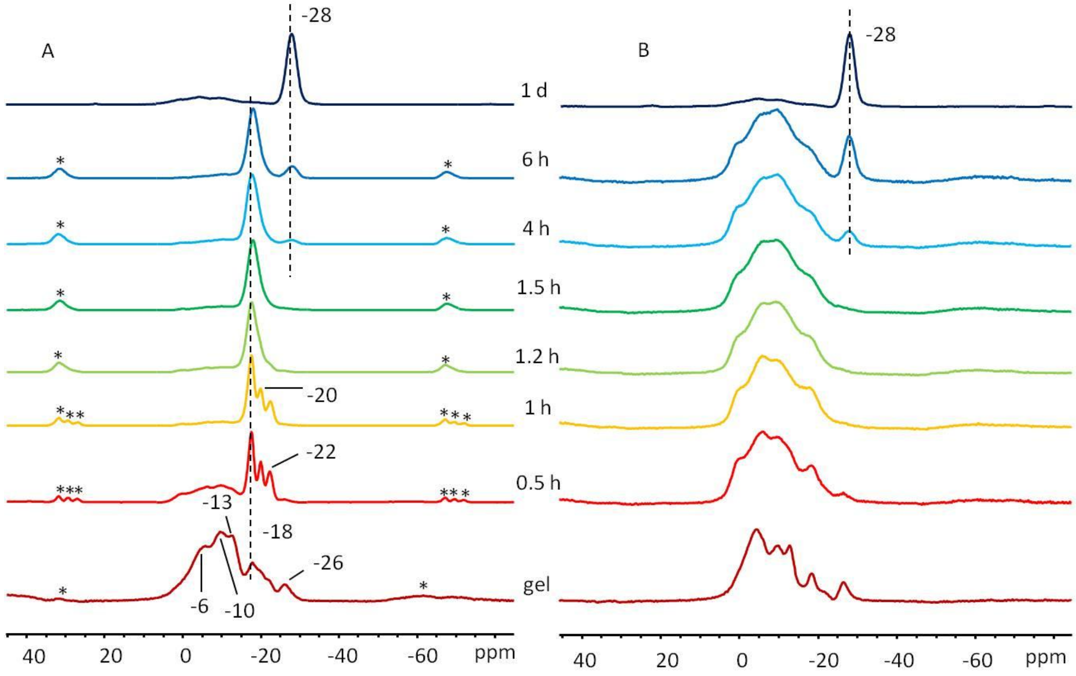

Figure 5.11 ^{31}P MAS spectra of (A) unwashed and (B) washed DGC without HF dry gel samples. Asterisks indicate spinning sidebands.

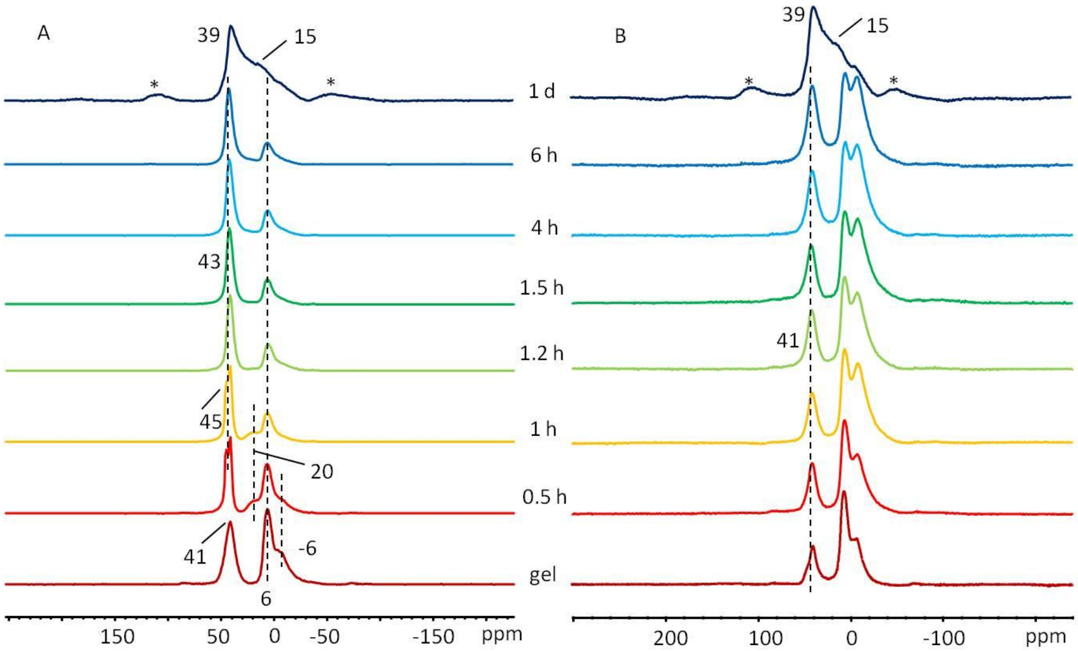

Figure 5.12 ^{27}Al MAS spectra of (A) unwashed and (B) washed DGC without HF dry gel samples. Asterisks indicate spinning sidebands.

The ^{27}Al spectrum (Figure 5.12A) of the unwashed initial dry gel shows two broad peaks at 41 and 6 ppm with the latter one containing a broad shoulder centered at around -6 ppm. The signal at 41 ppm falls in the range of 35-48 ppm and can be assigned to tetrahedral Al. The peak at 6 ppm is likely due to unreacted alumina.[29] The weak shoulder at -6 ppm can be attributed to 6-coordinated Al species.[69] Upon heating the dry gel for 0.5 h, two additional peaks at 45 and 20 ppm appeared with the signals at 41 and 6 ppm becoming shaper and weaker, respectively. Upon washing, both the new signals disappeared, demonstrating that they result from Al species in the crystalline layered phase. Further heating for 1.2 h or longer, the resonances due to the crystalline layered phase disappeared and the spectra did not change a lot with increasing the heating time. The spectrum of final product (1 d sample) shows a characteristic peak at 39 ppm, which is due to Al in tetrahedral environment of SAPO-34. However, the resonance line is quite unsymmetrical and broad, suggesting the interaction of Al with extraframework H_2O and/or the SDA molecules in the CHA cages.[2,69]

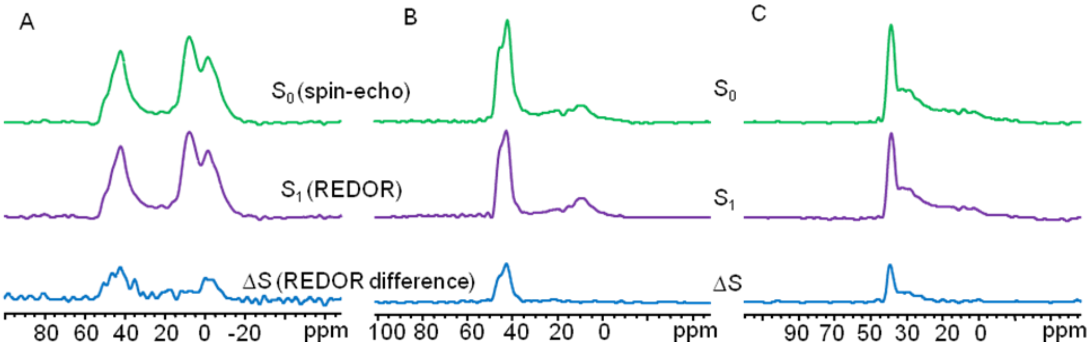

Figure 5.13 ^{27}Al{^{31}P} REDOR spectra of unwashed initial dry gel (A), 1 h (B), and 1 d (C) samples with a dephasing time of 0.75 ms.

To further characterize the nature of various Al peaks, ^{27}Al{^{31}P} REDOR experiments were carried out on selected samples (the initial gel, 1 h, and 1 d samples). For all three samples, the REDOR difference spectra only show tetrahedral and octahedral Al peaks (Figure 5.13). The signal at 6 ppm seen in the MAS spectra is absent in the REDOR difference spectra. These results unambiguously indicate that the peak is due to unreacted aluminum oxide with no P atoms in the secondary coordination sphere. To separate the overlapping peaks in the ^{27}Al MAS spectrum of 1 d sample, a ^{27}Al 3QMAS spectrum was obtained (Figure 5.5B), which exhibits four signals. The peak at 39 ppm is actually composed of two signals with isotropic chemical shift values of about 45 and 50 ppm. Based on literature, the peak at 45 ppm is assigned to the tetrahedral Al with a $Al(OP)_4$ environment and the peak at 50 ppm to the tetrahedral Al with Si in its secondary coordination sphere.[69] Further, isotropic chemical shifts of 15 and -5 ppm in the F1 dimension suggests the presence of unreacted alumina and octahedral Al in the final product.

The dry gel samples without HF heated for less than 1 h exhibit similar ^{29}Si MAS spectra to the initial dry gel with HF, containing two peaks with a strong one at -111 ppm (Figure 5.14A) and another one at -101 ppm in the corresponding CP spectra (Figure 5.14B). As discussed above, this indicates the AlPO nature of these samples. Heating the dry gel for 1 h, there appears a new signal at -85 ppm in the CP spectrum, which corresponds to $(AlO)_3SiOH$ or $(SiO)(AlO)Si(OH)_2$ in amorphous aluminosilicates.[70] This demonstrates that Si started to be incorporated into framework via the formation of aluminosilicate species, which is similar to the incorporation of Si under DGC with HF conditions. After 4 h of heating, two new resonance lines at -91 and -95ppm appeared. They can be assigned to $Si(OAl)_4$ and $Si(OAl)_3(OSi)_1$ species, respectively.[49] Their emergence suggests the formation of SAPO-34 phase, which coincides with the corresponding powder XRD pattern and ^{31}P MAS spectrum. The ^{29}Si MAS spectrum of the final product shows a strong and sharp signal at -91 ppm, a broad signal centered at around -111 ppm, and two weak ones at -95 and -100 ppm. This signifies that that Si is mainly in $Si(OAl)_4$ and $Si(OSi)_4$ environments. The average Si content (19 mol.%) and the (Si + P)/Al ratio (1.13) indicates that in addition to isolated $Si(OAl)_4$ species, certain amount of Si island is also present, which is consistent with the ^{29}Si peaks between -95 and -110 ppm. Both the EDX data and the ^{29}Si NMR results imply that Si is incorporated via a combination of SM II and III.

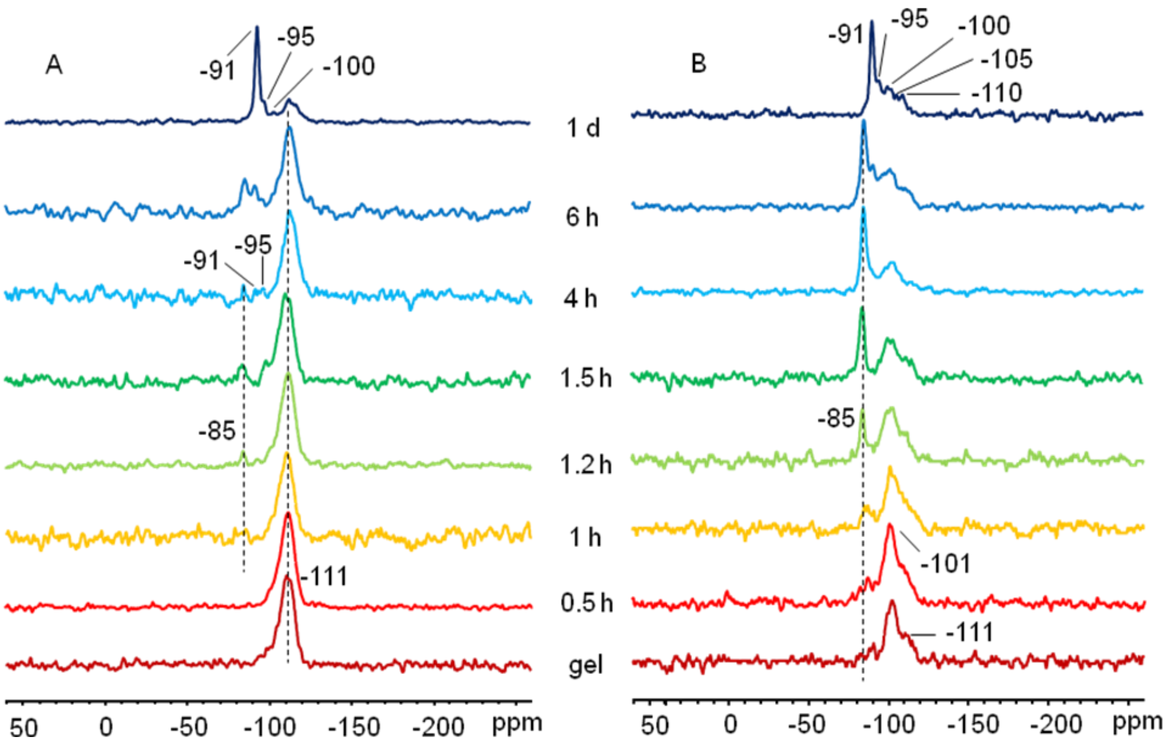

Figure 5.14 ^{29}Si MAS (A) and ^{1}H → ^{29}Si CP spectra of selected unwashed DGC without HF dry gel samples with a contact time of 0.5 ms (B).

In summary, upon mixing Si, Al, P, and morpholine, an amorphous material with certain degree of long-range ordering was formed under the heating treatment at 353 K. Upon heating under DGC without HF conditions, the amorphous material transformed into a crystalline layered phase. This crystalline phase is a transient phase during the formation of SAPO-34. Upon further heating treatment, it was converted into a semi-crystalline layered phase. Both the layered phases are mainly AlPO in nature with little Si. In the meantime, Si reacted with Al and aluminosilicate particles were formed, which are presumed to be dispersed between the AlPO layers. The final stage is that the semi-crystalline layered phase was cross-linked together, forming SAPO-34 framework. It is at this stage that Si atoms were incorporated into the framework.

5.3.3 Differences in Si species in final products

Under DGC with HF conditions, there are six Si species in as-synthesized SAPO-34 compared to two major $Si(OAl)_4$ and $Si(OSi)_4$ species under DGC without HF conditions. The initial DGC with HF dry gel is composed of the prephase of AlPO nature and the unreacted silica with $Si(OSi)_4$ environments,[71] which suggests that formation of SAPO-34 involves reactions between the prephase and the silica. As $Si(OAl)_n(OSi)_{4-n}$ species are formed by first breaking -Si-O-Si- linkages and then connecting -Si-OH and HO-Al- groups via condensation, water may have played an important role in promoting such process under DGC with HF conditions. To study the influence of water in Si dispersion in final product under DGC with HF conditions, different amount of water was put at the bottom of an autoclave, and the powder XRD patterns of these samples are shown in Figure 5.15. The results indicate that a minimum amount of 0.5 g water is needed for the synthesis of pure SAPO-34, and that some prephase will coexist with SAPO-34 if the water amount is below this value. The ^{29}Si MAS NMR spectrum (Figure 5.16) of the sample synthesized using 0.3 g of water shows an extremely broad peak at around -110 ppm. The broadness of this peak suggests that most silica has not reacted. When the water amount was increased to 0.5 g and 0.7 g, there appear more ^{29}Si signals with the chemical shift values between -90 and -105 ppm, and that the peak at -110 ppm becomes sharper. These results support the idea that the water occluded in the gel assists in reacting the prephase with the silica; if sufficient water is applied for DGC with HF synthesis, the ^{29}Si NMR spectrum of the final product is likely to be similar to that under HTS conditions,[29] containing less Si species.

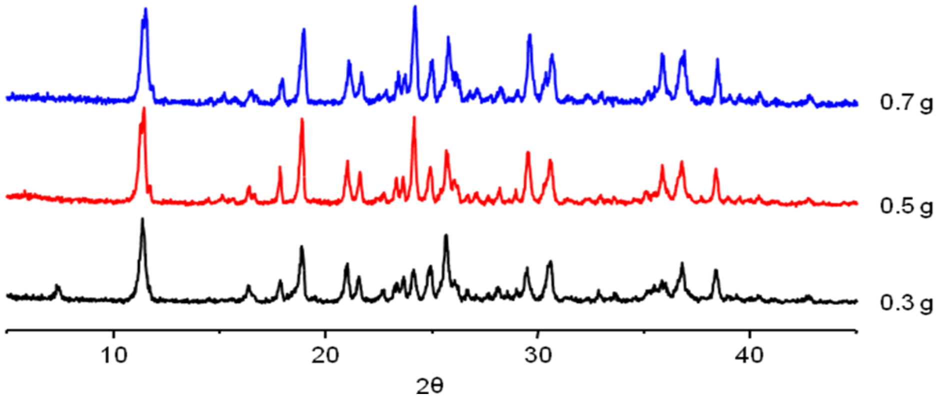

Figure 5.15 Powder XRD patterns of DGC with HF dry gel samples synthesized using different amount of water. For each sample, 1 g of the initial dry gel was used and the crystallization time was 7 d.

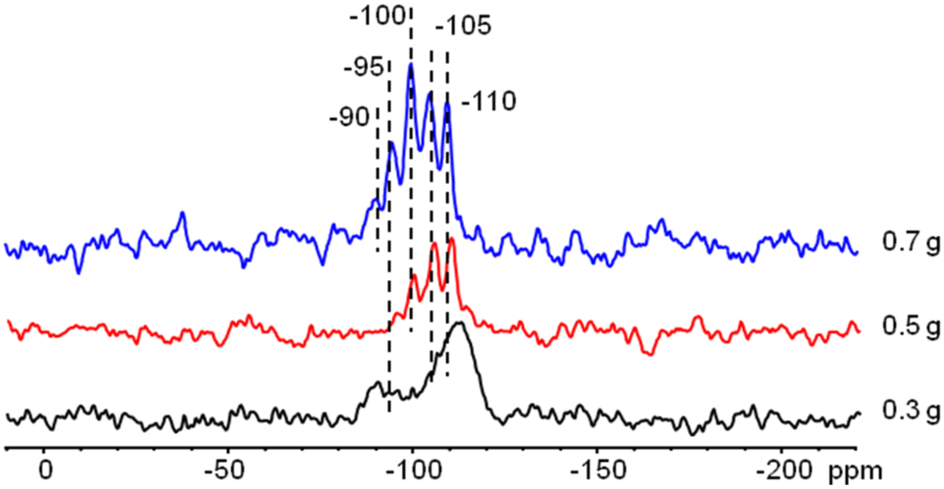

Figure 5.16 ^{29}Si MAS spectra of DGC with HF dry gel samples synthesized using different amount of water. For each sample, 1 g of the initial dry gel was used and the crystallization time was 7 d.

Further, under DGC with HF conditions, the triclinic phase competes with the trigonal phase to consume Si, Al, and P and the formation of a triclinic framework mainly depends on Al and P. Previous work has shown that in the presence of fluoride ions (F^- ions), triclinic $AlPO_4$-34 can be synthesized. F^- ions not only play a constructing role to covalently bond two Al atoms (Figure 5.1B), but also play a charge-balancing role to neutralize the two positive morpholinium molecules entrapped in each CHA cage. Upon calcination, trigonal $AlPO_4$-34 is formed. It is not stable and could easily transform back to triclinic phase upon hydration in air.[72] The stable product, which adopts trigonal symmetry of the CHA topology, is SAPO-34 or other metal-substituted APO_4-34 other than $AlPO_4$-34.[72] The consumption of Al by the triclinic phase causes less Al availability to trigonal phase, which results in various Si species in the trigonal SAPO-34 obtained under DGC with HF conditions. To confirm this, the molar ratio of Al to Si in the initial DGC with HF dry gel was increased to 2.4:1.0 while keeping other parameters constant. The PXRD pattern of the as-synthesized sample shown in Figure 5.17A indicates that it is pure SAPO-34. The corresponding ^{29}Si MAS NMR spectrum (Figure 5.17BI) shows more Si atoms with a chemical shift in the range of -90 to -104 ppm than the spectrum of the sample with an Al to Si molar ratio of 2.0:1.0 (Figure 5.17BII). These findings have undoubtedly substantiated the viewpoint that the triclinic phase competes with the trigonal phase to consume Al and P.

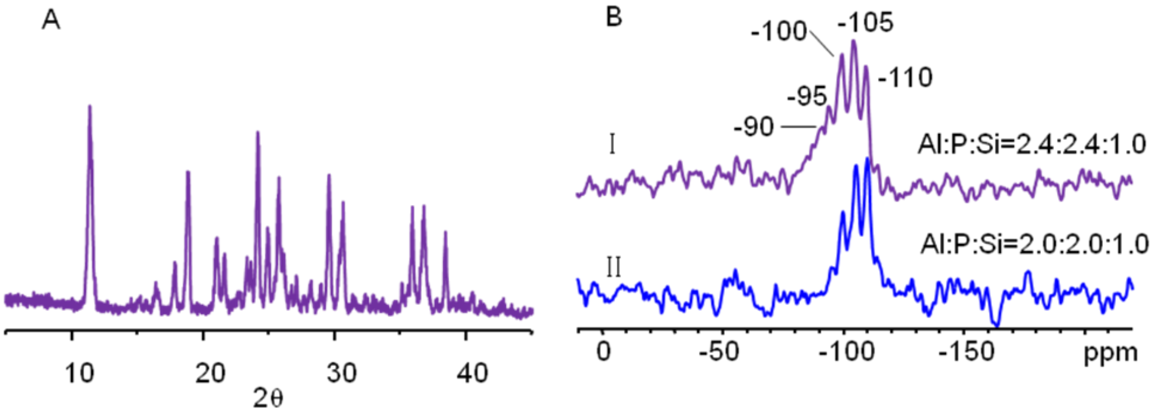

Figure 5.17 Powder XRD powder pattern (A) and ^{29}Si MAS spectrum (B Ⅰ) of DGC with HF gel sample (containing higher Al to Si ratio) with 0.5 g of water at the bottom. B Ⅱ shows the ^{29}Si MAS spectrum of a previous sample (Figure 5.16) with 0.5 g of water at the bottom for comparison.

5.3.4 MTO reactions

To check the influence of the Si distribution on the catalytic performances of SAPO-34 products, experiments on MTO reactions were performed. The DGC sample with/without HF was calcined first to remove the SDA molecules. The corresponding powder XRD patterns (Figure 5.18A) indicate that the two samples keep the high crystallinity upon calcination. The powder pattern of the calcined DGC sample with HF only presents reflections resulting from trigonal phase because triclinic phase was converted to trigonal phase due to loss of fluorine ions. Moreover, the ^{29}Si MAS NMR spectrum of the calcined DGC with HF sample presents at least four ^{29}Si signals and that of the calcined DGC sample without HF shows two ^{29}Si signals, which are similar to the ^{29}Si NMR spectra of the as-made counterparts. Further, the decreased intensity of the ^{29}Si peaks in the range of -94 to -105 ppm in the calcined DGC sample with HF and the peak at -90 ppm in the calcined DGC sample without HF can be attributed to dealumination resulting from the thermal treatments.[73]

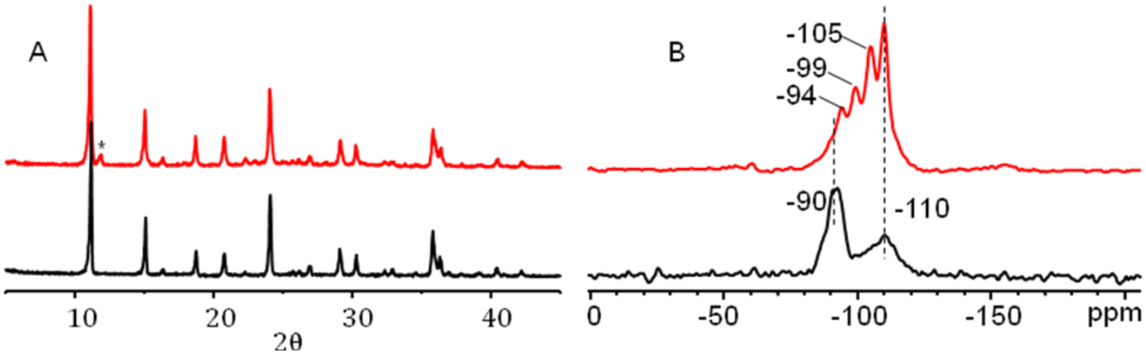

Figure 5.18 Powder XRD patterns (A) and ^{29}Si MAS NMR spectra (B) of calcined SAPO-34 samples: DGC with HF (top) and without HF (bottom). The two samples were calcined at 773 K.

Figure 5.19 illustrates the methanol conversion as a function of time-on-stream. The DGC sample with HF deactivated slower and has a longer lifetime than the DGC sample without HF. Figure 5.20 shows the selectivities towards different hydrocarbons. Below 50 min of time-on-stream, the yield of light olefins (C_2H_4 and C_3H_6) was apparently higher for the DGC sample without HF (Figure 5.20A), while during the same period the production of propane was higher on the DGC sample with HF (Figure 5.20B). The two samples show similar product selectivities after 50 min on stream.

As shown above, the calcined DGC sample with HF has various Si environments. Similar to the as-made sample, most of these Si species result from the Si islands, the formation of which introduces higher acid strength at the border. The lower ethylene and propylene selectivity and higher propane selectivity on the DGC sample with HF before 50 min of time-on-stream can thus be ascribed to its stronger acidity on the surface, which facilitated hydrogen transfer reaction of the light olefins to produce alkanes.[72] The

XRF results indicate that the bulk compositions of the two DGC samples show the same Si content, which is 0.19. Under the same calcination conditions, it is anticipated that the dealumination rate and degree in the two samples is similar. Therefore, the same bulk Si contents in the as-made samples imply that the two samples have similar acidity and acid amount,[22] which thus result in the similar light olefin and propane selectivity after 50 min on stream. The longer lifetime of the DGC sample with HF may result from its relatively smaller crystal size (around 5 μm) than the DGC sample without HF (around 12 μm).

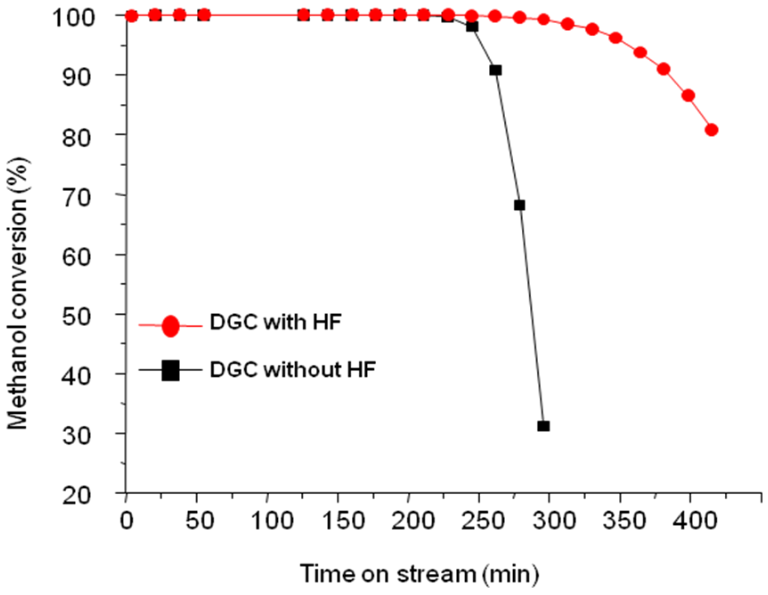

Figure 5.19 Methanol conversion vs. time-on-stream for DGC with and without HF samples.

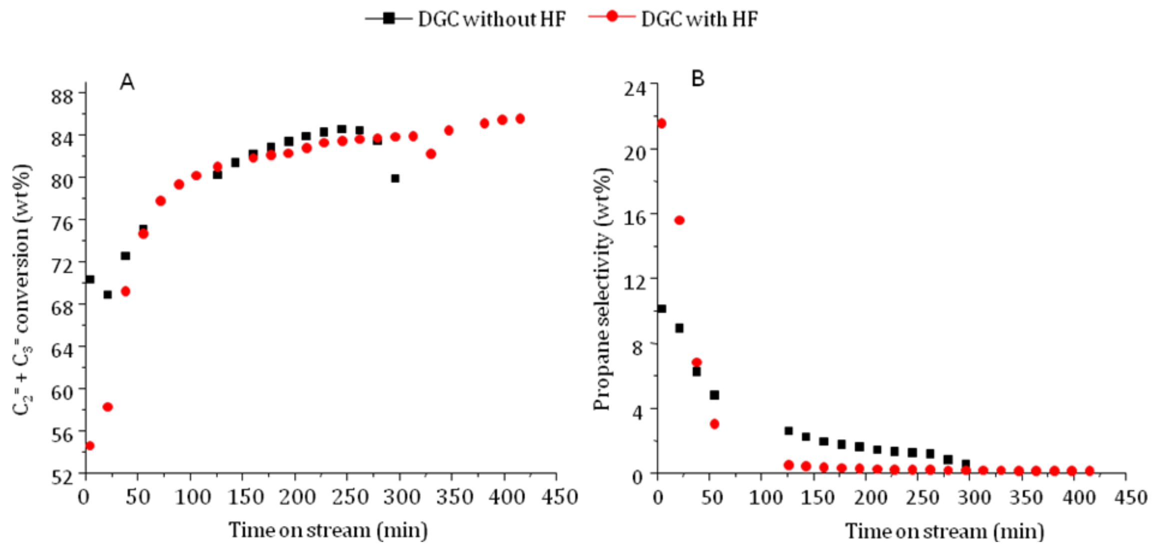

Figure 5.20 Light olefin and propane selectivities for DGC with and without HF samples.

5.4 Summary

The crystallization of SAPO-34 molecular sieve was examined under DGC conditions with and without HF by using powder XRD, EDX, and particularly solid-state NMR. Particular attention was paid to Si distribution in final products. The catalytic performance of SAPO-34 products was also tested.

The crystallization process by DGC with HF method is similar to that by HTS with HF method. It involves the transformation of a highly crystalline layered prephase to a mixture of triclinic and trigonal phases. Triclinic phase formed prior to trigonal phase. The structure of the prephase is held by covalent bonding, which is the reason why the crystallization time is much longer than that under HTS with HF conditions. The ^{29}Si NMR results suggest that silica reacted with alumina to form a more reactive aluminosilicate species before it was incorporated into framework via SM II and III. In the final product, there are six different Si species. The majority of them belong to the trigonal phase and more specifically, are in AS domains in the trigonal phase. Different from previously reported two main Si species in the product obtained under HTS with HF conditions, the formation of various Si species in the product under DGC with HF conditions is probably due to that the amount of external water is very small (0.7 g of water for 1.0 g of dry gel).

Using the DGC method without HF, the crystallization involves three transformation stages. The structures of intermediate crystalline and semi-crystalline layered phases are held by weak nonbonding interactions, which facilitate their transformation into trigonal SAPO-34. Therefore, the reaction time needed to obtain pure trigonal phase is not long. These intermediate phases are mainly AlPO in nature. The ^{29}Si NMR results indicate that Si was incorporated in a similar way to that under DGC with HF conditions, by forming aluminosilicate. Similar to DGC with HF, a combination of SM II and III occurred.

The MTO reaction test results show the DGC sample with HF possessed longer lifetime than the DGC sample without HF and similar light olefin selectivity to the latter one after 50 min of time-on-stream. Its relatively smaller crystal size and the same bulk Si content may account for this.

5.5 References

(1) Martucci, A.; Alberti, A.; Cruciani, G.; Frache, A.; Coluccia, S.; Marchese, L. *J. Phys. Chem. B* **2003**, *107*, 9655-9661.
(2) Prakash, A. M.; Unnikrirhnan, S. *J. Chem. Soc. Faraday Trans.* **1994**, *90*, 2291-2296.
(3) Chen, J.; Thomas, J. M. *Catal. Lett.* **1991**, *11*, 199-207.
(4) Li, S.; Falconer, J. L.; Noble, R. D. *Microporous Mesoporous Mater.* **2008**, *110*, 310-317.
(5) Carreon, M. A.; Li, S.; Falconer, J. L.; Noble, R. D. *J. Am. Chem. Soc.* **2008**, *130*, 5412-5413.

(6) Hong, M.; Li, S.; Falconer, J. L.; Noble, R. D. *J. Membr. Sci.* **2008**, *307*, 277-283.
(7) Hong, M.; Li, S.; Funke, H. F.; Falconer, J. L.; Noble, R. D. *Microporous Mesoprous Mater.* **2007**, *106*, 140-146.
(8) Jee, S. E.; Sholl, D. S. *J. Am. Chem. Soc.* **2009**, *131*, 7896-7904.
(9) Li, S.; Falconer, J. L.; Noble, R. D. *Adv. Mater.* **2006**, *18*, 2601-2603.
(10) Li, S.; Falconer, J. L.; Noble, R. D. *J. Membr. Sci.* **2004**, *241*, 121-135.
(11) Li, S.; Carreon, M. A.; Zhang, Y.; Funke, H. H.; Noble, R. D.; Falconer, J. L. *J. Membr. Sci.* **2010**, *352*, 7-13.
(12) Hudiono, Y. C.; Carlisle, T. K.; LaFrate, A. L.; Gin, D. L.; Noble, R. D. *J. Membr. Sci.* **2011**, *370*, 141-148.
(13) Lin, S.; Li, J.; Sharma, R. P.; Yu, J.; Xu, R. *Top. Catal.* **2010**, *53*, 1304-1310.
(14) Chew, T.; Ahmad, A.; Bhatia, S. *J. Porous Mater.* **2010**, *17*, 1-6.
(15) Schnabel, K. H.; Fricke, R.; Girnus, I.; Jahn, E.; Löffler, E.; Parlitz B.; Peuker, C. *J. Chem. Soc. Faraday Trans.* **1991**, *87*, 3569-3574.
(16) Ashtekar, S.; Satyanarayana, C. V. V.; Chakrabarty, D. K. *Proc. Indian Acad. Sci.* **1994**, *106*, 621-628.
(17) Hendrik van Heyden, S. M.; Bein, T. *Chem. Mater.* **2008**, *20*, 2956–2963.
(18) Mertens, M. M.; Engels, B. US Patent 6,685,905, 2004.
(19) Lok, B. M.; Messina, C. A.; Patton, R. L.; Gajek, R. T.; Cannan, T. R.; Flanigen, E. M. US Patent 4,440,871, 1984.
(20) Zhou, H.; Wang, Y.; Wei, F.; Wang, D.; Wang, Z. *Appl. Catal., A* **2008**, *341*, 112–118.
(21) Xu, Y.; Maddox, P. J.; Couves, J. W. *J. Chem. Soc. Faraday Trans.* **1990**, *86*, 425-429.
(22) Liu, G.; Tian, P.; Li, J.; Zhang, D.; Zhou, F.; Liu, Z. *Microporous Mesoporous Mater.* **2008**, *111*, 143-149.
(23) Tian, P.; Su, X.; Wang, Y.; Xia, Q.; Zhang, Y.; Fan, D.; Meng, S.; Liu, Z. *Chem. Mater.* **2011**, *23*, 1406-1413.
(24) Dumitriu, E.; Azzouz, A.; Vasile Hulea a, D. L.; Kessler, H. *Microporous Mater.* **1997**, *10*, 1-12.
(25) Vistad, Ø. B.; Akporiaye, D. E.; Lillerud, K. P. *J. Phys. Chem. B* **2001**, *105*, 12437-12447.
(26) Vistad, Ø. B.; Akporiaye, D. E.; Taulelle, F.; Lillerud, K. P. *Chem. Mater.* **2003**, *15*, 1639-1649.
(27) Harding, M. M.; Kariuki, B. M. *Acta Crystallogr. C* **1994**, *50*, 852-854.
(28) Vistad, Ø. B.; Hansen, E. W.; Akporiaye, D. E.; Lillerud, K. P. *J. Phys. Chem. A* **1999**, *103*, 2540-2552.
(29) Yan, Z.; Chen, B.; Huang, Y. *Solid State Nucl. Magn. Reson.* **2009**, *35*, 49-60.
(30) Li, N.; Wu, J.; Zhao, H.; Luo, Q.; He, C.; Guan, N.; Xiang, S. *Cryst. Eng. Comm.* **2012**, *14*, 8671-8676.
(31) Liu, G.; Tian, P.; Zhang, Y.; Li, J.; Xu, L.; Meng, S.; Liu, Z. *Microporous Mesoporous Mater.* **2008**, *114*, 416-423.
(32) Ito, M.; Shimoyama, Y.; Saito, Y.; Tsurita, Y.; Otake, M. *Acta Crystallogr. C* **1985**, *41*, 1698-700.
(33) Harding, M. M.; Kariuki, B. M. *Acta Crystallogr. C* **1994**, *50*, 852-854.
(34) Chen, B.; Huang, Y. *J. Phys. Chem. C* **2007**, *111*, 15236-15243.

(35) Xu, W.; Dong, J.; Li, J.; Li, J.; Wu, F. *J. Chem. Soc., Chem. Commun.* **1990**, 755-6.
(36) Matsukata, M.; Ogura, M.; Osaki, T.; Hari Prasad Rao, P. R.; Nomura, M.; Kikuchi, E. *Top. Catal.* **1999**, *9*, 77-92.
(37) Hari Prasad Rao, P.; Ueyama, K.; Matsukata, M. *Appl. Catal., A* **1998**, *166*, 97-103.
(38) Matsukata, M.; Osaki, T.; Ogura, M.; Kikuchi, E. *Microporous Mesoporous Mater.* **2002**, *56*, 1-10.
(39) Chen, B.; Huang, Y. *J. Am. Chem. Soc.* **2006**, *128*, 6437-6446.
(40) Chen, B.; Kirby, C. W.; Huang, Y. *J. Phys. Chem. C* **2009**, *113*, 15868-15876.
(41) Chen, B.; Huang, Y. *Microporous Mesoporous Mater.* **2011**. *143*, 14-21.
(42) Zhang, L.; Bates, J.; Chen, D.; Nie, H. Y.; Huang, Y. *J. Phys. Chem. C* **2011**, *119*, 22309-22319.
(43) Chen, B.; Huang, Y. *Microporous Mesoporous Mater.* **2009**, *123*, 71-77.
(44) Bandyopadhyay, R.; Kubota, Y.; Sugimoto, N.; Fukushima, Y.; Sugi, Y. *Microporous Mesoporous Mater.* **1999**, *32*, 81-91.
(45) Huang, Y.; Richer, R.; Kirby, C. W. *J. Phys. Chem. B* **2003**, *107*, 1326-1337.
(46) Gullion, T.; Schaefer, J. *J. Magn. Reson.* **1989**, *81*, 196-200.
(47) Fyfe, C. A.; Lewis, A. R.; Chezeau, J. M.; Grondey, H. *J. Am. Chem. Soc.* **1997**, *119*, 12210-12222.
(48) Amoureux, J.; Fernandez, C.; Steuernagel, S. *J. Magn. Reson., Ser. A* **1996**, *123*, 116-118.
(49) Prakash, A. M.; Unnikrishnan, S. *J. Chem. Soc. Faraday Trans.* **1994**, *90*, 2291-2296.
(50) Chuang, I. S.; Kinney, D. R.; Maciel, G. E. *J. Am. Chem. Soc.* **1993**, *115*, 8695-705.
(51) Doremieux-Morin, C.; Martin, C.; Bregeault, J. M.; Fraissard, J. *Appl. Catal.* **1991**, *77*, 149-61.
(52) Appleyard, I. P.; Harris, R. K.; Fitch, F. R. *Chem. Lett.* **1985**, 1747-50.
(53) Sastre, G.; Lewis, D. W.; Richard, C.; Catlow, A. *J. Phys. Chem. B* **1997**, *101*, 5249-5262.
(54) Sanchez del Campo, A. E.; Gayubo, A. G.; Aguayo, A. T.; Tarrio, A.; Bilbao, J. *Ind. Eng. Chem. Res.* **1998**, *37*, 2336-2340.
(55) Izadbakhsh, A.; Farhadi, F.; Khorasheh, F.; Sahebdelfar, S.; Asadi, M.; Feng, Y. Z. *Appl. Catal., A* **2009**, *364*, 48-56.
(56) Vomscheid, R.; Briend, M.; Peltre, M. J.; Man, P. P.; Barthomeuf, D. *J. Phys. Chem.* **1994**, *98*, 9614-18.
(57) Diaz-Cabanas, M.-J.; Barrett, P. A. *Chem. Commun.* **1998**, 1881-1882.
(58) Strohmaier, K. G.; Reyes, S. C.; Levin, D. US Patent 7,435,863,B2, 2008.
(59) Parlitz, B.; Lohse, U.; Schreier, E. *Microporous Mater.* **1994**, *2*, 223-228.
(60) Ejaz, T.; Jones, A. G.; Graham, P. *J. Chem. Eng. Data* **1999**, *44*, 574-576.
(61) Addai-Mensah, J.; Li, J.; Rosencrance, S.; Wilmarth, W. *J. Chem. Eng. Data* **2004**, *49*, 1682-1687.
(62) Gasteiger, H. A.; Frederick, W. J.; Streisel, R. C. *Ind. Eng. Chem. Res.* **1992**, *31*, 1183-1190.
(63) Akporiaye, D. E.; Dahl, I. M.; Mostad, H. B.; Wendelbo, R. *J. Phys. Chem.* **1996**, *100*, 4148-53.
(64) Prakash, A. M.; Unnikrishnan, S.; Rao, K. V. *Appl. Catal., A* **1994**, *110*, 1-10.
(65) Lohse, U.; Parlitz, B.; Altrichter, B.; Jancke, K.; Löuffler, E.; Schreier, E.; Vogt, F.

J. Chem. Soc., Faraday Trans. **1995**, *91*, 1155-1161.
(66) Martens, J. A.; Grobet, P. J.; Jacobs, P. A. *J. Catal.* **1990**, *126*, 299-305.
(67) Lobo, R. F.; Annen, M. J.; Davis, M. E. *J. Chem. Soc., Faraday Trans.* **1992**, *88*, 2791-5.
(68) Huang, Y.; Yan, Z. *J. Am. Chem. Soc.* **2005**, *127*, 2731-2740.
(69) Yan, Z.; Zhuang, J.; Lei, X.; Han, X.; Liu, Z.; Bao, X. *Chin. Chem. Lett.* **2003**, *14*, 87-90.
(70) Doremieux-Morin, C.; Martin, C.; Bregeault, J. M.; Fraissard, J. *Appl. Catal.* **1991**, *77*, 149-61.
(71) Zhuravlev, L. *Colloids Surf., A* **2000**, *173*, 1-38.
(72) Tuel, A.; Caldarelli, S.; Meden, A.; McCusker, L. B.; Baerlocher, C.; Ristic, A.; Rajic, N.; Mali, G.; Kaucic, V. *J. Phys. Chem. B* **2000**, *104*, 5697-5705.
(73) Van Donk, S.; Janssen, A. H.; Bitter, J. H.; de Jong, K. P. *Catal. Rev.* **2003**, *45*, 297-319.
(74) Álvaro-Muñoz, T.; Márquez-Álvarez, C.; Sastre, E. *Catal. Today*, **2012**, *179*, 27-34.

Chapter 6 A Study of the Formation of Microporous Material SAPO-37

6.1 Introduction

Since the first report by Lok *et al.* in 1984,[1] silicoaluminophosphate molecular sieves (SAPO-*n*) have received much attention due to that they have been widely used in industry for separation and catalysis. These microporous solids not only exhibit properties characteristic of zeolites and aluminophosphate ($AlPO_4$-*n*) based molecular sieves, but also present physicochemical traits unique to their chemical compositions.[2,3]

SAPO-based molecular sieves consist of tetrahedral oxide (TO_4) frameworks (T = Si, P, and Al) and can be viewed as silicon atoms being incorporated into an $AlPO_4$-*n* framework.[2] Flanigen and co-workers[4] proposed three Si substitution mechanisms: (1) Si incorporated into an Al site (SM I), (2) Si incorporated into a P site (SM II), and (3) two Si atoms for an Al-P pair (SM III). Lok *et al.*[5] and Flanigen *et al.*[4] further suggested that silicon mainly substitutes via the SM II and SM III. This argument was confirmed later by lattice simulations,[6] which showed that Si islands with only Si-O-Al and Si-O-Si bridges formed by a combination of SM II and III are energetically favorable and that at lower concentrations, the substituted Si is dispersed.

SAPO-37 has faujasite framework (FAU topology, Scheme 6.1),[3,7-9] and attracted much attention due to its catalytic performances.[10-12] Like most molecular sieves, SAPO-

---

* A version of this chapter has been published: Zhang, L.; Chen, D.; Nie, H. Y.; Huang, Y. *Microporous Mesoporous Mater.* **2013**, *175*, 147-156.

37 is usually prepared by hydrothermal synthesis method (HTS) from an aqueous hydrogel prepared by mixing phosphoric acid, alumina, fumed silica, as well as structure-directing agents (SDAs). Several studies on the structure, synthesis conditions, and thermal stability of SAPO-37 were reported, but relatively few dealt with details of the crystallization process.[3,7,13-23] Thus, the formation of SAPO-37 is still not well understood at a molecular level.

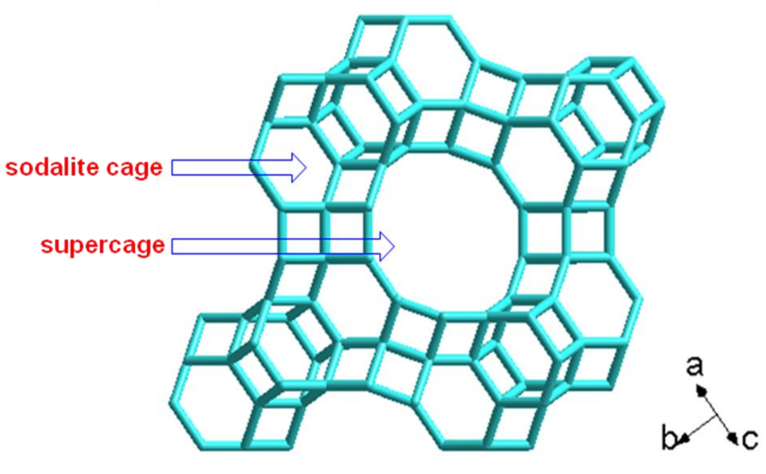

Scheme 6.1 Framework of SAPO-37.

A different synthetic approach, namely dry-gel conversion (DGC), was introduced years ago as an alternative method to HTS.[24-29] This method involves conversion of pre-dried gel powder to a crystalline microporous material at elevated temperature and autogenous pressure (Scheme 6.2). Unlike hydrothermal synthesis, DGC has several advantages for examining crystallization owing to its simpler reaction system where all the reactive species are confined in the solid phase.[30] However, the lack of the apparent liquid phase may result in limited mass transport, and therefore lower crystal growth rates. As such, the intermediates may be captured under the favourable circumstances. Since the dry-gel powder contains about 40% water, it is widely recognized that the information obtained under DGC conditions does provide insight into crystallization under HTS conditions.[30]

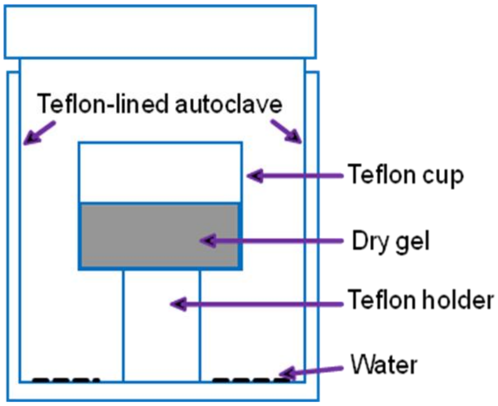

Scheme 6.2 Diagram of the reaction vessel used for DGC method.

In this paper, our work on the formation of SAPO-37 under both HTS and DGC conditions is presented. A mixture of tetramethylammonium (TMA) and tetrapropylammonium (TPA) hydroxides was used as the structure-directing agents (SDAs). Si incorporation was also studied. The local environments of P, Al, Si, and SDA molecules in various solid intermediate phases formed during the synthesis were probed by ^{31}P, ^{27}Al, ^{29}Si, and ^{13}C magic-angle spinning (MAS) NMR. The ^{27}Al{^{31}P} and ^{31}P{^{27}Al} rotational-echo double-resonance (REDOR) were also used to detect the Al-O-P connectivity in the gel wherever needed. The evolution of the long-range ordering within intermediates was monitored by powder X-ray diffraction (PXRD). Scanning electron microscopy (SEM) was utilized to observe the morphological changes. Further, the nucleation and crystal growth were examined by atomic force microscopy (AFM). The combination of these techniques provides new physical insights into the formation of SAPO-37.

6.3 Experimental

6.2.1 Sample preparation

The silicon, aluminum, and phosphorous sources were fumed silica Aerosil® 300 (Degussa), pseudo-boehmite (Catapal-B, Vista, ca. 65% Al_2O_3), and H_3PO_4 (EM Science, 85%). A mixture of tetramethylammonium hydroxide pentahydrate ($TMAOH \cdot 5H_2O$, Sigma-Aldirch) and tetrapropylammonium hydroxide (TPAOH, Alfa Aesar, 40% in water) was used as the SDAs. The initial gel molar composition (TPA_2O:TMA_2O:Al_2O_3:P_2O_5:SiO_2:H_2O) was 1.0:0.025:1.0:1.0:0.4:50 in a molar ratio.[3] The reaction mixture was prepared according to the work reported by Davis group.[2] Under HTS conditions, the mixture was put into several autoclaves and the crystallization was then carried out at 443 K. The autoclaves were quenched after specified lengths of time in cold water and the liquid phase in each autoclave was separated from the solid phase by centrifugation. The solid intermediates were carefully dried in air at room temperature and kept in tightly sealed glass vials once dried for further analysis. Under DGC conditions, the same reaction mixture was dried at 353 K with constant stirring until water was evaporated and solids formed. The solid dry gel was then ground into a fine powder and sealed in glass vials. It is hereafter referred to as the initial DGC dry gel. A series of intermediates were synthesized by placing 1.0 g of the initial DGC dry gel powder into small Teflon cups. Each cup was placed in a 23-mL Teflon-lined autoclave with 0.3 g distilled water at the bottom, and the autoclaves were heated in an oven at 473 K for different times. The reactions were quenched in cold water. For comparison, the solid sample from each cup was divided into two parts. One part was directly dried in air (unwashed sample) and the other part was first washed by stirring it with a small amount of water in a beaker and then dried in the same beaker in air without isolation from the liquid phase (washed sample). This ensured that no solid particles could be washed away. The solid gel samples were kept in tightly sealed glass vials.

6.2.2 Characterization

PXRD patterns were recorded on a Rigaku diffractometer using Co K_α radiation (λ = 1.7902 Å). A LEO 1540XB Field Emission Scanning Electron Microscope equipped with an energy-dispersive X-ray spectrometer was used for recording SEM images and elemental analysis. Representative samples were first coated with 3 nm osmium metal using a Filgen OPC-80T instrument.

All the NMR experiments were carried out on a Varian/Chemagnetics Infinityplus 400 WB spectrometer equipped with three rf channels operating at the field strength of 9.4 T. The Larmor frequencies of ^{1}H, ^{13}C, ^{31}P, ^{27}Al, and ^{29}Si were 399.5, 100.4, 161.7, 104.1, and 79.4 MHz, respectively. The magic angle was set using the ^{79}Br resonance of KBr. The chemical shifts of ^{13}C, ^{31}P, ^{27}Al, and ^{29}Si were referenced to adamantane, $NH_4H_2PO_4$, 1M $Al(NO_3)_3$, and tetrakis(trimethylsilyl)-silane (TTMSS). Depending on the requirements of the individual experiment, we used three NMR probes (Varian/Chemagnetics 7.5 mm, 4.0 mm H/X/Y triple-tuned T3 MAS probe, and 5.0 mm H/F/X/Y triple-tuned MAS probe). The ^{13}C cross-polarization MAS (CP MAS) spectra were recorded by using the 5.0 mm probe with the Hartmann-Hahn conditions being optimized on adamantane. The ^{1}H 90° pulse length was 4 μs. A contact time of 2 ms was used and the pulse delay was 9 s. The proton-decoupling field was about 60 kHz. For ^{31}P MAS experiments, a 30° pulse was typically used and the recycle delay was 60 s. The ^{27}Al spectra were acquired using a very small pulse angle with a pulse delay of 1 s. For the ^{29}Si MAS experiments, a 45° pulse was used with a pulse delay of 60 s. For ^{1}H to ^{29}Si CP experiments, the ^{1}H 90° pulse length was 5 μs and the Hartmann-Hahn condition was determined using TTMSS. The rotational-echo double-resonance (REDOR) technique is a rotor-synchronized technique involving two separate experiments.[31] The first one is a normal spin-echo (S_0) on observed spin. The second (REDOR) experiment is also a spin-echo (S), but during the echo, a series of π-pulses are applied to the dephasing spin, which prevent the dipolar coupling from being refocused at the end of each rotor cycle. The REDOR difference spectrum ($\Delta S = S_0 - S$) indicates the dipolar interaction. $^{31}P\{^{27}Al\}$ and $^{27}Al\{^{31}P\}$ REDOR experiments were performed using the standard REDOR the pulse sequence described in literature.[31] A 5.0 mm probe with a spinning speed of 8 kHz was used.

Surface structures of our SAPO-37 samples were studied with a Park Systems XE-100 AFM operated in the dynamic force mode using a cantilever with nominal spring constant of 40 N/m, resonant frequency of 300 kHz, and tip radius of 10 nm (NSC15, Mikro Masch). In this mode, the cantilever is vibrated at around the resonant frequency and its amplitude reduces when the tip is in proximity with the sample surface caused by the tip - sample interaction. Reduced amplitude is set as the feedback parameter (set point) so that the AFM system scans the surface contour of the sample with minimized error signals (the difference between the set point and the amplitude measured) by adjusting the distance between the tip and the sample surface. Mapping of this distance constructs topographic image for the surface morphology. On the other hand, mapping the error signal results in an image removing the height contribution and stressing only the shape of surface features. When the height range is large, surface features with small height differences are obscured in a topographic image. In this case, it is advantageous to use the error signal image to show the shapes of surface features, while using the topographic image to estimate the height distribution. The scan rate for obtaining images in an area of 45×45 μm^2 is 0.5 Hz and for images in an area of 10×10 μm^2 is 1 Hz. The experiment was conducted in air with a relative humidity of ~40%.

6.3 Results and discussion

6.3.1 HTS method

To follow the development of the long-range ordering of the intermediate phases, the PXRD patterns of gel samples were recorded as a function of crystallization time (Figure 6.1). The pattern of the initial gel without heating and that of the gel samples heated below 16.5 h exhibit the patterns similar to that of the Al source, pseudo-boehmite (not shown), indicating that the solid phases are X-ray amorphous and that most of the Al source has not yet reacted. Sharp diffraction peaks matching the pattern for SAPO-37 started to appear after heating the gel for 19 h and their intensities increase with the heating time. The PXRD patterns of the samples heated for 2 d or longer show only the reflections due to SAPO-37.

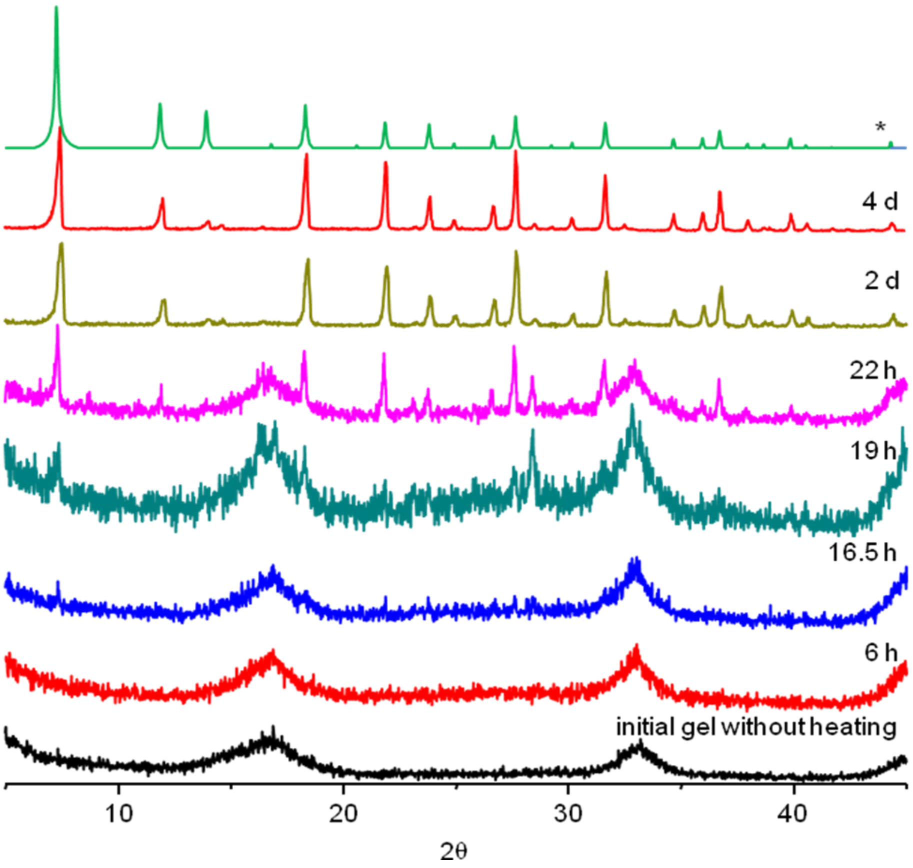

Figure 6.1 Powder XRD patterns of the HTS samples. * is simulated XRD data of SAPO-37.[9]

Figure 6.2 shows the SEM images of the selected HTS samples. Figure 6.2A shows that for 22 h sample (Figure 6.2A), the amorphous materials and SAPO-37 single crystals with typical octahedral morphology coexist, which is consistent with the corresponding PXRD pattern (Figure 6.1) showing that the sample is a mixture of an amorphous phase and SAPO-37. Also visible are several spherical particles. There spherical particles are immediate precursor to SAPO-37, from which SAPO-37 crystallites develop. One such spherical particle labeled with a circle clearly exhibits an emerging (111) face. The 4 d sample is pure SAPO-37. Its SEM image (Figure 6.2B) shows intergrown octahedra with (111) faces clearly visible.

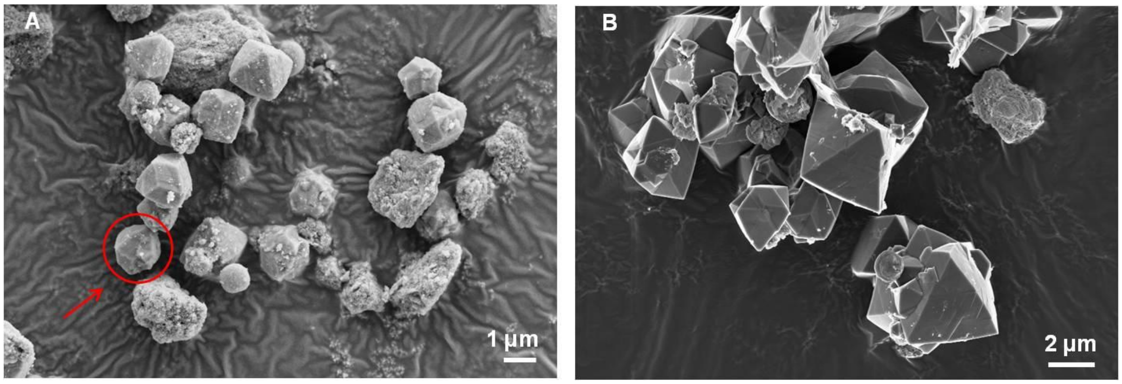

Figure 6.2 SEM images of selected HTS samples. (A) 22 h and (B) 4 d.

The development of the local chemical environments of P and Al atoms in the gel phases as a function of crystallization time under HTS conditions is monitored by ^{31}P and ^{27}Al MAS NMR. In the ^{31}P MAS spectrum of the initial gel without heating (Figure 6.3A), there is a very broad peak centered at around -12 ppm. The broadness of the peak indicates a wide distribution of P environment and the existence of many P containing species, which is consistent with the amorphous nature of the sample. These species are likely due to not fully condensed P sites with $P(OAl)_x(OH)_{4-x}$ or $(O)P(OAl)_x(OH)_{3-x}$ (x = 1-3) environments in the amorphous AlPO materials.[32] After heating the initial gel for 16.5 h, a new peak emerged at -26 ppm in the ^{31}P MAS spectrum. The chemical shift of this new peak is almost identical to the $P(OAl)_4$ environment in pure SAPO-37.[33] It seems that although the sample is still X-ray amorphous, the local $P(OAl)_4$ environment similar to that of SAPO-37 has begun to form. The intensity of this peak increases with increasing the crystallization time at the expenses of the broad amorphous peak and eventually become a single sharp peak at -26 ppm, indicating that the amorphous materials have transformed into SAPO-37. A weak signal at -35 ppm in the 19 h sample is likely due to $AlPO_4$-20 impurity since it can also be synthesized by using a mixture of TPA^+ and TMA^+ as co-templates.[34]

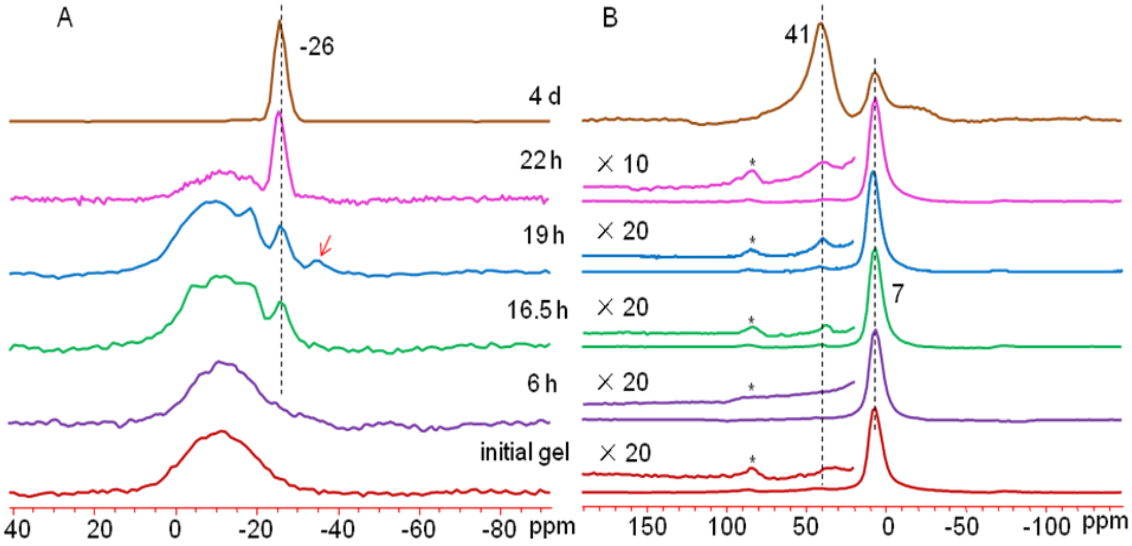

Figure 6.3 (A) ^{31}P MAS and (B) ^{27}Al MAS spectra of selected HTS samples. Asterisks indicate spinning sidebands. The peak labeled with an arrow is due to AlPO-20 impurity.

The ^{27}Al MAS spectrum of the initial gel without heating (Figure 6.3B) shows a strong signal at 7 ppm and an extremely weak one at 41 ppm. The peak at 41 ppm falls within the reported range of 35-48 ppm for tetrahedral Al environment, $Al(OP)_4$, in the AlPO-based phase.[34-37] The resonance at 7 ppm results from the unreacted alumina (pseudo-boehmite) which also displays a peak at the same position.[39] The observed spectrum is consistent with those reported in the literature.[22,23]

^{13}C CP MAS NMR technique is an effective tool to probe the tetraalkylammonium ions trapped in a microporous structure.[39] Figure 6.4A shows the ^{13}C CP MAS NMR spectra of selected HTS samples. In the initial gel without heating, there are four signals. According to the literature, all of them belong to TPA^+ cations.[2,17]

The signals at 61 and 16 ppm are assigned to the C_1- and C_2-methylene. The two peaks at 10 and 11 ppm originate from the methyl groups of the TPA^+ cations. The fact that the C_3-methyl group exhibits two signals in the initial gel indicates that the TPA^+ cations exist in different environments. A previous work found that the chemical shifts of TMA^+ cations adsorbed on the outer surface of SAPO framework and trapped inside sodalite (SOD) cage are 56 and 58 ppm, respectively.[40] Interestingly, none of these peaks was observed, suggesting that the TMA^+ cations are not present in the initial gel. Ito and co-workers[22,23] previously studied the crystallization of SAPO-37 by using ^{129}Xe NMR and reported that the initial gel and the sample heated for 5 h at 473 K already contain species having large cavities with 25 Å in diameter corresponding to the space of two supercages (the diameter of a supercage is 13 Å, see Scheme 6.3A for illustrations). They also pointed out that the connection between these species having large cavities is small and the arrangement of these species in solids is disordered. Since similar HTS synthesis conditions are used in the present case, the initial gel may also contain these large pore species. This is supported by the observation of a signal at 11 ppm, which is known to be the methyl of the TPA^+ trapped inside the supercage.[2] The peak at 10 ppm is assigned to the TPA^+ adsorbed outside the large cavities.[2] The lack of ^{13}C signals due to TMA^+ indicates that no significant amount of sodalite cage has been developed.

Heating the initial gel for 16.5 h led to the appearance of a new peak as a weak shoulder at 58 ppm. As mentioned earlier, the chemical shift corresponds to the TMA^+ trapped inside the sodalite cage. It seems that the sodalite cages start to form in the gel, presumably associated with the large pore species (Scheme 6.3A).[2] In the final product of SAPO-37, the ^{13}C peak assigned to the trapped TMA^+ becomes sharper, and the signals due to the TPA^+ are relatively broader, which suggests that the TMA^+ cations in the sodalite cages have higher mobility than the TPA^+ cations in supercages.

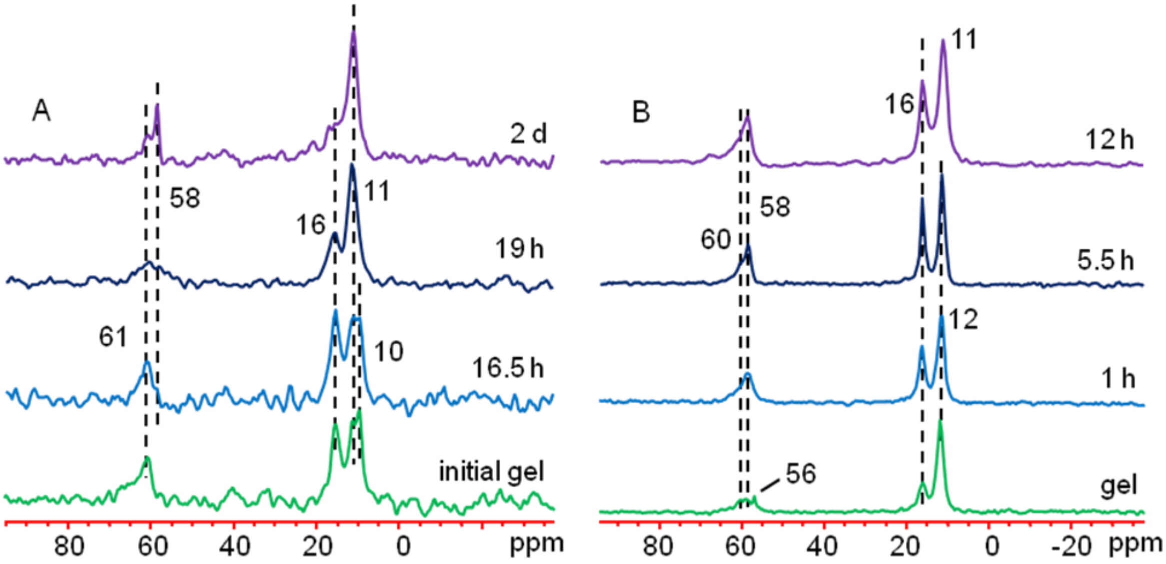

Figure 6.4 ^{13}C CPMAS spectra of selected HTS samples (A) and SAC gel samples (B) with a contact time of 2 ms.

To examine the incorporation of the silicon atom into the framework under HTS conditions, ^{29}Si MAS NMR experiments were carried out (Figure 6.5). Unlike other SAPOs[41-43] where the Si species in the initial gel and the gel obtained in the early stage of the crystallization are simply unreacted silica whose ^{29}Si spectra usually have a broad peak at -110 ppm, no meaningful ^{29}Si signal was observed in the solids heated for less than 19 h in this study. Since the silicon source used in this study is fumed silica that is in the form of very small particles, it seems that within short crystallization time, vast majority of fumed silica still remain suspended in the solution and were separated from the solids by centrifugation. In the 22 h sample, a weak signal at -90 ppm appears. The position of this peak is characteristic of isolated $Si(OAl)_4$ species in SAPOs,[3,33,44] indicating the beginning of Si incorporation into the FAU framework. The intensity of the signal becomes sharper and stronger in the 2 d and 4 d samples, indicating that more Si atoms are incorporated into the SAPO-37 structure with increasing the heating time. There is also a broad shoulder at -94 ppm in these two samples, suggesting a small amount of Si(OAl)$_3$(OSi)$_1$ species.[45]

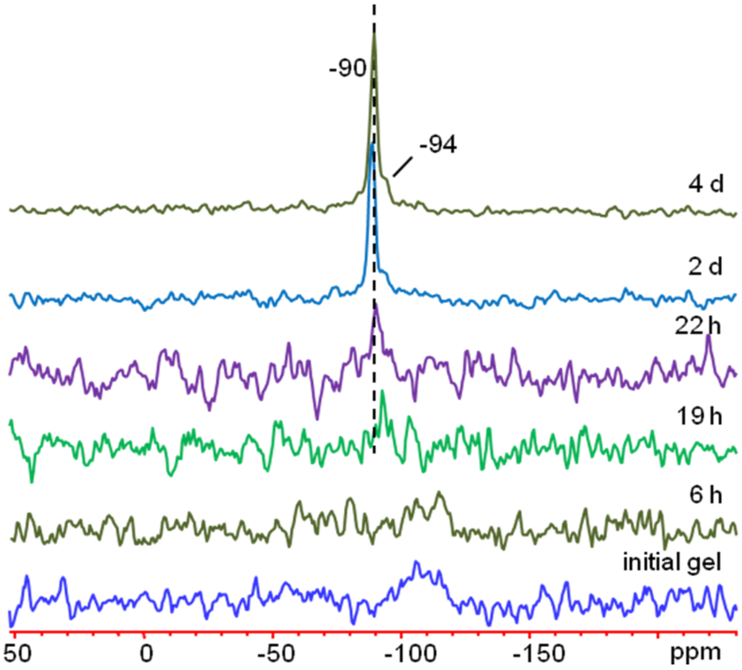

Figure 6.5 ^{29}Si MAS spectra of selected HTS samples.

EDX experiments were also carried out to semi-quantitatively estimate the substitution degree of Si atoms (Table 6.1). The Si content is about 14 mol.% in the final SAPO-37 sample, which is comparable to the upper threshold value (13%) of SM II mechanism in SAPO-37 framework.[46] The EDX data agree well with the corresponding ^{29}Si NMR spectrum discussed earlier. Both ^{29}Si NMR and EDX results suggest that under HTS conditions employed, Si is incorporated into the framework via both SM II and III mechanisms with SM II being the dominant one.

Table 6.1 Elemental compositions (molar basis) of selected gel samples.

Method	Sample	Si	Al	P	P/Al	(Si + P)/Al
HTS	4 d	0.14	0.48	0.37	0.77	1.08
DGC	5.5 h	0.09	0.48	0.43	0.90	1.08
	45 h	0.13	0.49	0.38	0.78	1.04

AFM has been used to image the detailed surface structures of zeolites and is able to provide key information on zeolitic crystal growth.[47-51] Several studies on the crystal growth of microporous materials with FAU structure such as zeolite Y and zincophosphate-faujasite (ZnPO-FAU) were reported.[52-55] In the present study, the AFM is utilized to examine the surface feature of SAPO-37 crystals synthesized by HTS method. To date, this is the first study of nucleation and crystal growth of SAPO-37 by AFM.

Figure 6.6A depicts an 8×8 μm^2 AFM image of one (111) face in a SAPO-37 crystal. Besides the intergrown structure in the face centre, several terraces can be found on the surface. The magnified image (Figure 6.6B) presents a rough (111) surface covered with these terraces as well as the nuclei on top of the terraces. This suggests that the rate of the terraces spreading to cover the whole (111) surface is slower than the nucleation rate. The nuclei grow all over the surface and on top of the terraces or other nuclei. They spread and coalesce with the terraces or nuclei underneath to cover the surface. This crystal growth mechanism is referred to as “birth and spread”.[50] Similar surface structures were reported before on the (111) face of the ZnPO-FAU crystals.[56] Section analysis (Figures. 6.6C and D) reveals that the terraces and nuclei in Figure 6.6B have an average thickness of approximately 7.5 and 10.5 nm, which corresponds to the thickness of about 5 and 7 FAU layers (each FAU layer has a thickness of 1.43 nm).[55] The thickness corresponding to one FAU layer was previously observed on the (111) surface of the zeolite Y and ZnPO-X crystals synthesized under HTS conditions.[53,55,56] Under the current synthesis conditions, both the heights of terraces and nuclei have much larger sizes than the reported value in zeolite materials.[52,54,55]

Besides the above mentioned details on the SAPO-37 crystal surface, other crystal growth features were also observed. Figure 6.6E shows the (111) face of a different crystal. Its magnified image (Figure 6.6F) indicates that the steps on the (111) surface have triangular shapes rotated by 60° with respect to the crystal edge. Similar observations were reported for zeolite Y.[54] Figure 6.6G shows a (111) face of a crystal with a large hollow pit in the center of the surface, indicating that SAPO-37 crystals have preference to start growing from the edges and then towards the center. A similar growth pattern was also observed for ZnPO-FAU.[55] Figure 6.6G also displays a triangle-shaped dent near the edge of the crystal face. This type of triangular dent likely results from the coalescence of triangular shaped terraces as illustrated in Figure 6.6H.

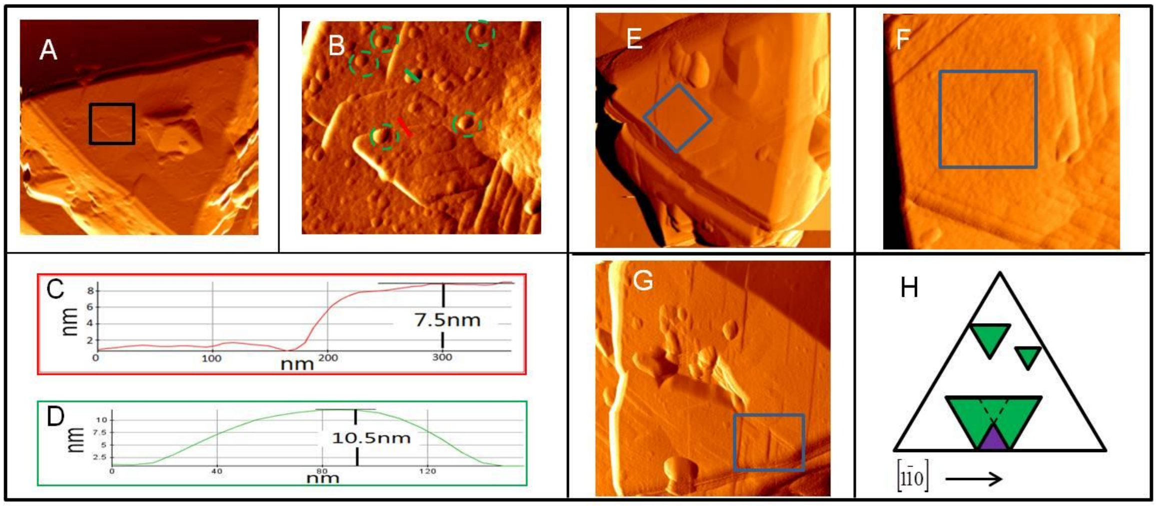

Figure 6.6 AFM images of the (111) face of SAPO-37 crystals (4 d sample). (A) top-view AFM image (error signals are shown here for clarity) in the size of 8×8 μm^2; (B) enlarged view of a square area in the black box in (B), 2×2 μm^2 ; (C) and (D) cross-sectional height profile from the topographic image along red and green lines shown in (B), showing the average height of surface steps and nuclei; (E) AFM image (error signals are shown here for clarity) of the (111) face on another crystal in the size of 8×8 μm^2 ; (F) zoomed-in image of the blue square area in (A); (G) AFM error signal image of a (111) face on a crystal in the size of 4×4 μm^2; (H) an illustrative scheme of triangle-shaped steps and dent pits on the (111) surface.

It should be pointed out the seemingly flat area on a given terrace such as the area in blue box in Figure 6.6F is not atomically flat. For example, when zooming in on the terrace as indicated by the blue box area (Figure 6.7A), a variation in height was observed. Interestingly, the heights are less than 1.43 nm (the height of one FAU layer). Two cross-sectional lines are drawn in the 'flat" area inside box and their height profiles are shown in Figs. 7B and C. The height profiles along the two cross-sectional lines show the peaks with various heights such as 0.31 nm (corresponding to a 6-membered ring, 6R), 0.56 nm (corresponding to a double 6-membered ring, D6R), 0.87 nm (corresponding to an incomplete sodalite cage), and 1.28 nm (a height between that of a complete sodalite cage without D6R parallel to (111) plane (1.12 nm) and that of one FAU layer (1.43 nm)). See Figure 6.7D for illustrations.

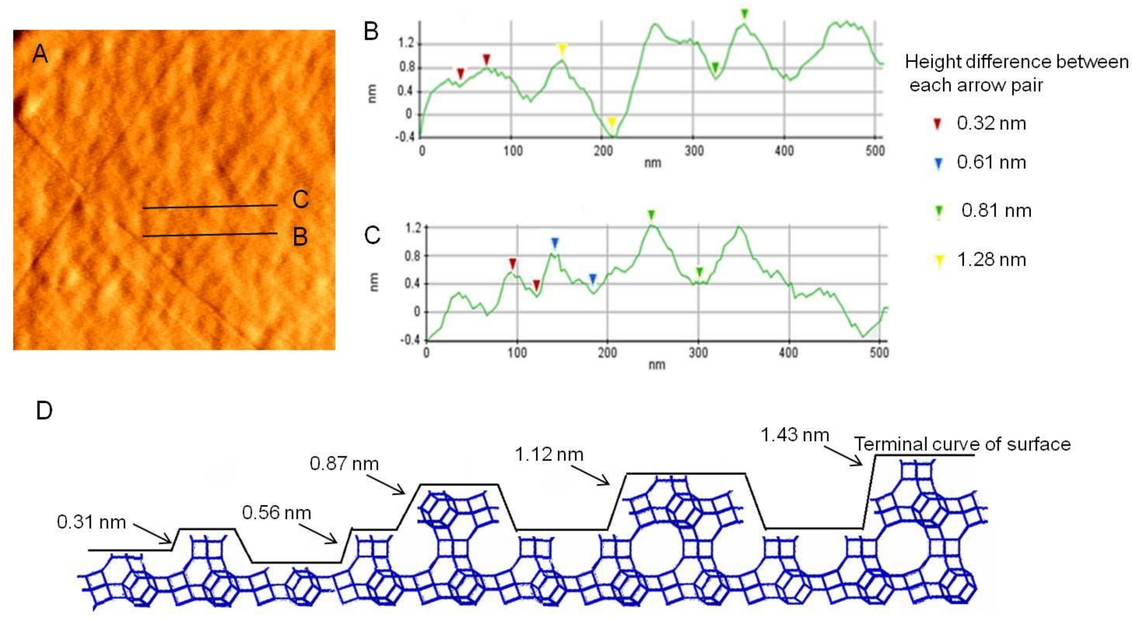

Figure 6.7 (A) AFM image of the boxed area in Figure 6F on a crystal in the size of 800×800 nm^2; (B-C) cross- sectional profiles along the lines in (A). Heights of ca. 1.28, 0.87, 0.56 and 0.31 nm are observed; (D) a model of the terminal structure of SAPO-37 along the lines in (A).

Multiple steps with heights less than 1.43 nm were previously observed on the (111) face of zeolite Y crystals grown in aluminosilicate solutions.[52] By modeling the observed terminal structures, it was reported that complete D6Rs were the major surface structure. However, in the present study, the (111) surface growth is not terminated by the complete D6R. Instead, the (111) surfaces of SAPO-37 were terminated by different microstructures. It seems that instead of having uniform terminal structure on the surface, the (111) face of SAPO-37 crystals tends to be terminated by several building units such as 6Rs, D6Rs, as well as incomplete sodalite cages (Figure 6.7D).

In summary, in the HTS study described earlier, the initial gel without heating appears to contain some species having large cavities with the TPA^+ cations trapped inside. These large cavities can evolve into supercgaes. Sodalite cages, on the other hand, form later, and they are templated by TMA^+ cations. These sodalite cages are likely to be associated with the species containing large pores. The amorphous material formed at this stage is a precursor and eventually evolves into FAU framework. Si incorporation occurs at later stage of the crystallization. Crystal growth on (111) face follows “birth and growth” mechanism. The surface structure is not terminated uniformly by one type of secondary building unit. The fact that the “incomplete soldiate cage” is found as terminal structure, suggesting that sodalite cage does not exist in the solution.

6.3.2 DGC method

The SAPO-37 formation was also studied by DGC method which simplifies the reaction system as all the reactive species present is confined in the solids. Figure 6.8A shows the PXRD patterns of the unwashed gel samples heated for different times under DGC conditions. The pattern of the initial dry gel dried at 353 K indicates that only amorphous materials exist. Upon heating the dry gel for 0.5 h, the PXRD pattern shows the appearance of a new broad peak with a very low 2θ value (labeled with an arrow). This peak becomes much strong after 1 h heating, implying that the majority of the amorphous materials transformed into a semi-crystalline layered phase. After washing with distilled water, the strong low-angle peak in 1 h sample became weaker and broader

(Figure 6.8B), demonstrating that part of the semi-crystalline phase transformed back to amorphous materials after washing. This indicates that the semi-crystalline phase is held by weak nonbonding forces such as van der Waals and weak hydrogen bonding; similar situation is also found in the crystallization of SAPO-34 and $AlPO_4$-based molecular sieves under DGC conditions.[57-60]

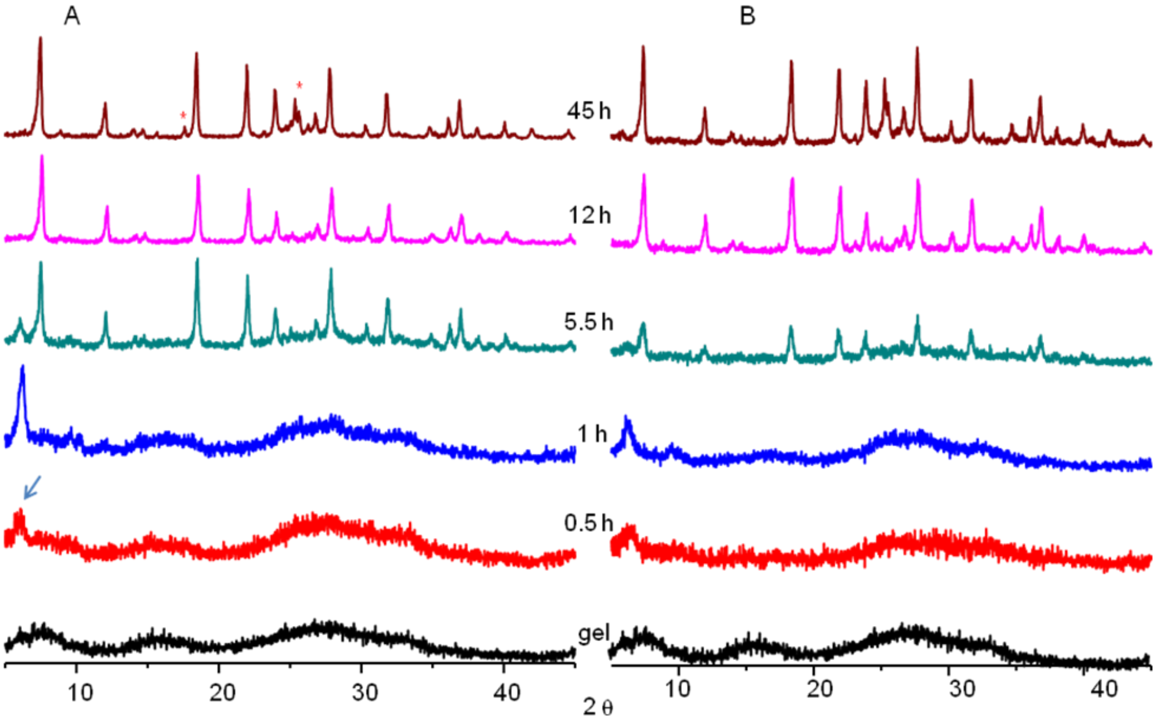

Figure 6.8 (A) Unwashed and (B) washed powder XRD patterns of DGC gel samples. * indicates impurities.

After 5.5 h, the intensity of the strong low-angle peak due to the semi-crystalline phase began to decrease. The characteristic reflections due to SAPO-37 started to appear concomitantly, indicating the transformation of the semi-crystalline phase into the FAU framework. Heating the gel for 12 h results in the complete disappearance of the low-angle peak and the PXRD pattern indicates pure SAPO-37 with high crystallinity.[3]

Further heating leads to the appearance of a small amount of impurity as shown in the PXRD pattern of the 45 h sample.

The SEM images of the selected DGC samples are shown in Figure 6.9. The picture of 5.5 h sample shows a large number of aggregated small octahedral crystals. The micrograph of 45 h shown in Figure 6.9B is analogous to that of 5.5 h sample except that the crystal sizes are slightly larger (0.2-0.3 μm). Due to the small crystal size, AFM characterization cannot be conducted on SAPO-37 crystals synthesized under DGC conditions.

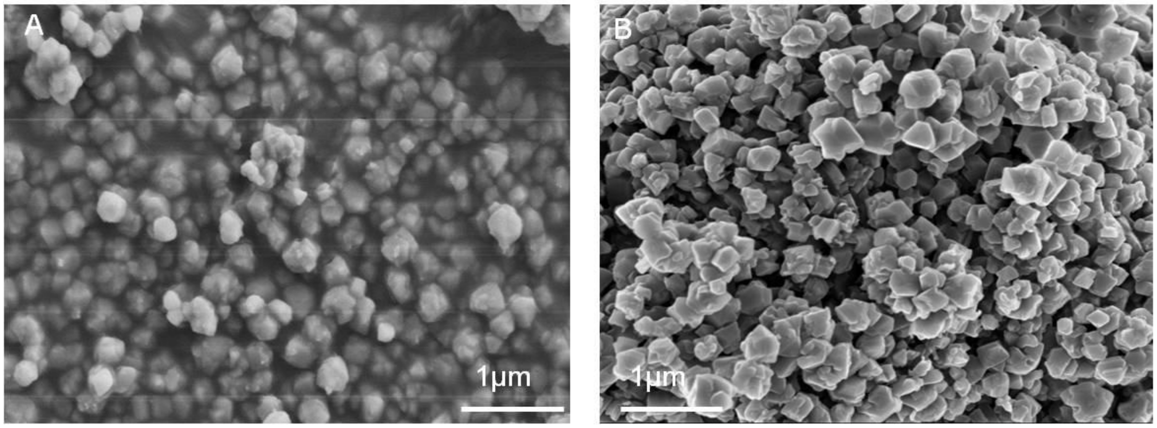

Figure 6.9 SEM images of selected DGC gel samples. (A) 5.5 h and (B) 45 h.

The ^{31}P MAS spectrum (Figure 6.10A) of the initial DGC dry gel shows a peak at -20 ppm and a broad hump on its high-frequency side. The presence of the broad hump is consistent with the amorphous nature of the initial dry gel. The ^{27}Al MAS spectrum of the initial gel (Figure 6.10B) contains a relatively narrow peak at 41 ppm and a broad resonance at 6 ppm.

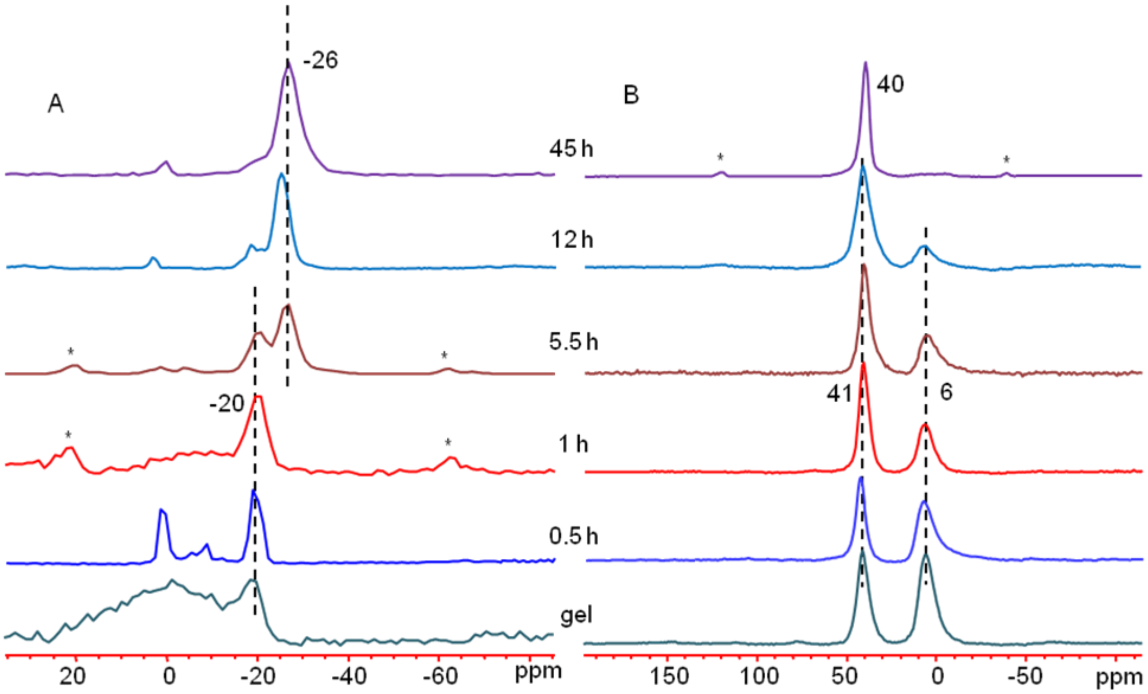

Figure 6.10 ^{31}P MAS (A) and ^{27}Al MAS (B) spectra of selected unwashed DGC gel samples. Asterisks indicate spinning sidebands.

To further understand the nature of the initial dry gel without heating, ^{27}Al{^{31}P} and ^{31}P{^{27}Al} REDOR experiments were carried out to establish the connectivity between P and Al atoms in the dry gel. The ^{27}Al{^{31}P} REDOR difference (ΔS) spectrum is shown in Figure 6.11A. As mentioned earlier, REDOR technique is based on heteronuclear dipolar coupling. In the ^{27}Al{^{31}P} REDOR difference (ΔS) spectrum, only Al with P in its proximity will be observed. The fact that Figure 6.11A only contains the peak at 41 ppm confirms that the tetrahedral Al is indeed in the AlPO-based material. The peak at 6 ppm did not appear in the ΔS spectrum, indicating unambiguously that this peak is due to unreacted alumina. ^{31}P{^{27}Al} REDOR difference spectrum (Figure 6.11B) shows that the P site at -20 ppm is connected to the tetrahedral Al at 41 ppm and vast majority of the low-frequency signals in the ^{31}P MAS spectra are from phosphate species (presumably amine phosphates) without Al nearby. It seems that the initial dry gel contains unreacted alumina and amine phosphates as well as AlPO-based materials.

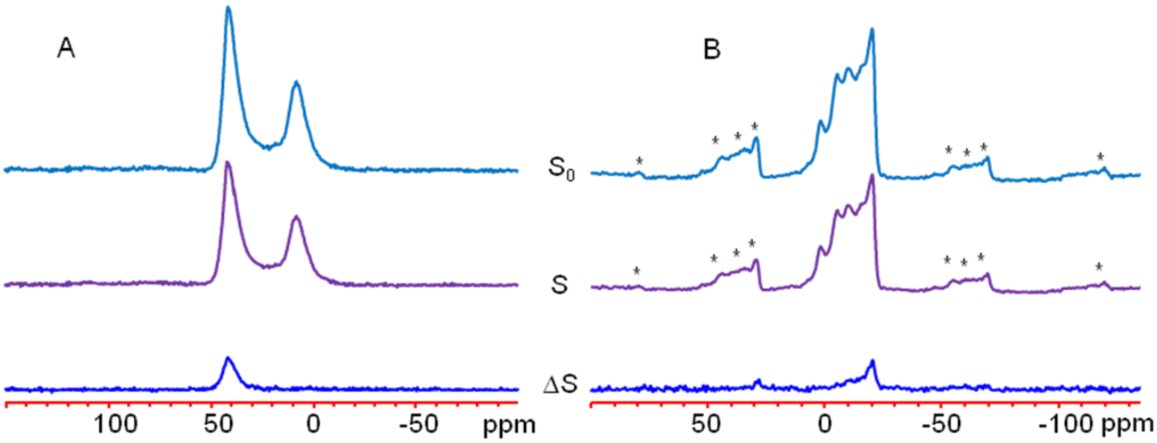

Figure 6.11 (A) ^{27}Al{^{31}P} REDOR and (B) ^{31}P{^{27}Al} REDOR spectra of the initial DGC dry gel with a dephasing time of 1.25 ms. The peaks labeled with * are due to spinning sidebands.

With increasing heating time, the peak at 6 ppm in ^{27}Al MAS spectra and broad high-frequency signals in ^{31}P MAS spectra become weaker, implying that they further react with each other to form AlPO-based layered semi-crystalline intermediate. After heating the dry gel for 1 h, the very broad high-frequency signals in the ^{31}P MAS spectrum of the initial dry gel has almost diminished and the peak at -20 ppm is now the strongest peak (Figure 6.10A). In the corresponding ^{27}Al MAS spectrum (Figure 6.10B), the intensity of the resonance at 41 ppm due to the tetrahedral Al site in the AlPO phase is increased significantly at the expense of the intensity of the peak at 6 ppm. The changes in the ^{31}P and ^{27}Al MAS spectra coincide with the observed changes in the PXRD pattern of this sample, suggesting that the phosphates and alumina further react to form AlPO-based layered semi-crystalline intermediate. Upon heating the dry gel for 5.5 h, a new ^{31}P resonance at around -26 ppm started appearing with the peak at -20 ppm decreasing in its intensity. The formation of the peak at -26 ppm suggests the development of a new phase in the gel sample. This agrees very well with the corresponding PXRD pattern (Figure 6.8), which shows the appearance of the characteristic peaks due to SAPO-37 phase. The ^{31}P MAS and ^{27}Al MAS spectra of the 45 h sample (Figure 6.10) only exhibit resonances characteristic of SAPO-37, confirming that the semi-crystalline phase transformed into SAPO-37 phase.

The ^{13}C CP MAS NMR spectra of selected DGC gel samples are shown in Figure 6.4B. For the DGC dry gel, the peaks 58 and 56 ppm are from methyl groups of TMA$^+$. As mentioned before, these two peaks correspond to the TMA$^+$ cations trapped inside the sodalite cage (58 ppm) and adsorbed outside the surface of the solids (56 ppm). Seeing these peaks suggests that in the DGC dry gel, sodalite cage or quasi-sodalite cage already exists. The initial DGC dry gel was prepared by drying a solution containing all the reactive species at 353 K. It appears that under these conditions, quasi-sodalite cage forms around TMA$^+$. As discussed earlier, the signals at 60, 16 and 12 ppm are due to the C_1- and C_2-methylene as well as C_3-methyl groups of TPA$^+$, respectively. Observing the 12 ppm methyl peak from TPA$^+$ suggests that similar to the gel phase obtained under HTS conditions, the initial dry gel also contains the AlPO species having large cavities with trapped TPA$^+$.

Upon heating the dry gel for 1 h, the peak assigned to the adsorbed TMA$^+$ disappeared and only the signal due to the trapped TMA$^+$ is present, indicating that the TMA$^+$ ions initially adsorbed on the outer surface further direct the formation of the sodalite cage. Since the corresponding PXRD pattern and ^{31}P MAS spectrum show unambiguously that the sample only contains semi-crystalline layered phase and that

SAPO-37 has not formed at this point, the ^{13}C NMR data suggest that the semi-crystalline layered intermediate contains the quasi-sodalite cage.

^{29}Si MAS NMR spectra (Figure 6.12A) were acquired to follow the incorporation of Si into the framework under DGC conditions and ^{1}H to ^{29}Si CP technique was also utilized to select the Si species with protons in its close proximity (Figure 6.12B). The ^{29}Si MAS spectra of the DGC dry gel and the gel sample heated for 1 h show a broad peak centered at around -112 and -108 ppm, respectively. These broad peaks can be assigned to the unreacted amorphous silica with $Si(OSi)_4$ environments.[61] This indicates that the majority of the silica in the samples heated below 1 h has not reacted and the semi-crystalline phase is mainly AlPO in nature. The CP spectrum of the 1 h sample presents two signals at about -85 and -95 ppm. The peak at -95 ppm is due to $(SiO)_2Si(OH)_2$ on the surface of the silica particles.[61,62] The one at -85 ppm is likely due to the $(AlO)_3SiOH$ or $Si(OAl)_4$ with a SDA nearby in a small amount of amorphous aluminosilicates.[61,62] The results indicate that the silica is activated via formation of aluminosilicate species which are subsequently incorporated into the FAU framework. A similar situation has been reported for SAPO-34.[57] A sharp peak appears in the ^{29}Si MAS and CP spectra of the 5.5 h sample at around -90 ppm, which is characteristic of isolated $Si(OAl)_4$ species in SAPO-37.[3,33] The presence of this peak agrees with the corresponding PXRD pattern, ^{31}P and ^{27}Al MAS spectra, which show the existence of SAPO-37 in this sample. ^{29}Si NMR data suggest that the silica first reacts with alumina to form aluminosilicates. The aluminosilicate species then react with the semi-crystalline layered AlPO phase, leading to the Si incorporation and corresponding SAPO-37 formation.

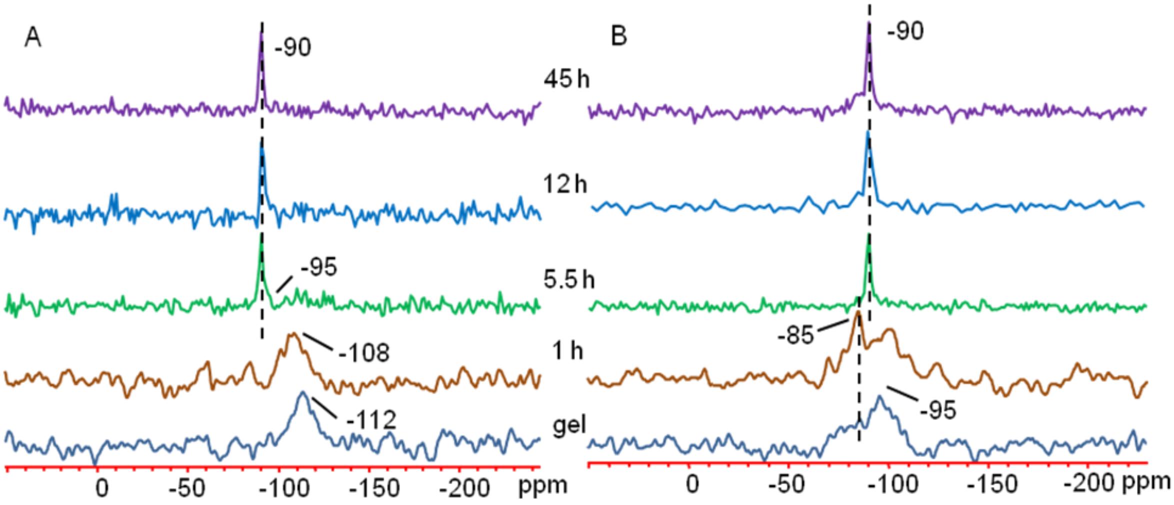

Figure 6.12 ^{29}Si MAS (A) and ^{1}H → ^{29}Si CP spectra of selected unwashed DGC gel samples with a contact time of 0.5 ms (B).

EDX results on selected DGC gel samples are shown in Table 6.1. A comparison of the Si molar percentages in the two samples synthesized under DGC conditions revealed that Si is gradually incorporated into the framework upon heating the dry gel. The average Si content in 45 h sample is about 13 mol.%, which is the proposed upper threshold value (13%) of SM II mechanism in SAPO-37 framework.[47] Furthermore, the (Si + P)/Al ratio (1.04) is very close to 1, which further supports the SM II mechanism. Therefore, EDX data indicate that under DGC conditions, Si enters into the FAU framework only via substitution for P (SM II), which is consistent with the presence of a single sharp peak at -90 ppm in the ^{29}Si MAS spectrum of the 45 h sample (Figure 6.12A). This is similar to the synthesis under HTS conditions, where Si is also incorporated into the framework mainly via SM II.

6.3.3 SAPO-37 formation pathways

For HTS synthesis, the ^{13}C NMR data indicate that the solids heated for less than 16.5 h at 443 K contain the species having the large cavities corresponding to two supercgaes. Such species is likely the precursor to final FAU framework and was previously identified existing in the solid phases obtained during SAPO-37 synthesis under very similar conditions.[22,23] ^{13}C NMR data also suggest that this precursor does not have sodalite cages, but likely has 4-membered rings (4Rs) and 6Rs since the existence of 4Rs and 6Rs in the solid phase at the initial stage of crystallization was confirmed by *in situ* and *ex situ* UV Raman studies on the assembly mechanism of zeolite X.[64,65] Further heating leads to the cross-linking of the large pore species, developing of sodalite cages under the influence of TMA^+ and the eventual formation of the FAU framework. Such pathway is illustrated in Scheme 6.3A.

The AFM findings show that the crystal growth mechanism is “birth and spread” with the nuclei containing at least 7 FAU layers, coalescing with the terraces underneath to form the (111) faces of SAPO-37 framework. The AFM data also suggest that the hydrothermally synthesized SAPO-37 has rough surfaces that are terminated with 6Rs, D6Rs and incomplete sodalite cages.

While the HTS synthesis is carried out in an extremely complicated system where the crystallization involves solid, liquid, and gaseous phases, the DGC method, on the other hand, is conducted in a relatively simple way with all the reactive species are confined in the solids. Like the HTS initial gel, the initial DGC dry gel also contains the AlPO species having large cavities without long-range ordering. This is not surprising, considering that the initial DGC dry gel is prepared by drying the same initial gel solution. Unlike the HTS initial gel where sodalite cage (which is the secondary building units of the FAU framework) doesn't exist, the DGC dry gel does contain, at least, quasi-sodalite cages that trap the TMA^+, which are presumably attached to the large pore species. This is consolidated by the finding that the sodalite cage exists in the intermediate phase during the formation of zeolite X.[63,65] In the initial DGC dry gel, the large cavities species with quasi-sodalite cages are disordered in the amorphous material, but they cross-link together to form semi-crystalline layered phase under prolonged heating under DGC conditions. Eventually, each large pore in the layer evolves into two well separated supercages. Meanwhile, silica slowly reacts with alumina, yielding small aluminosilicate particles, which are possibly dispersed between the AlPO layers. As mentioned earlier, the forces holding the layers together are weak nonbonding interactions, which promote bond breaking and reforming in the absence of bulk water and hence facilitate the transformation from the layered phase to SAPO-37. In the last step these layers are reorganized and cross-linked together to form the FAU structure and at the same time Si atoms are incorporated into the framework as isolated $Si(OAl)_4$ species. Scheme 6.3B is the illustration of this pathway.

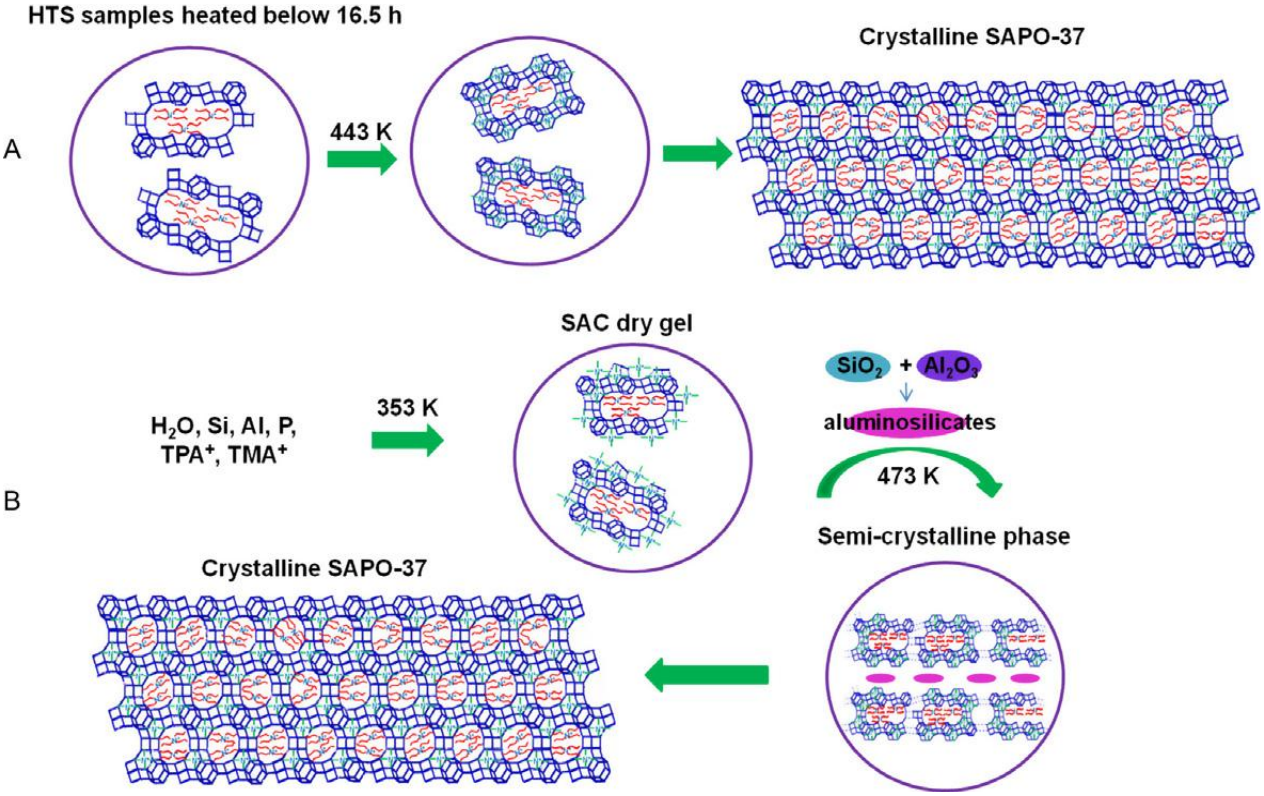

Scheme 6.3 Illustration of the formation of SAPO-37 under HTS (A) and DGC (B) conditions.

6.4 Conclusions

The formation of SAPO-37 was examined under both HTS and DGC conditions by using an assortment of techniques including PXRD, SEM, AFM, and solid-state NMR. The results indicate that crystallization pathways for HTS and DGC are similar. Under HTS conditions, the precursor initially is only composed of the large cavities whose size is equivalent to two directly connected supercages. Increasing the crystallization time leads to the slow formation of sodalite cages that are connected to the cavities. Under DGC conditions, the precursor initially not only contains the large cavities, but also quasi-sodalite cages. Thus, the precursors are almost the same. Further, the precursors are mainly AlPO in nature with little or no Si. The Si incorporation involves forming aluminosilicates first and then incorporating isolated $Si(OAl)_4$ species into the FAU framework. The AFM data suggest that SAPO-37 crystal growth under HTS conditions follows the "birth and spread" mechanism and the (111) crystal surfaces are terminated by different structural building units.

6.5 References

(1) Lok, B. M.; Messina, C. A.; Patton, R. L.; Gajek, R. T.; Cannan, T. R.; Flanigen, E. M. US Patent 4,440,871, 1984.
(2) Sierra de Saldarriaga, L.; Saldarriaga, C.; Davis, M.E. *J. Am. Chem. Soc.* **1987**, *109*, 2686- 2691.
(3) Ojo, A. F.; Dwyer, J.; Dewing, J.; Karim, K. *J. Chem. Soc., Faraday Trans.* **1991**, *87*, 2679-2684.
(4) Flanigen, E. M.; Patton, R. L.; Wilson, S. T. *Stud. Surf. Sci. Catal.* **1988**, *37*, 13-27.
(5) Lok, B. M.; Messina, C. A.; Patton, R. L.; Gajek, R. T.; Cannan, T. R.; Flanigen, E. M. *J. Am. Chem. Soc.* **1984**, *106*, 6092-6093.
(6) Sastre, G.; Lewis, D.W.; Catlow, C. R. A. *J. Phys. Chem.* **1996**, *100*, 6722-6730.
(7) Maistriau, L.; Dumont, N.; Nagy, J. B.; Gabelica, Z.; Derouane, G. *Zeolites* **1990**, *10*, 243-250.
(8) Dzwigaj, S.; Briend, M.; Shikholeslami, A.; Peltre, M. J.; Barthomeuf, D. *Zeolites* **1990**, *10*, 157-62.
(9) Parise, J.; Corbin, D.; Abrams, L.; Cox, D. *Acta Crystallogr., Sect. C: Cryst. Struct. Commun.* **1984**, *C40*, 1493-1497.
(10) Martens, J. A.; Grobet, P. J.; Jacobs, P. A. *J. Catal.* **1990**, *126*, 299-305.
(11) Su, B. L.; Barthomeuf, D. *J. Catal.* **1993**, *139*, 81-92.
(12) Fernandes, G.; Fernandes, V. *Catal. Today* **2002**, *75*, 233-238.
(13) Peltre, M. J.; Man, P. P.; Briend, M.; Derewinski, M.; Barthomeuf, D. *Catal. Lett.* **1992**, *16*, 123-128.
(14) Briend, M.; Peltre, M. J.; Lamy, A.; Man, P. P.; Barthomeuf, D. *J. Catal.* **1992**, *138*, 90-100.
(15) Franco, M. J.; Perez-Pariente, J.; Mifsud, A.; Blasco, T.; Sanz, J. *Zeolites* **1992**, *12*, 386-394.
(16) Corma, A.; Fornes, V.; Perez-Pariente, J. *J. Chem. Soc. Chem. Commun.* **1993**, *8*, 676-678.
(17) Briend, M.; Lamy, A.; Peltre, M. J.; Man, P. P.; Barthomeuf, D. *Zeolites* **1993**, *13*, 201-211.
(18) Davis, M. E. *Microporous Mater.* **1996**, *7*, 159-160.
(19) Chen, T. H.; Wouters, B. H.; Grobet, P. J. *J. Phys. Chem. B* **1999**, *103*, 6179-6184.
(20) Chen, T. H.; Wouters, B. H.; Grobet, P. J. *Colloids Surf. A* **1999**, *158*, 145-149.

(21) Maistriau, L.; Dumont, N.; Nagy, J.; Gabelica, Z.; Derouane, E. Stud. Surf. Sci. Catal. **1989**, *52*, 209-213.

(22) Dumont, N.; Ito, T.; Nagy, J.; Gabelica, Z.; Derouane, E. *Stud. Surf. Sci. Catal.* **1991**, *65*, 591-602.

(23) Ito, T.; Dumont, N.; Nagy, J.; Gabelica, Z.; Derouane, E. *Stud. Surf. Sci. Catal.* **1991**, *60*, 11-20.

(24) Xu, W.; Dong, J.; Li, J.; Li, J.; Wu, F. *J. Chem. Soc., Chem. Commun.* **1990**, *10*, 755-756.

(25) Kim, M. H.; Li, H. X.; Davis, M. E. *Microporous Mater.* **1993**, *1*, 191-200.

(26) Rao, P. R. H. P.; Matsukata, M. *Chem. Commun.* **1996**, 1441-1442.

(27) Rao, P. R. H. P.; Leon y Leon, C. A.; Ueyama, K.; Matsukata, M. *Microporous Mesoporous Mater.* **1998**, *21*, 305-313.

(28) Tatsumi, T.; Jappar, N. *J. Phys. Chem. B* **1998**, *102*, 7126-7131.

(29) Bandyopadhyay, R.; Kubota, Y.; Sugimoto, N.; Fukushima, Y.; Sugi, Y.; *Microporous Mesoporous Mater.* **1999**, *32*, 81-91.

(30) Matsukata, M.; Ogura, M.; Osaki, T.; Rao, P. R. H. P.; Nomura, M.; Kikuchi, E. *Top. Catal.* **1999**, *9*, 77-92.

(31) Gullion, T.; Schaefer, J. *J. Magn. Reson.* **1989**, *81*, 196-200.

(32) Huang, Y.; Demko, B. A.; Kirby, C.W. *Chem. Mater.* **2003**, *15*, 2437-2444.

(33) Fyfe, C. A.; Wong-Moon, K. C.; Huang, Y.; Grondey, H. *Microporous Mater.* **1995**, *5*, 29-37.

(34) Hasha, D.; Sierra de Saldarriaga, L.; Saldarriaga, C.; Hathaway, P. E.; Cox, D.F.; Davis, M. E. *J. Am. Chem. Soc.* **1988**, *110*, 2127-2135.

(35) Zhou, D.; Xu, J.; Yu, J.; Chen, L.; Deng, F.; Xu, R. *J. Phys. Chem. B* **2006**, *110*, 2131-2137.

(36) Blackwell, C.; Patton, R. *J. Phys. Chem.* **1988**, *92*, 3965-3970.

(37) Gao, Q.; Chen, J.; Xu, R.; Yue, Y. *Chem. Mater.* **1997**, *9*, 457-462.

(38) Yan, Z.; Chen, B.; Huang, Y. *Solid State Nucl. Magn. Reson.* **2009**, *35*, 49-60.

(39) Tuel, A.; Taarit, Y. B. Zeolites **1994**, *14*, 169-176.

(40) Hayashi, S.; Suzuki, K.; Shin, S.; Hayamizu, K.; Yamamoto, O. *Chem. Phys. Lett.* **1985**, *113*, 368-371.

(41) Liu, G.; Tian, P.; Li, J.; Zhang, D.; Zhou, F.; Liu, Z. *Microporous Mesoporous Mater.* **2008**, *11*, 143-149.

(42) Xu, L.; Du, A.; Wei, Y.; Wang, Y.; Yu, Z.; He, Y.; Zhang, X.; Liu, Z. *Microporous Mesoporous Mater.* **2008**, *115*, 332-337.

(43) Liu, G.; Tian, P.; Zhang, Y.; Li, J.; Xu, L.; Meng, S.; Liu, Z. *Microporous Mesoporous Mater.* **2008**, *114*, 416-423.

(44) Qiu, S.; Tian, W.; Pang, W.; Sun, T.; Jiang, D. *Zeolites* **1991**, *11*, 371-375.

(45) Derewinski, M.; Peltre, M. J.; Briend, M.; Barthomeuf, D.; Man, P. P. *J. Chem. Soc., Faraday Trans.* **1993**, *89*, 1823-1828.

(46) Barthomeuf, D. *J. Phys. Chem.* **1993**, *97*, 10092-10096.

(47) Anderson, M.W. *Curr. Opin. Solid State Mater. Sci.* **2001**, *5*, 407-415.

(48) Ono, S. S.; Matsuoka, O.; Yamamoto, S. *Microporous Mesoporous Mater.* **2001**, *48*, 103-110.

(49) Holme, B.; Cubillas, P.; Cavka, J. H.; Slater, B.; Anderson, M. W. Akporiaye, D. *Cryst. Growth Des.* **2010**, *10*, 2824-2828.

(50) Cubillas, P.; Anderson, M. W. In *Zeolites and Catalysis: Synthesis, Reactions and Applications,* 1st ed.; Čejka, J.; Corma, A.; Zones, S., Eds.; Wiley-VCH: Weinheim, Germany, 2010; Vol. 1, pp 1-55.
(51) Paredes, J. I.; Martinez-Alonso, A.; Tascon, J. M. D. *Microporous Mesoporous Mater.* **2003**, *65*, 93-126.
(52) Wakihara, T.; Sugiyama, A.; Okubo, T. *Microporous Mesoporous Mater.* **2004**, *70*, 7-13.
(53) Wakihara, T.; Okubo, T. *J. Chem. Eng. Jpn.* **2004**, *37*, 669-674.
(54) Anderson, M. W.; Agger, J. R.; Thornton, J. T.; Forsyth, N. *Angew. Chem. Int. Ed.* **1996**, *35*, 1210-1213.
(55) Cubillas, P.; Holden, M. A.; Anderson, M. W. *Cryst. Growth Des.* **2011**, *11*, 3163-3173.
(56) Singh, R.; Doolittle, J.; George, M. A.; Dutta, P. K. *Langmuir* **2002**, *18*, 8193-8197.
(57) Zhang, L.; Bates, J.; Chen, D.; Nie, H. Y.; Huang, Y. *J. Phys. Chem. C* **2011**, *115*, 22309-22319.
(58) Chen, B.; Huang, Y. *J. Phys. Chem. C* **2007**, *111*, 15236-15243.
(59) Chen, B.; Kirby, C. W.; Huang, Y. *J. Phys. Chem. C* **2009**, *113*, 15868-15876.
(60) Chen, B.; Huang, Y. *Microporous Mesoporous Mater.* **2011**, *143*, 14-21.
(61) Maciel, G. E.; Bronnimann, C. E.; Zeigler, R. C.; Chuang, I. S.; Kinney, D. R.; Keiter, E. A. *Adv. Chem. Ser.* **1994**, *234*, 269-269.
(62) Doremieux-Morin, C.; Martin, C.; Bregeault, J. M.; Fraissard, J. *Appl. Catal.* **1991**, *77*, 149-61.
(63) Xiong, G.; Yu, Y.; Feng, Z.; Xin, Q.; Xiao, F. S.; Li, C. *Microporous Mesoporous Mater.* **2001**, *42*, 317-323.
(64) Fan, F.; Feng, Z.; Li, G.; Sun, K.; Ying, P.; Li, C. *Chem. Eur. J.* **2008**, *14*, 5125-5129.
(65) Lok, B.; Cannan,T.; Messina, C. Zeolites **1983**, *3*, 282-291.

Chapter 7 Examining the Crystallization Process of Zeolite LSX

7.1 Introduction

Zeolites are crystalline microporous aluminosilicates and have three-dimensional framework formed by connecting SiO_4 and AlO_4 tetrahedra. There is a negative charge associated with every Al atom, which is balanced by an exchangeable cation, thus resulting in a neutral structure.[1,2] Depending on their structures and compositions, zeolites have been widely used in industry as catalysts, adsorbents, and ion exchangers.[3] Among over 190 types of zeolite structures that have been identified, a limited number of them have exhibited practical applications.[4] Therein, faujasite zeolite (FAU framework) is one kind of the most important zeolitic materials.

The FAU framework (Figure 7.1) consists of two interconnecting 3D networks of cavities with the larger ones (supercages) of a free diameter of about 13 Å and smaller ones (sodalite or β cages) of a free diameter of about 7 Å.[5] By virtue of Si content, faujasite zeolite is categorized into two kinds: zeolite X having a Si/Al atomic ratio ranging from 1.0 to 1.5 and zeolite Y having a Si/Al atomic ratio above 1.5.[6] The application of faujasite zeolites in base-catalysed reactions is based on their negatively charged framework. The basicity of the zeolite can be increased with decreasing Si/Al ratio or compensating the negative framework charges by alkali metal cations or depositing basic oxides on the zeolite surface.[7] Low silicon X (LSX) has a Si/Al ratio of from 1.0 to about 1.1, and therefore, the maximum possible number of exchangeable cations.[5,8] Due to its high extraframework cation content, zeolite LSX is also one of the best sorbents in industry used for N_2/O_2 separation in air by adsorption processes.[9,10]

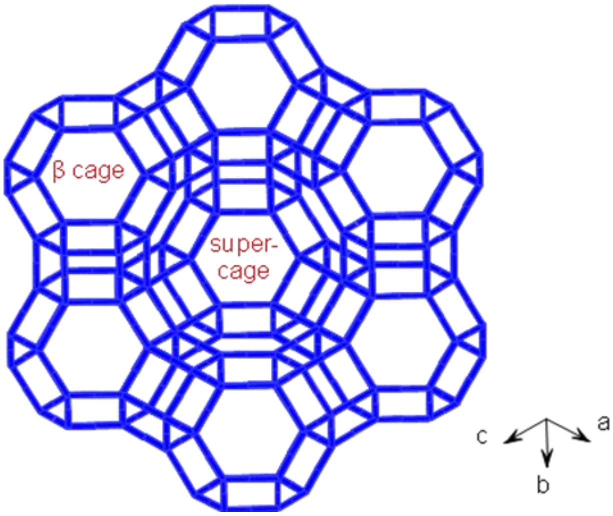

Figure 7.1 Structure of faujasite framework.

To date, much data has been obtained on the synthesis, characterization, and application of zeolite LSX.[11-31] Kühl has found that pure zeolite LSX can only be obtained when the reaction mixture contains both sodium and potassium ions.[32] The K/(Na+K) ratio is a critical factor for the synthesis of zeolite LSX.[33]

The growing applications of zeolite LSX require a better understanding of its nucleation and crystal growth process. Can Li group previously took advantage of *in situ* and *ex situ* UV Raman techniques to probe the formation process of zeolite X (Si/Al atomic ratio is between 1.1 and 1.5).[34-36] They proposed that the crystalline zeolite X framework was formed via the assembly of four-membered rings (4Rs) and 4R branched derivatives in the solid phase and monomeric silicate species in the liquid phase. Later Depla *et al.* carried out *in situ* studies of the crystallization of zeolite LSX by simultaneous UV Raman and X-ray diffraction (XRD) measurements. They pointed out the existence of 4Rs and 6Rs in the amorphous gel at an early stage of crystallization. By intermediate addition of K^+ ions into the synthesis solution, Iwama *et al*. proposed that K^+ ions played a strong salting-out effect during the formation of zeolite LSX and prevented aluminosilicate precursors from assembling into zeolite A (LTA framework, also composed of sodalite cages connected by double 4Rs).[33] In spite of much progress in studying the self-assembly process of zeolite LSX, detailed knowledge of its crystallization process is still lacking. For instance, Na^+ and K^+ ions are considered to play a structure-directing role in the formation of many zeolites.[37] The chemical environments of the two types of cations during the crystallization of zeolite LSX, however, have not been studied. Here, our recent work on the investigations of the crystallization of zeolite LSX is presented. Relations between the structures of the intermediates and the local environments of ^{27}Al, ^{29}Si, ^{23}Na, and ^{39}K nuclei were probed by solid state NMR in combination with other characterization techniques such as powder XRD and Raman spectroscopy.

7.2 Experimental

7.2.1 Sample preparation

Zeolites LSX was synthesized by using the method reported by Kühl.[32] The reagents were sodium aluminate (Strem Chemicals, ca. 92 wt% $NaAlO_2$), sodium hydroxide (Caledon Laboratory Chemicals, ca. 97 wt %), potassium hydroxide (BDH, ca. 85 wt %), and sodium silicate (Aldrich, ca. 7 wt% Na_2O and 27 wt % SiO_2). The initial gel molar composition was $5.5Na_2O:1.65K_2O:1.0Al_2O_3:2.2SiO_2:122H_2O$.

A typical procedure for the HTS synthesis of zeolite LSX gel samples was the following: 13.0 g potassium hydroxide, 8.7 g sodium hydroxide, and 34.4 g water were combined and subjected to vigorous stirring for 10 min. Separately, 7.2 g sodium aluminate and 20.4 g water were mixed and added to the former mixture after being stirred for 5 min. Subsequently, a mixture of 19.6 g sodium silicate and 20 g water was added. The final solution was first stirred at room temperature for 10 min and then transferred into several polypropylene bottles, which were capped and sealed with paraffin films (referred to as the initial gel). After static aging in an oven at 343 K for 3 h, crystallization was carried out at 373 K for different times. The bottles were taken out of the oven and quenched in cold water after specified lengths of time. The product in each autoclave was filtered and the solid phase was washed by using 0.01 M sodium hydroxide instead of water to avoid overwashing and hydrolysis.[32] The solid materials which are intermediates were then dried in air at room temperature and kept in tightly sealed glass vials for analysis.

7.2.2 Characterization

PXRD patterns were recorded on a Rigaku diffractometer using Co Kα radiation (λ = 1.7902 Å). Raman experiments were carried out with a customized Raman microspectroscopy system. A 514 nm line produced from an Ar^+ laser (Coherent Inc.) was used as the excitation source. The resolution was 0.1 cm^{-1}.

All the NMR experiments were carried out on a Varian/Chemagnetics Infinityplus 400 WB spectrometer equipped with three rf channels operating at the field strength of 9.4 T. The Larmor frequencies of ^{1}H, ^{23}Na, ^{27}Al, and ^{29}Si were 399.5, 105.7, 104.1, and 79.4 MHz, respectively. The chemical shifts of ^{23}Na, ^{27}Al, and ^{29}Si were referenced to 1 M NaCl (0 ppm), 1 M $Al(NO_3)_3$ (0 ppm), and tetrakis(trimethylsilyl)-silane ($SiMe_3$, −9.9 ppm with respect to liquid tetramethylsilane).[38] Depending on the requirements of individual experiment, three MAS probes were used (a Varian/Chemagnetics 7.5 mm, a 4.0 mm H/X/Y triple-tuned T3 MAS, and a 5.0 mm H/F/X/Y triple-tuned MAS probe). Both the ^{23}Na and ^{27}Al spectra were acquired using a very small pulse angle with a pulse delay of 1 s. For the ^{29}Si MAS experiments, a 45° pulse was used with a pulse delay of 60 s.

For selected LSX intermediate gel samples, ^{39}K NMR experiments were carried out at 21.1 T on a Bruker Advance-900 spectrometer at the National Ultrahigh-Field NMR Facility for Solids in Ottawa, Canada. The Larmor frequency of ^{39}K is 42.0 MHz. The chemical shift was referenced to 1.0 M KCl (aq) in H_2O. The spectra were acquired using a 7.5-mm H/X MAS Bruker probe with a spinning speed of 5 kHz.

^{39}K NMR parameters, including C_Q, η_Q, and δ_{iso}, were determined by analytical simulations of NMR spectra using the WSOLIDS simulation package.[39] The experimental error for each measured parameter was determined by visual comparison of experimental spectra with simulations. The parameter of concern was varied bidirectionally starting from the best fit value and all other parameters were kept constant, until noticeable differences between the spectra were observed.

7.3 Results and discussion

Figure 7.2 shows the powder XRD patterns of LSX gel samples recorded as a function of crystallization time. For the initial gel and samples heated for less than 3.2 h, all of the powder XRD patterns look identical and only contain a broad signal in the middle 2θ angle range, suggesting the amorphous nature of these solid samples. After heating the initial gel for 3.3 h, the corresponding XRD pattern shows several very weak reflection peaks, the positions of which coincide with the reflections of pure crystalline zeolite LSX.[40] This indicates that part of the amorphous phase has evolved into microporous FAU framework. Upon heating the gel for 3.5 h or longer, pure zeolite LSX with high crystallinity was yielded.

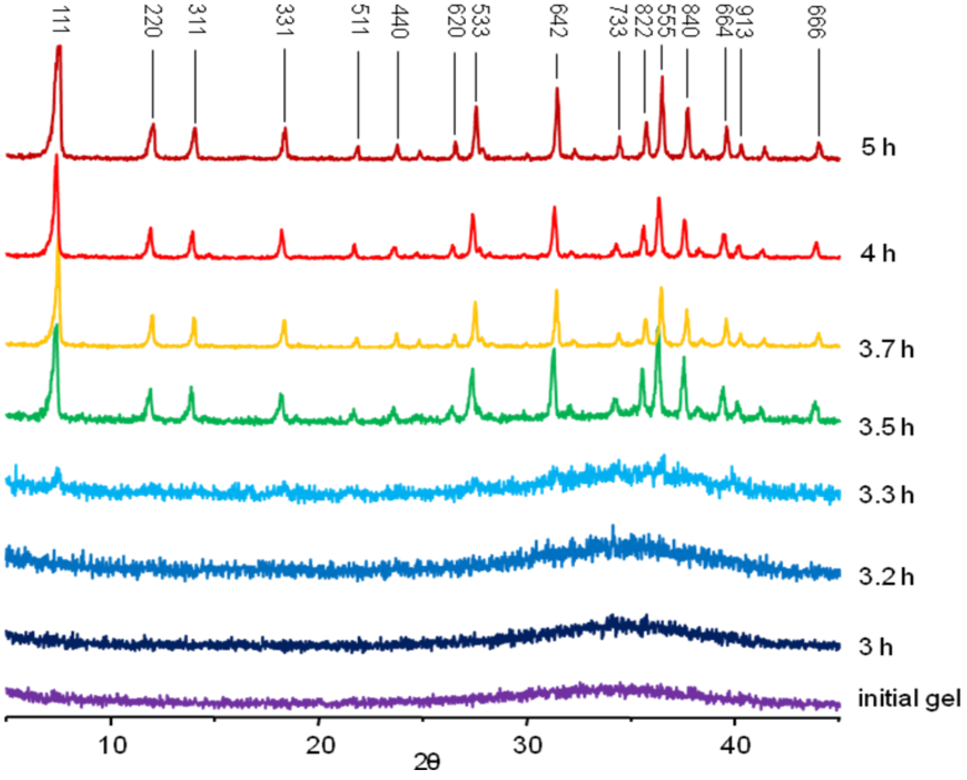

Figure 7.2 Powder XRD patterns of LSX gel samples.

Based on vibrational motions of zeolite framework, Raman spectroscopy can also provide structural information regarding ring sizes present in the intermediates.[41,42] It was used to monitor the development of pore openings during the formation process of zeolite LSX in this study (Figure 7.3). The Raman spectra of zeolite X (Si/Al ratio is above 1.1) were previously reported by Can Li group.[34,35] As zeolites LSX and X have the same structures, the assignments of the following Raman bands were made mainly according to their work. In the initial gel there are several bands at 500, 575, 850, 1024, and 1060 cm^{-1}, which are not characteristic Raman signals of zeolite LSX.[34] The bands at 500 and 850 cm^{-1} result from the T-O-T bending mode of four-membered rings (4Rs) and the T-O symmetric stretching mode, respectively (T = Si or Al).[34,43] The band at 575 cm^{-1} is due to ring structures with branched chains (see Scheme 7.1 for illustrations).[35] The bands observed at 1024 and 1060 cm^{-1} can be attributed to the T-O-T asymmetric stretching mode.[44] Further, the band at 1060 cm^{-1} may also result from CO_3^{2-} formed by the reaction of excess NaOH in the initial gel with ambient CO_2, which, however, has no influence in other species in the gel.[45] These findings, as suggested by Li group, indicate that the amorphous species mainly consists of 4Rs and branched 4Rs.

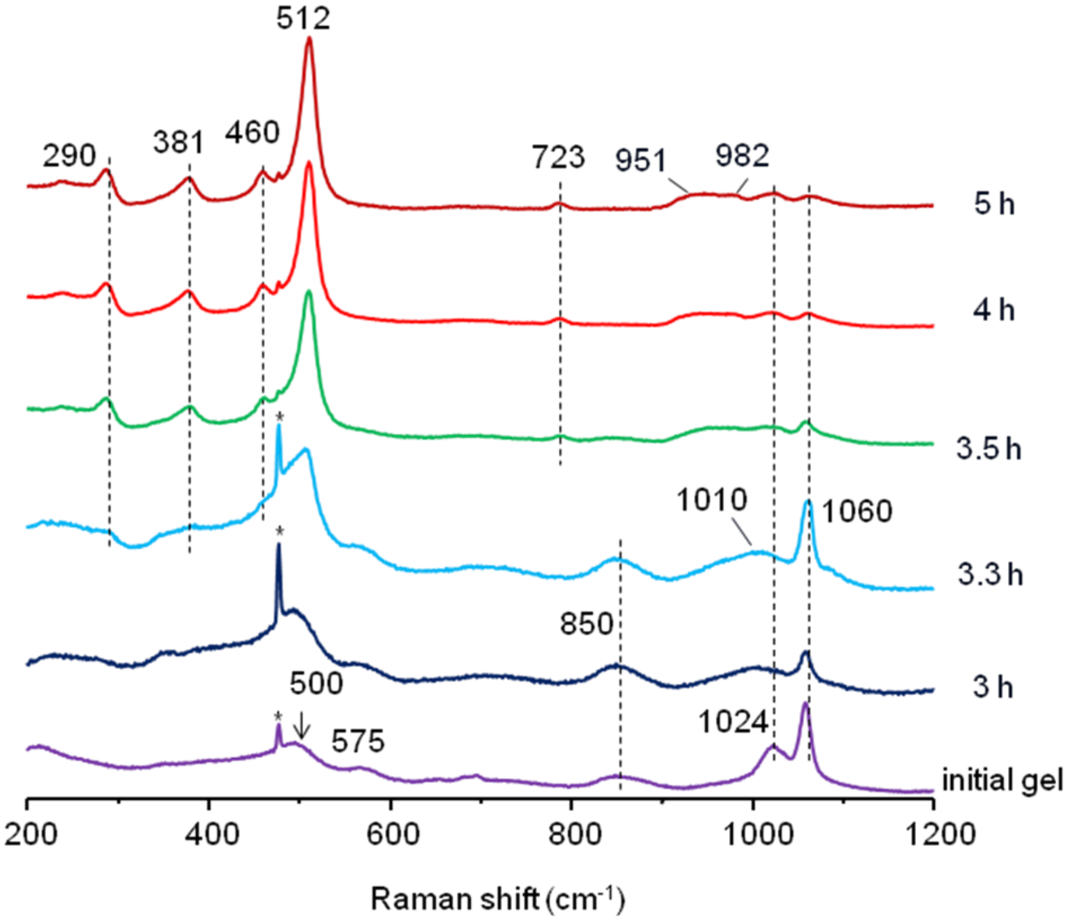

Figure 7.3 Raman spectra of selected LSX gel samples. The sharp band labeled with * is from glass slide, which was used to support the solid samples for Raman analysis.

After 3 h of heating under HTS conditions, a broad band at 1010 cm^{-1} became visible. It was also present in the initial gel, but buried under the 1024 cm^{-1} signal. It is due to sodalite cages.[34] This suggests that few complete or nearly complete sodalite cages were formed immediately when aluminum and silicon sources were mixed together. After heating the initial gel for 3.3 h, the broad band at 500 cm^{-1} became sharper and shifted to 512 cm^{-1}, characteristic of the 4R breathing vibration mode for crystalline zeolite LSX.[34,35] Further, two new weak bands at 290 and 381 cm^{-1}, which are assigned to the bending mode of double six-membered rings (D6Rs),[46] appeared. The band at 460

cm^{-1} results from the deformation of the T-O-T angle of 4Rs adjacent to K^+ ions.[47] These changes indicate that sodalite cages were connected with D6Rs to form crystalline zeolite LSX. Agreeing with the powder XRD pattern, this reveals the beginning of the crystallization. Upon heating the gel for 3.5 h or longer, the Raman bands remained unchanged. They are identical to the Raman signatures of the LSX framework.[47] The new band at 723 cm^{-1} is due to the symmetric T-O stretches.[47] The intensities of the bands at 1024 and 1060 cm^{-1} decreased a lot and two new bands at 951 and 982 cm^{-1} appeared, all of which are assigned to the asymmetric T-O stretches of T bonded to four different oxygen atoms.[48] The band between 900 and 1250 cm^{-1} is very sensitive to the Si/Al ratio of the zeolite framework. The presence of the four bands in this region suggests that the as-synthesized FAU framework has the Si/Al ratio of around 1,[48] which is consistent with our ^{29}Si MAS NMR results (see discussions below). Further, the band at 575 cm^{-1} appeared at the very beginning of the crystallization process and then disappeared when the bands at 290 and 381 cm^{-1} appeared (3.5 h sample). This suggests that the branched 4Rs were closely related to the formation of D6Rs, and that the latter was formed from the assembly of the former.[35]

The ^{27}Al MAS experiments were performed to characterize the local chemical environments of Al atoms in the intermediate phases (Figure 7.4A). The spectra of the initial gel and the gel samples heated for less than 3.3 h exhibit a broad signal centered at around 59 ppm. This indicates the absence of $Al(OSi)_2(OH)_2$ species in the samples, which gives a signal at around 70 ppm.[49] This peak can be attributed to $Al(OSi)_3(OH)_1$ or $Al(OSi)_4$ species in amorphous aluminosilicate phase.[49] This result suggests that individual 4Rs containing only $Al(OSi)_2(OH)_2$ species were not present in these samples.

A reasonable explanation is that complete or nearly complete sodalite cages and other 4R units such as joint 4R units and branched 4Rs were formed,[50] as only $Al(OSi)_3(OH)_1$ or $Al(OSi)_4$ species exists in these structures. The formation of these structures agrees with the Raman results that show bands at 1010 (sodalite cages), 500 (joint 4R units), and 575 (branched 4Rs) cm^{-1}. Their structures are shown in Scheme 7.1. Heating the initial gel for 3.5 h or longer resulted in a sharper peak at 61 ppm. The corresponding powder XRD patterns and Raman spectra show the formation of crystalline zeolite LSX. This signal is due to $Al(OSi)_4$ species with the high local ordering around Al in the crystalline zeolite framework.

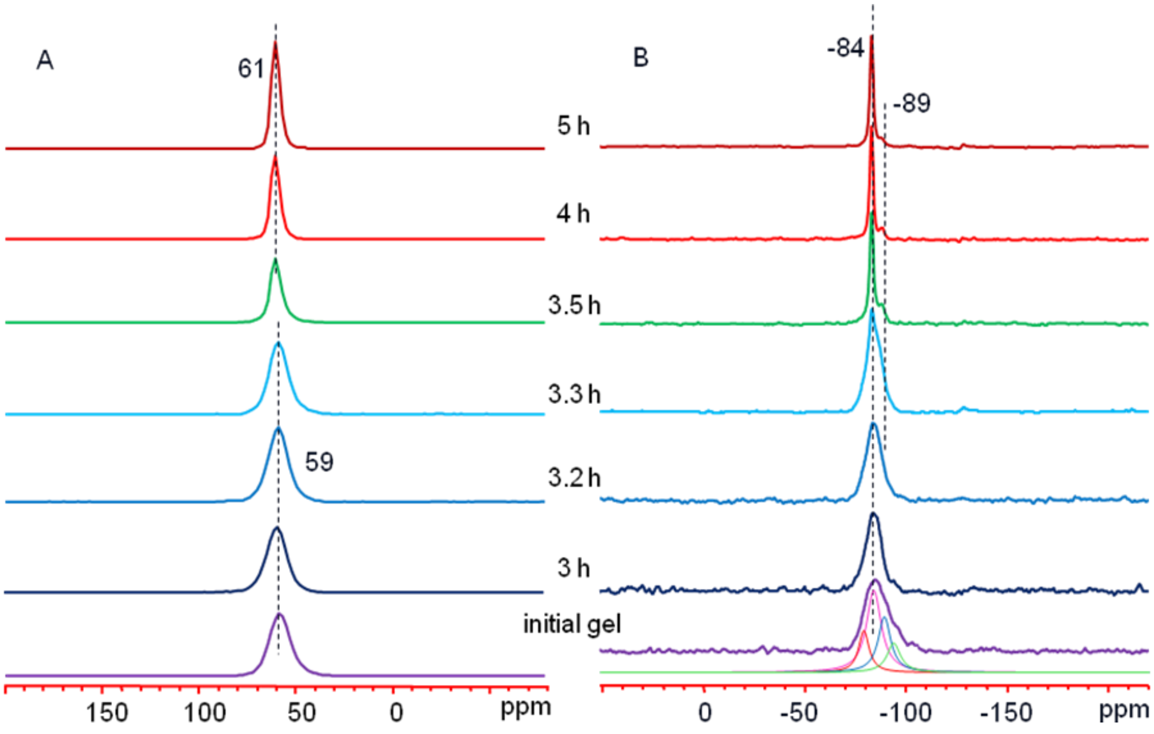

Figure 7.4 ^{27}Al MAS (A) and ^{29}Si MAS (B) spectra of selected LSX gel samples.

^{29}Si MAS spectra were obtained to examine the short-range ordering around Si atoms during crystallization (Figure 7.4B). The spectra of the initial gel and the gel samples heated for less than 3.3 h show a broad peak at around -84 ppm. After deconvolution, besides the major signal at -84 ppm, others including -80, -90, and -95 ppm coexisted. They can be attributed to $(AlO)_3SiOH$ or $(SiO)(AlO)Si(OH)_2$ (-85 ppm), $(AlO)_2Si(OH)_2$ (-80 ppm), $(SiO)_2Si(OH)_2$ (-90 ppm), and $(SiO)_2(AlO)_1SiOH$ (-95 ppm) species, respectively.[51-53] Together with the ^{27}Al NMR spectroscopy results, this observation supports the presence of joint 4R units in these samples. Heating the initial gel for 3.5 h or longer resulted in a sharp peak at -84 ppm and a much weaker one at -89 ppm. They can be ascribed to $Si(OAl)_4$ and $(SiO)_1Si(OAl)_3$ species in zeolite LSX.[54]

The Si/Al atomic ratio of zeolite framework can be calculated accurately from the relative intensities of different ^{29}Si signals.[55] A Si/Al ratio of 1.03 for zeolite LSX is obtained from the ^{29}Si MAS spectrum of 5 h sample. The elemental composition obtained from the Raman spectrum and the ^{29}Si MAS spectrum agrees with each other very well, both suggesting that the as-synthesized zeolite LSX has the Si/Al atomic ratio of around 1.

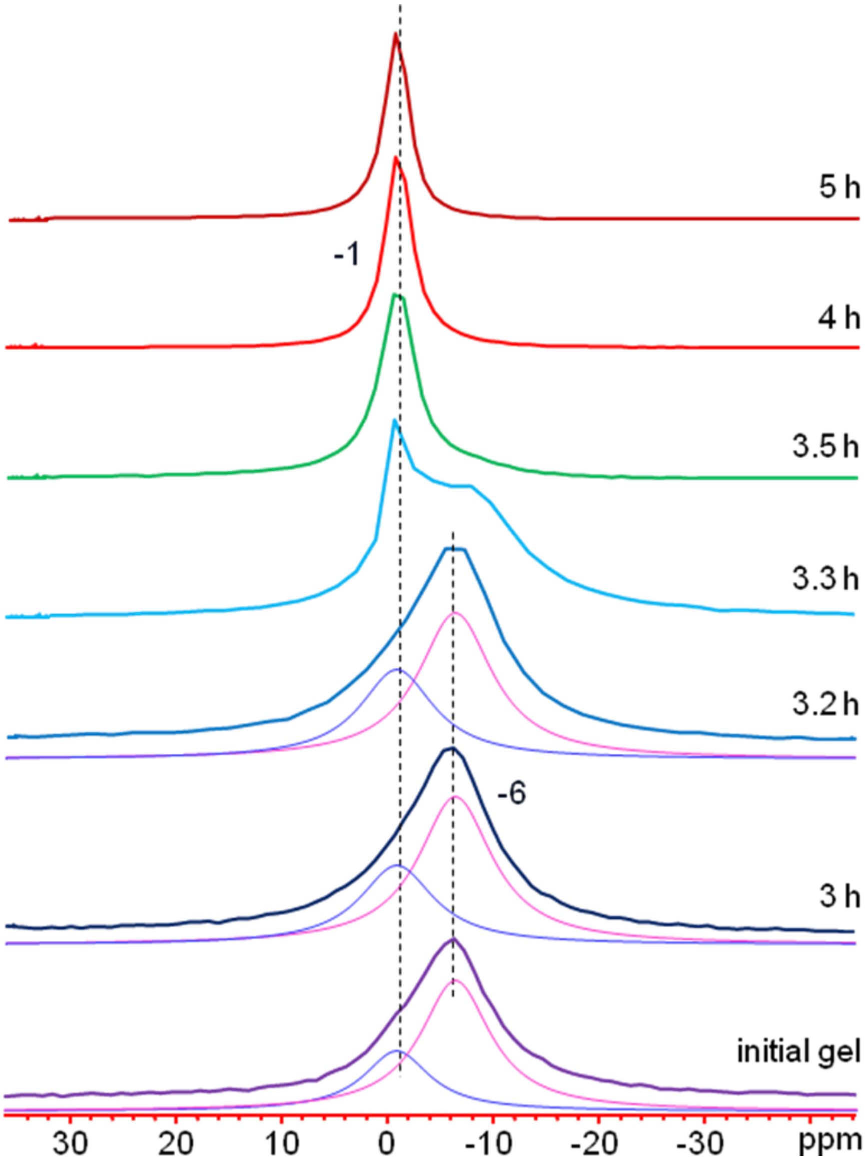

Figure 7.5 ^{23}Na MAS spectra of selected LSX gel samples.

^{23}Na NMR spectroscopy has been proven to be a powerful tool to determine cation distribution in hydrated and dehydrated zeolites.[56] Located at different crystallographic sites, Na^+ ions exhibit NMR signals with different chemical shifts. Thus, ^{23}Na MAS spectra were acquired to investigate the evolution of the local chemical environments of Na^+ ions as a function of crystallization time (Figure 7.5).

For the initial gel and the gel samples heated below 3.2 h, the spectra contain a broad and asymmetric resonance at -6 ppm. The deconvoluted spectra indicate that besides the peak at -6 ppm, there is another weaker one at -1 ppm. In crystalline hydrated faujasite zeolite, the resonance lines at -6 and -1 ppm are assigned to hydrated Na^+ ions in the sodalite cage and supercage cage, respectively.[6,57,58] The signal at -6 ppm in the gel samples below 3.2 h indicates that the cavities similar to sodalite cages were formed. This agrees with the Raman and ^{27}Al NMR spectroscopy results. The signal at -1 ppm suggests that another type of large cavities, which may result from the assembly of sodalite cages, joint 4Rs, and branched 4Rs, is likely to exist in these gel samples. The close to zero chemical shift value indicates that highly hydrated Na^+ ions may give rise to the signal. Its broadness suggests that the cations probably sat in the large cavities that were randomly distributed. Thus, the gel samples obtained at an early stage of the crystallization were mainly composed of sodalite cages and large cavities (Scheme 7.1). Upon heating the initial gel for 3.3 h, the signal at -1 ppm became more prominent. The corresponding powder XRD pattern shows the appearance of several weak reflection peaks due to the FAU structure and the Raman spectrum shows the formation of D6Rs. As this stage, it can be considered that supercages were formed. Sodalite cages were connected with each other by D6Rs to form supercages. Upon further heating, the peak at -1 ppm grew at the expense of the -6 ppm one and it is the single one in the final product (5 h sample). This reveals that under heating treatment, more supercages were formed from the reorganization within the above-mentioned structures. Further, this signal was much narrower, suggesting that highly hydrated Na^+ ions were located in a more uniform environment, which was supercage.

There are very few solid-state ^{39}K NMR applications because of difficulties in obtaining spectra, as the two NMR-active isotopes of potassium, ^{39}K and ^{41}K (natural abundance of 93.7 and 6.3%, resectively), are spin 3/2 quadrupolar nuclei with low magnetogyric ratios.[59] To investigate the role played by K^+ ions, ^{39}K MAS NMR experiments were carried out on selected gel samples at a magnetic field of 9.4 T at first. Unfortunately, no signals were observed due to the low sensitivity and broad resonances. To overcome the unfavourable properties of ^{39}K, the experiments were then performed at 21.1 T (Figure 7.6). The simulated results of the ^{39}K spectra are presented in Table 7.1.

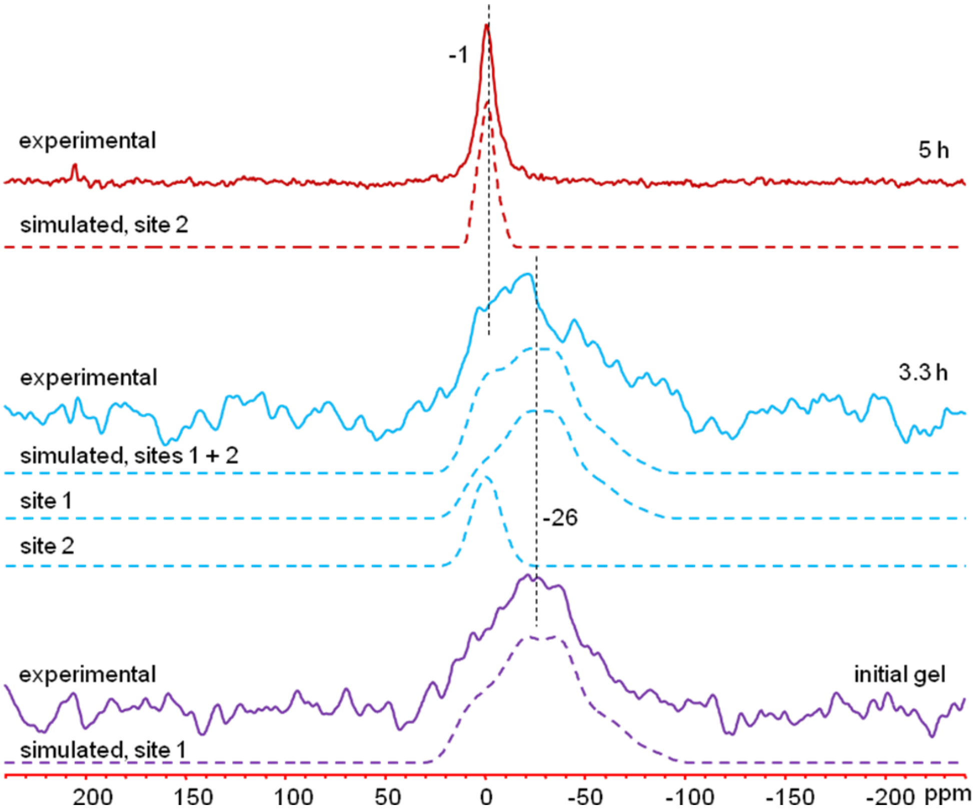

Figure 7.6 ^{39}K MAS spectra of selected LSX gel samples (5 KHz spinning speed; 2 s pulse delay; 22000 scans for each sample)

In 5 h sample, a sharp peak at -1 ppm is present. This chemical shift value is close to zero and also near -9 ppm reported for hydrated potassium gallium silicate inorganic polymers.[60] This suggests that K^+ ions in as-made LSX were highly hydrated.[60] The simulated result of the ^{39}K spectrum shows a small C_Q value (0.7 MHz), indicating a relatively symmetric local environment around K^+ ions. The signal at -1 ppm may be mainly due to highly hydrated K^+ ions located in the supercages.

Different from that of 5 h sample, the spectrum of the initial gel exhibits a much broader signal centered at around -26 ppm. This value is not only smaller than -1 ppm but larger than -97 ppm due to highly dehydrated K^+ ions in potassium aluminosilicate inorganic polymers heated up to 1673 K.[61] The signal at -26 ppm, therefore, is tentatively assigned to partially hydrated K^+ ions.[62] Further, despite of its broadness, it is not a featureless signal. It shows a lineshape due to quadrupolar interaction and can be simulated using one site (Figure 7.6 and Table 7.1). The C_Q value is 1.7 MHz, larger than 0.7 MHz due to highly hydrated K^+ ions in the product. This signifies that the local environment of partially hydrated K^+ ions in the initial gel, to a certain degree, had short-range ordering. These K^+ ions may sit within the large cavities or outside the complete or nearly complete sodalite cages, as suggested by the ^{23}Na NMR results. They may be coordinated to both water molecules and oxygen atoms of 4R structures or sodalite cages. Upon heating the initial gel for 3.3 h, the peak at -26 ppm now has a smaller C_Q value (1.6 MHz), suggesting that partially hydrated K^+ ions were located in a more ordered environment. Further, a shoulder at around -1 ppm appeared. This suggests the formation of supercages and that some partially hydrated K^+ ions moved into supercages. This result agrees with the ^{23}Na NMR discussions above. Further, the Raman spectrum of 3.3

h sample presents a 460 cm^{-1} band due to the interactions between K$^+$ ions and 4Rs.[47] The appearance of the signal at -1 ppm thus suggests that partially hydrated K$^+$ ions organized the assembly of these 4R structures and large cavities into supercages and then became more hydrated.

Table 7.1 ^{39}K NMR parameters obtained from the simulation of ^{39}K NMR spectra.

Samples	Sites	C_Q (MHz)	η_Q	δ_{iso} (ppm)
Initial gel	1	1.70 (2)	0.60 (2)	18 (1)
3.3 h	1	1.60 (2)	0.60 (2)	13 (1)
	2	0.70 (2)	0.75 (2)	7.3 (2)
5 h	2	0.70 (2)	0.75 (2)	7.3 (2)

7.4 Summary

At the very beginning of the synthesis process when different reactive species were mixed together, the amorphous initial gel dominated by the aluminosilicate phase in the form of complete or nearly complete sodalite cages, large cavities, joint 4Rs, and branched 4Rs was formed. Upon the heating treatment under HTS conditions, D6Rs were formed from the connection of joint 4Rs and branched 4Rs. They were assembled with sodalite cages or large cavities to form the crystalline framework of zeolite LSX. An illustration of the crystallization process of zeolite LSX is shown in Scheme 7.1. ^{23}Na and ^{39}K NMR results indicate that the positions of hydrated Na$^+$ and K$^+$ ions changed during the crystallization and such changes accompanied the transformation process above. The two types of cations may work together to template the assembly process of zeolite LSX.

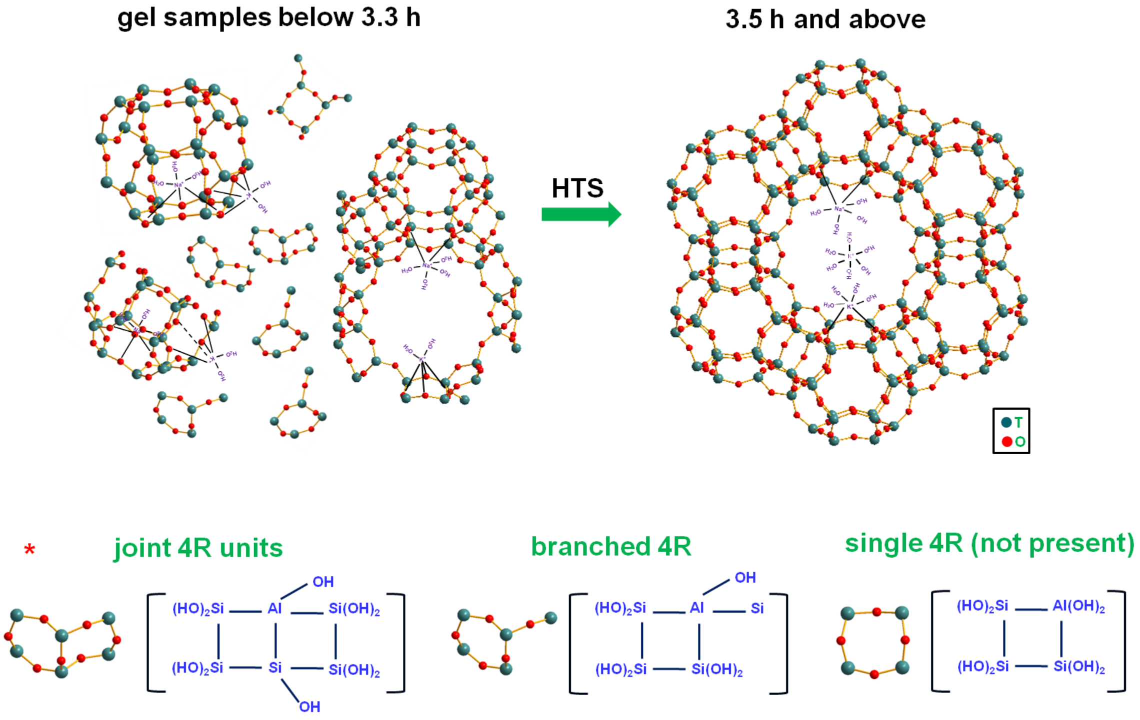

Scheme 7.1 Formation process of zeolite LSX. The structure of branched 4R is drawn according to work by Can Li group.

7.5 References

(1) Davis, R. J. *J. Catal*. **2003**, *216*, 396-405.
(2) Schoonheydt, R. A.; Geerlings, P.; Pidko, E. A.; van Santen, R. A. *J. Mater. Chem.* **2012**, *22*, 18705-18717.
(3) Smit, B.; Maesen, T. L. M. *Chem. Rev*. **2008**, *108*, 4125.
(4) Zhang, L.; Laak, A. N. C.; Jongh, P. E.; Jong, K. P. *Microporous Mesoporous Mater*. **2009**, *126*, 115-124.
(5) Lee, Y.; Carr, S. W.; Parise, J. B. *Chem. Mater.* **1998**, *10*, 2561-2570.
(6) Frising, T.; Leflaive, P. *Microporous Mesoporous Mater*. **2008**, *114*, 27-63.
(7) Kovacheva, P.; Arishtirova, K.; Predoeva, A. *React. Kinet. Catal. Lett.* **2003**, *79*, 149-155.
(8) Ojo, A. F.; Fitch, F. R.; Bülow, M.; Gittleman, C. S.; Jale, S. R. US Patent 6,596,256, 2003.
(9) Yang, R. T.; Hutson, N. D. US Patent 6,780,806, 2004.
(10) Jasra, R.; Choudary, N.; Bhat, S. *Ind. Eng. Chem. Res.* **1996**, *35*, 4221-4229.
(11) Basaldella, E.; Tara, J. *Zeolites* **1995**, *15*, 243-246.
(12) Vitale, G.; Bull, L. M.; Morris, R. E.; Cheetham, A. K.; Toby, B. H.; Coe, C. G.; MacDougall, J. E. *J. Phys. Chem.* **1995**, *99*, 16087-16092.
(13) Schaefer, D.; Favre, D.; Wilhelm, M.; Weigel, S.; Chmelka, B. *J. Am. Chem. Soc.* **1997**, *119*, 9252-9267.
(14) Plevert, J.; Di Renzo, F.; Fajula, F.; Chiari, G. *J. Phys. Chem. B* **1997**, *101*, 10340-10346.
(15) Feuerstein, M.; Engelhardt, G.; McDaniel, P.; MacDougall, J.; Gaffney, T. *Microporous Mesoporous Mater*. **1998**, *26*, 27-35.
(16) Jale, S. R.; Büow, M.; Fitch, F. R.; Perelman, N.; Shen, D. *J. Phys. Chem. B* **2000**, *104*, 5272-5280.
(17) Plee, D. US Patent 6,264,881, 2001.
(18) Caldarelli, S.; Buchholz, A.; Hunger, M. *J. Am. Chem. Soc.* **2001**, *123*, 7118-7123.
(19) Plévert, J.; Okubo, T.; Wada, Y.; O'Keeffe, M.; Tatsumi, T. *Chem. Commun.* **2001**, 2112-2113.
(20) Kazansky, V. B.; Bülow, M.; Tichomirova, E. *Adsorpt*. **2001**, *7*, 291-299.
(21) Shen, D.; Bülow, M.; Jale, S. R.; Fitch, F. R.; Ojo, A. F. *Microporous Mesoporous Mater*. **2001**, *48*, 211-217.
(22) Loeser, T.; Freude, D.; Mabande, G. T. P.; Schwieger, W. *Chem. Phys. Lett.* **2003**, *370*, 32-38.
(23) Buhl, J. C.; Gerstmann, M.; Lutz, W.; Ritzmann, A. Z. *Anorg. Allg. Chem.* **2004**, *630*, 604-608.
(24) Romero, M.; Gomez, J.; Ovejero, G.; Rodriguez, A. *Mater. Res. Bull.* **2004**, *39*, 389-400.
(25) Readman, J. E.; Grey, C. P.; Ziliox, M.; Bull, L. M.; Samoson, A. *Solid State Nucl. Magn. Reson.* **2004**, *26*, 153-159.
(26) Kazansky, V. B.; Sokolova, N. A.; Bülow, M. *Microporous Mesoporous Mater*. **2004**, *67*, 283-289.
(27) Sokolova, N.; Kazanskii, V. *Kinet. Catal*. **2005**, *46*, 879-883.

(28) Khemthong, P.; Wittayakun, J.; Prayoonpokarach, S. *Suranaree J. Sci. Technol.* **2007**, *14*, 367-379.

(29) Wozniak, A.; Marler, B.; Angermund, K.; Gies, H. *Chem. Mater.* **2008**, *20*, 5968-5976.

(30) Schneider, D.; Toufar, H.; Samoson, A.; Freude, D. *Solid State Nucl. Magn. Reson.* **2009**, *35*, 87-92.

(31) Guesmi, H.; Massiani, P.; Nouali, H.; Paillaud, J. L. *Microporous Mesoporous Mater.* **2012**, *159*, 87-95.

(32) Kuhl, G. H. *Zeolites* **1987**, *7*, 451-457.

(33) Iwama, M.; Suzuki, Y.; Plévert, J.; Itabashi, K.; Ogura, M.; Okubo, T. *Cryst. Growth Des.* **2010**, *10*, 3471-3479.

(34) Xiong, G.; Yu, Y.; Feng, Z.; Xin, Q.; Xiao, F. S.; Li, C. *Microporous Mesoporous Mater.* **2001**, *42*, 317-323.

(35) Fan, F.; Feng, Z.; Li, G.; Sun, K.; Ying, P.; Li, C. *Chem. Eur. J.* **2008**, *14*, 5125-5129.

(36) Fan, F.; Feng, Z.; Li, C. *Chem. Soc. Rev.* **2010**, *39*, 4794-4801.

(37) Lok, B.; Cannan, T.; Messina, C. *Zeolites* **1983**, *3*, 282-291.

(38) Le Caér, S.; Brunet, F.; Chatelain, C.; Durand, D.; Dauvois, V.; Charpentier, T.; Ph. Renault, J. *J. Phys. Chem. C*, **2012**, *116*, 4748-4759.

(39) Eichele, K.; Wasylishen, R. E.; v. 1.19.15 ed. 2009.

(40) Inayat, A.; Knoke, I.; Spiecker, E.; Schwieger, W. *Angew. Chem. Int. Ed.* **2012**, *51*, 1962-1965.

(41) Dutta, P. K.; Rao, K. M.; Park, J. Y. *J. Phys. Chem.* **1991**, *95*, 6654-6656.

(42) Dutta, P. K.; Shieh, D.; Puri, M. *Zeolites* **1988**, *8*, 306-309.

(43) Bremard, C.; Le Maire, M. *J. Phys. Chem.* **1993**, *97*, 9695-9702.

(44) Miecznikowski, A.; Hanuza, J. *Zeolites* **1985**, *5*, 188-193.

(45) Twu, J.; Dutta, P. K.; Kresge, C. T. *Zeolites* **1991**, *11*, 672-679.

(46) Dutta, P. K.; Shieh, D.; Puri, M. *J. Phys. Chem.* **1987**, *91*, 2332-2336.

(47) Depla, A.; Verheyen, E.; Veyfeyken, A.; Gobechiya, E.; Hartmann, T.; Schaefer, R.; Martens, J. A.; Kirschhock, C. E. A. *Phys. Chem. Chem. Phys.* **2011**, *13*, 13730-13737.

(48) Dutta, P. K.; Twu, J. *J. Phys. Chem.* **1991**, *95*, 2498-2501.

(49) Bodart, P.; Nagy, J. B.; Gabelica, Z.; Derouane, E. G. *J. Chim. Phy.* **1986**, *83*, 777-790.

(50) Ren, L.; Li, C.; Fan, F.; Guo, Q.; Liang, D.; Feng, Z.; Li, C.; Li, S.; Xiao, F. S. *Chem. Eur. J.* **2011**, *17*, 6162-6169.

(51) Doremieux-Morin, C.; Martin, C.; Bregeault, J. M.; Fraissard, J. *Appl. Catal.* **1991**, *77*, 149-161.

(52) Maciel, G. E.; Bronnimann, C. E.; Zeigler, R. C.; Chuang, I. S.; Kinney, D. R.; Keiter, E. A. *Adv. Chem. Ser.* **1994**, *234*, 269-269.
(53) Liu, C. C.; Maciel, G. E. *J. Am. Chem. Soc.* **1996**, *118*, 5103-5119.
(54) Ogura, M.; Kawazu, Y.; Takahashi, H.; Okubo, T. *Chem. Mater.* **2003**, *15*, 2661-2667.
(55) Lippmaa, E.; Maegi, M.; Samoson, A.; Tarmak, M.; Engelhardt, G. *J. Am. Chem. Soc.* **1981**, *103*, 4992-4996.
(56) Koller, H.; Engelhardt, G.; Kentgens, A. P. M.; Sauer, J. *J. Phys. Chem.* **1994**, *98*, 1544-1551.
(57) Hannus, I.; Kiricsi, I.; Lentz, P.; Nagy, J. *Colloids Surf. A* **1999**, *158*, 29-34.
(58) Seidel, A.; Tracht, U.; Boddenberg, B. *J. Phys. Chem.* **1996**, *100*, 15917-15922.
(59) Moudrakovski, I. L.; Ripmeester, J. A. *J. Phys. Chem. B* **2007**, *111*, 491-495.
(60) Durant, A. T.; MacKenzie, K. J.; Maekawa, H. *Dalton Trans. 40*, 4865-4870.
(61) Barbosa, V. F.; MacKenzie, K. J. *Mater. Lett.* **2003**, *57*, 1477-1482.
(62) Smith, M. *Clays Clay Miner.* **1992**, *40*, 253-261.

Chapter 8 Examining the Formation of Titanosilicates ETS-10 and ETS-4

8.1 Introduction

Zeolites, which are also termed as molecular sieves, have been widely used industrially in the fields of chemisorptions and heterogeneous catalysis.[1] The replacement of Si by Al in a pure silica framework leads to a charge imbalance that must be balanced by either protons or cations in the framework. Protonic zeolites exhibit strong Brønsted acidity, which allows them to play a central role in acid-catalyzed petrochemical processes.[2,3] Cation exchanged zeolites, on the other hand, are often used both in adsorption and catalysis, which depends on the nature of the cations.

A novel class of molecular sieves that consists of microporous titanosilicates, is receiving great interest because of its zeolite-like properties and novel applications.[4] To date, ten structurally proven open framework titanosilicates have been synthesized.[5] Among them, the most studied ones are ETS-10 and ETS-4 (ETS refers to Engelhard Titanium Silicate).

Microporous titanosilicate ETS-10 is a large-pore zeotype material, which was first synthesized by Engelhard Corporation in 1989.[6] It belongs to a family of Ti-containing silicates that consist of corner-sharing TiO_6 octahedra and SiO_4 tetrahedra as building units.[7] The presence of each Ti^{4+} ion in an octahedron generates two negative charges, which are balanced by non-framework and exchangeable Na^+ and K^+ ions.[8] The as-formed crystalline ETS-10 is a mixture of two polymorphs, A and B. Polymorph A has either $P4_1$ or $P4_3$ symmetry and polymorph B belongs to space group $C2/c$.[9,10] Polymorph A has identical projections along $[100]$ and $[010]$ to that of polymorph B along $[110]$ and $[1\bar{1}0]$. The pore structure of ETS-10 comprises 12, 7, 5, and 3-membered rings (12, 7, 5, and 3Rs) and has one dimensional channel system. The diameter of the pore is defined by 12R apertures (8 × 5 Å). The framework of ETS-10 contains -Ti-O-Ti-O- chains, which run in two perpendicular directions (Figure 8.1).

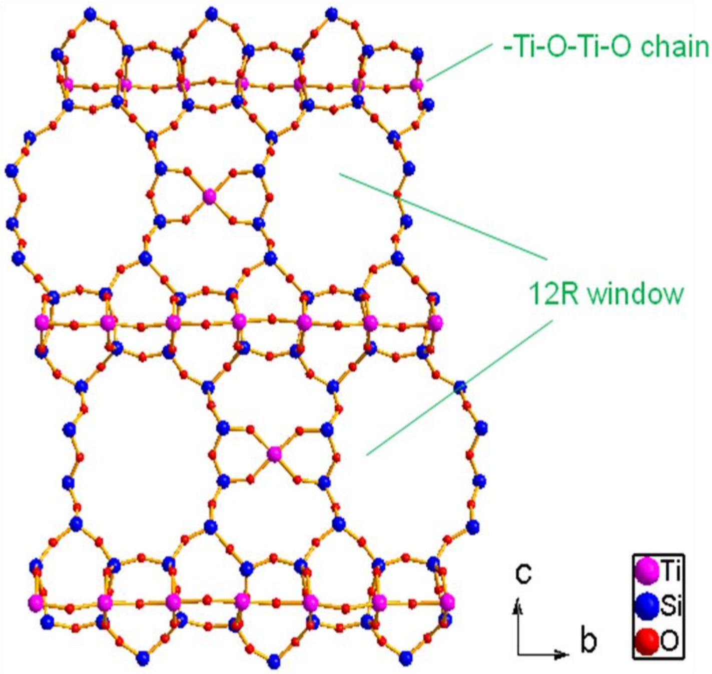

Figure 8.1 Framework of ETS-10 polymorph A viewed along the *a* axis.

Different from ETS-10, besides $[TiO_6]$ octahedra and $[SiO_4]$ tetrahedra, the framework of ETS-4 also contains square-pyramidal $[TiO_5]$ titanate units (Figure 8.2A). Although 12R pores are present in the structure of ETS-4, access to the channel system is limited to relatively narrow 8Rs due to faulting of the larger pores.[11-13] ETS-4 is considered as a small pore molecular sieve (*ca.* 4 Å pore diameter) and its structure is similar to that of the mineral zorite.[11-13] It was first discovered in 1990.[14] The TiO_6

octahedra connect each other by sharing opposite corners, forming one-dimensional linear -O-Ti-O-Ti- chains that run zigzag along the *b* axis (Figure 8.2B) and exhibit quantum confinement effects in the framework.[15,16]

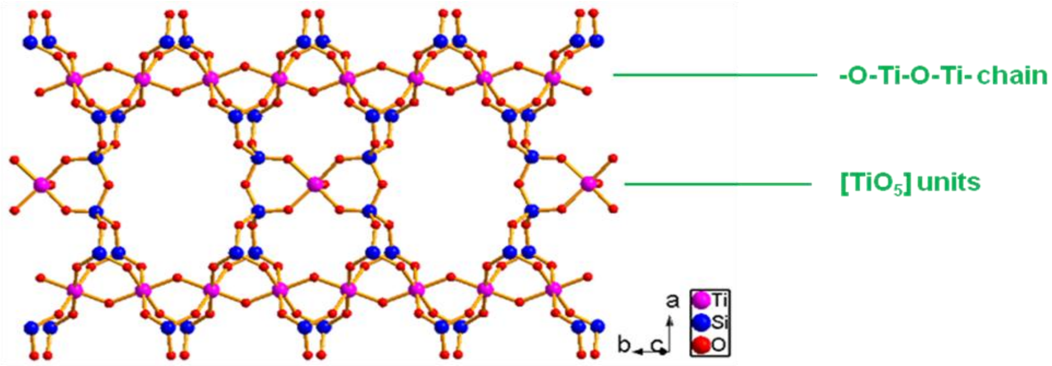

Figure 8.2 Framework of ETS-4 viewed along the *c* axis.

Up to now, ETS-10 and ETS-4 have attracted extensive attention as ion-exchangers, adsorbents, and heterogeneous catalysts due to their high cation exchange capacity, good accessibility for guest molecules, and the presence of electrically isolated titanium chains.[17-21] The hydrothermal synthesis method (HTS) is the most commonly used method for the synthesis of these two molecular sieves.

The crystallization kinetics of ETS-10 has been extensively studied, with or without organic templates, using various Ti and Si sources.[22-36] However, few of them dealt with the crystallization mechanism. Li and co-workers studied the synthetic mechanism of ETS-10 by Raman and ^{29}Si solid-state NMR spectroscopies.[37] They proposed that the formation of Ti-O-Si species in the form of 3Rs was the key step during the hydrothermal synthesis process of ETS-10. There have also been a number of studies reported on the synthesis of ETS-4, but most of them were focused on synthesis methods and conditions used, properties of as-formed products, as well as crystallization kinetics.[34,36,38-43] To the best of our knowledge, the assembly process of ETS-4 has not been reported. In the present work, the formation of these two molecular sieves prepared by the HTS method was investigated. Furthermore, an alternative method, dry gel conversion (DGC), was also employed to examine the assembly process of ETS-10. New insights into the crystallization of ETS-10 and ETS-4 were obtained.

8.2 Experimental section

8.2.1 Sample preparation

8.2.1.1 HTS method

8.2.1.1 Preparation of ETS-10

ETS-10 was synthesized by using the method of the Sivasanker group.[24] The reagents were choline chloride (Sigma, ca. 98 wt%), titanium trichloride (Sigma-Aldrich, 12 wt% in 5-12 wt% hydrochloric acid), sodium silicate (Aldrich, ca. 7 wt% Na_2O and 27 wt% SiO_2), sodium hydroxide (Caledon Laboratory Chemicals, ca. 97 wt%), and potassium fluoride (Aldrich, spray-dried, 99 wt%). The initial gel molar composition was $1.14C_5H_{14}ClNO:1.0TiO_2:5.71SiO_2:3.7Na_2O:0.95KF:256.9H_2O$.

A typical procedure for the HTS synthesis of ETS-10 gel samples was the following. Solution A consisting of 15.9 g of sodium silicate solution and 11.6 g of distilled water was stirred vigorously for 5 min. At the same time, Solution B was prepared by dissolving 1.8 g of sodium hydroxide pallets in 11.6 g of distilled water and was added slowly to Solution A under stirring. The gel was mixed for 15 min and then a solution containing 2.0 g of choline chloride and 11.6 g of distilled water was added slowly. The mixture was stirred for 30 min. When a uniform solution was obtained, 16.1 g of titanium trichloride solution was added to this mixture dropwise, followed by adding 1.4 g of potassium fluoride. The final sticky grey gel (pH = 10.8-11.0) was stirred vigorously for 60 min at room temperature (pH = 10.7-10.8). It (referred to as the initial gel) was then subdivided into several proportions and put into a series of Teflon-lined autoclaves. The crystallization was carried out at 473 K in an oven for different reaction times. The intermediate samples were taken out of the oven during the reaction after specified lengths of time and quenched in cold water. The solids in each autoclave were filtered and then washed thoroughly by distilled water. The solid materials were then carefully dried in air at room temperature and kept in tightly sealed glass vials for analysis.

8.2.1.1.2 Preparation of ETS-4

ETS-4 was synthesized by using the method of the Kim group.[44] The reagents were titanium trichloride (Sigma-Aldrich, 12 wt% in 5-12 wt% hydrochloric acid), sodium silicate (Aldrich, ca. 7 wt% Na_2O and 27 wt% SiO_2), sodium hydroxide (Caledon Laboratory Chemicals, ca. 97 wt%), and potassium fluoride (Aldrich, spray-dried, 99 wt%). The initial gel molar composition (TiO_2:SiO_2:Na_2O:KF:H_2O) is 1.0:5.5:6.5:2.5:273 in a molar ratio.

A typical procedure for the HTS synthesis of ETS-4 gel samples was the following: 7.6 g of sodium silicate solution was first added to 7.9 g of distilled water and mixed vigorously for 20 min in Beaker A. At the same time, in Beaker B, 2.2 g of sodium hydroxide pallets were dissolved in 6 g of distilled water and subjected to vigorous stirring for 20 min. The solution in Beaker B was then added to the solution in Beaker A and mixed vigorously for 60 min under stirring until a homogeneous solution was obtained. Thereafter, 8 g of titanium trichloride solution was added to this mixture dropwise, followed by another 20 min of mixing. Finally, a solution containing 0.9 g of potassium fluoride and 6 g of distilled water was added to the mixture obtained above. The final solution (referred to as the initial gel) was mixed vigorously for 60 min at room temperature. Upon completion of mixing, the solution (pH $\approx$ 12.1) was subdivided into several proportions and put into a series of Teflon-lined autoclaves. The crystallization was carried out at 443 K in an oven for different reaction times. The intermediate samples were taken out of the oven and quenched in cold water. The product in each autoclave was filtered and the solid phase was washed thoroughly by using distilled water. The solid materials were then carefully dried in air at room temperature and kept in tightly sealed glass vials for analysis.

8.2.1.2 DGC method

A typical procedure for the DGC synthesis of ETS-10 gel samples was the following. According to the corresponding hydrothermal synthesis procedures, the final uniform mixture was made. It was then dried at 353 K under constant stirring until a solid gel without apparent liquid was formed. This solid gel was then ground into a fine powder and sealed in glass vials. It was referred to as the initial DGC dry gel. A series of intermediates were synthesized by placing 1.0 g of the initial dry gel powder into small Teflon cups. Each cup was placed in a 23-mL Teflon-lined autoclave with certain amount of distilled water at the bottom and heated in an oven at 473 K for different reaction times. The reactions were quenched in cold water. For comparison, the solid sample from each cup was divided into two parts. One part was directly dried in air (unwashed sample) and the other part was washed using lots of distilled water and the solids were separated from the liquids by centrifugation (washed sample). The solid gel samples were kept in tightly sealed glass vials.

8.2.2 Characterization

Powder XRD patterns were recorded on a Rigaku diffractometer using Co Kα radiation (λ = 1.7902 Å). Representative samples used for SEM study were first coated with 3 nm osmium metal using a Filgen OPC-80T instrument and their morphology was then examined using a FIB/SEM 1540XB microscope. Raman experiments were carried out with a customized Raman microspectroscopy system. A 514 nm line produced from an Ar^+ laser (Coherent Inc.) was used as the excitation source. The resolution was 0.1 cm^{-1}.

Most NMR experiments were carried out on a Varian/Chemagnetics Infinityplus 400 WB spectrometer equipped with three rf channels operating at the field strength of 9.4 T. The Larmor frequencies of ^{1}H, ^{13}C, ^{23}Na, and ^{29}Si were 399.5, 100.4, 105.7, and 79.4 MHz, respectively. The chemical shifts of ^{13}C, ^{23}Na, and ^{29}Si were referenced to adamantane (tertiary carbons, 38.6 ppm with respect to liquid tetramethylsilane), 1 M NaCl aqueous solution (0 ppm), and tetrakis(trimethylsilyl)-silane ($SiMe_3$, −9.9 ppm with respect to liquid tetramethylsilane). Depending on the requirements of individual experiment, three MAS probes were used (a Varian/Chemagnetics 9.5-mm, a 4.0-mm H/X/Y triple-tuned MAS, and a 3.2-mm H/X double-tuned MAS probe). The ^{13}C CP

MAS spectra recorded by using the 4.0 mm probe with the Hartmann-Hahn conditions set on adamantane, and the ^{1}H 90° pulse length was 4 μs. A contact time of 2 ms was used, and the pulse delay was 9 s. The proton decoupling field was about 60 kHz. The ^{23}Na spectra were acquired using a very small pulse angle with a pulse delay of 1 s. For the ^{29}Si MAS experiments, a 45° pulse was used with a pulse delay of 60 s. ^{23}Na 3QMAS experiments were performed using the 3.2-mm probe and the spinning speed was 20 kHz. The spectra were obtained by utilization of a three-pulse z-filter sequence.[45] The rf strengths of the first two hard pulses and third soft pulse were optimized individually, and the optimized pulse lengths were 2.86, 1.03, and 10.00 μs for the three consecutive pulses.

For selected ETS-10 samples, ^{39}K NMR experiments were carried out at 21.1 T on a Bruker Advance-900 spectrometer at the National Ultrahigh-Field NMR Facility for Solids in Ottawa, Canada. The Larmor frequency of ^{39}K (natural abundance of 93.7%) is 42.0 MHz. The chemical shift was referenced to 1.0 M KCl (aq) in H_2O. The spectra were acquired using a 7.5-mm H/X MAS Bruker probe with a spinning speed of 5 kHz.

^{23}Na and ^{39}K NMR parameters, including C_Q, η_Q, and δ_{iso}, were determined by analytical simulations of NMR spectra using the WSOLIDS simulation package.[46] The experimental error for each measured parameter was determined by visual comparison of experimental spectra with simulations. The parameter of concern was varied bidirectionally starting from the best fit value and all other parameters were kept constant, until noticeable differences between the spectra were observed.

8.3 Results and discussion

8.3.1 Formation of ETS-10

8.3.1.1 Crystallization under HTS conditions

Figure 8.3 shows the powder XRD patterns of selected HTS gel samples. The XRD pattern of as-made product (9 d sample) is characteristic of ETS-10 material with high crystallinity. The *d*-spacings are very similar to those reported in the literature,[6,9] implying that the product is a pure ETS-10 molecular sieve.

The gel samples heated for less than 4 d exhibit only a featureless broad reflection pattern, indicating that these samples are essentially amorphous. After 5 d of heating under HTS treatments, a very weak broad reflection peak with 2θ values of around 29° is observed (labeled as an inverted triangle), suggesting that a new phase has been formed. The position of this peak is the same as that of the strongest peak in the crystalline product, implying that the new phase is ETS-10. Upon heating the initial gel for 6 d, the powder pattern exhibits a series of reflections in the low and middle 2θ regions, the positions of which are identical to those in ETS-10, demonstrating that more amorphous phase has transformed into ETS-10. Highly crystalline ETS-10 was obtained after heating for 9 d.

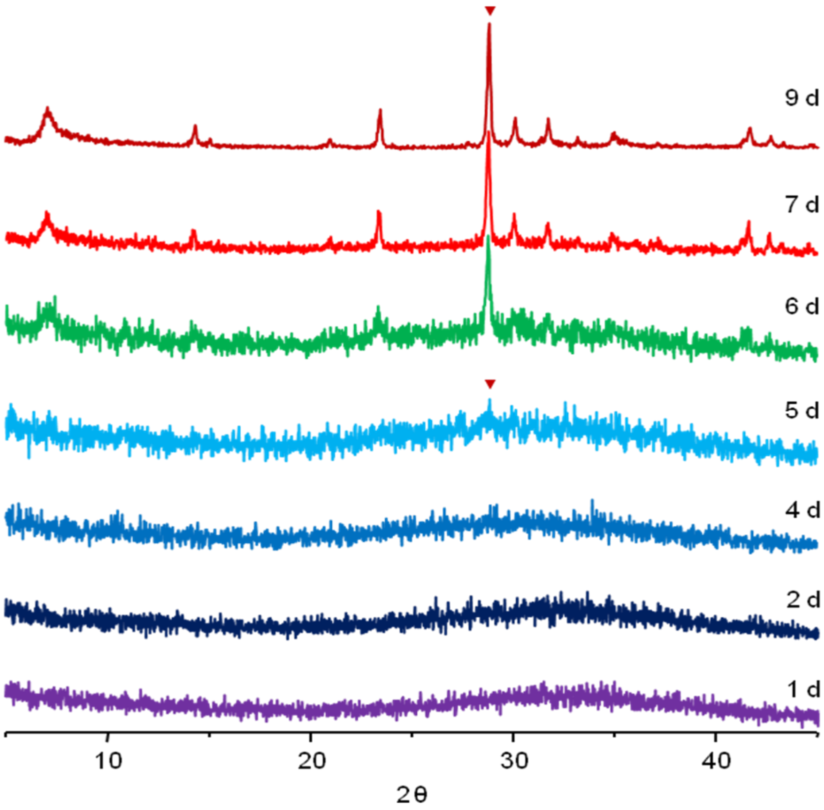

Figure 8.3 Powder XRD patterns of selected ETS-10 HTS gel samples. ▼ indicates the formation of ETS-10 phase.

Figure 8.4 shows the SEM images of selected HTS gel samples. The pictures of 1 d sample (Figures 8.4A and B) exhibit disordered aggregates. After heating the initial gel for 6 d, the number of disordered aggregates has decreased significantly, and a phase with layered morphology has appeared (Figures 8.4C and D). Agreeing with the corresponding powder XRD pattern, this suggests that the reorganization of the gel structure has occurred. The images of 9 d sample in Figures 8.4E and F reveal plenty of intergrown fine crystals and the presence of wheat-shaped tiny crystallites.[24] The morphological evolution as a function of heating time illustrated by SEM pictures agrees with the XRD results.

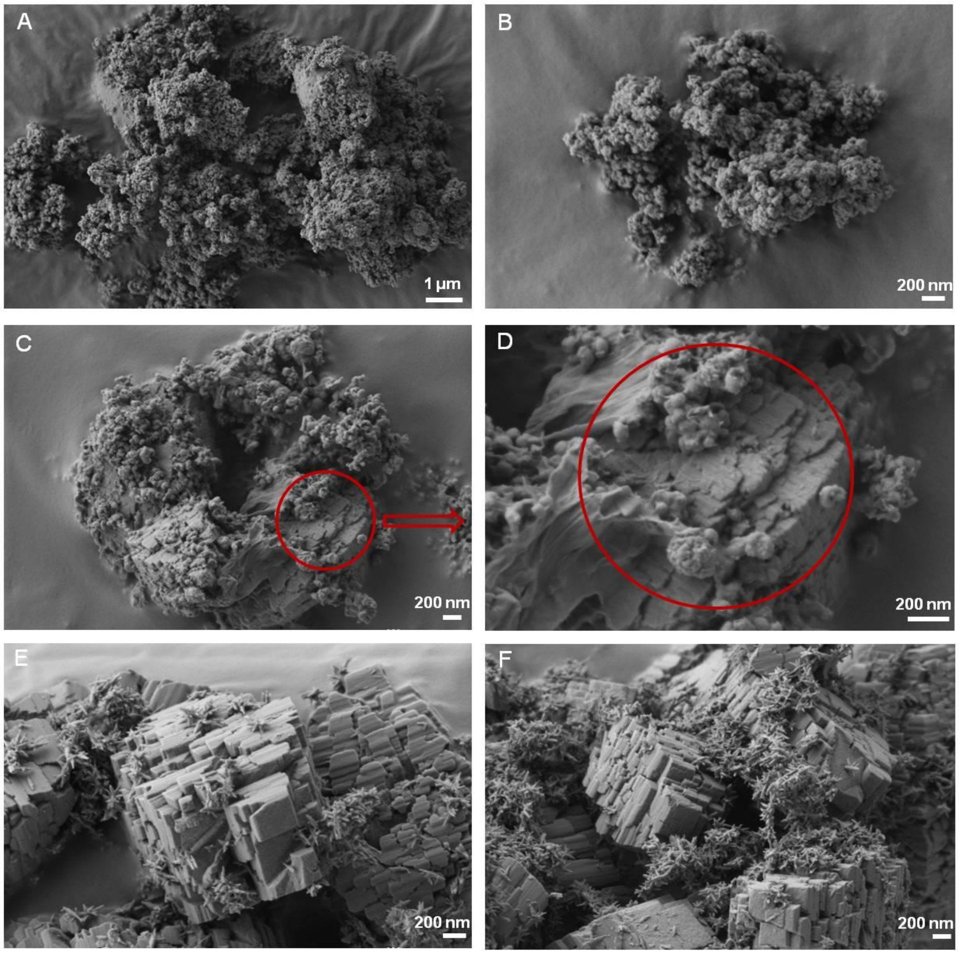

Figure 8.4 SEM images of 1 d (A and B), 6 d (C and D), and 9 d samples (E and F).

^{23}Na MAS NMR experiments were carried out in order to get an insight into the crystallization process in more detail at an atomic level (Figure 8.5). The ^{23}Na spectra of gel samples below 4 d contain a broad peak at around -11 ppm. The linewidth of the peak decreased with increasing the heating time and it shifted to -10 ppm upon heating the initial gel for 4 d or longer. The much narrower linewidth of the peak in as-made product (9 d sample) suggests that Na^+ ions were hydrated with a high degree of mobility, while the broader linewidth at the beginning of the synthesis indicates a much slower mobility and a wider distribution of local environments. This may be due to that Na^+ ions were complexed with negatively charged groups.[47] Employing Raman spectroscopy, Can Li’s group pointed out the presence of negatively charged monomeric silicate species during the formation of ETS-10.[37] Na^+ ions can complex with these monomeric silicate anions. A weak peak at around 7 ppm is due to sodium chloride (chloride is from choline chloride and titanium trichloride).[48]

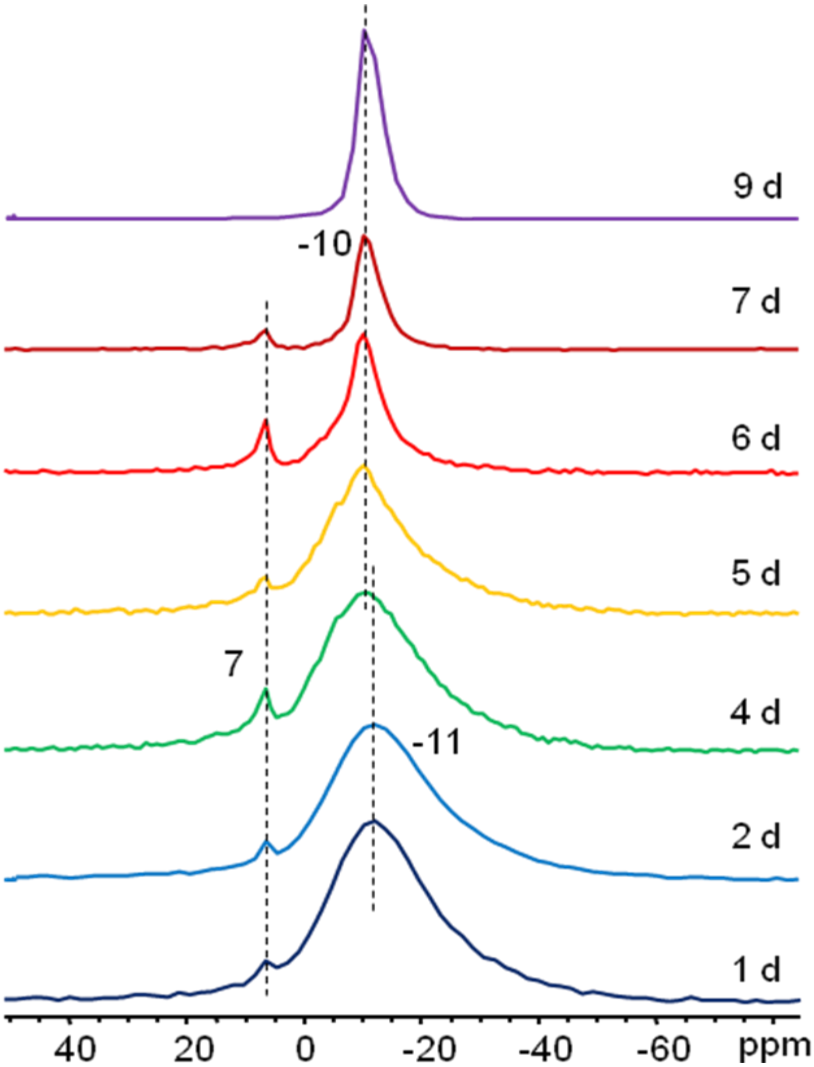

Figure 8.5 ^{23}Na MAS spectra of selected ETS-10 HTS gel samples.

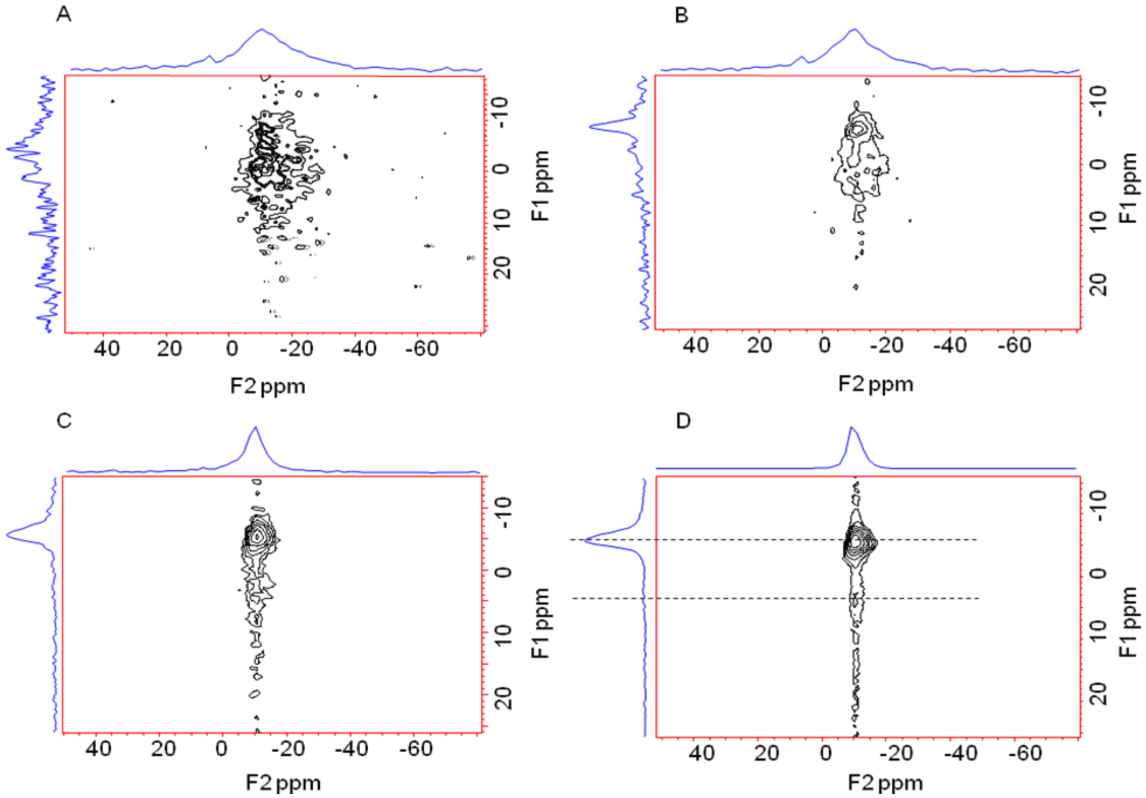

Figure 8.6 ^{23}Na 3QMAS spectra of (A) 4 d, (B) 5 d, (C) 6 d, and (D) 9 d samples.

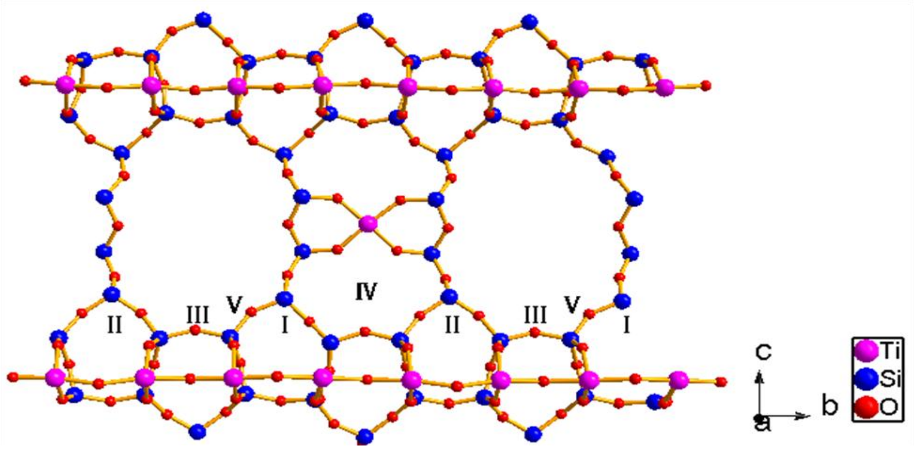

Figure 8.7 Five proposed cation sites in ETS-10.[49]

^{23}Na 3QMAS has been widely used to investigate the number of non-equivalent sites and quadrupolar parameters of Na$^+$ ions in zeolites.[49-52] To obtain information about sodium behavior during crystallization, the ^{23}Na 3QMAS technique was employed in the present work on selected HTS gel samples (Figure 8.6). The spectra of 6 d and 9 d samples are similar (Figures 8.6C and D). They exhibit two signals in the F1 dimensions with a strong one at -6 ppm and much weaker one at around 4 ppm. On the basis of the previous work by Anderson's group,[49] the peak at -6 ppm can be assigned to the Na$^+$ site close to 5R apices on either side of the 12R pore (site I or II, Figure 8.7) and the one at 4 ppm to a Na$^+$ site either near the -O-Ti-O-Ti- chain at the top of the 12R pore (site III) or in the 12R pore (site V) (Figure 8.7). The spectrum of 4 d sample presents an extremely weak signal at around -5 ppm in the isotropic F1 dimension (Figures 8.6A). This may imply the presence of very few 5Rs. Upon heating for 5 d, the peak became sharper and stronger in the F1 dimension, indicating the formation of more 5Rs.

The gel molar composition used to synthesize ETS-10 contains an organic compound, which is choline chloride. To investigate its impact on the crystallization, the ^{13}C CP MAS spectra were obtained on selected HTS gel samples (Figure 8.8A). The results indicate that the signals due to carbon sites in choline chloride appeared when the initial dry gel was heated for 6 d or longer.[53] The corresponding powder XRD patterns show the formation of ETS-10 phase. This implies that choline chloride was encapsulated inside large pores and played a space-filling role, making it difficult to wash them away by centrifugation. This, in combination with ^{23}Na NMR results, suggests that 12Rs were formed later than 5Rs. Moreover, it is reported that with the presence of choline chloride, the nucleation rate and crystallinity of ETS-10 are enhanced considerably.[24] This may result from the smaller activation energy for crystal growth, as claimed by Pavel *et al.*[54]

The ^{29}Si MAS NMR spectra of selected HTS gel samples are shown in Figure 8.8B. The spectra of gel samples heated for less than 4 d show a broad resonance centered at around -95 ppm. The broad linewidth implies that the local environment around the Si atoms is quite disordered. Employing Raman spectroscopy and ^{29}Si NMR, Can Li's group pointed out that this signal is from $(TO)_3Si$ species in 3R structures during the formation of ETS-10 (for illustrations of 3R structures, see Scheme 8.1).[37] The broad signal likely results from silanol Q^3 groups in unreacted silica or Q^3 species in the 3R structures.[55] After 5 d of heating, the peak became asymmetric and a shoulder at the high-field side with chemical shift values of around -104 and -113 ppm appeared. This peak results from Si species in a $Si(OSi)_4$ environment.[9] Agreeing with the powder pattern and ^{23}Na NMR results, this indicates the formation of ETS-10 phase. A much weaker peak at -113 ppm may be ascribed to amorphous silica.[55] The spectrum also shows that the signal at -95 ppm evolved into two resonance lines at -94 and -98 ppm. Both of them are due to $(TiO)_1Si(OSi)_3$ species in ETS-10.[9] After heating treatment for 6 d, the linewidths of three signals due to ETS-10 became much narrower. This implies that the Si atoms were in a more ordered environment as the crystallization of ETS-10 increased with time. The spectra of the 7 d and 9 d samples look identical to those of ETS-10 reported in the literature.[24,56] They contain three signals which are assigned to $(TiO)_1Si(OSi)_3$ (-94 and -98 ppm) and $Si(OSi)_4$ (-104 ppm). The intensity ratio of them is around 1.8:2.0:1.0. This agrees with that there are four $(TiO)_1Si(OSi)_3$ sites and one $Si(OSi)_4$ site in ETS-10.[10]

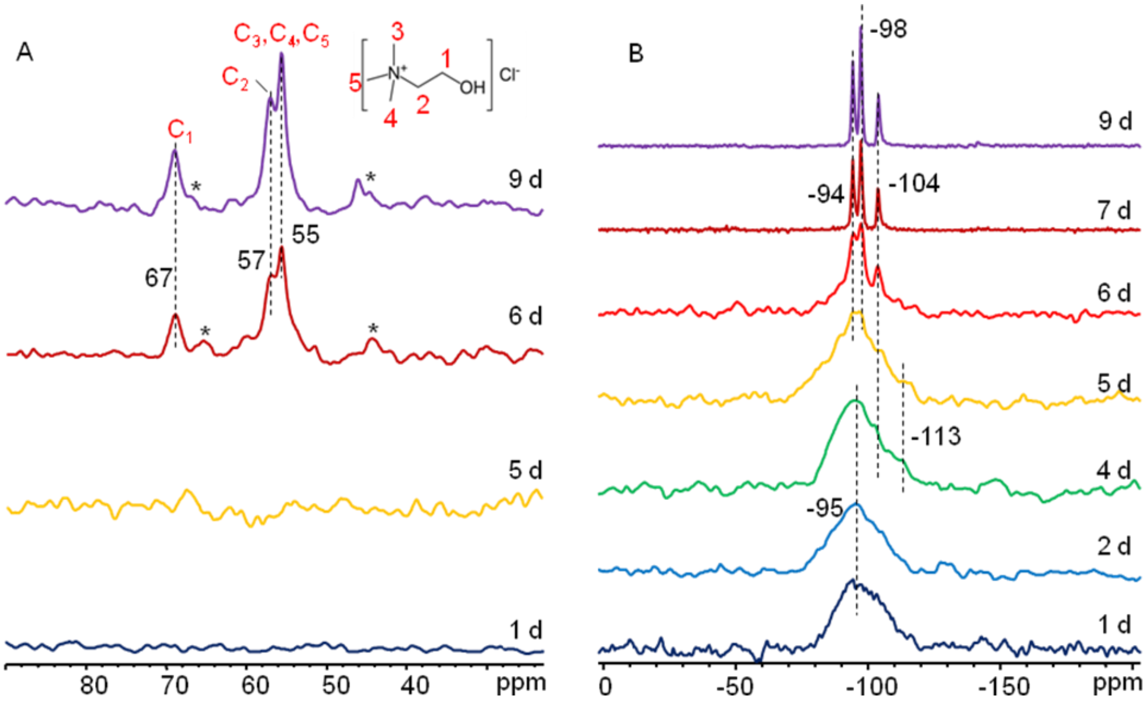

Figure 8.8 ^{13}C CP MAS (A) and ^{29}Si MAS (B) spectra of selected ETS-10 HTS gel samples. * indicates spinning sidebands.

To further examine the structures of intermediate gel samples, ^{39}K NMR experiments were conducted on selected gel samples (Figure 8.9). The spectrum of 9 d sample presents only a single signal. The simulations result in the following NMR spectral parameters: C_Q = 1.9 (1) MHz, η_Q = 0 (1), and δ_{iso} = -19 (3) ppm. Based on literature, K^+ ions may sit in the 7Rs (site IV) or at both sites IV and V (Figure 8.7).[49] These two possibilities were reported to stabilize the lattice most.[49] Because only one ^{39}K signal is observed in as-formed ETS-10, it is thus proposed that K^+ sat at site IV in ETS-10. For 1 d sample, the spectrum shows two relatively sharp signals (K1 and K2) and an extremely broad shoulder (K3) in the high frequency region. Upon heating, the K2 site disappeared and the intensity of site K1 decreased a lot in 6 d sample. Both of them transformed to K3 as well as K4, which is the only K site in final crystalline ETS-10.

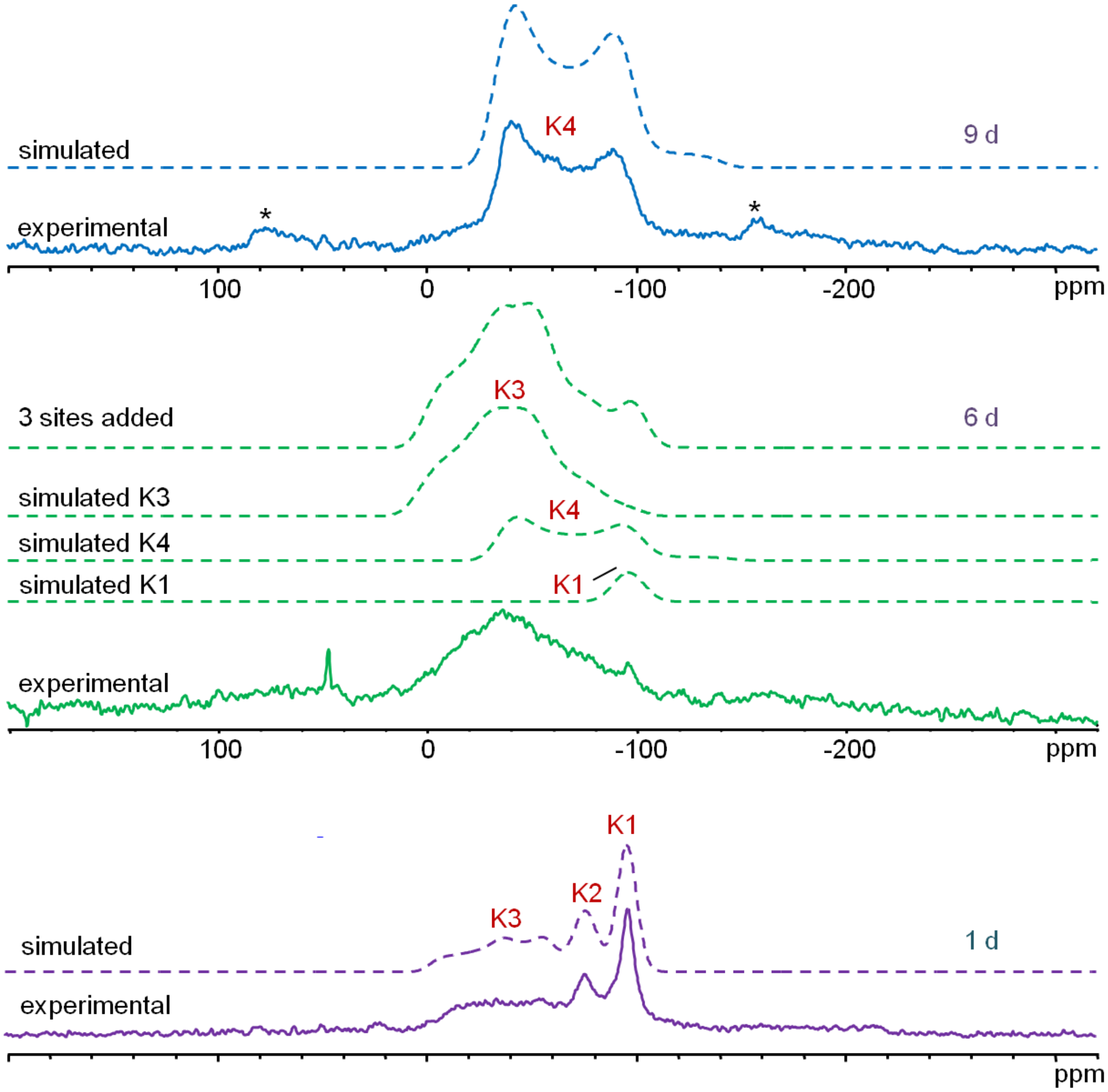

Figure 8.9 ^{39}K MAS NMR spectra of selected ETS-10 HTS gel samples (5 KHz spinning speed; 2 s pulse delay; 22000 scans for each sample). * indicates spinning sidebands. A sharp peak at 50 ppm in 6 d sample is from KCl.

The ^{39}K NMR parameters of the different signals obtained from the spectral simulation are shown in Table 8.1. The isotropic chemical shift values of the K1 (-92 ppm) and K2 (-71 ppm) signals in 1 d sample were previously reported in potassium silicates.[57] Partially hydrated K$^+$ ions in $(H_2O)_n$-K(-O-Si-O-) environments are likely to result in the two peaks in the present case. These K^+ ions were coordinated with both water molecules and silicate anions.[58,59] The K3 signal has similar C_Q and different η_Q and δ_{iso} values in 1 d sample compared to the K4 site in 9 d sample. This suggests that not fully developed 7Rs were formed in 1 d sample. There is also a small peak due to the K4 site in the 6 d sample. In line with the powder XRD pattern, this indicates the presence of ETS-10 phase in this sample. Therefore, besides few 5Rs and 3R structures as suggested by ^{23}Na and ^{29}Si NMR results, ^{39}K NMR data suggest that incomplete 7Rs were formed below 4 d samples.

Table 8.1 ^{39}K NMR parameters obtained from the simulation of ^{39}K NMR spectra.

Samples	Sites	C_Q (MHz)	η_Q	δ_{iso} (ppm)
1 d	K1	0.5 (1)	0.7 (1)	-92 (5)
	K2	0.6 (1)	0.7 (1)	-71 (5)
	K3	1.7 (2)	0.6 (1)	0 (5)
6 d	K1	0.5 (1)	0.7 (1)	-92 (5)
	K3	1.7 (1)	0.6 (1)	7 (2)
	K4	1.9 (2)	0 (1)	-19 (2)
9 d	K4	1.9 (1)	0 (1)	-19 (3)

In summary, the formation of ETS-10 was investigated under HTS conditions using powder XRD, SEM, and solid-state NMR as the characterization methods. The results indicate that an amorphous titanosilicate phase containing few SBUs of ETS-10 was formed at an early stage of crystallization process. These SBUs were mainly composed of 3R structures, 5R, and 7Rs. Upon heating, 12Rs were formed from the reorganization, the appearance of which can be considered as a sign of the formation of crystalline ETS-10 phase. The ^{23}Na and ^{39}K NMR data suggest that upon mixing different reactive species and heating the mixture for a short period of time, Na^+ or K^+ ion complexes with anionic silicate species as the ligands were formed. Under HTS treatments, such a species was solvated and reacted with titanate forming ETS-10 that only contains Q^4 species. Clearly, Na^+ and K^+ ions have involved in the formation of SBUs of ETS-10. It appears that Na^+ and K^+ ions play some structure-directing role for the synthesis of ETS-10. An illustration of the crystallization is shown in Scheme 8.1.

8.3.1.2 Crystallization under DGC conditions

Formation of ETS-10 was also investigated by DGC method. The powder XRD pattern of the initial dry gel exhibits a sharp peak and two much weaker ones with 2θ values of around 38° and in the region of 30° - 35°, respectively (Figure 8.10A). They result from sodium chloride (NaCl). Upon centrifugation with lots of distilled water, the peaks due to NaCl almost disappeared. The powder pattern looks similar to the HTS gel samples heated for less than 4 days (Figure 8.3), suggesting that the washed sample is an amorphous phase (Figure 8.10B). This result indicates that the initial dry gel is a mixture of amorphous materials and NaCl. Upon heating the dry gel for 20 d under DGC conditions, peaks characteristic of ETS-10 appeared. Simultaneously, the peaks due to NaCl decreased a lot. This may imply that under DGC conditions, NaCl was first dissolved in water vapor. The resultant hydrated Na^+ ions then played a templating role in forming ETS-10 phase. As shown in Figure 8.11, for 1 g of initial dry gel if 2.0 g of distilled water was applied under DGC conditions, diffraction peaks resulting from ETS-10 showed up after heating the dry gel for 13 d. On the other hand, the powder pattern only has peaks due to NaCl for the same reaction time in the case of 0.4 g of distilled water (Figure 8.10A). This is due to that more hydrated Na^+ ions were formed using more water for the same amount of dry gel, which then promoted the crystallization of ETS-10. This implies the important structure-directing role of hydrated Na^+ ions for the formation of ETS-10.

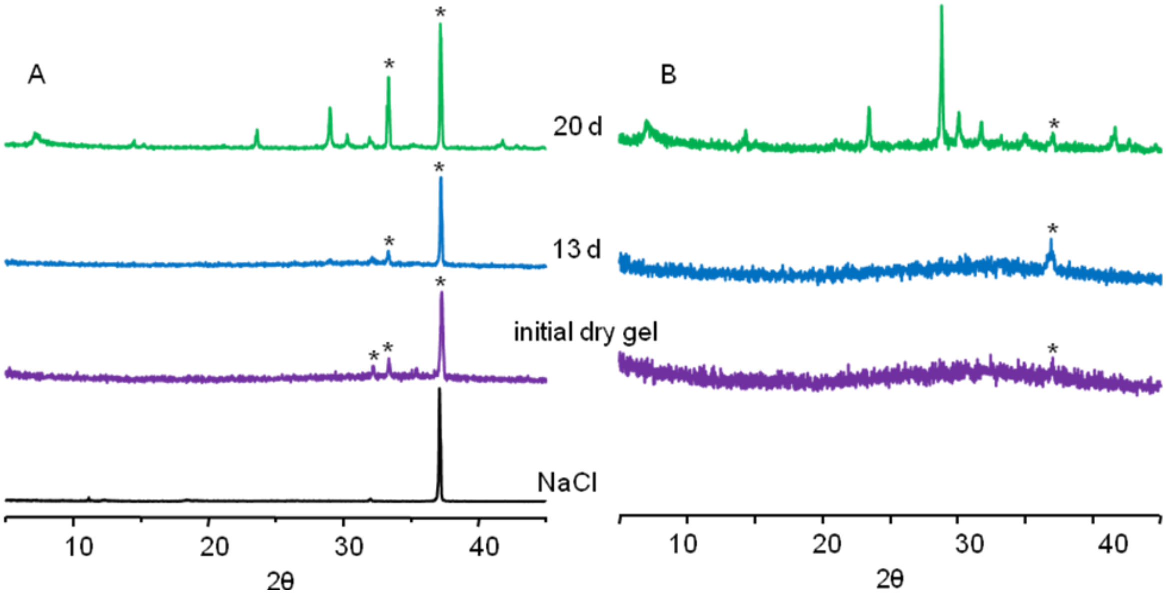

Figure 8.10 Powder XRD patterns of unwashed (A) and washed (B) ETS-10 dry gel samples. For 1 g of dry gel, 0.4 g of distilled water was used. * indicates sodium chloride (chloride is from choline chloride and titanium trichloride).

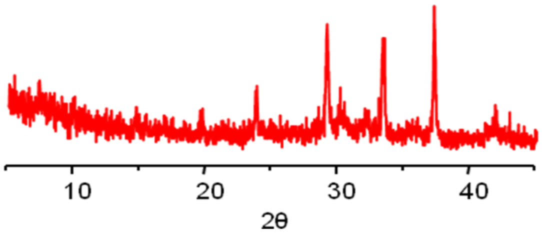

Figure 8.11 Powder XRD patterns of a ETS-10 dry gel sample heated for 13 days. For 1.0 g of dry gel, 2.0 g of distilled water was used.

The corresponding ^{23}Na MAS spectra of DGC dry gel samples all show a sharp peak at around 7 ppm and a much weaker one at -11 ppm (Figure 8.12A). As discussed earlier, they are due to sodium in NaCl and partially hydrated Na^+, respectively. Upon centrifugation, the intensity of the signal at -11 ppm was greatly enhanced while that at 7 ppm was decreased (Figure 8.12B). Consistent with the powder XRD results, this implies that most of NaCl adsorbed on the dry gel sample surface was washed away. The presence of the signal at -11 ppm in the initial dry gel and 13 d sample suggests that Na^+ ions templated the crystallization of ETS-10 under DGC conditions in a similar way to that under HTS conditions. The ^{29}Si MAS spectrum of the washed 20 d dry gel sample resembles that of the 9 d HTS sample (not shown), indicating that this sample is pure crystalline ETS-10.

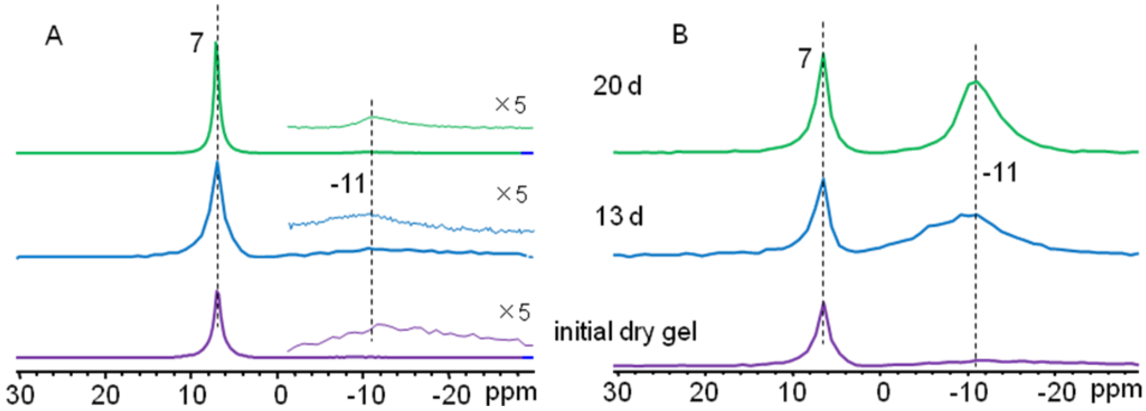

Figure 8.12 ^{23}Na MAS spectra of unwashed (A) and washed (B) ETS-10 dry gel samples. For 1 g of dry gel, 0.4 g of distilled water was used.

8.3.1.3 Summary of formation of ETS-10

The formation of titanosilicate ETS-10 was examined using HTS and DGC methods. Our studies indicate that ETS-10 crystallized in a similar way under both conditions. An amorphous phase containing somewhat similar structural features to ETS-10 was formed at an early stage of crystallization process. SBUs of ETS-10 such as 3R structures, 5Rs, and incomplete 7Rs were present in it. Upon heating, these SBUs were reorganized and transformed into ETS-10. The results also reveal that the amount of hydrated sodium determines the crystallization time to obtain ETS-10. This is not surprising because pure Na-ETS-10 was synthesized previously when a Na-only gel was used.[60] Although in the present case potassium and sodium worked cooperatively to direct the crystallization of ETS-10, sodium seems to be a more important structure-directing agent.

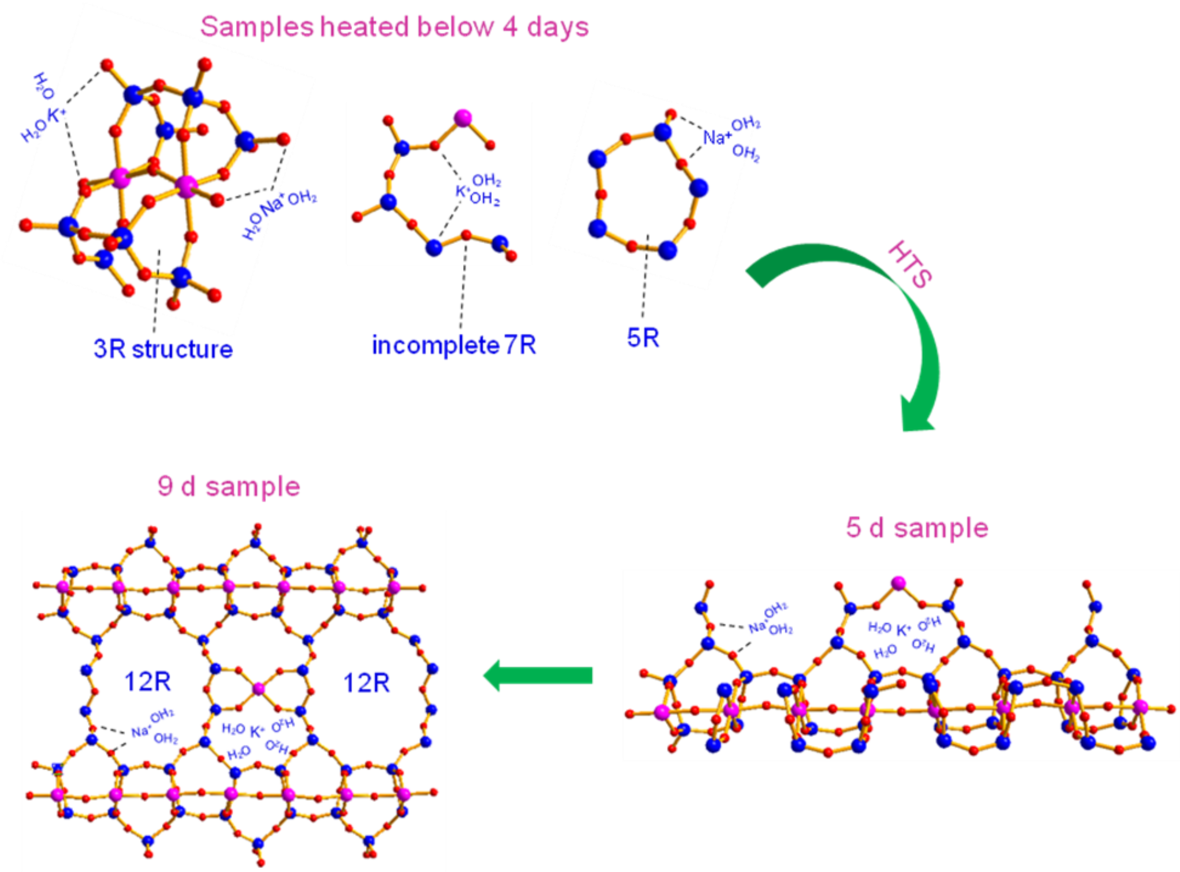

Scheme 8.1 Proposed formation process of ETS-10. 3R structures are drawn according to work by the Li group.[37]

8.3.2 Formation of ETS-4

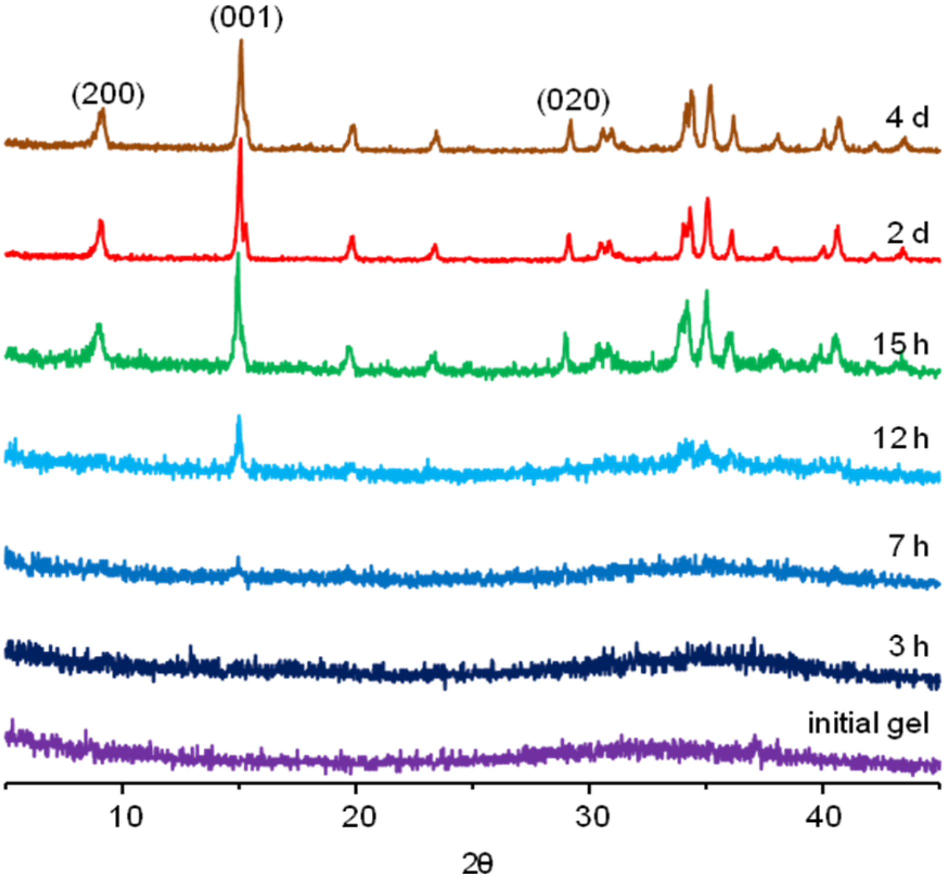

Figure 8.13 Powder XRD patterns of ETS-4 HTS gel samples.

Crystallization of ETS-4 was examined under HTS conditions. The powder XRD patterns of the gel samples heated for less than 3 h exhibit one broad halo centered at 2θ around 32° (Figure 8.13). This indicates that amorphous phase with no long-range ordering was dominating in these samples. After heating the initial gel for 7 h, a relatively sharp, but very weak reflection peak at around 15° appeared, suggesting that upon heating, a very small portion of the amorphous phase transformed into an ordered phase. Further, the position of the peak is in line with the *(001)* reflection in as-synthesized ETS-4, implying that the ordered phase has some structural features similar to ETS-4. After heating the initial gel for 12 h, the intensity of this peak increased further at the expense of the amorphous phase, and several weak diffractions with 2θ values of around 35° also appeared. This phenomenon demonstrates that a transformation to ETS-4 framework was ongoing. Further increasing the heating time to 15 h or longer, the appearance of those characteristic reflections due to ETS-4, such as *(200)*, *(001),* and *(020)*, indicates that fully crystalline ETS-4 was formed. The XRD patterns of the 2 d and 4 d samples are the same as those reported in literature.[15,61]

Figure 8.14 presents the SEM micrographs of selected gel samples. The picture of the initial gel (Figure 8.14A) exhibits only disordered aggregates. Upon heating for 12 h, a significant decrease in the size of aggregates can be observed (Figure 8.14B), and also, a closer look of the 12 h sample suggests the formation of few ETS-4 crystals (circled in Figure 8.14C). Consistent with the powder XRD results, this demonstrates that the ordered phase is actually small ETS-4 crystallites, which formed from the amorphous aggregates. The image of 4 d sample shown in Figure 8.14D reveals the formation of crystalline ETS-4 phase with uniform morphology, which is consistent with earlier observations in ETS-4 synthesis.[41,61] Magnified pictures of two distinct regions in Figure 8.14D indicate that intergrown polycrystalline spherulitic particles were produced. Each of them is composed of two hemispheres (Figures 8.14E and F). The average length of the particle is around 20 μm, and the average thickness is 15 μm.

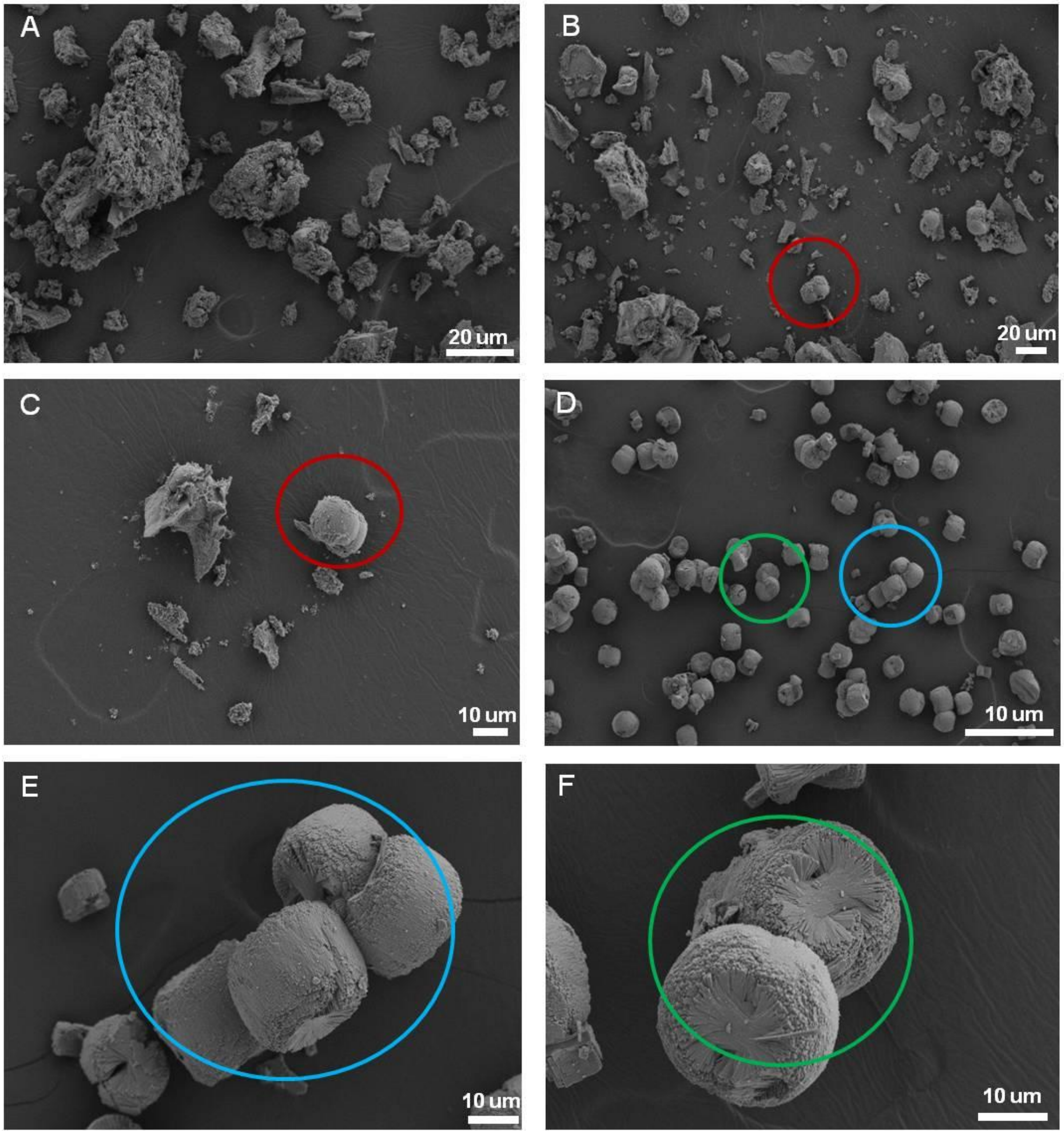

Figure 8.14 SEM images of selected ETS-4 HTS gel samples: (A) initial gel; (B) and (C) 12 h; (D) - (F) 4 d.

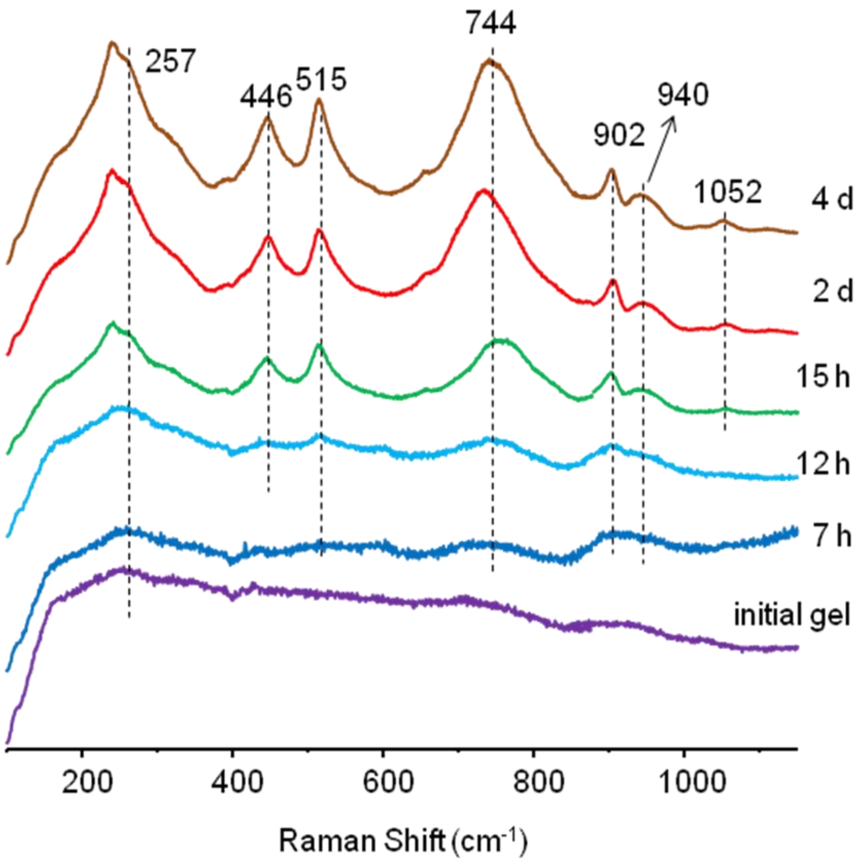

Figure 8.15 Raman spectra of selected ETS-4 HTS gel samples.

Raman spectra of selected gel samples are shown in Figure 8.15. In the spectrum of the initial gel, no apparent bands can be seen except an extremely weak band at 257 cm^{-1}, which is mainly due to Si-O-Ti bonding.[62] Upon heating the initial gel for 12 h, characteristic bands due to ETS-4 such as those at 446, 515, and 744 cm^{-1} appeared. The peaks at 446 and 515 cm^{-1} result from internal vibrational modes of TiO_6 octahedra and TiO_5 pyramids.[12] The band at 744 cm^{-1} can be assigned to the -O-Ti-O-Ti-O- chains. The bands at 902 and 940 cm^{-1} correspond to Si-O symmetric and asymmetric stretching vibration in Si-O-Ti bridges, respectively.[1] Agreeing with the powder XRD pattern and SEM image, this observation confirms the emergence of ETS-4. Upon heating the initial gel for 15 h or longer, the intensities of these characteristic bands have increased a lot, suggesting that crystalline ETS-4 was formed. A new band appears at 1050 cm^{-1}, which is due to asymmetric stretching of Si-O-Si bridges.[5]

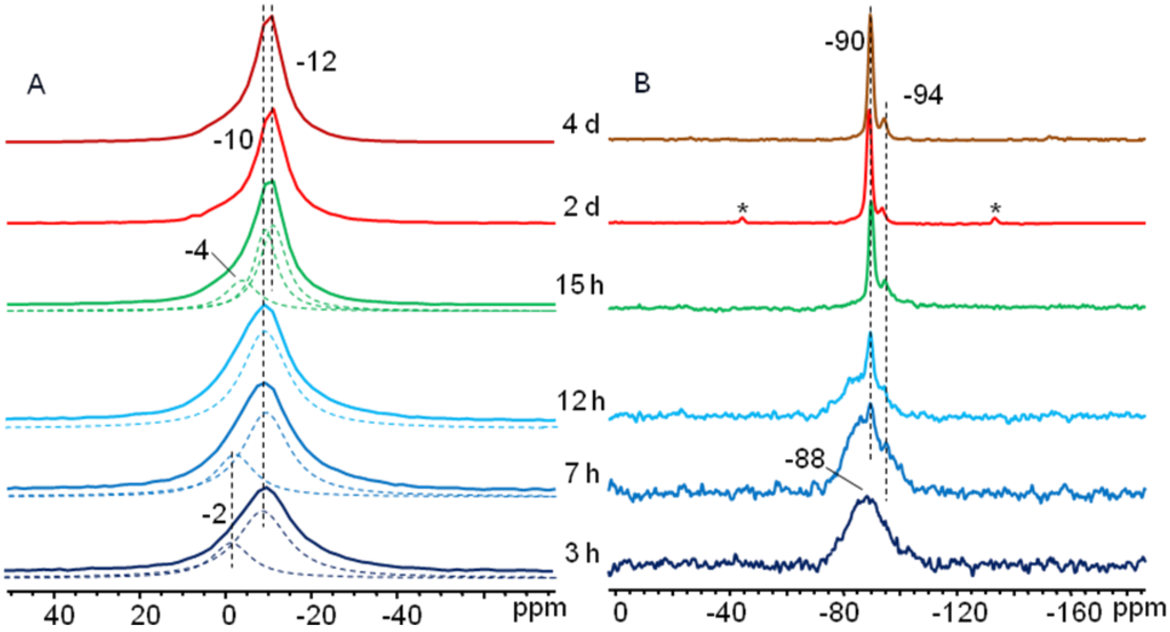

Figure 8.16 ^{23}Na MAS (A) and ^{29}Si MAS (B) NMR spectra of selected ETS-4 HTS gel samples. * indicates spinning sidebands.

^{23}Na and ^{29}Si MAS NMR experiments were carried out to follow the formation process as a function of crystallization time. The ^{23}Na MAS NMR spectra of selected ETS-4 gel samples all contain a broad peak at -10 ppm (Figure 8.16A). A similar chemical shift value was observed in ETS-10 HTS gel samples. Thus, this peak is ascribed to Na^{+} ions complexed to monomeric silicate anions. Heating the initial gel for 15 h resulted in another broad signal at -12 ppm. It may result from the sodium complexes in a different chemical environment. The small peaks at -2 and -4 ppm may be due to highly hydrated Na^{+} ions.[63] The ^{23}Na 3QMAS spectra of selected ETS-4 gel samples are shown in Figure 8.17. The linewidth of the contour plots in the F2 dimension decreases as increasing the crystallization time. As discussed above, this suggests the changes in the local environments around sodium. The ^{23}Na 3QMAS spectrum of 4 d sample shows two signals in the F1 dimension (Figure 8.17C). The peaks at -10 and -12 ppm in the MAS spectrum present an isotropic chemical shift of 11 and 1 ppm, respectively. The ^{23}Na slices taken through the two isotropic peaks can each be simulated (for the signal at 11 ppm, C_Q = 2.0 (1) MHz, η_Q = 0.77 (1), and δ_{iso} = -0.2(1) ppm; for the signal at 1 ppm, C_Q = 1.6 (1) MHz, η_Q = 0.7 (1), and δ_{iso} = -4 (1) ppm). Based on literature,[64] the resonance line at 11 ppm is tentatively assigned to the Na^+ site in 7R site, which is coordinated to five framework O atoms and two O atoms in water molecules, and the resonance line at 1 ppm to the Na^+ site in double 6-membered ring site (D6R), which is coordinated to four framework O atoms and two O atoms in water molecules (Figure 8.18).

Along the *c* axis are 7R pores (Figure 8.2). The powder XRD results indicate that a diffraction peak due to the *(001)* reflection first appeared in 7 h sample and other characteristic peaks due to ETS-4 showed up at a later stage. A single peak at the -10 ppm, which is assigned to Na^+ ions in 7Rs, is present in the ^{23}Na spectrum of 7 h sample. These findings imply that 7 h sample may contain 7Rs. Upon heating, 7Rs were reorganized with other amorphous phase forming 7R structures, which transformed into ETS-4 later (Scheme 8.2).

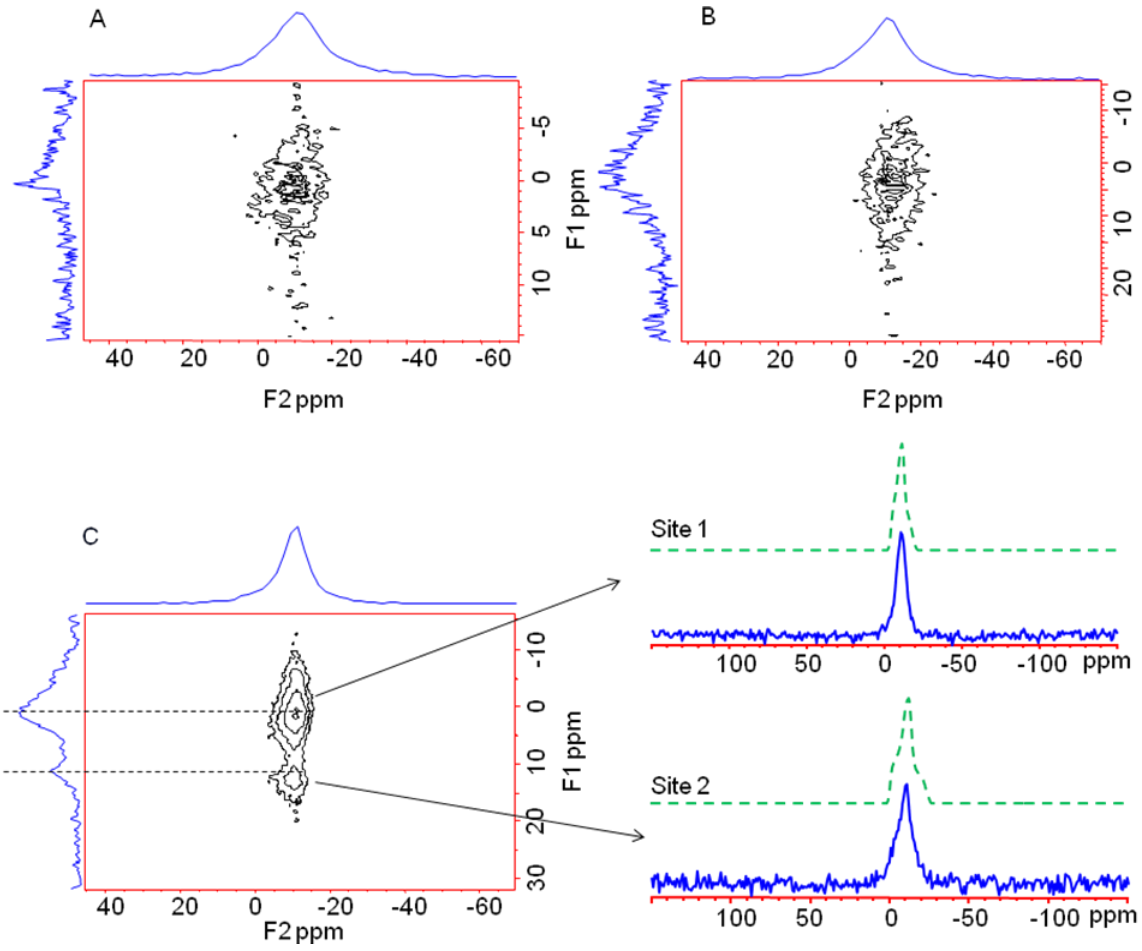

Figure 8.17 ^{23}Na 3QMAS spectra of (A) 3 h, (B) 12 h, and (C) 4 d samples.

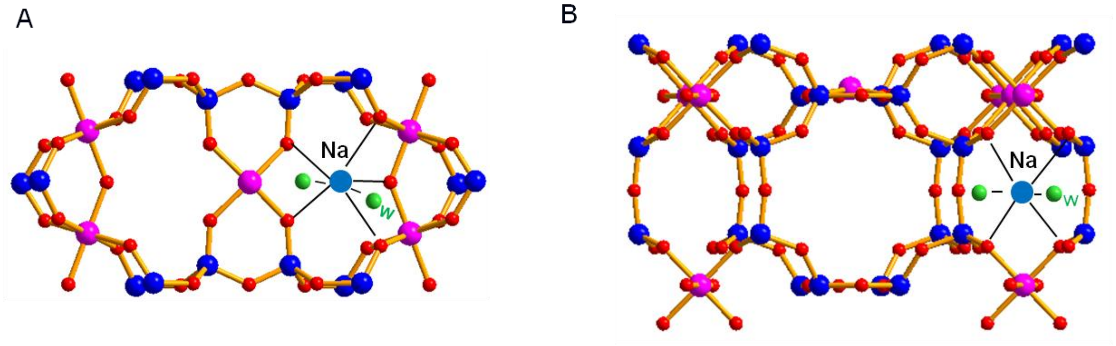

Figure 8.18 Na$^+$ ion sites in ETS-4 (A) 7R and (B) D6R.

^{29}Si MAS NMR spectra are shown in Figure 8.16B. The spectrum of 3 h sample exhibits a broad signal centered at around -88 ppm. It may result from $(TO)_2(HO)_1SiO^-Na^+$.[65,66] The broad linewidth of this resonance suggests that the sample is quite amorphous. Upon heating the initial gel for 7 h, two relatively sharp peaks at -90 and -94 ppm appear. Consistent with the presence of 7Rs in 7 h sample, these two peaks can be assigned to Si atoms in $(SiO)_2Si(OTi_{oct})_2$ and $(SiO)_3Si(OTi_{semi\text{-}oct})_1$ environments in ETS-4 framework, respectively.[13,67] Further treating the initial gel for 12 h or longer, the intensities of the peaks at -90 and -94 ppm increased a lot at the expense of the broad one at -88 ppm, implying that the amorphous phase gradually transformed into ETS-4. The spectra of the 2 d and 4 d samples resemble those in literature.[13]

In summary, the formation of molecular sieve ETS-4 was examined under HTS conditions. Our studies show that upon mixing different sources, an amorphous phase was formed first. Upon heating, some of the amorphous phase was transformed into an ordered at a rapid rate in the hydrothermal alkaline environment. This ordered phase is small ETS-4 crystallite. It is supposed to contain layers composed of 7Rs, the distance between which is the same as the *d*-spacing of the *(001)* plane of crystalline ETS-4. Upon further heating treatment under HTS conditions, the unreacted amorphous phase and/or the ordered phase was reorganized and transformed into ETS-4 gradually (Scheme 8.2).

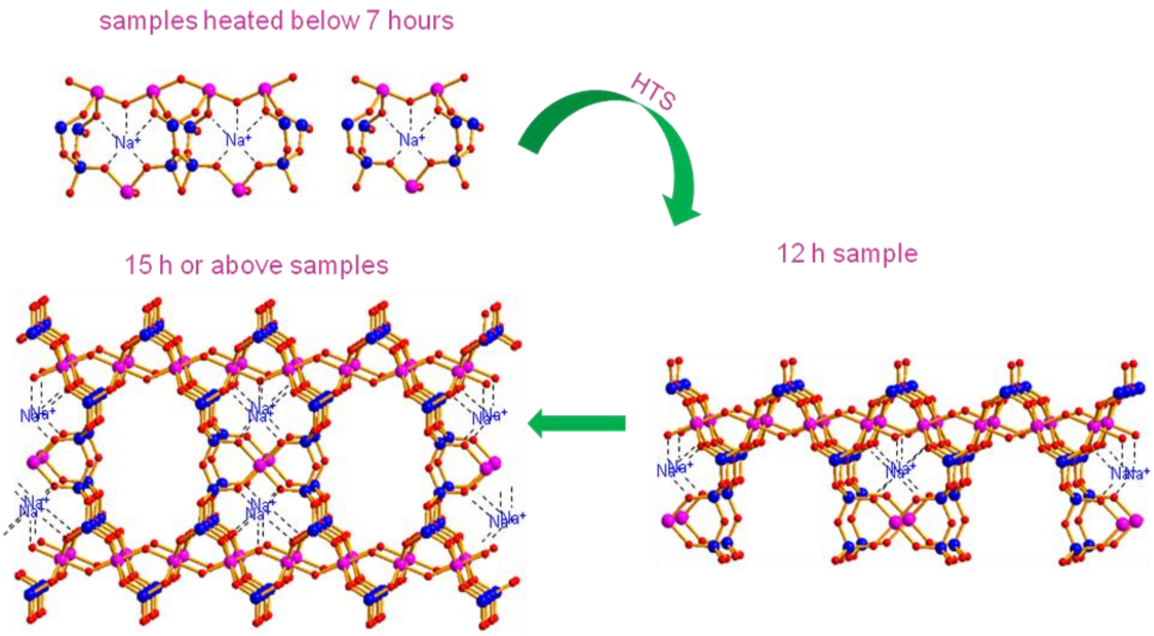

Scheme 8.2 Proposed formation process of ETS-4.

8.4 References

(1) Armaroli, T.; Milella, F.; Bregani, F.; Toledo, G.; Nastro, A.; De Luca, P.; Bagnasco, G.; Turco, M. *J. Mater. Chem.* **2000**, *10*, 1699-1705.

(2) Venuto, P. B.; Habib, T. E. *Fluid Catalytic Cracking with Zeolite Catalysts*; Marcel Dekker: New York, **1979**.

(3) Satterfield, C. N. *Heterogeneous Catalysis in Industrial Practice*, 2nd ed.; McGraw-Hill: New York, **1991**.

(4) Schüth, F.; Sing, K. S. W.; Weitkamp, J. *Handbook of Porous Solids*; Wiley-VCH: Weinheim, Germany, **2002**; Vol. 3.

(5) Craveiro, R.; Lin, Z. *J. Solid State Chem.* **2012**, *190*, 162-168.

(6) Kuznicki, S. M. US Patent 4,853,202, 1989.

(7) Pavel, C. C.; Zibrowius, B.; Loeffler, E.; Schmidt, W. *Phys. Chem. Chem. Phys.* **2007**, *9*, 3440-3446.

(8) Lv, L.; Su, F.; Zhao, X. *Microporous Mesoporous Mater.* **2004**, *76*, 113-122.

(9) Anderson, M. W.; Terasaki, O.; Ohsuna, T.; Philippou, A.; Mackay, S. P.; Ferreira, A.; Rocha, J.; Lidin, S. *Nature* **1994**, *367*, 347-351.

(10) Anderson, M. W.; Terasaki, O.; Ohsuna, T.; Malley, P. J. O.; Philippou, A.; Mackay, S. P.; Ferreira, A.; Rocha, J.; Lidin, S. *Philos. Mag. B* **1995**, *71*, 813-841.

(11) Sacerdoti, M.; Cruciani, G. *Minerals as Advanced Materials;* Springer-Verlag: Berlin Heidelberg, **2012**, pp 187-197.

(12) Valtchev, V.; Mintova, S.; Mihailova, B.; Konstantinov, L. *Mater. Res. Bull.* **1996**, *31*, 163-169.

(13) Cruciani, G.; De Luca, P.; Nastro, A.; Pattison, P. *Microporous Mesoporous Mater.* **1998**, *21*, 143-153.

(14) Kuznicki, S. M. US Patent 4,938,939, 1990.

(15) Kuznicki, S. M.; Bell, V. A.; Nair, S.; Hillhouse, H. W.; Jacubinas, R. M.; Braunbarth, C. M.; Toby, B. H.; Tsapatsis, M. *Nature* **2001**, *412*, 720-724.

(16) Yilmaz, B.; Warzywoda, J.; Sacco Jr, A. *Nanotechnology* **2006**, *17*, 4092-4099.

(17) Rocha, J.; Lin, Z. *Rev. Mineral. Geochem.* **2005**, *57*, 173-201.

(18) Anderson, M. W.; Rocha, J. In *Handbook of Porous Solids.* Schüth, F.; Sing, K.S.W.; Weitkamp, J., Eds.; John Wiley & Sons, Ltd., **2008**.

(19) Marathe, R.; Mantri, K.; Srinivasan, M.; Farooq, S. *Ind. Eng. Chem. Res.* **2004**, *43*, 5281-5290.

(20) Popa, K.; Pavel, C.; Bilba, N.; Cecal, A. *J. Radioanal. Nucl. Chem.* **2006**, *269*, 155-160.

(21) Pinto, M. L.; Rocha, J.; Gomes, J. R. B.; Pires, J. *J. Am. Chem. Soc.* **2011**, *133*, 6396-6402.

(22) Das, T. K.; Chandwadkar, A.; Sivasanker, S. *Bull. Mater. Sci.* **1994**, *17*, 1143-1153.

(23) Das, T. K.; Chandwadkar, A.; Sivasanker, S. *Chem. Commun.* **1996**, 1105-1106.

(24) Das, T. K.; Chandwadkar, A.; Budhkar, A.; Sivasanker, S. *Microporous Mater.* **1996**, *5*, 401-410.

(25) Das, T. K.; Chandwadkar, A.; Sivasanker, S. *J. Mol. Catal. A: Chem.* **1996**, *107*, 199-205.

(26) De Luca, P.; Nastro, A. *Stud. Surf. Sci. Catal.* **1997**, *105*, 221-228.

(27) Rocha, J.; Ferreira, A.; Lin, Z.; Anderson, M. W. *Microporous Mesoporous Mater.* **1998**, *23*, 253-263.

(28) Yang, X.; Paillaud, J. L.; Van Breukelen, H.; Kessler, H.; Duprey, E. *Microporous Mesoporous Mater.* **2001**, *46*, 1-11.

(29) Goa, Y.; Yoshitake, H.; Wu, P.; Tatsumi, T. *Microporous Mesoporous Mater.* **2004**, *70*, 93-101.

(30) Ji, Z.; Yilmaz, B.; Warzywoda, J.; Sacco Jr, A. *Microporous Mesoporous Mater.* **2005**, *81*, 1-10.

(31) Turta, N. A.; Vuono, D.; De Luca, P.; Bilba, N.; Nastro, A. *J. Therm. Anal. Calorim.* **2007**, *88*, 431-435.

(32) Ji, Z.; Warzywoda, J.; Sacco Jr, A. *Microporous Mesoporous Mater.* **2008**, *109*, 1-11.

(33) Ng, Y. C.; Jei, C. Y.; Shamsuddin, M. *Microporous Mesoporous Mater.* **2009**, *122*, 195-200.

(34) Kim, W. J.; Lee, M. C.; Yoo, J. C.; Hayhurst, D. T. *Microporous Mesoporous Mater.* **2000**, *41*, 79-88.

(35) Pavel, C. C.; De Luca, P.; Bilba, N.; Nagy, J. B.; Nastro, A. *Thermochim. Acta* **2005**, *435*, 213-221.

(36) Turta, N. A.; Veltri, M.; Vuono, D.; De Luca, P.; Bilba, N.; Nastro, A. *J. Porous Mater.* **2009**, *16*, 527-536.

(37) Guo, M.; Feng, Z.; Li, G.; Hofmann, J. P.; Pidko, E. A.; Magusin, P. C. M. M.; Guo, Q.; Weckhuysen, B. M.; Hensen, E. J. M.; Fan, F.; Li, C. *Chem. Eur. J.* **2012**, *18*, 12078-12084.

(38) Yang, H.; Liu, Q.; Liu, Z.; Gao, H.; Xie, Z. *Microporous Mesoporous Mater.* **2010**,

127, 213-218.

(39) Liu, L.; Singh, R.; Li, G.; Xiao, P.; Webley, P.; Zhai, Y. *J. Hazard. Mater.* **2011**, *195*, 340-345.

(40) Liu, X.; Thomas, J. K. *Chem. Commun.* **1996**, 1435-1436.

(41) Yilmaz, B.; Miraglia, P. Q.; Warzywoda, J.; Sacco, A. *Microporous Mesoporous Mater.* **2004**, *71*, 167-175.

(42) Marathe, R.; Srinivasan, M.; Farooq, S. *Chem. Eng. Sci.* **2004**, *59*, 6021-6025.

(43) Yilmaz, B.; Warzywoda, J.; Sacco, A. *J. Cryst. Growth* **2004**, *271*, 325-331.

(44) Dong Kim, S.; Hyun Noh, S.; Kim, W. J. *Microporous Mesoporous Mater.* **2003**, *65*, 165-175.

(45) Amoureux, J. *J. Magn. Reson., Ser A* **1996**, *123*, 116-118.

(46) Eichele, K.; Wasylishen, R. E.; v. 1.19.15 ed. 2009.

(47) Sanchez, J.; McCormick, A. *Chem. Mater.* **1991**, *3*, 320-324.

(48) Almond, G. G.; Harris, R. K.; Franklin, K. R.; Graham, P. *J. Mater. Chem.* **1996**, *6*, 843-847.

(49) Anderson, M. W.; Agger, J. R.; Luigi, D.-P.; Baggaley, A. K.; Rocha, J. *Phys. Chem. Chem. Phys.* **1999**, *1*, 2287-2292.

(50) Valtchev, V.; Rigolet, S.; Bozhilov, K. N. *Microporous Mesoporous Mater.* **2007**, *101*, 73-82.

(51) Hu, K. N.; Hwang, L. P. *Solid State Nucl. Magn. Reson.* **1998**, *12*, 211-220.

(52) Lim, K. H.; Clare, P. *J. Am. Chem. Soc.* **2000**, *122*, 9768-9780.

(53) Shah, F. U.; Glavatskih, S.; Dean, P. M.; MacFarlane, D. R.; Forsyth, M.; Antzutkin, O. N. *J. Mater. Chem.* **2012**, *22*, 6928-6938.

(54) Pavel, C.; B Nagy, J.; Bilba, N.; Nastro, A.; Perri, C.; Vuono, D.; De Luca, P.; Asaftei, I. *Microporous Mesoporous Mater.* **2004**, *71*, 77-85.

(55) Van Grieken, R.; Sotelo, J.; Martos, C.; Fierro, J.; Lopez-Granados, M.; Mariscal, R. *Catal. Today* **2000**, *61*, 49-54.

(56) Das, T. K.; Chandwadkar, A. J.; Budhkar, A. P.; Belhekar, A. A.; Sivasanker, S. *Microporous Mater.* **1995**, *4*, 195-203.

(57) Barbosa, V. F. F.; MacKenzie, K. J. D. *Mater. Lett.***2003**, *57*, 1477-1482.

(58).Yang, C.-S.; Mora-Fonz, J. M.; Catlow, C. R. A. *J. Phys. Chem. C*, *115*, 24102-24114.

(59) Mora-Fonz, M. J.; Catlow, C. R. A.; Lewis, D. W. *Phys. Chem. Chem. Phys.* **2008**, *10*, 6571-6578.

(60) Yang, X.; Blosser, P. W. *Zeolites* **1996**, *17*, 237-243.

(61) Ke, X.; Xu, L.; Zeng, C.; Zhang, L.; Xu, N. *Microporous Mesoporous Mater.* **2007**, *106*, 68-75.

(62) Zhang, Y. Q.; Zhou, W.; Liu, S.; Navrotsky, A. *Chem. Mater.* **2011**, *23*, 1166-1173.

(63) Nair, S.; Jeong, H. K.; Chandrasekaran, A.; Braunbarth, C. M.; Tsapatsis, M.; Kuznicki, S. M. *Chem. Mater.* **2001**, *13*, 4247-4254.

(64) Egan, J.; Mueller, K. *J. Phys. Chem. B* **2000**, *104*, 9580-9586.

(65) Maciel, G. E.; Sindorf, D. W. *J. Am. Chem. Soc.* **1980**, *102*, 7606-7607.

(66) Ai, X.; Deng, F.; Dong, J.; Chen, L.; Ye, C. *J. Phys. Chem. B* **2002**, *106*, 9237-9244.

(67) Philippou, A.; Anderson, M. W. *Zeolites* **1996**, *16*, 98-107.

Chapter 9 Summary and Future Work

9.1 Summary

The applications of molecular sieves have been studied extensively in various fields. Exploring novel synthetic approaches to these microporous materials with application prospect is of great importance in controlling their properties. To fulfill this purpose, examining the self-assembly process of molecular sieves is very helpful. Although significant progress has been made in their crystallization under hydrothermal synthesis (HTS) conditions, the detailed understanding of the formation mechanisms has not been obtained. In this thesis, we applied an alternative method, dry gel conversion (DGC), to the study of the crystallization of molecular sieves. Depending on the types of molecular sieves, the HTS method was also utilized in combination with DGC or separately to examine the formation process. Although the results reported in this work are only for several selected molecular sieves including SAPOs, aluminosilicates, and titanosilicates, the methods can be extended to other molecular sieves of different structures. The general procedures developed in this thesis are the following: (1) several representative molecular sieves including SAPO-34, SAPO-37, LSX, mordenite, ETS-10, and ETS-4 were chosen because they have demonstrated great potentials in catalytic applications such as MTO reactions (SAPO-34), hydrocracking (LSX), and oxidation reactions (ETS-10 and -4); (2) depending on the nature of DGC or HTS, a series of intermediate dry gel or HTS gel samples for different molecular sieves were prepared. To avoid breaking the fragile bonding interactions in dry gel samples, each sample was divided into washed and unwashed parts for comparison; (3) all gel samples were characterized by powder XRD, which was used to check the long-range ordering, and solid state NMR, which was used to determinate the local chemical environments of involved nuclei. Further, selected samples were chosen to be characterized by Raman spectroscopy to monitor the pore system and SEM to follow the morphological changes. On the basis of a careful analysis of the experimental results, the crystallization mechanisms of different molecular sieves were proposed as follows.

For SAPO-34, its crystallization was investigated using either diethylamine (DEA) or morpholines as the template. When DEA was used as the template, SAPO-34 forms through a similar pathway under SAC and VPT conditions. It crystallizes from a semi-crystalline precursor with a layered structure, which is held by weak nonbonding interactions. Si incorporation proceeds slowly via amorphous aluminosilicate species. When morpholine was used as the template, three formation pathways exist under different batch composition conditions. When the synthesis gel contains HF (DGC with HF), SAPO-34 in both triclinic and trigonal forms crystallizes from a crystalline prephase held by covalent bonds. When the synthesis gel does not contain HF, SAPO-34 solely in trigonal form forms from an amorphous phase held by weak nonbonding interactions (DGC without HF) or from an amorphous phase and a dense phase (VPT). Similar to the formation process when using DEA as the template, silica reacts with alumina to form aluminosilicate species before Si is incorporated into framework. Under DGC with HF conditions, the as-made SAPO-34 with mixed phases contains six different Si species. Alkaline treatment of final product and NMR results suggest that most Si is located in aluminosilicate (AS) domains of trigonal SAPO-34. On the other hand, under DGC without HF and VPT conditions, the as-made trigonal SAPO-34 contains two major Si species.

A comparison of the catalytic performances of different SAPO-34 samples is shown in Figure 9.1 and Table 9.1. The differences in the lifetime, as discussed earlier, are mainly ascribed to the variations in the crystal sizes. All samples show over 80% selectivity of light olefins. Compared to hydrothermally synthesized SAPO-34, these DGC-synthesized ones have similar catalytic properties (either lifetime or light olefin selectivity) or even better.[1-3]

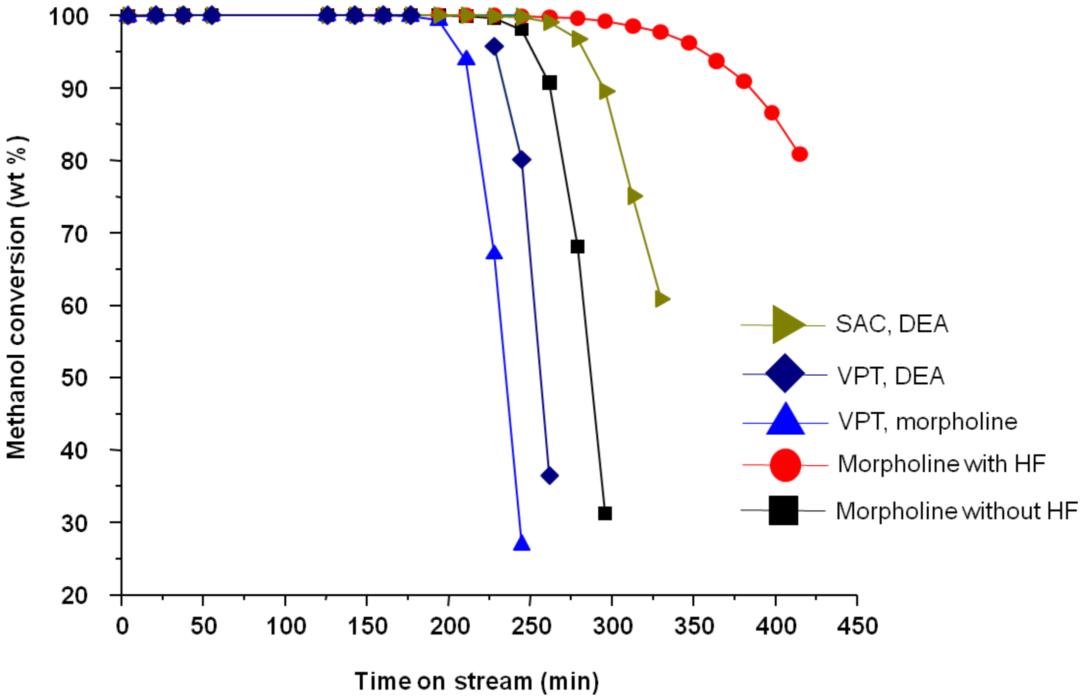

Figure 9.1 Methanol conversion vs. time-on-stream for different SAPO-34 products.

Table 9.1 MTO reaction results for different SAPO-34 samples.

Samples	Selectivity (wt%)[a]								
	CH_4	C_2H_4	C_2H_6	C_3H_6	C_3H_8	C_4	C_5	C_6	$C_2^= + C_3^=$
SAC, DEA	1.3	46.7	0.5	35.9	1.6	9.3	3.6	1.0	82.6
VPT, DEA	1.3	45.4	0.8	36.6	2.7	10.1	2.5	0.6	81.9
VPT, MOR	1.5	45.6	1.0	36.6	2.5	9.6	2.6	0.6	82.1
MOR, HF	1.7	47.0	0.3	35.8	0.3	9.9	3.9	1.2	82.8
MOR, no HF	1.5	45.1	1.1	35.8	3.4	10.2	2.5	0.5	80.9

[a] The highest selectivity of (C_2H_4 + C_3H_6) under 100% methanol conversion.

For SAPO-37, under HTS conditions, it crystallizes from a precursor initially only composed of large cavities whose size equals two directly connected supercages. Sodalite cages are formed later when increasing the crystallization time and they are connected to the cavities forming SAPO-37 framework. Under DGC conditions, the formation pathway is somewhat similar to that under HTS conditions. The precursor is almost the same as the HTS precursor but contains both large cavities and quasi-sodalite cages. The two precursors are mainly AlPO in nature. Similar to the Si incorporation process during the crystallization of SAPO-34, aluminosilicates form first and then isolated $Si(OAl)_4$ species is incorporated into SAPO-37 framework.

For zeolite LSX, amorphous aluminosilicate phase in the form of complete or nearly complete sodalite cages, large cavities, joint 4Rs, and branched 4Rs is formed at the beginning of crystallization upon mixing different reactive species. Under HTS conditions, D6Rs are formed from the reorganization of 4Rs. They then assemble with sodalite cages or large cavities to form crystalline framework of zeolite LSX.

For ETS-10, both HTS and DGC follow the same crystallization mechanism, involving the formation of an amorphous phase containing some SBUs of ETS-10. Under the reaction conditions, these SBUs are reorganized and transformed into ETS-10. The results also reveal that partially hydrated sodium cations are a crucial factor in determining the crystallization time to obtain ETS-10. For ETS-4, the studies show that small ETS-4 crystallites are formed quickly from an amorphous phase in the hydrothermal alkaline environment. The crystallites are supposed to contain layers composed of 7Rs and the distance between adjacent layers is the same as the *d*-spacing of the *(001)* plane of crystalline ETS-4. Further heating under HTS conditions result in the transformation of the unreacted amorphous phase and the small crystallites into large ETS-4 crystals.

9.2 Suggestions for future work

1. The synthesis of porous materials with hierarchical porosity has attracted immense interest.[4] In the thesis, only microporous SAPO-34 is obtained using different methods. A suggestion is that by doing some modifications of the intermediate structures formed in the DGC process, hierarchical SAPO-34 may be formed. In *Chapters* 3 and 5, a crystalline or semi-crystalline layered phase with certain interlayer spacing is found to

be formed during crystallization of SAPO-34. By embedding swelling agents between the layers, the interlayer spacing will be increased. Upon heating under DGC conditions, each layer will transfom to SAPO-34. When crystallization is done, the swelling agent can be removed by calcinations. The as-formed products are expected to contain micropores within the layers and macro/meso-pores between layeres. Such materials are expected to exhibit better properties due to the presence of different pore sizes.

2. In *Chapters* 3-5, it is shown that the MTO performances of different SAPO-34 products depend on acid strength and crystal sizes. As the acid strength depends on Si distribution, by balancing the formation of dispersed Si and Si island species, SAPO-34 with different acid strength will be formed. In the future, the influence of different Si contents on the MTO performances can be investigated. Moreover, the formation of SAPO-34 with nm crystal sizes under DGC conditions is also worth studying.

3. In *Chapters* 7 and 8, the influence of Na^+ to K^+ ion ratio on the catalytic properties of LSX, ETS-10, and ETS-4 should be investigated. As the two types of cations have different Lewis acidity, if they are in different ratios in each of the three molecular sieves, the framework basicity is different. This, in turn, could influence the catalytic performances in either Lewis acid or base-catalyzed reactions.

4. Either DGC or HTS study can be extened to investigate other types of important molecular sieves.

8.4 References

(1) Liu, G.; Tian, P.; Li, J.; Zhang, D.; Zhou, F.; Liu, Z. *Micropoous Mesoporous Mater.* **2008**, *111*, 143-149.
(2) Liang, J.; Li, H.; Zhao, S.; Guo, W.; Wang, R.; Ying, M. *Appl. Catal.* **1990**, *64*, 31-40.
(3) Wilson, S.; Barger, P. *Micropoous Mesoporous Mater.* **1999**, *29*, 117-126.

(4) Lopez-Orozco, S.; Inayat, A.; Schwab, A.; Selvam, T.; Schwieger, W. *Adv. Mater.* **2011**, *23*, 2602-2615.

Appendix: Copyright Permission

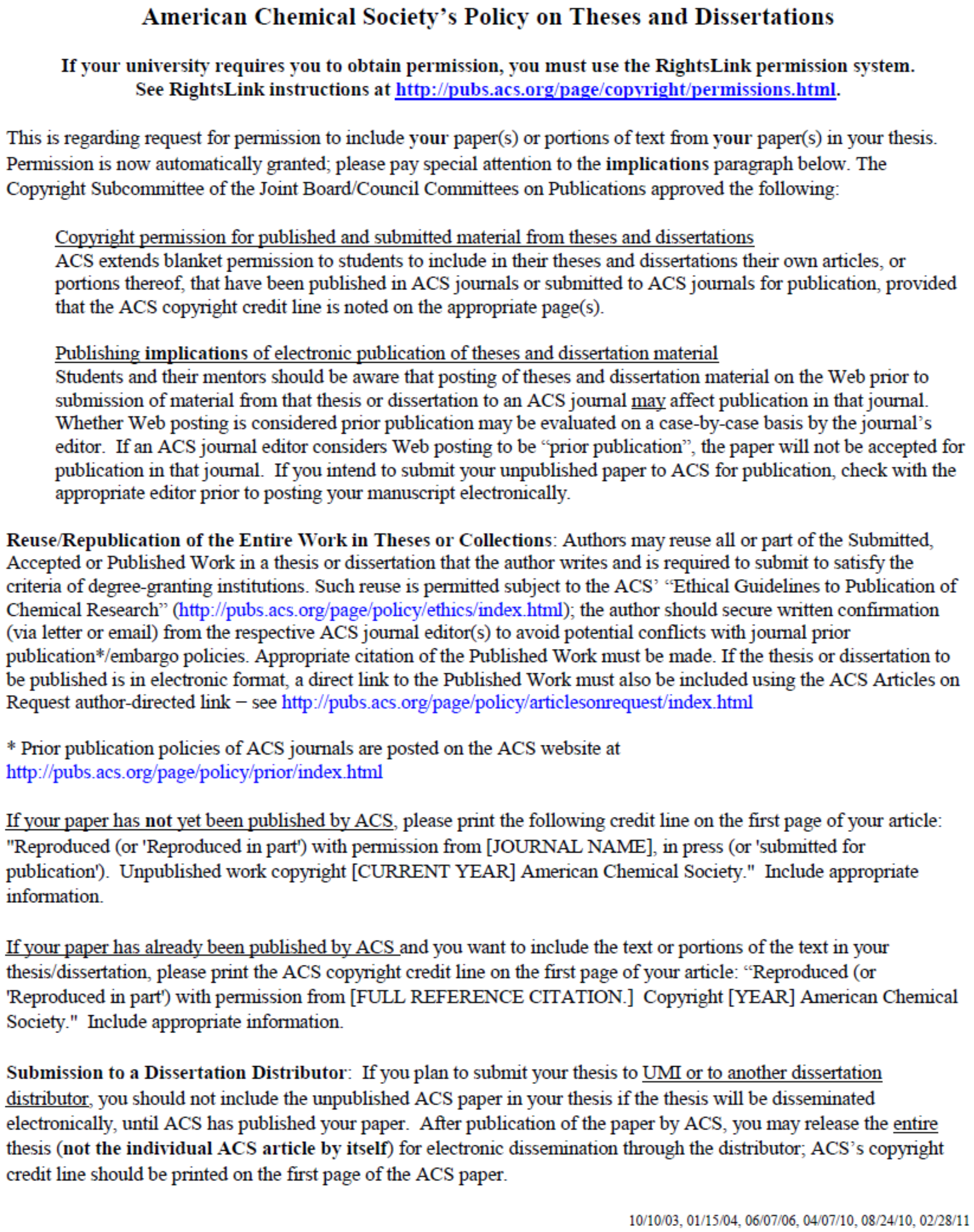

American Chemical Society's Policy on Theses and Dissertations

If your university requires you to obtain permission, you must use the RightsLink permission system.
See RightsLink instructions at http://pubs.acs.org/page/copyright/permissions.html.

This is regarding request for permission to include **your** paper(s) or portions of text from **your** paper(s) in your thesis. Permission is now automatically granted; please pay special attention to the **implications** paragraph below. The Copyright Subcommittee of the Joint Board/Council Committees on Publications approved the following:

> Copyright permission for published and submitted material from theses and dissertations
> ACS extends blanket permission to students to include in their theses and dissertations their own articles, or portions thereof, that have been published in ACS journals or submitted to ACS journals for publication, provided that the ACS copyright credit line is noted on the appropriate page(s).
>
> Publishing **implications** of electronic publication of theses and dissertation material
> Students and their mentors should be aware that posting of theses and dissertation material on the Web prior to submission of material from that thesis or dissertation to an ACS journal may affect publication in that journal. Whether Web posting is considered prior publication may be evaluated on a case-by-case basis by the journal's editor. If an ACS journal editor considers Web posting to be "prior publication", the paper will not be accepted for publication in that journal. If you intend to submit your unpublished paper to ACS for publication, check with the appropriate editor prior to posting your manuscript electronically.

Reuse/Republication of the Entire Work in Theses or Collections: Authors may reuse all or part of the Submitted, Accepted or Published Work in a thesis or dissertation that the author writes and is required to submit to satisfy the criteria of degree-granting institutions. Such reuse is permitted subject to the ACS' "Ethical Guidelines to Publication of Chemical Research" (http://pubs.acs.org/page/policy/ethics/index.html); the author should secure written confirmation (via letter or email) from the respective ACS journal editor(s) to avoid potential conflicts with journal prior publication*/embargo policies. Appropriate citation of the Published Work must be made. If the thesis or dissertation to be published is in electronic format, a direct link to the Published Work must also be included using the ACS Articles on Request author-directed link – see http://pubs.acs.org/page/policy/articlesonrequest/index.html

* Prior publication policies of ACS journals are posted on the ACS website at http://pubs.acs.org/page/policy/prior/index.html

If your paper has **not** yet been published by ACS, please print the following credit line on the first page of your article: "Reproduced (or 'Reproduced in part') with permission from [JOURNAL NAME], in press (or 'submitted for publication'). Unpublished work copyright [CURRENT YEAR] American Chemical Society." Include appropriate information.

If your paper has already been published by ACS and you want to include the text or portions of the text in your thesis/dissertation, please print the ACS copyright credit line on the first page of your article: "Reproduced (or 'Reproduced in part') with permission from [FULL REFERENCE CITATION.] Copyright [YEAR] American Chemical Society." Include appropriate information.

Submission to a Dissertation Distributor: If you plan to submit your thesis to UMI or to another dissertation distributor, you should not include the unpublished ACS paper in your thesis if the thesis will be disseminated electronically, until ACS has published your paper. After publication of the paper by ACS, you may release the entire thesis (**not the individual ACS article by itself**) for electronic dissemination through the distributor; ACS's copyright credit line should be printed on the first page of the ACS paper.

10/10/03, 01/15/04, 06/07/06, 04/07/10, 08/24/10, 02/28/11

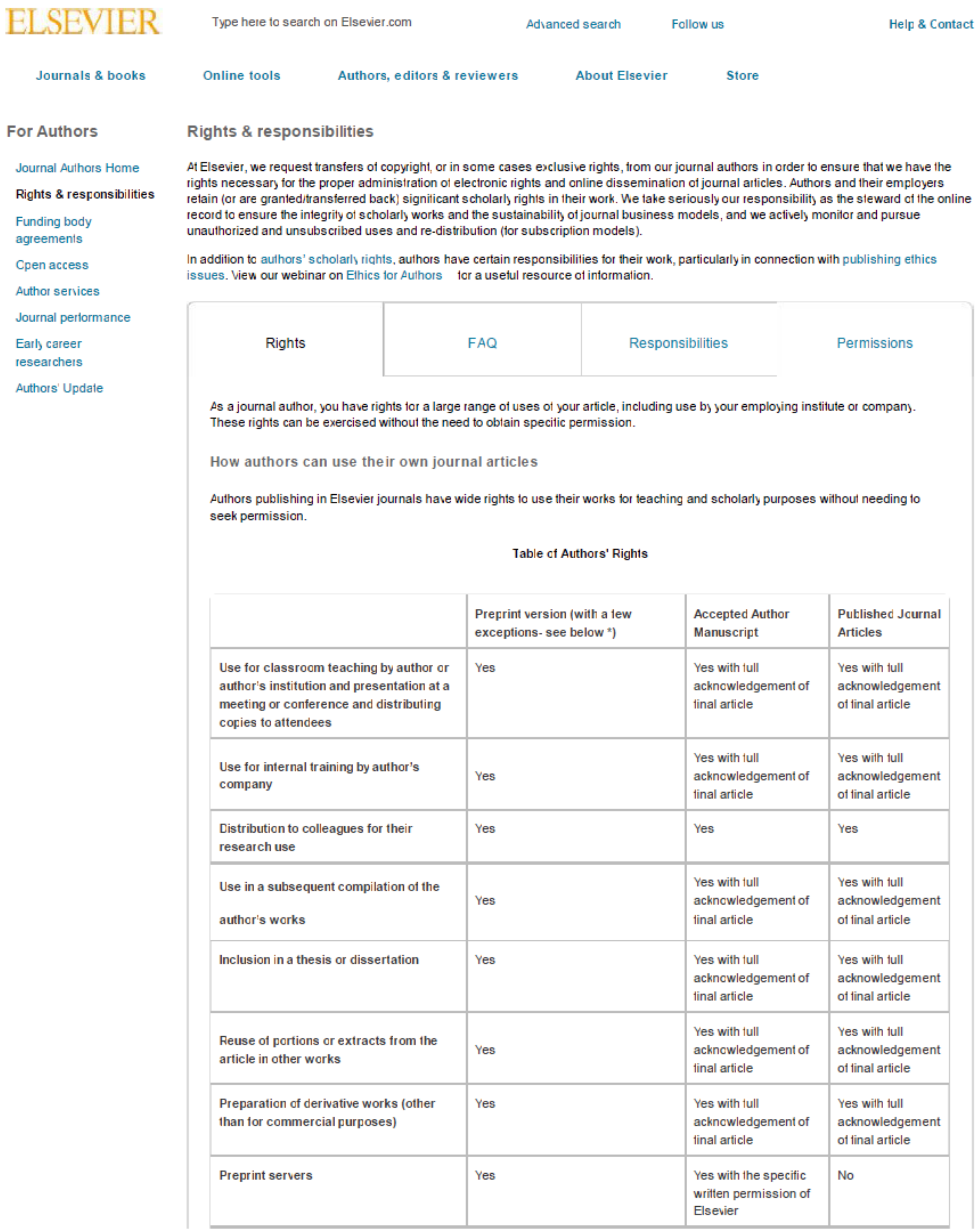

For Authors

Rights & responsibilities

At Elsevier, we request transfers of copyright, or in some cases exclusive rights, from our journal authors in order to ensure that we have the rights necessary for the proper administration of electronic rights and online dissemination of journal articles. Authors and their employers retain (or are granted/transferred back) significant scholarly rights in their work. We take seriously our responsibility as the steward of the online record to ensure the integrity of scholarly works and the sustainability of journal business models, and we actively monitor and pursue unauthorized and unsubscribed uses and re-distribution (for subscription models).

In addition to authors' scholarly rights, authors have certain responsibilities for their work, particularly in connection with publishing ethics issues. View our webinar on Ethics for Authors for a useful resource of information.

As a journal author, you have rights for a large range of uses of your article, including use by your employing institute or company. These rights can be exercised without the need to obtain specific permission.

How authors can use their own journal articles

Authors publishing in Elsevier journals have wide rights to use their works for teaching and scholarly purposes without needing to seek permission.

Table of Authors' Rights

	Preprint version (with a few exceptions- see below *)	Accepted Author Manuscript	Published Journal Articles
Use for classroom teaching by author or author's institution and presentation at a meeting or conference and distributing copies to attendees	Yes	Yes with full acknowledgement of final article	Yes with full acknowledgement of final article
Use for internal training by author's company	Yes	Yes with full acknowledgement of final article	Yes with full acknowledgement of final article
Distribution to colleagues for their research use	Yes	Yes	Yes
Use in a subsequent compilation of the author's works	Yes	Yes with full acknowledgement of final article	Yes with full acknowledgement of final article
Inclusion in a thesis or dissertation	Yes	Yes with full acknowledgement of final article	Yes with full acknowledgement of final article
Reuse of portions or extracts from the article in other works	Yes	Yes with full acknowledgement of final article	Yes with full acknowledgement of final article
Preparation of derivative works (other than for commercial purposes)	Yes	Yes with full acknowledgement of final article	Yes with full acknowledgement of final article
Preprint servers	Yes	Yes with the specific written permission of Elsevier	No

Curriculum Vitae

Name:	Lu Zhang
Post-secondary Education and Degrees:	*The* University of Western Ontario London, Ontario, Canada 2008-2013 Ph.D. candidate (Inorganic Chemistry) Beijing Jiaotong University Beijing, China 2005-2008 M.Sc. China University of Petroleum, Beijing Beijing, China 2001-2005 B.Sc.
Honours and Awards:	Western Graduate Research Scholarship, 2012-2013 International Gradduate Student Scholarship 2008-2013 First-rate scholarship at Beijing Jiaotong University, 2005-2008 Third-rate scholarship at China Univ. of Petroleum, 2002, 2003
Related Work Experience	Graduate Teaching Assistant (UWO), 2008-2013 Research Assistant (Beijing), 2008-2013, 2005

Publications:

- Zhang, L.; Chen, D.; Nie, H. Y.; Huang, Y. A Study of the Formation of Microprous Material SAPO-37. *Microporous Mesoporous Mater*. **2013**, *175*, 147-156.
- Zhang, L.; Bates, J.; Chen, D.; Nie, H. Y.; Huang. Y. “Investigations of Formation of Molecular Sieve SAPO-34”, *J. Phys. Chem. C*, **2011**, *115*, 22309-22319.

- Zhu, H.; Zhang, L. CN Patent 1,009,854,9, 2007.

Presentations:

- (Poster presentation) Zhang, L.; Huang, Y. “Examining the Crystallization Process of Zeolite LSX”, CAMBR Day at Western University, Ontario, Canada, Nov. 13, **2012**.
- (Poster presentation) Zhang, L.; Huang, Y. “A Study of Silicon Incorporation and Distribution in Microporous Material SAPO-34”, 94th Canadian Society for Chemistry Conference, Montreal, Canada, June 6-10, **2011**.
- (Poster presentation) Zhang, L.; Huang, Y. “A study of the Crystallization of SAPO-34 Molecular Sieve by Dry Gel Conversion Method”, 93th Canadian Society for Chemistry Conference, Toronto, Canada, May 29-June 2, **2010**.
- Zhu, H.; Zhang, L.; Guo, H.; Cao, X. “One Way to Produce Iron and Iron Carbide Filled Carbon Nanotubes from Coal”, the 8th National Symposium of New Carbon Materials, Guilin, China, Oct. 17-22, **2007**.

Volunteer Activity:

- Demonstrated “Fancy chemistry experiments” to secondary school students and supervise them to perform the experiments.